Top-quark Physics as a Prime Application of Automated Higher-order Corrections

Dissertation zur Erlangung des Doktorgrades an der Fakultät für Mathematik, Informatik und Naturwissenschaften Fachbereich Physik der Universität Hamburg

vorgelegt von Christian Weiss

Hamburg, Mai 2017

1. Gutachter: Dr. Jürgen Reuter
2. Gutachter: Prof. Dr. Bernd Kniehl

Tag der Disputation: 19.06.2017

Zusammensetzung der Prüfungskommission:
Dieter Horns (Uni Hamburg, Vorsitzender)
Jürgen Reuter (DESY)
Bernd Kniehl (Uni Hamburg)
Wolfgang Kilian (Uni Siegen)
Géraldine Servant (Uni Hamburg)

Abstract

Experiments in high energy physics have reached an unprecedented accuracy. This accuracy has to be matched by the theoretical predictions used to search for new physics. For this purpose, sophisticated computer programs are necessary, both for the calculation of matrix elements (tree-level and loop) and in the field of Monte-Carlo event generation.

The hadronic initial state at the LHC poses signifcant challenges for measurement and simulation. A future lepton collider, like the proposed international linear collider (ILC) in Japan or compact linear collider (CLIC) at CERN would have a much cleaner initial state. Such a machine would achieve an even higher precision. In the field of lepton colliders, the WHIZARD event generator has been established as the program of choice due to its unique treatment of beam structure functions and initial-state radiation. In this thesis, we present the extension of WHIZARD to next-to-leading order accuracy, thus augmenting it to the state of the art. We use the Frixione-Kunszt-Signer (FKS) subtraction scheme to subtract divergences, of which a detailed outline is given. This new functionality is used to perform in-depth studies of the top quark. Being the heaviest particle in the standard model, its strong connection to the Higgs sector as well as its abundant production at a future lepton collider makes it an excellent object of study. Yet, its lifetime is very short and high-multiplicity final-states of its decay products are decayed in the detector.

This thesis investigates the influence of NLO QCD corrections to the fully off-shell top production processes $e^+e^- \to \mu^+\nu_\mu e^-\bar{\nu}_e b\bar{b}$ and $e^+e^- \to \mu^+\nu_\mu e^-\bar{\nu}_e b\bar{b}H$. These calcuations have not been performed for the first time. Moreover, the incorporation of NLO QCD corrections into the resummation of the top production threshold and its matching to the relativistic continuum for the process $e^+e^- \to bW^+\bar{b}W^-$. All results are obtained with WHIZARD interfaced to the matrix-element generator OPENLOOPS.

Zusammenfassung

Die aktuellen Experimente der Hochenergiephysik besitzen eine bisher unerreichte Präzision. Diese Messgenauigkeit muss durch eine entsprechende Präzision der theoretischen Rechnungen begleitet werden, insbesondere in der Suche nach neuer Physik. Zu diesem Zweck werden fortgeschrittene Computerprogramme, sowohl zur Berechnung von tree-Level- und Loop-Matrixelementen als auch für die Monte-Carlo Eventsimulation, benötigt.

Der hadronische Initial State am LHC stellt eine Herausforderung fr experimentelle Messungen und theroetische Rechnungen dar. Ein zukünfter Leptoncollider, wie z.B. der geplante International Linear Collider (ILC) in Japan oder der Compact Linear Collider (CLIC) am CERN, hätte einen weitaus sauberen Initial State und könnte somit eine noch höhere Messgenauigkeit erreichen. Im Gebiet der Leptoncollider hat sich der Eventgenerator WHIZARD wegen seiner Fähigkeit, Beamstrahlung und -strukturfunktionen zu berücksichtigen, als Standardprogram etabliert. In dieser Arbeit präsentieren wir die Erweiterung WHIZARDs zu next-to-leading order Präzision, womit es auf den Stand der Technik gebracht wird. Wir verwenden das Frixione-Kunszt-Signer (FKS) Subtraktionsschema, über ein detaillierter Überblick gegeben wird. Die neue Funktionalität wird verwendet um das Top-Quark tiefgehend zu studieren. Als das schwerste Teilchen im Standardmodell ist es besonders stark mit dem Higgssektor verknüpft und stellt darüberhinaus wegen seiner ausgiebigen Produktion an einem Leptoncollider ein hervorragendes Forschungsobjekt dar. Allerdings wird es aufgrund seiner geringen Lebensdauer nur durch seine Zerfallsprodukte im Detektor registriert.

Diese Arbeit untersucht den Einfluss von NLO QCD Korrekturen auf off-shell Topproduktion an Hand der Prozesse $e^+e^- \to \mu^+\nu_\mu e^-\bar{\nu}_e b\bar{b}$ und $e^+e^- \to \mu^+\nu_\mu e^-\bar{\nu}_e b\bar{b}H$. Die Rechnungen hierfür wurden dafü das erste mal durchgeführt. Weiterhin studieren wir die Integration von NLO QCD Korrekturen in the Resummierung der Top-Produktionsschwelle und dessen Matching an das relativistische Kontinuum für den Prozess $e^+e^- \to bW^+\bar{b}W^-$. Alle Ergebnisse wurden mit WHIZARD in Verknüpfung mit dem Matrixelementgenerator OPENLOOPS erstellt.

List of publications

This thesis is based on the following publications:

NLO QCD Corrections to off-shell $t\bar{t}$ and $t\bar{t}H$ at the ILC
B. Chokoufé, W. Kilian, J. Lindert, S. Pozzorini, J. Reuter, C. Weiss. *Proceedings to the International Workshop on Future Linear Colliders 2016 (LCWS2016)*, Mar 2017. [1].

NLO QCD predictions for off-shell $t\bar{t}$ and $t\bar{t}H$ production and decay at a linear collider
B. Chokoufé, W. Kilian, J. Lindert, S. Pozzorini, J. Reuter, C. Weiss. *Journal of High Energy Physics*, Oct 2016. [2].

Top Physics in Whizard
J. Reuter, F. Bach, B. Chokoufé, A. Hoang, W. Kilian, M. Stahlhofen, T. Teubner, C. Weiss. *Proceedings, International Workshop on Future Linear Colliders (LCWS15)*, Feb 2016. [3].

Automation of NLO processes and decays and Powheg matching in Whizard
J. Reuter, B. Chokoufé, A. Hoang, W. Kilian, M. Stahlhofen, T. Teubner, C. Weiss. *Journal of Physics: Conference Series, ACAT2016*, Feb 2016. [4].

QCD NLO with Powheg matching and top threshold matching in Whizard
J. Reuter, F. Bach, B. Chokoufé, W. Kilian, M. Stahlhofen, C. Weiss. *Proceedings, 12th International Symposium on Radiative Corrections*, Jan 2016. [5].

Matching NLO QCD corrections in Whizard with the Powheg scheme
B. Chokoufé, W. Kilian, J. Reuter, C. Weiss. *Proceedings of Science, EPS-HEP2015*, Oct 2015. [6].

Automated NLO QCD Corrections with Whizard
C. Weiss, B. Chokoufé, W. Kilian, J. Reuter. *Proceedings of Science, EPS-HEP2015*, Oct 2015. [7].

Modern Particle Physics Event Generation with Whizard
J. Reuter, F. Bach, B. Chokoufé, W. Kilian, T. Ohl, M. Sekulla, C. Weiss. *Journal of physics: Conference Series, ACAT2014*, Oct 2014. [8].

It is further based on a work in preparation:

Matching NLL threshold resummation with fixed-order QCD for differential top-pair production (working title)
F. Bach, B. Chokoufé, A. Hoang, W. Kilian, M. Stahlhofen, T. Teubner, C. Weiss.

Some content is taken from my master's thesis:

Electroweak Corrections in the POWHEG BOX
C. Weiss. *RWTH Aachen University*, Sep 2013. [9].

List of Figures

List of Tables

Contents

1. Introduction

In 1947, Lamb and Retherford measured a difference in the energy of the $^2S_{1/2}$ and $^2P_{1/2}$ niveaus of the hydrogen atom [10]. This small shift could not be explained by the Dirac equation alone, and subsequently lead to the realization that interactions of atoms with the electromagnetic vacuum exist and lead to measurable effects. Shortly after Lamb and Retherford's discovery, the shift was explained by Bethe [11], taking into account self-interactions of the hydrogen atom with virtual photons. In the calculation, divergences due to arbitrarily large photon energies occur, renormalized by redefining the zero point of the energy scale. The insights gained here were used by Schwinger to compute the first-order correction to the electron magnetic moment one year later [12], which was confirmed experimentally shortly thereafter [13]. The Lamb shift can be considered as the first higher-order correction encountered and calculated by physicists in relativistic quantum mechanics. Along with the anomalous magnetic moment, it strongly stimulated the development of modern quantum field theory and especially the understanding of renormalization.

Nowadays, vacuum interactions are incorporated routinely in predictions for collider experiments. Rooted in the standard model of particle physics, they have long moved past virtual photons and also take into account the exchange of gluons, quarks and electroweak gauge bosons. For example, the neutral pion decay $\pi^0 \to \gamma\gamma$ is only possible via a triangle quark-loop interaction. The study of this decay was fruitful for the development of quantum chromodynamics (QCD), as its decay rate crucially depends on the number of colors and the quark charges. Moreover, the triangle diagrams with an interaction of an axial vector and two vector particles, as they are contained in the pion decay, lead to a violation of tree-level symmetries. Similar anomalies for local symmetries have to cancel in a consistent and renormalizable theory, which puts restrictions on each physics model. Loop interactions therefore play a crucial role in the internal theoretical consistency of the standard model. For the anomaly introduced by the triangle diagrams, this cancellation leads to a fundamental connection between the number of colors and the charge of the quarks [14],

$$3(Q_u + Q_d) + Q_e = 0. \tag{1.0.1}$$

Moreover, this condition has been a strong hint on the existence of the top quark after

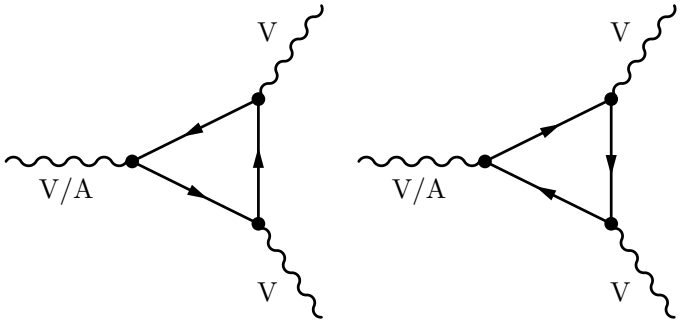

Figure 1.1. Triangle diagrams with two vector and one axial vector current which give rise to anomalies that cancel for the correct (physical) choice of fermions in the loop.

the discovery of the bottom quark in 1977. Nowadays, Higgs production at the LHC contains loop-induced gluon-gluon fusion channels, which are well understood.

Radiative corrections are computed according to a well-defined procedure. Starting from the leading-order (LO) process, all diagrams with one additional coupling constant are constructed. This includes diagrams with virtual particles as well as such with an additional real final-state particle. While the loop diagrams follow directly from perturbation theory and the Wick theorem, the addition of real-emission amplitudes is not so obvious. It follows from the requirement that infrared divergences cancel, as discussed further below. In general, k additional coupling constants make up the N^kLO computation. A precise control of higher-order corrections is essential for the discrimination of SM backgrounds and BSM signals. For example, a long-standing puzzle at the Tevatron was the measurement of a non-vanishing top-quark forward-backward asymmetry [15–17], which in the SM should be zero. This discrepancy was removed and the measurements brought into accordance with the standard model by including QCD corrections up to NNLO [18] and NLO electroweak (EW) corrections [19] in the predictions. Another important case is the muon anomalous magnetic moment, where the theoretical uncertainty is of the same size as the experimental one, but a disagreement of three to four standard deviations is observed.

Loop diagrams comprise integrals over k additional virtual momenta q_i. These integrals can diverge for $q_i \to \infty$ (ultraviolet / UV) as well as for $q_i \to 0$ (infrared / IR). The UV divergences are unphysical and can be removed by the procedure of renormalization, where they are absorbed into the parameters of the theory (e.g. couplings or masses). Consistently using renormalized quantities then only leaves IR divergences, which appear both in loop and real-emission diagrams. These singularities arise due to the production of an infinite amount of quanta with vanishing energies (soft emission) or emissions collinear to other particles. Divergences of matrix elements are parameterized with a regularization scheme. In the case of IR divergences, for example a fictitious small mass can be attributed to the radiated particle or a lower cut-off on the emis-

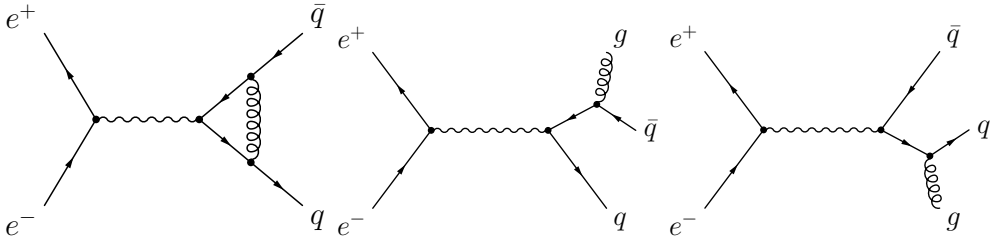

Figure 1.2. IR-divergent QCD loop and real-emission corrections to $e^+e^- \to q\bar{q}$. Note that no quark self-energy diagrams are depicted because they only have UV divergences.

.

sion energy can be applied. The most common approach is dimensional regularization [20]. It is based on the observation that to check if singularities arise from loop and phase-space integrals, it suffices to count the powers of the momenta in the numerator and denominator, including the integration measure. In dimensional regularization, the dimensionality of the integration differs from four so that, by power counting, the matrix element is finite. Divergences appear systematically in a Laurent expansion in the (non-integer) dimension $\varepsilon = 2 - d/2$, giving poles $1/\varepsilon$, $1/\varepsilon^2$, as well as finite terms and terms of $\mathcal{O}(\varepsilon)$ and higher which vanish in four dimensions ($\varepsilon = 0$). Applying this scheme to the basic example of QCD corrections to hadroproduction at a lepton collider, for which all IR-divergent diagrams are depicted in fig. 1.2, the real-emission and virtual cross sections are given as a function of ε by [14]

$$\sigma_R^{q\bar{q}g}(\varepsilon) = \sigma_0 \frac{\alpha_s C_F}{2\pi} \mathcal{N}(\varepsilon) \left(\frac{2}{\varepsilon^2} + \frac{3}{\varepsilon} + \frac{19}{2} + \mathcal{O}(\varepsilon) \right), \tag{1.0.2}$$

$$\sigma_V^{q\bar{q}(g)}(\varepsilon) = \sigma_0 \frac{\alpha_s C_F}{2\pi} \mathcal{N}(\varepsilon) \left(-\frac{2}{\varepsilon^2} - \frac{3}{\varepsilon} - 8 + \mathcal{O}(\varepsilon) \right). \tag{1.0.3}$$

We observe that the ε-poles exactly cancel and that the total NLO correction is finite in the four-dimensional limit $\varepsilon \to 0$[1]. This IR-cancellation is known since the early days of relativistic quantum mechanics in the context of photon emissions from electrons. Discovered by Bloch and Nordsieck in 1937 [21], and elaborated further upon by Yennie, Frautschi and Suura [22], it was put on a systematic footing by Kinoshita, Lee and Nauenberg [23, 24]. The so-called KLN theorem states that higher-order amplitudes are IR-finite, given that degenerate configurations are suitably averaged over. It is the foundation on which the subtraction methods discussed in this thesis are based.

In the last decade, next-to-leading order has become standard in calculations for LHC physics. This can to a large extend be attributed to the relatively easy availability of

[1]The factor $\mathcal{N}(\varepsilon)$ is a normalization constant with $\mathcal{N}(\varepsilon \to 0) = 1$. Its expansion leads to ε and ε^2 terms which produce additional finite contributions to the cross sections, which are nevertheless irrelevant because, if $\mathcal{N}(\varepsilon)$ is chosen consistently, they cancel in the sum of the virtual and real contribution.

one-loop matrix elements for high multiplicities, based on an in-depth understanding of scattering amplitudes. At NNLO and higher, this automation is not yet realized. The state-of-the art calculations are made available to other physicists amongst others by the means of Monte Carlo event generators. These are more or less specialized tools, and in a full experimental study, which might also include parton showers, hadronization and detector simulation, various combinations of them are used. Parton-level event generators with automated or semi-automated NLO setups are e.g. Helac [25], MG5_aMC@NLO [26, 27], MCFM [28, 29], Sherpa [30], VBFNLO [31] and Whizard [32]. Furthermore, Pythia [33, 34] and Herwig [35–37] are the most commonly used parton showers in high energy physics. Automated next-to-leading order calculations in these event generators have emerged in the last years, thus meeting the need for increasing calculational accuracy in collider experiments. It is a very field of research, especially in the context of electroweak and mixed corrections. A complexity in numerical NLO calculations arises because they cannot access dimensionally regularized expressions as in eq. (1.0.2) and eq. (1.0.3) fully analytically. This would require a d-dimensional Monte-Carlo integration, with in general $d \in \mathbb{C}$. Also, approaches based on cut-off or mass-regularization introduce dependencies of the results on unphysical parameters. Monte-Carlo NLO calculations are therefore most commonly based on subtraction schemes, which rely on the KLN theorem to add and subtract terms to the total cross section which cancel the divergences individually in the real and virtual contribution. The two most common subtraction schemes are the Catani-Seymour approach [38] and the Frixione-Kunszt-Signer (FKS) scheme [39, 40]. Catani-Seymour subtraction is used e.g. in Sherpa or Helac, whereas Madgraph and Whizard use FKS. Another challenge in the NLO-completion of event generation is the interface of NLO hard interactions to parton showers. Already at LO, large logarithms are resummed by Sudakov factors. In order to keep NLO accuracy, the fixed-order matrix element of the hard interaction needs to be matched to the resummed parton shower accordingly. Also here, two major approaches exist. MC@NLO [41, 42] relies on the subtraction of the $\mathcal{O}(\alpha_s)$ terms introduced by the parton shower. The Powheg method [43], on the other hand, rearranges the parton shower in such a way that restores overall fixed-order accuracy. It is implemented in the Powheg Box [44], which had a large influence on automated FKS calculations. Monte-Carlo event generators not only play a major role in currently running LHC experiments, but are also essential in the design of future particle accelerators. Especially lepton colliders, such as the proposed International Linear Collider (ILC) [45, 46] or the Compact Linear Collider (CLIC) [47] promise to provide an unprecedented precision in the electroweak and top sector. Higgs bosons and top quarks will be produced in abundance at such a machine. Since the top quark has the largest mass of all particles in the standard model, they are deeply connected, with far-reaching consequences e.g. for the (meta-)stability of the universe, which crucially depends on

m_t and m_H [48–50]. A precise determination of top-quark properties, particularly its weak couplings, is thus a powerful opportunity to find hints of new physics and might also give input to other areas of fundamental physics such as cosmology.

The center-of-mass energy at a linear collider is tunable. On the other hand, it has a low spread. Combined with the high precision of modern particle detectors, this makes the study of the top quark feasible also in the threshold region at $\sqrt{s} \approx 2m_t$ [51, 52]. Here, the top quarks are non-relativistic and form a quasi-bound state which decays into the final state $bW^+\bar{b}W^-$. This production process at threshold is strongly enhanced due to large contributions from virtual gluon exchange. To get a precise theoretical treatment of the production cross section, these large corrections need to be resummed, which is commonly done in the non-relativistic QCD (NRQCD) framework [53–56].

This thesis contains two parts. The first one is an introduction to FKS subtraction and its implementation in the event generator WHIZARD [4–8], presenting examples for its NLO features. The second part contains detailed studies of off-shell top-quark production both in the continuum and at threshold with WHIZARD based on ref. [2] and ref. [57]. Each part consists of several chapters. In chapter 2, we give a detailed introduction into the FKS subtraction scheme. Papers on FKS [39, 40, 44, 58–61], usually have a focus on a certain aspect of the method, leaving out the overall picture. The intention of that chapter is to present a coherent review of all relevant aspects required to understand state-of-the art applications of the method. The chapter starts out by a brief overview of the soft and collinear factorization of matrix elements and then implements this knowledge in the derivation of real and virtual subtraction terms. Moreover, although this thesis focuses on lepton colliders, also a brief introduction into the subtraction of initial-state divergences and structure functions is given. The chapter concludes with a brief discussion on pure electroweak and mixed QCD–electroweak corrections. Chapter 3 presents the WHIZARD event generator. We focus on the overall architecture of the program with a focus on the inclusion of NLO calculations. It follows a collection of WHIZARD+NLO applications which serve as validation of the program. Some aspects not mentioned in the previous chapters are elaborated in more detail, like the subtraction of divergences in particle decays, POWHEG matching or the validation of resonance-aware subtraction. An essential part of this chapter is a comparison of WHIZARD results with those of MADGRAPH presented in ref. [62] for a diverse set of lepton collider processes and their discussion.

The first chapter in part two, chapter 5, presents a study of fully off-shell top-quark pair production with and without an associated Higgs boson at NLO QCD at a lepton collider. Thereby, the W is assumed to decay only leptonically. A detailed study of the phenomenology of the process is given, with a focus on the effect of NLO corrections on the high-precision measurement of top-quark and Higgs boson properties. Also, we elaborate on the feasibility of BSM searches in the top-quark sector by investigating

the dependence of the NLO cross section on the top Yukawa coupling as well as NLO effects on the forward-backward asymmetry. The subsequent chapter 6 is a summary of top threshold resummation in WHIZARD, focusing on the role of fixed-order NLO corrections therein. They are modified to match the requirements of a factorized computation, leading both to modified FKS regions as well as color-correlations. With this adaptations, we discuss the effect of real and virtual corrections to the resummed NLL matrix elements as well as the matching to the top continuum.

Part I.

Aspects of automated NLO calculations

2. The FKS Subtraction Scheme

Next-to-leading order Monte-Carlo computations have no possibility to perform dimensional regularization to cancel divergences, because the very essence of the approach is the sampling of four-dimensional momenta. Instead, they rely on the so-called subtraction approach. The idea behind divergence subtraction is to work out the singular limits of the part of the NLO cross section, $d\sigma_S$ and subtract them from the real contribution. Integrating over the whole phase space, the singular regions have a vanishing weight, given that the limit is accurate enough. As discussed in the introduction, the KLN theorem [23, 24] ensures that the same subtraction term, added to the virtual contribution, also cancels its divergences and allows for a separate integration. This motivates a general formula for the total next-to-leading order cross section in the subtraction approach,

$$\sigma^{\mathrm{NLO}} = \sigma^{\mathrm{Born}} + \int d\Phi_{n+1} \underbrace{\left[\mathcal{R}(\Phi_{n+1}) - d\sigma_S(\Phi_{n+1})\right]}_{\text{Finite by construction}} + \underbrace{\int d\Phi_n \mathcal{V}(\Phi_n) + \int d\Phi_{n+1} d\sigma_S(\Phi_{n+1})}_{\text{Finite by KLN}} . \tag{2.0.1}$$

$\mathcal{R}$ denotes the squared real amplitude and $\mathcal{V}$ the interference term of the Born and virtual amplitudes.[1]

Like $\mathcal{R}$, $d\sigma_S$ is a function of the full $n+1$-particle phase space. This requires an integration of the three additional real degrees of freedom, making the construction of the virtual subtraction terms distinctly more involved than that of the real ones. It leads to non-trivial integrals, which will be outlined in section 2.3 While the soft and collinear limits of the matrix elements are unambiguous, there are different approaches in the way the singular regions are sampled. A concrete implementation of the subtraction scheme must yield smooth transitions to zero as a phase-space point approaches a singular region. A complicated multi-leg process can have a multitude of configurations in which divergences occur, and the proper choice of the subtraction procedure can be

[1] It should be noted that we did write σ^{Born} instead of σ^{LO}, because in general, there is a difference between the LO cross section and the Born contribution to the NLO cross section. For example, a different scale might be used in a pure LO calculation and the Born part of an NLO one. Also, the requirement of NLO values for gauge boson and quark widths lead to significant differences between the two quantities. An example of a process where this distinction is of crucial importance is off-shell top-quark production, where σ^{LO} and σ^{Born} differ by several percent.

the bottleneck of computational efficiency.

There are two major approaches to NLO subtraction, dipole-based [38, 63] methods and Frixione-Kunszt-Signer (FKS) subtraction [39, 40, 58]. Dipole-based methods, the most popular one being Catani-Seymour (CS) subtraction [38, 64], focus on soft emissions. A soft emission is made up of the soft particle itself and the two colored partons which exchange the first parton. These three indices make up a dipole, and a summation occurs over all allowed index configurations. FKS subtraction emphasizes collinear singularities, so that the underlying summation is de facto two-dimensional. Indeed, as also the authors of ref. [40] claim, this leads to reduced number of subtraction terms than in the CS formalism. Furthermore, a subtraction scheme based on modified splitting functions, so-called Nagy-Soper dipoles, has been developed recently [63, 65–67]. It is based on a parton-shower approach with the possibility to keep quantum interference effects such as spin or color correlations [68, 69]. The NLO+PS matching in this framework was achieved in ref. [70]. FKS was first applied to three-jet production at a hadron collider [39] and later generalized in ref. [58]. From its beginning, the FKS scheme has been closely related to the study of NLO parton shower matching procedures, like MC@NLO [71] and especially POWHEG [43]. In combination with POWHEG, the FKS scheme obtained its first automated Monte-Carlo implementation in form of the POWHEG BOX[2] [44, 59]. Other event generators to include FKS subtraction are MADGRAPH [26, 27],HERWIG++ [37] and WHIZARD [2, 32].

In this chapter, we give a detailed description of FKS subtraction for QCD. We start with the discussion of collinear and soft factorization in section 2.1. The knowledge gained there about the corresponding limits enables us to derive real subtraction terms in section 2.2. Their integration in the context of the virtual matrix element is discussed thereafter in section 2.3. At this point, all requirements for a subtraction calculation of a lepton-lepton collision process are met. The rest of the chapter gives details about the subtraction in the presence of hadron structure functions (PDFs) in section 2.4 and the resonance-aware FKS modification in section 2.6. We conclude with some aspects of electroweak corrections.

2.1. Prerequisites

All subtraction schemes rely on the factorization of collinear and soft emissions to extract the corresponding limits from which subtraction terms can be produced. We therefore give an overview about collinear and soft singularities in QCD. Further, we discuss namings and conventions used in the rest of the chapter.

[2]The homepage of the POWHEG BOX, `http://powhegbox.mib.infn.it/` contains an extensive list of phenomenological studies performed with it.

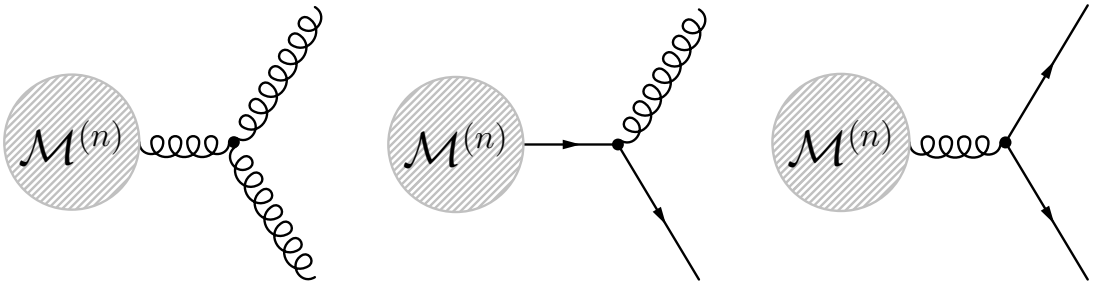

Figure 2.1. QCD splittings which can induce a collinear divergence.

2.1.1. Collinear singularities

We start our discussion with an analysis of collinear factorization in QCD splittings. Let $\mathcal{M}_{ij}$ denote the amplitude of the Feynman diagram in which a collinear massless parton j is emitted by another massless parton i. In QCD, these can be any of the three splittings depicted in fig. 2.1. The complete squared matrix element is $|\mathcal{M}^{n+1}|^2 = \left|\sum_{i,j} \mathcal{M}_{ij}\right|^2$, which contains interference terms between diagrams with emissions from different legs. This interference can be removed by replacing the numerator in the propagator of the splitting parton by a sum over spinors or gluon polarization vectors. Choosing a suitable gauge, the splitting kinematics can then be decoupled from $\mathcal{M}^{(n)}$. The splitting parton then defines the collinear direction, with a momentum $p^\mu = (p, 0, 0, p)$. We further denote with p_1 and p_2 the momenta of the two splitting particles, cf. fig. 2.1, and $p_{12} = p_1 + p_2$. Note that $p_{12} \neq p$, as the latter one is only a light-like auxiliary momentum. Also, let

$$z = \frac{p_1^0}{p_{12}^0}. \tag{2.1.1}$$

be the energy fraction of one of the splitting partons. Analogously, $p_2^0 = (1-z)p_{12}^0$. To parameterize the collinear limit of p_1 and p_2, we introduce the transverse momentum $k_\perp^\mu$. To restore on-shellness, we further use a unit vector n^μ, so that

$$p_1^\mu = zp^\mu + k_\perp^\mu - \frac{k_\perp^2}{z}\frac{n^\mu}{2p\cdot n}, \tag{2.1.2}$$

and

$$p_2^\mu = (1-z)p^\mu - k_\perp^\mu - \frac{k_\perp^2}{1-z}\frac{n^\mu}{2p\cdot n}. \tag{2.1.3}$$

The unit vector n^μ is orthogonal to $k_\perp$, $n\cdot k_\perp = 0$, and moreover $n^2 = 0$. Using eq. (2.1.2),

a detailed calculation for the triple-gluon splitting gives

$$\left|\mathcal{M}_{gg}^{n+1}\right|^2 = \frac{8\pi\alpha_s C_A}{p_{12}^2}\left[-2g^{\mu\nu}\left(\frac{z}{1-z}+\frac{1-z}{z}\right) - 4(1-\varepsilon)z(1-z)\frac{k_\perp^\mu k_\perp^\nu}{k_\perp^2}\right]\mathcal{M}_\mu^n\mathcal{M}_\nu^n. \tag{2.1.4}$$

There is a factor of $8\pi\alpha_s$ instead of just a factor of $4\pi\alpha_s$ because an additional factor of two enters through the Dirac algebra of the vertices. The ε-pole originates from the use of d-dimensional Dirac algebra. We observe the emergence of spin correlation terms in the second summand of eq. (2.1.4), i.e. $k_\perp^\mu k_\perp^\nu \mathcal{M}_\mu^n \mathcal{M}_\nu^n$. The Lorentz indices μ and ν of the amplitude $\mathcal{M}^n$ are associated with gluon polarization vectors. Thus, this term mix amplitudes with different Lorentz polarizations. These spin-correlated matrix elements are a distinct feature of the collinear factorization. Calculations for $\left|\mathcal{M}_{qg}^{n+1}\right|^2$ and $\left|\mathcal{M}_{qg}^{n+1}\right|^2$ yield the same structure for the collinear-factorized squared matrix element, so that in general

$$\left|\mathcal{M}_{ij}^{n+1}\right|^2 = \frac{8\pi\alpha_s}{k^2}\hat{P}_{ij}^{\lambda}(z,k_\perp;\varepsilon)|\mathcal{M}_\lambda^n|^2, \tag{2.1.5}$$

where k is the momentum of the emitter in the Born phase space and λ stands either for two spinor or vector indices. The $\hat{P}_{ij}^{\lambda}$ expressions are called the **generalized Altarelli-Parisi splitting functions** [72], given by

$$\hat{P}_{qg}^{ss'}(z,k_\perp;\varepsilon) = \delta^{ss'}C_F\left[\frac{1+z^2}{1-z} - \varepsilon(1-z)\right], \tag{2.1.6}$$

$$\hat{P}_{q\bar{q}}^{\mu\nu}(z,k_\perp;\varepsilon) = T_F\left[-g^{\mu\nu} + 4z(1-z)\frac{k_\perp^\mu k_\perp^\nu}{k_\perp^2}\right], \tag{2.1.7}$$

$$\hat{P}_{gg}^{\mu\nu}(z,k_\perp;\varepsilon) = 2C_A\left[-g^{\mu\nu}\left(\frac{z}{1-z}+\frac{1-z}{z}\right) - 2(1-\varepsilon)z(1-z)\frac{k_\perp^\mu k_\perp^\nu}{k_\perp^2}\right]. \tag{2.1.8}$$

It can be seen that only the splitting of gluons (and more generally, vector particles) induce spin correlations. The spin structure of the $q \to qg$ splitting, eq. (2.1.6), is trivially given by $\delta^{ss'}$. Equation (2.1.5) in combination with the splitting functions give a complete description of final-state collinear emissions which we will use in section 2.2 to construct subtraction terms. Similar expressions can be derived for initial-state emissions.

2.1.2. Soft singularities and eikonal currents

The splittings in eq. (2.1.6) – eq. (2.1.8) also show the soft behavior of the respective splittings for $z = 0$ and $z = 1$. The $g \to gg$ and $q \to qg$ splittings exhibit a singularity for soft emissions [3], whereas the $g \to q\bar{q}$ splitting is soft-finite. The emission of a soft

[3] In fact, it is the only sufficient way to prove the existence of soft singularities. The frequently found explanation utilizing a single propagator (usually one for a quark) has the shortcoming that the

gluon does not affect the momenta of the radiating partons. It also does not change the spin[4]. However, the gluon always carries away color charge, so the color structure of the radiating partons is changed. This leads to the appearance of color correlations in the expressions involving the soft limit, which are the topic of this section.

Soft gluon factorization is best described using the notation common in the literature [38, 74], where the matrix element is decomposed in color space,

$$\mathcal{M}_{c_1,\dots,c_n}(p_1,\dots,p_n) = \langle c_1,\dots,c_n|\mathcal{M}(p_1,\dots,p_n)\rangle. \tag{2.1.9}$$

The squared matrix element is then simply

$$|\mathcal{M}(p_1,\dots,p_n)|^2 = \langle \mathcal{M}(p_1,\dots,p_n)|\mathcal{M}(p_1,\dots,p_n)\rangle. \tag{2.1.10}$$

We introduce the color charge operator $\mathbf{T}_i$, which is associated with the emission of a gluon from a specific parton i. We single out the color index of the emitted gluon as a. $\mathbf{T}_i$ is defined by its action on color space,

$$\langle a, c_1,\dots,c_i,\dots,c_n|\mathbf{T}_i|b_1,\dots,b_i,\dots,b_n\rangle = \delta_{c_1,b_1}\dots T^a_{c_i,b_i}\dots\delta_{c_n,b_n}, \tag{2.1.11}$$

where

$$T^a_{c_i,b_i} = \begin{cases} if_{c_i a b_i} & \text{if } i = \text{gluon} \\ t^a_{c_i b_i} & \text{if } i = \text{FS quark or IS antiquark} \\ \bar{t}^a_{c_i b_i} = -t^a_{b_i c_i} & \text{if } i = \text{IS quark or FS anti-quark.} \end{cases} \tag{2.1.12}$$

Color-charge operators commute if $i \neq j$, otherwise $\mathbf{T}_i^2 = C_i$, where $C_i = C_A$ if i is a gluon and $C_i = C_F$ if i is a quark or anti-quark. The tree-level soft-gluon current, or eikonal current, is defined as

$$\mathbf{J}^\mu = \sum_{i=1}^{n} \mathbf{T}_i \frac{p_i^\mu}{p_i\cdot q}, \tag{2.1.13}$$

where the summation is performed over all external (colored) particles and q denotes the gluon momentum[5] To see its connection to soft gluon emissions, consider a $q \to qg$

factor $E \to 0$ in the denominator is cancelled by the phase-space volume.

[4]If this sounds unintuitive, consider that in an soft emission, the gluon is practically non-existent. Instead, the emission process can be approximated by an infinitesimal "kick" to the emitter. In QED, it can be shown that the eikonal currents of eq. (2.1.13) emerge from the Fourier transform of a fermion current

$$j^\mu(x) = e\int_0^\infty dt \frac{p'^\mu}{m}\delta^{(4)}\left(x - \frac{p'}{m}t\right) - e\int_{-\infty}^0 dt\frac{p^\mu}{m}\delta^{(4)}\left(x-\frac{p}{m}t\right)$$

which experiences such a sudden change [73].

[5]Sometimes, the less strict formulation $J^\mu = \sum_i \frac{2p_i^\mu - q^\mu}{2p_i\cdot q - q^2}\mathbf{T}_i$ is used, since eq. (2.1.13) can lead to scaleless integrals.

splitting. Let $m \neq 0$ be the quark mass. The emission from one leg can then be written as

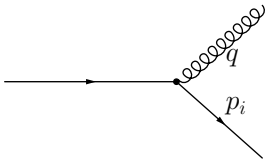

$$\sim g_s \bar{u}(p_i)\gamma^\mu T^a_{bc} \frac{\not{p}_i - \not{q} + m}{(p_i - q)^2 - m^2} \varepsilon^\mu(q). \tag{2.1.14}$$

In eq. (2.1.14), the quark mass cancels in the denominator since $p_i^2 = m^2$. In the numerator, we can use the Dirac equation after substituting $\gamma^\mu(\not{p}_i + m) = (-\not{p}_i + m)\gamma^\mu + 2p_i^\mu$, rendering the whole expression independent of the quark mass. In the limit $q \to 0$ the soft limit the $n+1$-particle matrix element can thus be expressed with a color decomposition w.r.t to the gluon

$$\langle a|\mathcal{M}^{n+1}(q, p_1, \ldots, p_n)\rangle \approx g_s \varepsilon^\mu(q) J^a_\mu(q) |\mathcal{M}^n(p_1, \ldots, p_n)\rangle, \tag{2.1.15}$$

where we have made use of the eikonal current from eq. (2.1.13). The spinor present in eq. (2.1.14) is absorbed into $\mathcal{M}^n$ and $\mathcal{M}^{n+1}$. Squaring the amplitude is now a straightforward task. It yields

$$|\mathcal{M}^{n+1}(q, p_1, \ldots, p_n)|^2 \approx -4\pi\alpha_s \sum_{i,j=1,n} \frac{p_i \cdot p_j}{(p_i \cdot q)(p_j \cdot q)} |\mathcal{M}^n_{(i,j)}(p_1, \ldots, p_n)|^2. \tag{2.1.16}$$

$|\mathcal{M}^n_{(i,j)}|^2$ includes the effects of possibly non-trivial color interactions in the soft limit and is from now on referred to as the color-correlated Born matrix element[6] It is given by

$$\begin{aligned} |\mathcal{M}^n_{(i,j)}(p_1, \ldots, p_n)|^2 &= \langle \mathcal{M}^n(p_1, \ldots, p_n)|\mathbf{T}_i \cdot \mathbf{T}_j|\mathcal{M}^n(p_1, \ldots, p_n)\rangle \\ &= \left[\mathcal{M}^n_{c_1,\ldots,b_i,\ldots,b_j,\ldots c_n}(p_1, \ldots, p_n)\right]^* T^a_{b_i d_i} T^a_{b_j d_j} \mathcal{M}^n_{c_1,\ldots,d_i,\ldots,d_j,\ldots,c_n}(p_1, \ldots, p_n), \end{aligned} \tag{2.1.17}$$

where a summation over identical indices is implied.

2.1.3. Notation

We define a basic notation to be used throughout this thesis. The Born phase space for a $2 \to n$ process is given by

$$\bar{\Phi}_n = \{\bar{k}_\oplus, \bar{k}_\ominus, \bar{k}_1, ..., \bar{k}_n\}, \tag{2.1.18}$$

[6]Some authors prefer the term "color-linked".

i.e. final-state particles are numbered starting by 1 and the indices $\oplus$ and $\ominus$ are used to denote initial-state momenta parallel and anti-parallel to the beam axis. Likewise, the phase space including one additional gluon emission is

$$\Phi_{n+1} = \{k_\oplus, k_\ominus, k_1, ..., k_n, k_{n+1}\}. \tag{2.1.19}$$

It is always assumed that the emitter momentum is at position n and that k_{n+1} is the momentum of the radiated particle. The spatial part of a four-momentum k is described by $\mathbf{k}$. Moreover, $\underline{k} = |\mathbf{k}|$.

The gluon momentum has three independent parameters. In FKS, they are given by the following dimensionless quantities:

- ξ parameterizes the gluon energy. In the standard approach, it is

$$\xi = \frac{2k^0_{n+1}}{\sqrt{s}}, \tag{2.1.20}$$

  but different definitions are possible, e.g. for the treatment of resonances.

  The gluon energy is bounded from above by $\xi_{\max}$, i.e. $\xi \in [0, \xi_{\max}]$ with $\xi_{\max} \leq 1$. This bound arises because, loosely speaking, the gluon cannot take away more energy than available from the emitter. Thus, in the massless case,

$$\xi_{\max} = \frac{2\bar{k}^0_{\text{em}}}{\sqrt{s}}. \tag{2.1.21}$$

  More complicated expressions arise for emissions from massive particles, which are discussed in appendix A.3.

- $y \in [-1, 1]$ parameterizes the polar angular separation of the emitter and the gluon. For massless emitters, it is simply

$$y = \cos\theta_{n,n+1}. \tag{2.1.22}$$

  The definition of y for massive emitters is a bit more involved. The simple definition in eq. (2.1.22) is replaced by the slope of a line in a Dalitz plot. Details about this are given in appendix A.1.3.

- $\phi \in [0, 2\pi]$ is the azimuthal angle difference of the two splitting particles in the transversal plane.

The total NLO matrix element for lepton collisions without structure functions is the sum

$$\sigma_{\text{NLO}} = \sigma^{\text{Born}}_{\text{NLO}} + \sigma^{\text{Real}}_{\text{NLO}} + \sigma^{\text{Virt}}_{\text{NLO}}. \tag{2.1.23}$$

The involvement of structure functions like parton densities introduces additional terms to be discussed later. Note that, in general, the first summand does not equal the LO cross section σ_{LO}, because the physical parameters it consists of, such as e.g. particle widths or coupling constants, can have differing values at leading and next-to-leading order. The integrands of the summands in eq. (2.1.23) are denoted by $\mathcal{B}$, $\mathcal{R}$ and $\mathcal{V}$, respectively. We will also use the notation $d\sigma^i$ for integrands with a meaning of i defined beforehand. For the treatment of integrated cross sections, phase-space factorization is of crucial importance. This means that

$$d\Phi_{n+1} = d\bar{\Phi}_{\mathrm{rad}} d\Phi_n = (\mathcal{J} d\xi dy d\phi)\, d\Phi_n, \tag{2.1.24}$$

where the Jacobian $\mathcal{J}$ depends on the specific real-emission construction. Phase-space factorization, combined with matrix-element factorization discussed in the previous two sections, leads to a structure of $\mathcal{R}$ and $\mathcal{V}$ which mainly involves a Born-like matrix element times a kinematical function. Finally, to label particles, we adopt the notation of ref. [40],

$$n_H : \quad \#\text{ Strongly interacting massive particles}, \tag{2.1.25}$$
$$n_L^{(B,R)} : \quad \#\text{ Strongly interacting light particles (Born or Real)}, \tag{2.1.26}$$
$$n_\emptyset : \quad \#\text{ Non-strongly interacting final-state particles}. \tag{2.1.27}$$

Since, next to collision processes, we also want to include particle decays in our FKS setup, we introduce a slight modification to ref. [40] by denoting the number of initial state particles by n_I. In ref. [40], n_I stands for the index of the first strongly-interacting particle, which we call n_F. Thus, $n_F = 1$ for hadron-hadron collisions, $n_F = 2$ for lepton-hadron collisions, and $n_F = 3$ for lepton-lepton collisions (assuming that $n_L \neq$ or $n_H \neq 0$). With this notation, we assume that the particles in the process definition are ordered in the following way:

$$\begin{aligned}
&1 \leq i \leq n_I && : \text{Initial state},\\
&n_I + 1 \leq i \leq n_L^{(B,R)} + n_I && : \text{massless quarks and gluons},\\
&n_L^{(B,R)} + n_I + 1 \leq i \leq n_L^{(B,R)} + n_H + n_I && : \text{heavy quarks},\\
&n_L^{(B,R)} + n_H + n_I + 1 \leq i \leq n_L^{(B,R)} + n_H + n_\emptyset + n_I && : \text{non strongly-interacting particles}.
\end{aligned}$$

Furthermore, $\mathcal{I}_i$ denotes the identity of the particle with index i. E.g., if i is an anti quark, $\mathcal{I}_i = \bar{q}$.

2.2. Real subtraction terms

In this section, we construct subtraction terms for the real matrix element. We assume that the Born phase space is divergence-free, i.e. that appropriate cuts are applied to remove infrared divergences such as for example those arising in the emission of a jet. Let $\mathcal{R}$ denote the squared amplitude of the real matrix element, associated with the radiative corrections to a given process. It contains both soft and collinear divergences, which in terms of the parameterizations in eq. (2.1.20) and eq. (2.1.22) means $\xi \to 0$ and $y \to \pm 1$. Moreover, we assume that the radiative corrections only affect final-state particles, such as for QCD corrections to lepton collisions. The extension to initial-state divergences involves corrections to parton densities and is discussed in section 2.4.

2.2.1. Singular regions and $\mathcal{S}$ functions

The full knowledge about the real phase space Φ_{n+1} allows to identify several disjoint regions, in which at most one collinear and one soft divergence exists. This way, $\mathcal{R}$ is split up into different contributions, each related to one particular **singular region**,

$$\mathcal{R} = \sum_{i,j} \mathcal{R}_{ij}. \tag{2.2.1}$$

Here, $\mathcal{R}_{ij}$ becomes divergent only when the momentum k_i or k_j becomes soft, or $\mathbf{k}_i \parallel \mathbf{k}_j$ (collinear divergence). Everywhere else, $\mathcal{R}_{ij}$ is finite. Especially, in the singular region associated with another (i,j)-pair, it approaches zero. The (i,j) tuples are called FKS pairs. In words, an FKS pair is a pair of particles which induce soft and / or collinear divergences in $\mathcal{R}$, excluding the (appropriately removed) divergences already present at Born level. As it is common, we will use the index α to refer to a given FKS pair.

In QCD, FKS pairs can be put into three basic groups:

- $\mathcal{I}_\alpha = (q,g)$ and $\mathcal{I}_\alpha = (\bar{q},g)$ (and vice versa), .i.e. gluon emission off a quark or anti-quark, respectively. These regions always induce soft divergences, and collinear ones if $m_q = 0$.
- $\mathcal{I}_\alpha = (g,g)$, which are soft and collinear divergent.
- $\mathcal{I}_\alpha = (q,\bar{q})$ (and vice versa), i.e. a $g \to q\bar{q}$ splitting. These regions are finite in the soft limit, cf. eq. (2.1.8), but induce collinear divergences if $m_q = 0$.

Out of these FKS pairs, the summation in eq. (2.2.1) either runs over combinations of the first two kinds, or exclusively contains those of the last one. This is because while (q,g) and (g,g) correspond to an additional gluon in the real flavor structure, $(q,\bar{q})$ have an additional quark and one gluon less. Therefore, they do not have the same real

matrix element $\mathcal{R}$. All FKS pairs belonging to the same real flavor structure f_r are put together in the set $\mathcal{P}_{\text{FKS}}^{\text{sym}}(f_r)$, defined as

$$\mathcal{P}_{\text{FKS}}^{\text{sym}}(f_r) = \Big\{(i,j) : \overbrace{n_F \leq i \leq n_L^{(R)} + n_H + n_I}^{\text{can contain initial state}}, \overbrace{n_I + 1 \leq j \leq n_L^{(R)} + n_H + n_I}^{\text{constrained to final state}}, i \neq j, \\ \mathcal{R}(f_r) \to \infty \quad \text{if} \quad k_i^0 \to 0 \quad \text{or} \quad k_j^0 \to 0 \quad \text{or} \quad \mathbf{k}_i \parallel \mathbf{k}_j \Big\}. \tag{2.2.2}$$

Here, the second line contains the condition that (i,j) must induce a soft or collinear divergence. Since an FKS pair can never be made up of two initial-state particles, one index can be constrained to the final state. In our case, this is j, which starts at $n_I + 1$.[7] The second index is thus the radiated particle, which is also referred to as the FKS parton. Note that we also include the possibility of particle decays in definition (2.2.3) by using a variable n_I. The superscript *sym* emphasizes that both final-state pairs (i,j) and (j,i) are treated identically. However, they yield the same matrix element, so that their contribution appears twice in eq. (2.2.1). This is for example the case for the collinear divergence in a $(q,\bar{q})$ region. There are two ways to solve this problem. The first one is to apply appropriate symmetrization factors to $\mathcal{R}_\alpha$, which decrease the contribution of each of them, so that the divergence is effectively only subtracted once. The second solution is to asymmetrize $\mathcal{P}_{\text{FKS}}^{\text{sym}}$. However, this requires a distinction of FKS pairs according to their identity. We define

$$\mathcal{P}_{\text{FKS}}(f_r) = \Big\{(i,j) : n_F \leq i \leq n_L^{(R)} + n_H + n_I,\ n_I + 1 \leq j \leq n_L^{(R)} + n_I, i \neq j, \\ \mathcal{R}(f_r) \to \infty \quad \text{if} \quad k_j^0 \to 0 \quad \text{or} \quad \mathbf{k}_i \parallel \mathbf{k}_j, \\ \text{non-redundancy conditions} \Big\}, \tag{2.2.3}$$

with the non-redundancy conditions

$$\mathcal{I}_j = g, \mathcal{I}_i \neq g, \quad (j,i) \in \mathcal{P}_{\text{FKS}} \quad \Rightarrow \quad (i,j) \notin \mathcal{P}_{\text{FKS}} \quad \text{if} \quad n_I + 1 \leq i, \tag{2.2.4}$$

$$\mathcal{I}_j \neq g, \mathcal{I}_i = g, \quad (j,i) \in \mathcal{P}_{\text{FKS}} \quad \Rightarrow \quad (i,j) \notin \mathcal{P}_{\text{FKS}} \quad \text{if} \quad n_I + 1 \leq i < j. \tag{2.2.5}$$

Only those FKS pairs which both contain gluons are kept symmetrically. Here, a symmetrization factor in $\mathcal{R}_\alpha$ is required. In the case of gluon emissions from a quark or anti-quark, only the pair with the quark at the first position is kept. This also allows us to let j only be defined for massless partons, since massive partons do not induce singularities and do not need to be subtracted. As a consequence, the condition $k_i^0 \to 0$

[7] Note that this is in striking difference to ref. [40], where the first index denotes the radiated particle. We change this in order to be more consistent with the rest of the FKS literature.

becomes redundant. The asymmetrization solution is definitely the preferable one, since it also significantly decreases the number of singular regions which have to be sampled. Given $\mathcal{P}_{\text{FKS}}$, the partition of eq. (2.2.1) is realised by multiplying $\mathcal{R}$ with phase-space partition functions $\mathcal{S}_\alpha$,

$$\mathcal{R}_\alpha = \mathcal{S}_\alpha \cdot \mathcal{R}, \tag{2.2.6}$$

which also have to be a partition of unity, cf. eq. (2.2.1),

$$1 = \sum_{\alpha \in \mathcal{P}_{\text{FKS}}} \mathcal{S}_\alpha. \tag{2.2.7}$$

The $\mathcal{S}$-functions have to vanish in phase-space regions which do not induce the singularity of the FKS pair (i, j). This means that, in a collinear region, $\lim_{\mathbf{k}_k \parallel \mathbf{k}_l} \mathcal{S}_{ij} = 0$ if $(k, l) \neq (i, j)$. Moreover, for a soft emission not associated with (i, j) but another FKS pair (k, l), $\lim_{k_l^0 \to 0} \mathcal{S}_{ij} = 0$. On the other hand, for a phase-space point which maps the singularity of an FKS pair, the $\mathcal{S}$-function needs to have a finite value less than one. In regular phase-space regions, $\mathcal{S}_\alpha$ can take any value between 0 and 1. In a collinear region, it is required that

$$\lim_{\mathbf{k}_i \parallel \mathbf{k}_j} \mathcal{S}_{ij} = h_{ij}(z_{ij}) = h_{ij}\left(\frac{E_i}{E_i + E_j}\right). \tag{2.2.8}$$

The argument z_{ij} of h_{ij} can be understood as a measure of the softness of the emission. Further, it takes into account a possible symmetrization of $\mathcal{R}_\alpha$. To this end, it has to fulfill the condition $h_{ij}(z) + h_{ij}(1 - z) = 1$. For a soft emission, which only exists for $\mathcal{I}_j = g$, we require

$$\lim_{k_j^0 \to 0} \mathcal{S}_{ij} = c_{ij}, \quad \text{with} \quad \sum_{i,(i,j) \in \mathcal{P}_{\text{FKS}}} c_{ij} = 1. \tag{2.2.9}$$

The concrete implementation of $\mathcal{S}_\alpha$ as a function of Φ_{n+1} is of course arbitrary The original works on jet cross sections in QCD [39, 58], use jet measuring functions closely related to clustering algorithms. There, singular regions where strictly separated by Heaviside Θ-functions. Smooth $\mathcal{S}$ functions were introduced in ref. [71], leading to an improved numerical behaviour. Nowadays, the canonical, process-independent definition of $\mathcal{S}_\alpha$ is [40, 59]

$$\mathcal{S}_{ij} = \frac{1}{\mathcal{D}} \frac{h_{ij}(z_{ij})}{d_{ij}}, \qquad (i, j) \in \mathcal{P}_{\text{FKS}} \tag{2.2.10}$$

$$\mathcal{D} := \sum_{kl} d_{kl}^{-1} h_{kl}(z_{kl}), \quad (k, l) \in \mathcal{P}_{\text{FKS}} \tag{2.2.11}$$

where $d_{ij} = 0$ if and only if $E_i = 0$ or $E_j = 0$ or $\mathbf{k}_i \parallel \mathbf{k}_j$. h_{ij} is the symmetrization factor

mentioned in the context of $\mathcal{P}_{\text{FKS}}^{\text{sym}}$. In an asymmetrized setup, it is

$$h_{ij}(z_{ij}) = \begin{cases} z_{ij} = \frac{E_i}{E_i+E_j} & \text{if} \quad \mathcal{I}_{(i,j)} = (g,g) \\ 1 & \text{else} \end{cases} . \tag{2.2.12}$$

The standard expression for the phase-space weights is

$$d_{ij} = 2k_i \cdot k_j \frac{E_i E_j}{(E_i + E_j)^2}, \tag{2.2.13}$$

which can easily be confirmed to fulfill the required conditions. For a better understanding of FKS partitions, consider the example of the process $e^+e^- \to q\bar{q}$. There is only one real-radiation correction here, namely $e^+e^- \to q\bar{q}g$. The particles are numerated from 1 to 5 so that $\mathcal{P}_{\text{FKS}} = \{(3,5),(4,5)\}$. Here, $(3,5)$ denotes the region in which the gluon is collinear to the quark, and likewise $(4,5)$ corresponds to the region with a collinear divergence with respect to the anti-quark. Note that both regions include soft-gluon configurations. Because of coherent radiation, soft divergences cannot to attributed to the emission from an individual particle. We defer the discussion of the soft limit of the $\mathcal{S}$ functions to further below. We demand that $\mathcal{R}_{35}$ diverges for $\mathbf{k}_3 \parallel \mathbf{k}_5$ and vanishes for $\mathbf{k}_4 \parallel \mathbf{k}_5$. The $\mathcal{D}$ factor for this process is

$$\mathcal{D} = d_{35}^{-1} + d_{45}^{-1}, \tag{2.2.14}$$

such that the $\mathcal{S}$ function attributed to $\mathcal{R}_{35}$ is

$$\mathcal{S}_{35} = \frac{1}{1 + \frac{d_{35}}{d_{45}}} = \frac{1}{1+d'}. \tag{2.2.15}$$

For a phase-space point in the proximity of the $(3,5)$-divergence, $d_{35} = 0$, so that $\mathcal{S}_{35} = 1$. This is regardless of the value of d_{45}, as long as $d_{45} > 0$. On the other hand, in the disjoint singular region $(4,5)$, $d_{45} = 0$, so that $d' \to \infty$. This yields $\mathcal{S}_{35} = 0$, as desired. The performance of FKS subtraction can be improved further by grouping regions with identical matrix elements together. For example, the process $e^+e^- \to t\bar{t}j$ has a real correction $e^+e^- \to t\bar{t}gg$. There are two FKS pairs associated with gluon emission from the top quark, $(3,5)$ and $(3,6)$ (and the same for emission from the anti-top quark with $3 \leftrightarrow 4$). Both configurations yield the same matrix element. It is therefore possible to only include one of them in $\mathcal{P}_{\text{FKS}}$ and associate a multiplicity with the given emitter region. This multiplicity is then applied to the real matrix element, but not to the subtraction terms. Further details about FKS regions are given in appendix B.1 for various processes.

2.2.2. Construction of subtraction terms

The real, non-subtracted contribution to the total NLO cross section is given by

$$\sigma_{\mathrm{NLO}}^{\mathrm{real}} = \int d\Phi_n \sum_{\alpha \in \mathcal{P}_{\mathrm{FKS}}} \int d\Phi_{\mathrm{rad}}^{\alpha} \mathcal{R}_\alpha, \tag{2.2.16}$$

where we made use of phase-space factorization, eq. (2.1.24). We focus on one individual singular region α. Further, we assume that all particles are massless. Then the divergences in $\mathcal{R}_\alpha$ originate from propagators of the form $[p_1^0 p_2^0(1-\cos\theta)]^{-1}$. The first step in the construction of subtraction terms is to factor out this singular behavior from the real matrix element. We focus on final-state divergences, for which only $y = 1$ induces a collinear singularity. Real emissions from initial-state particles are singular also for $y = -1$ and are treated in section 2.4.1. We define $\tilde{\mathcal{R}}_\alpha$ as the finite part of $\mathcal{R}_\alpha$ in the given singular region α,

$$\mathcal{R}_\alpha = \frac{1}{\xi^2}\frac{1}{1-y}\left(\xi^2(1-y)\mathcal{R}_\alpha\right) = \frac{1}{\xi^2}\frac{1}{1-y}\tilde{\mathcal{R}}_\alpha. \tag{2.2.17}$$

Dimensional regularization with $d = 4 - 2\varepsilon$ is used to make the divergences explicit. The corresponding integration measure is given by

$$d\Phi_{n+1} = \frac{s^{1-\varepsilon}}{(4\pi)^{3-2\varepsilon}} \xi^{1-2\varepsilon} \left(1-y^2\right)^{-\varepsilon} d\xi dy d\Omega^{2-2\varepsilon} d\Phi_n, \tag{2.2.18}$$

where $d\Omega^{2-2\varepsilon}$ is the angular measure in $4-2\varepsilon$ dimensions including the Jacobian of this transformation. We further denote the pure radiation phase space by $d\Phi_{\mathrm{rad}}$, i.e. $d\Phi_{n+1} = d\Phi_{\mathrm{rad}} d\Phi_n$. Therefore, integrating over the real-emission phase space, eq. (2.2.17) yields

$$\int d\Phi_{\mathrm{rad}} \mathcal{R}_\alpha = \int d\Omega^{2-2\varepsilon} \int_{-1}^{1} dy\, (1-y)^{-1-\varepsilon} \int_0^1 d\xi \xi^{-1-2\varepsilon} \tilde{\mathcal{R}}_\alpha(\xi, y), \tag{2.2.19}$$

where here and in the following, we leave out the factor $s^{1-\varepsilon}/(4\pi)^{3-2\varepsilon}$ for ease of notation. To extract the divergences in the y-integral, consider the simple manipulation for a fixed value of ξ

$$\int_{-1}^{1} dy \frac{\tilde{\mathcal{R}}_\alpha(\xi, y)}{(1-y)^{1+\varepsilon}} = \int_{-1}^{1} \frac{\tilde{\mathcal{R}}_\alpha(\xi, y) - \tilde{\mathcal{R}}_\alpha(\xi, 1)}{(1-y)^{1+\varepsilon}} + \tilde{\mathcal{R}}_\alpha(\xi, 1) \int_{-1}^{1} dy (1-y)^{-1-\varepsilon}. \tag{2.2.20}$$

$\tilde{\mathcal{R}}_\alpha(\xi, y=1)$ is proportional to the collinear limit of the real matrix element, as discussed in section 2.1.1. The divergence at $y = 1$ is subtracted out in the first summand, as can be easily verified by expanding $\mathcal{R}_\alpha(\xi, y)$ around this point. All collinear divergences of

$\mathcal{R}_\alpha$ are therefore contained in the second summand. Expanding the first summand in eq. (2.2.20) in ε and integrating the second one over y yields a polynomial in ε,

$$\frac{1}{(1-y)^{1+\varepsilon}} = -\frac{2^{-\varepsilon}}{\varepsilon}\delta(1-y) + \left(\frac{1}{1-y}\right)_+ - \varepsilon\left(\frac{\log(1-y)}{1-y}\right)_+ + \mathcal{O}(\varepsilon^2). \tag{2.2.21}$$

The **plus-distribution** is defined as

$$\int_{-1}^{1} dy \left(\frac{g(y)}{1-y}\right)_+ f(y) = \int_{-1}^{1} dy g(y) \frac{f(y)-f(1)}{1-y}, \tag{2.2.22}$$

which is finite for all $y \in [-1,1]$. This way, introducing plus-distributions in eq. (2.2.19) allows to separate divergent from finite parts. A similar calculation gives an expression of the same form for the ξ-integral. Note that here, the factor $\xi^{1-2\varepsilon}$ in the integration measure is divided by ξ^2 due to eq. (2.2.17), giving an overall $\xi^{-1-2\varepsilon}$, for which we find

$$\xi^{-1-2\varepsilon} = -\frac{1}{2\varepsilon}\delta(\xi) + \left(\frac{1}{\xi}\right)_+ - 2\varepsilon\left(\frac{\log\xi}{\xi}\right)_+ + \mathcal{O}(\varepsilon^2). \tag{2.2.23}$$

The plus-distribution with respect to ξ is defined in same way as in eq. (2.2.22), with the replacement of $f(1)$ by $f(0)$ [8]. Inserting eq. (2.2.23) and eq. (2.2.21) into eq. (2.2.19) gives the total integrated real cross section, separated into a finite and a divergent part,

$$\begin{aligned}
\int d\Phi_{\text{rad}} \mathcal{R}_\alpha = {} & \frac{2^{-\varepsilon}}{2\varepsilon^2} \int d\Omega^{2-2\varepsilon}\, \tilde{\mathcal{R}}_\alpha(0,1) \\
& - \frac{1}{2}\int d\Omega^{2-2\varepsilon} \int_{-1}^{1} dy \left[\frac{1}{\varepsilon}\left(\frac{1}{1-y}\right)_+ - \left(\frac{\log(1-y)}{1-y}\right)_+\right] \tilde{\mathcal{R}}_\alpha(0,y) \\
& - \int d\Omega^{2-2\varepsilon} \int_0^1 d\xi\, 2^{-\varepsilon} \left[\frac{1}{\varepsilon}\left(\frac{1}{\xi}\right)_+ - 2\left(\frac{\log\xi}{\xi}\right)_+\right] \tilde{\mathcal{R}}_\alpha(\xi,1) \\
& + \int d\phi \int_{-1}^{1} dy \int_0^1 d\xi\, \mathcal{J}(\xi,y,\phi) \left(\frac{1}{\xi}\right)_+ \left(\frac{1}{1-y}\right)_+ \tilde{\mathcal{R}}_\alpha(\xi,y) + \mathcal{O}(\varepsilon) \\
& = I_{\text{soft}-\text{coll}} + I_{\text{soft}} + I_{\text{coll}} + I_{\text{fin}}.
\end{aligned} \tag{2.2.24}$$

The divergences in the sum $I_{\text{soft}-\text{coll}} + I_{\text{soft}} + I_{\text{coll}}$ in the first three lines are cancelled by the divergences of the virtual matrix element, as guaranteed by the KLN theorem. For this reason, these terms make up the subtraction terms to the one-loop matrix elements, as discussed further in section 2.3. The integral I_{fin} in the last line is finite due to the

[8] In the FKS literature it is common to use generalized plus distributions, in which additional θ-functions around cut-off parameters $\xi_c \in [0,1]$ and $\delta_0 \in [0,2]$ are used. This can in certain processes lead to a better performance in parton shower matching. Introducing ξ_c and δ_0 leads to additional logarithms in most FKS formulas, which we avoid by consistently implicitly choosing $\xi_c = 1$ and $\delta_0 = 2$, which reproduce the standard plus distributions.

plus-distributions and prescribes the construction of real-emission subtraction terms. It can be written in four dimensions, where $d\Omega^{2-2\varepsilon}$ transforms into $d\phi$ and the Jacobian $\mathcal{J}$. The product of the plus-distributions in $1-y$ and ξ gives four terms, an unregularized one, i.e. the pure real matrix-element, two with the single soft or collinear limit and one with the combined soft-collinear limit. Explicitly,

$$\begin{aligned} I_{\text{fin}} = &\int_0^{2\pi} d\phi \int_{-1}^{1} \frac{dy}{1-y} \int_0^1 d\xi \, \frac{\mathcal{J}(\xi, y, \phi)}{\xi} \\ &\times \Bigg[\underbrace{\tilde{\mathcal{R}}_\alpha(\xi, y)}_{\text{Full div. real ME}} - \underbrace{\tilde{\mathcal{R}}_\alpha(0, y)}_{\text{soft limit}} - \underbrace{\tilde{\mathcal{R}}_\alpha(\xi, 1)}_{\text{coll. limit}} + \underbrace{\tilde{\mathcal{R}}_\alpha(0, 1)}_{\text{soft-coll. limit}} \Bigg] . \end{aligned} \tag{2.2.25}$$

This is the master formula in the treatment of real-emission subtraction terms. It simply displays what one would have quite intuitively guessed: The finite real matrix element is obtained by subtracting all soft and collinear limits. However, only the parameterization in ξ and y as in eq. (2.2.25) ensures that the divergences are separated consistently. In eq. (2.2.25), the ξ-integration is performed on the full interval $[0, 1]$. However, due to kinematical bounds of the radiated particle, the most general integration range is $[0, \xi_{\max}]$, with $\xi_{\max} \leq 1$, cf. eq. (2.1.21). Therefore, in a Monte-Carlo implementation, the plus-distributions in eq. (2.2.25) are manipulated further so that simultaneously, only $\xi \in [0, \xi_{\max}]$ is sampled, but the random number range is kept at $[0, 1]$. This is outlined in appendix B.2. There, eq. (B.2.3) shows that the rescaling leads to additional terms, involving logarithms of $\xi_{\max}$, which have to be added to eq. (2.2.25) in a full treatment. In the following section, explicit expressions for the three subtraction terms $\tilde{\mathcal{R}}_\alpha(0, y)$, $\tilde{\mathcal{R}}_\alpha(\xi, 1)$ and $\tilde{\mathcal{R}}_\alpha(0, 1)$ in eq. (2.2.25), suitable for the use in a Monte-Carlo implementation, will be discussed.

Subtraction of soft divergences

We construct the soft limit of the real matrix element, i.e. $\tilde{\mathcal{R}}_\alpha(0, y) = \mathcal{R}_S$ from eq. (2.2.25). It has already mostly been discussed in the context of eikonal currents in section 2.1.2. The squared real matrix element $\mathcal{R}_S$ (we drop the index α here for ease of notation) factorizes into a kinematical factor and the color-correlated Born matrix element,

$$\mathcal{R}_S = 4\pi\alpha_s \sum_{i,j=1}^{n} \frac{k_i \cdot k_j}{(k_i \cdot k)(k_j \cdot k)} \mathcal{B}_{ij}. \tag{2.2.26}$$

This is eq. (2.1.16) with $\mathcal{B}_{ij} = -|\mathcal{M}^n_{(i,j)}|^2$. The momentum k is that of the emitted particle, i.e. the FKS parton. The summation in eq. (2.2.26) is performed over all pairs external legs, especially including identical ones. For a process with n final-state particles, the matrix $\mathcal{B}_{ij}$ has dimension n^2. However, color completeness implies that

$\sum_{j,i\neq j} \mathcal{B}_{ij} = -C_i\mathcal{B}$, where C_i is the emitter's Casimir operator. Moreover, $\mathcal{B}_{ij}$ is a symmetric matrix. Assuming $\mathcal{B}$ as known, $\mathcal{B}_{ij}$ therefore has

$$n_{\text{col}-\text{corr}} = \frac{n(n-1)}{2} \tag{2.2.27}$$

independent elements. Using this, the soft limit $\mathcal{R}_S$ can be written as

$$\mathcal{R}_S = 4\pi\alpha_s \left[2\sum_{i>j} \frac{k_i \cdot k_j}{(k_i \cdot k)(k_j \cdot k)} \mathcal{B}_{ij} - \mathcal{B} \sum_i \frac{k_i^2}{(k_i \cdot k)^2} C_i \right]. \tag{2.2.28}$$

Equation (2.2.28) does not have to be modified for non-colored particles, since for them $\mathcal{B}_{ij} = 0$ and their contribution trivially vanishes. However, some applications, e.g. the NLO-treatment of factorized decays, might require a different summation prescription, as described in section 6.2.2. The real-subtracted matrix element is multiplied by the $\mathcal{S}$-functions. They behave non-trivially in the soft limit, because more than one d_{ij}-terms can approach zero. This becomes explicit after rewriting eq. (2.2.10),

$$\mathcal{S}_{ij} = \frac{1}{1 + \sum_{(n,m)\neq(i,j)} \frac{d_{ij}}{d_{nm}}}. \tag{2.2.29}$$

Here, we assume a symmetrized FKS set, so that the indices j and m correspond the position of the FKS parton (gluon or quark). In the soft limit, both $d_{ij} \to 0$ and $d_{nm} \to 0$, so that the fraction in the denominator is ill-defined. Using the standard definition of d_{ij} in eq. (2.2.13) and the fact that in the soft limit $k_m \approx k_j \approx k \approx 0$, this ratio becomes

$$\frac{d_{ij}}{d_{nm}} = \frac{(k_i \cdot k) E_i k^0 (E_n + k_0)^2}{(k_n \cdot k) E_n k^0 (E_i + k^0)^2} \overset{k\to 0}{=} \frac{k_i \cdot k}{k_n \cdot k} \frac{E_n}{E_i}, \tag{2.2.30}$$

which is finite. Thus, in the soft limit, reduced phase-space functions are used,

$$d_i^{\text{soft}} = \frac{2k_i \cdot k}{E_i}, \tag{2.2.31}$$

where i denotes the emitter associated with the singular region α and k is the momentum of the radiated parton.

Subtraction of final-state collinear divergences

Collinear gluon factorization has been discussed in section 2.1.1. For the construction of final-state collinear subtraction terms in the FKS scheme, the limit eq. (2.1.5) can be

used with $\varepsilon = 0$. As in eq. (2.1.1), $z = k^0_{n+1}/\bar{k}^0_{\mathrm{em}}$, so that [9]

$$\mathcal{R}_C^{q\to qg} = \frac{8\pi\alpha_s C_F}{k^2_{\mathrm{em}}} \frac{1+z^2}{1-z}\mathcal{B}, \tag{2.2.32}$$

$$\mathcal{R}_C^{g\to qq} = \frac{8\pi\alpha_s T_F}{k^2_{\mathrm{em}}} \left[-g^{\mu\nu} + 4z(1-z)\hat{k}_\perp^\mu \hat{k}_\perp^\nu\right] \mathcal{B}_{\mu\nu}, \tag{2.2.33}$$

$$\mathcal{R}_C^{g\to gg} = \frac{8\pi\alpha_s C_A}{k^2_{\mathrm{em}}} \left[-2\left(\frac{z}{1-z} + \frac{1-z}{z}\right) g^{\mu\nu} - 4z(1-z)\hat{k}_\perp^\mu \hat{k}_\perp^\nu\right] \mathcal{B}_{\mu\nu}, \tag{2.2.34}$$

with the short-hand notation $\hat{k}_\perp^\mu = k_\perp^\mu/\sqrt{k_\perp^2}$. The spin-correlated Born matrix element $\mathcal{B}_{\mu\nu}$ is as introduced in section 2.1.1 with the explicit formulation [44]

$$\mathcal{B}_{\mu\nu} = \sum_{\{i\},s,s'} \mathcal{M}(\{i\},h)\mathcal{M}^*(\{i\},h') \cdot \epsilon_s^{\mu *}\epsilon_{s'}^{\nu}. \tag{2.2.35}$$

The summation is performed coherently over the spin indices of all particles not involved in the splitting, but mixes the gluon spins s and s'. $\mathcal{B}_{\mu\nu}$ fulfills the condition

$$\sum_{\mu,\nu} g^{\mu\nu}\mathcal{B}_{\mu\nu} = -\mathcal{B}, \tag{2.2.36}$$

so that, assuming that $\mathcal{B}$ is known, the number of independent elements of $\mathcal{B}_{\mu\nu}$ is 15 for every process. Due to the use of the transverse momentum sum used in the derivation of eq. (2.2.32) to eq. (2.2.34), there are no interference terms between different singular regions, so that eq. (2.1.5) only contains one divergence. For this reason, a multiplication of $\mathcal{R}_C$ with $\mathcal{S}_\alpha$ is not necessary.

Subtraction of final-state soft-collinear divergences

Vanishing gluon energy corresponds to $z = 0$, which corresponds to singularities in eq. (2.2.32) and eq. (2.2.34) (eq. (2.2.33) does not have a soft singularity, so that its soft-collinear approximation is zero). The zeroes in the denominators are cancelled due to the additional factor of ξ^2 which is included in the full calculation, cf. eq. (2.2.17). This is because

$$z' = \frac{z}{\xi} = \frac{k^0_{n+1}}{\bar{k}^0_{\mathrm{em}}} \frac{\sqrt{s}}{2k^0_{n+1}} = \frac{\sqrt{s}}{2\bar{k}^0_{\mathrm{em}}} \tag{2.2.37}$$

is finite. Thus, in a setup where z is computed from z' and ξ, the soft-collinear limit can straightforwardly be computed using eq. (2.2.32) and eq. (2.2.34).

[9] The implementation in WHIZARD has a different sign for the second summands in eq. (2.2.33) and eq. (2.2.34). This is due to a different choice of the collinear parameterization in eq. (2.1.2) in the POWHEG–style definition of $\mathcal{B}_{\mu\nu}$.

2.3. Virtual contributions and their subtraction terms

The KLN theorem assures that the divergences in the real and virtual contribution to the integrated cross section cancel each other. In other words, the pole structure of $\mathcal{V}$ can be extracted from the terms discussed in sections 2.1 and 2.2, by inverting the sign and integrating over the radiation phase space.

Using the knowledge gained in the last section, we can already infer the general form of the virtual-subtracted contribution to the cross section, $\mathcal{V}^{(0)}$. Obviously, it contains the $\mathcal{O}(\varepsilon^0)$-term of the one-loop amplitude, $\mathcal{V}_{\text{fin}}^{\text{loop}}$. The integration of the soft limit in eq. (2.2.26) does not affect the color correlations given by $\mathcal{B}_{ij}$, but removes the spin correlations due to the spatial averaging it performs. We denote the integrals of the factors $\frac{k_i \cdot k_j}{(k_i \cdot k)(k_j \cdot k)}$ in eq. (2.2.26) associated with $\mathcal{B}_{ij}$ by $\mathcal{E}_{ij,\rho}^{(m_i,m_j)}$. These eikonal integrals crucially depend on the masses of the particles at leg i and j, as each massive particle increases the complexity of the integrals. The index $\rho \in -2, -1, 0$ refers to the coefficient of ε it belongs to in the Laurent expansion of the integral. In the collinear limits of, eq. (2.2.32), eq. (2.2.33) and eq. (2.2.34) the spin-correlated matrix element $\mathcal{B}_{\mu\nu}$ transforms into the simple squared matrix element $\mathcal{B}$. For these reasons, the finite part of the virtual-subtracted contribution has the basic form

$$\mathcal{V}^{(0)} = \sum_{k,l} \mathcal{E}_{kl,0}^{(m_k,m_l)} \mathcal{B}_{kl} + \sum_i \mathcal{Q}_i \mathcal{B} + \mathcal{V}_{\text{fin}}^{\text{loop}}. \tag{2.3.1}$$

This is the master formula for the computation of σ^{virt} in the FKS approach and other subtraction schemes. In the remainder of this section, we will deal with the derivation of explicit formulas for $\mathcal{E}_{kl,0}^{(m_k,m_l)}$ and $\mathcal{Q}_i$. The computation of $\mathcal{V}_{\text{fin}}^{\text{loop}}$ requires the evaluation of loop integrals, a task outside of the subtraction implementation.

Beforehand, we want to note that the results presented in the following strongly depend on the chosen normalization. With the same reasoning as above, it can be seen that the singular part of the virtual-subtracted matrix element is given by

$$\mathcal{V}_{\text{div}} = \mathcal{N}(\varepsilon) \cdot \left\{ \sum_{k,l} \left[\frac{1}{\varepsilon^2} \mathcal{E}_{kl,-2}^{(m_k,m_l)} + \frac{1}{\varepsilon} \mathcal{E}_{kl,-1}^{(m_k,m_l)} \right] \mathcal{B}_{kl} + \frac{1}{\varepsilon} \sum_k \mathcal{Q}'_k \mathcal{B}_{f_k} + \mathcal{V}_{\text{div}}^{\text{loop}} \right\}. \tag{2.3.2}$$

The normalization factor $\mathcal{N}$ is a remainder of dimensional regularization and is equal to one in the limit $\varepsilon \to 0$. Nevertheless, the explicit form of all terms inside the brackets crucially depend on the choice of $\mathcal{N}$, which is important when matching the subtraction terms to the one-loop matrix elements which in the context of Monte-Carlo programs

are often obtained from external programs. We choose [10]

$$\mathcal{N}(\varepsilon) = \frac{(4\pi)^\varepsilon}{\Gamma(1-\varepsilon)} \left(\frac{\mu^2}{Q^2}\right)^\varepsilon . \tag{2.3.3}$$

Here μ is the renormalization scale and Q is the commonly used Ellis-Sexton scale [77], which allows to tune the terms in such a way that either the logarithms $\log(\mu^2/Q^2)$ or $\log(Q^2/s)$ vanish. A different normalization is for example used by RECOLA (cf. section 3.1.1), namely

$$\mathcal{N}(\varepsilon) = (4\pi)^\varepsilon \Gamma(1+\varepsilon). \tag{2.3.4}$$

Matching this to eq. (2.3.3) and ignoring the μ^2/Q^2 factor, the product $\Gamma(1+\varepsilon)\Gamma(1-\varepsilon)$ appears. Expanded in ε, it equals $1+\frac{\pi^2}{6}\varepsilon^2+\mathcal{O}(\varepsilon^4)$. This way, a summand $\pi^2/6 \sum_{k,l} \mathcal{E}^{(m_k,m_l)}_{kl,-2}$ is moved from the divergent to the finite part of $\mathcal{V}$, thus changing the integration result. We turn to the evaluation of the integrals required in eq. (2.3.1). They are obtained by integrating the real amplitude over the radiation phase space and extracting the finite remainders. Therefore, we start with

$$\int d\Phi_{n+1} \mathcal{R}_\alpha = \int d\Phi_n \frac{s^{1-\varepsilon}}{(4\pi)^{3-2\varepsilon}} \xi^{1-2\varepsilon} d\xi (1-y^2)^{-\varepsilon} dy d\Omega^{2-2\varepsilon} \mathcal{R}_\alpha, \tag{2.3.5}$$

where the d-dimensional volume integral is $\int d\Omega^{2-2\varepsilon} = 2\pi^{1-\varepsilon}/\Gamma(1-\varepsilon)$. We focus on one individual singular region α, where the splitting particles are well-defined. At the end of the calculation, to obtain the overall structure of the virtual matrix element, we sum over all α. The integral in eq. (2.3.5) contains collinear and soft divergences. Our approach to regularize them is depicted in fig. 2.2. We first regularize the soft divergence by expanding $\xi^{-1-2\varepsilon}$ as in eq. (2.2.23). Note that like in eq. (2.2.17) we factor out a factor of ξ^2 to make the product $\xi^2\mathcal{R}_\alpha$ finite in the soft limit. This way, the integral is split up into

$$\int d\Phi_{n+1} \mathcal{R}_\alpha = I_{s,\alpha} + I_{+,\alpha}, \tag{2.3.6}$$

where the $+$ implies that the ξ-singularity has been regularized using

$$\mathcal{P}_+(\xi) = \left(\frac{1}{\xi}\right)_+ - 2\varepsilon \left(\frac{\log\xi}{\xi}\right)_+ + \mathcal{O}(\varepsilon^2). \tag{2.3.7}$$

The remaining factor $-\delta(\xi)/2\varepsilon$ in eq. (2.2.23) is included in $I_{s,\alpha}$. This way

$$I_{s,\alpha} := -\frac{1}{2\varepsilon} \int d\Phi_n \frac{s^{1-\varepsilon}}{(4\pi)^{3-2\varepsilon}} d\Omega^{3-2\varepsilon} \lim_{\xi\to 0} \left[\xi^2 \mathcal{R}_\alpha\right], \tag{2.3.8}$$

[10] This normalization is also proposed by the BLHA standard [75, 76]

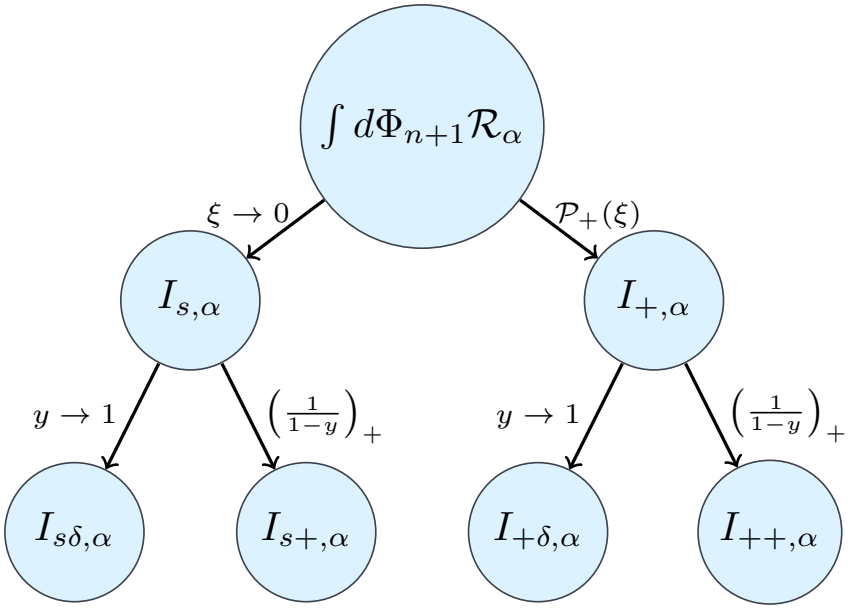

Figure 2.2. Regularization of the integral of the real matrix element. $I_{s\delta,\alpha}$ is equal to zero in standard FKS, but gives an additional contribution to $\mathcal{Q}$ in the resonance-aware approach, cf. eq. (2.6.20). The integral $I_{s+,\alpha}$ yields the eikonal integrals $\mathcal{E}_{ij,\rho}^{(m_i,m_j)}$, whereas $I_{+\delta,\alpha}$ gives another contribution to the $\mathcal{Q}$- factor in eq. (2.3.1). $I_{++,\alpha}$ is the finite real-subtracted expression discussed in section 2.2.

and

$$I_{+,\alpha} := \int d\Phi_{n+1} \frac{\mathcal{P}_+(\xi)}{\xi^{-1-2\varepsilon}} \mathcal{R}_\alpha. \tag{2.3.9}$$

Here, in eq. (2.3.8), the $\delta(\xi)$ function has been transformed into the limit $\xi \to 0$. The additional factor $\xi^{-1-2\varepsilon}$ in the denominator of eq. (2.3.9) appears because we have expanded by $\xi^{1-2\varepsilon}$ in order to restore the full $n+1$-particle integral measure $d\Phi_{n+1}$. Both integrals still contain collinear divergences. Like in section 2.2, they are regularized by expanding the y-expressions in terms of plus distributions. The plus distributions have to map the singularity at $y \to 1$, so that $(1-y^2)^{-\varepsilon}$ should be connected to $\left(\frac{1}{1-y}\right)_+$. This is achieved by using the identity

$$(1-y^2)^{-\varepsilon} = (1+y)^{-\varepsilon}(1-y)(1-y)^{-1-\varepsilon} = (1-y)\left[-\frac{2^{-2\varepsilon}}{\varepsilon}\delta(1-y) + \left(\frac{1}{1-y}\right)_+ + \mathcal{O}(\varepsilon)\right]. \tag{2.3.10}$$

Using this regularization, in total four different integrals are produced, each with a distinct singularity structure. This is completely analogous to the separation performed in eq. (2.2.24). For $I_{s,\alpha}$, we obtain

$$I_{s,\alpha} := I_{s+,\alpha} + I_{s\delta,\alpha} \tag{2.3.11}$$

where, as before, a + signifies that a divergence is regularized, in this case the collinear one. Analogously, $I_{+,\alpha}$ is split up into

$$I_{+,\alpha} := I_{+\delta,\alpha} + I_{++,\alpha} \tag{2.3.12}$$

The task is now to work out these four integrals.

2.3.1. The integrals I_{++} and $I_{+\delta}$

The I_{++}–integral is the exact same integral as in eq. (2.2.25). It creates the real-emission subtraction terms. The remaining integration over the radiation phase space is performed by the Monte-Carlo generator. The $I_{+\delta}$–integral is soft-regularized but contains collinear divergences. In the following, those singularities are made explicit and the finite parts of $I_{+\delta}$ are extracted. Let i denote the index of the radiated particle and j the emitter's index. Then, the emitter momentum in the Born phase space is given by $k = k_i + k_j$. Making the integration over both k_i and k_j explicit, the $I_{+\delta,\alpha}$–integral is

given by [11]

$$\begin{aligned} I_{+\delta,\alpha} = &\int (2\pi)^d \delta^{(d)} \left(k_\oplus + k_\ominus - \sum_{l=1}^{n+1} k_l \right) \left[\prod_{l\neq j,i} d\Phi_l \right] \\ &\times \frac{\left(k_j^0\right)^{1-2\varepsilon}}{2(2\pi)^{3-2\varepsilon}} dk_j^0 d\Omega_j^{3-2\varepsilon} dk^0 \delta(k^0 - k_j^0 - k_i^0) \\ &\times \left[-\frac{2^{-2\varepsilon}}{\varepsilon} \delta(1-y) \right] \frac{\left(k_i^0\right)^{1-2\varepsilon}}{2(2\pi)^{3-2\varepsilon}} dk_i^0 dy d\Omega_i^{2-2\varepsilon} \frac{\mathcal{P}_+(\xi)}{\xi^{-1-2\varepsilon}} \lim_{y\to 1} \left[(1-y)\mathcal{R}_\alpha \right]. \end{aligned} \tag{2.3.13}$$

We perform a change of variables by replacing ξ by z, defined by $k_j^0 = zk^0$ and $k_i^0 = (1-z)k^0$. This way,

$$\xi = \frac{2k_i^0}{\sqrt{s}} = \frac{2k^0}{\sqrt{s}}(1-z) = \xi_{\max}(1-z), \tag{2.3.14}$$

where we have identified the quantity $2k^0/\sqrt{s}$ as $\xi_{\max}$, as given in eq. (2.1.21). Considering the massive case is irrelevant for collinear emissions. Moreover, with the replacement $k_j^0 = zk^0$, we can combine the product $\prod_{l\neq i,j} d\Phi_l$ with the dk_j^0 integral to the Born phase-space measure $d\Phi_B$. Further, eq. (2.2.23) gives

$$\mathcal{P}_+(\xi) = \xi^{-1-2\varepsilon} + \frac{1}{2\varepsilon}\delta(\xi) = \xi_{\max}^{-1-2\varepsilon} \left((1-z)^{-1-2\varepsilon} + \frac{\xi_{\max}^{2\varepsilon}}{2\varepsilon}\delta(1-z) \right), \tag{2.3.15}$$

which can be used to eliminate the plus-distributions in eq. (2.3.13). We know the collinear limit of $\mathcal{R}_\alpha$ from eq. (2.1.5). Here it is applied with two modifications. First, the angular integration allows to use the space-averaged Altarelli-Parisi splitting functions $\langle \hat{P}_{ab} \rangle$ in eq. (B.3.20) to eq. (B.3.22). Second, there is the additional factor of $1-y$, which yields the slightly modified collinear limit

$$\left\langle \lim_{1\to y} \left[(1-y)\mathcal{R}_\alpha \right] \right\rangle = \frac{8\pi\alpha_s\mu^{2\varepsilon}}{2\left(k^0\right)^2 z(1-z)} \langle \hat{P} \rangle_\alpha(z,\varepsilon) \mathcal{B}_{f_\alpha}, \tag{2.3.16}$$

with the additional factor $z(1-z)$ in the denominator. The explicit expressions for the space-averaged Altarelli-Parisi-splitting functions are given in eq. (2.1.6) to eq. (2.1.8) and already appeared in the treatment of the real final-state collinear subtraction terms in eq. (2.2.32) to eq. (2.2.34). Altogether, integrating out the angular radiation phase

[11] The explicit limit $y \to 1$ is redundant due to the δ function, but we keep it to emphasize that this term has to be replaced by the appropriate collinear limit of $\mathcal{R}_\alpha$.

space, we obtain

$$\begin{aligned} I_{+\delta,\alpha} = &-\frac{\mathcal{N}(\varepsilon)}{\varepsilon}\frac{\alpha_s}{2\pi}\int d\Phi_n \mathcal{B}_{f_\alpha}\left(\frac{Q}{2k^0}\right)^{2\varepsilon} \\ &\times \int_0^1 dz z^{1-2\varepsilon}\left[(1-z)^{-1-2\varepsilon} + \frac{\xi_{\max}^{2\varepsilon}}{2\varepsilon}\delta(1-z)\right](1-z)\langle\hat{P}\rangle_\alpha(z,\varepsilon), \end{aligned} \tag{2.3.17}$$

where the normalization factor $\mathcal{N}(\varepsilon)$ is as in eq. (2.3.3). Finally, we are left with integrals of the form

$$I^{(0)}_{+\delta,\alpha} := \int_0^1 dz z^{-2\varepsilon}(1-z)^{-2\varepsilon}\langle\hat{P}\rangle_\alpha(z,\varepsilon), \tag{2.3.18}$$

and

$$I^{(1)}_{+\delta,\alpha} := \int_0^1 dz z^{-2\varepsilon}\frac{\xi_{\max}^{-2\varepsilon}}{2\varepsilon}\delta(1-z)(1-z)\langle\hat{P}\rangle_\alpha(z,\varepsilon). \tag{2.3.19}$$

which have to be evaluated for each of the three splitting functions individually. After the integration is performed for each of them, the $g \to q\bar{q}$ and $g \to gg$ case is combined into one term. The explicit results for $I^{(0)}_{+\delta,\alpha}$ are listed in eq. (B.3.23), eq. (B.3.24) and eq. (B.3.25). With $X(\varepsilon) = \xi_{\max}^{-2\varepsilon}/\varepsilon^2$, the integral $I^{(1)}_{+\delta,\alpha}$ can be determined to equal $-2C_F\cdot X(\varepsilon)$ for a $q \to qg$-splitting, $-2C_A\cdot X(\varepsilon)$ for a $g \to gg$-splitting and 0 for a $g \to q\bar{q}$-splitting. As mentioned above, the last two splittings are combined, so the integral can be written as $I_{+\delta,\alpha} = -X(\varepsilon)\cdot C_{f_\alpha}$, where C_{f_α} is the Casimir operator of the singular region α's emitter. Table 2.1 lists the integral contributions ordered by their power of ε, both for the gluon and quark splittings. For the $g \to qq$-splitting the number of flavors the gluon can split into is accounted for by the inclusion of n_f. The coefficients of the ε^0- and ε^{-1}-terms are called γ and γ', respectively. Using that, for a massless emitter, $\xi_{\max} = 2k^0/\sqrt{s}$, the factor $(Q/2k^0)^{2\varepsilon}$ in eq. (2.3.17) can be rewritten as $(Q^2/s)^\varepsilon\,\xi_{\max}^{-2\varepsilon}$. The expansion of this factor as well as that of the $\xi_{\max}^{-2\varepsilon}$-factor associated with the Casimir operator leads to a reshuffling of ε-poles and additional terms $\log(Q^2/s)$ and $\log\xi_{\max}$ in eq. (2.3.17). After summing over all α regions, the final result is thus

$$\sum_{\alpha\in\mathcal{P}_{\mathrm{FKS}}(f_b)} I_{+\delta,\alpha} = \mathcal{N}(\varepsilon)\frac{\alpha_s}{2\pi}\int d\Phi_n \sum_i \mathcal{B}_{i(f_b)}\left\{\frac{1}{\varepsilon}\left(-2\log\xi_{\max}C_{i(f_b)} + \gamma_{i(f_b)}\right) + \mathcal{Q}^{+\delta}_{i(f_b)}\right\}, \tag{2.3.20}$$

with

$$\mathcal{Q}^{+\delta}_{i(f_b)} = 2\log\xi_{\max}\left(\log\xi_{\max} - \log\frac{Q^2}{s}\right)C_{i(f_b)} + \left(\log\frac{Q^2}{s} - 2\log\xi_{\max}\right)\gamma_{i(f_b)} + \gamma'_{i(f_b)}, \tag{2.3.21}$$

which is part of the factor $\mathcal{Q}_i$ in the master formula in eq. (2.3.1).

Table 2.1. Collinear pole structure of all QCD splittings and definition of γ and γ'. Note that the final ε-series gets further reshuffled due to the expansion of $\xi_{\max}^{-2\varepsilon}$.

$g \to gg, q\bar{q}$	$\sum_\alpha I^{(0)}_{+\delta,\alpha}$	$\sum_\alpha I^{(1)}_{+\delta,\alpha}$
$\mathcal{O}(1)$	$\left(\frac{67}{9} - \frac{2\pi^2}{3}\right) C_A - \frac{23}{9} T_F n_f = \gamma'_g$	0
$\mathcal{O}(\varepsilon^{-1})$	$\frac{11}{6} C_A - \frac{2}{3} T_F n_f = \gamma_g$	0
$\mathcal{O}(\varepsilon^{-2})$	C_A	$-C_A \xi_{\max}^{-2\varepsilon}$

$q \to qg$	$\sum_\alpha I^{(0)}_{+\delta,\alpha}$	$\sum_\alpha I^{(1)}_{+\delta,\alpha}$
$\mathcal{O}(1)$	$\left(\frac{13}{2} - \frac{2\pi^2}{3}\right) C_F = \gamma'_q$	0
$\mathcal{O}(\varepsilon^{-1})$	$\frac{3}{2} C_F = \gamma_q$	0
$\mathcal{O}(\varepsilon^{-2})$	C_F	$-C_F \xi_{\max}^{-2\varepsilon}$

2.3.2. The integrals I_{s+} and $I_{s\delta}$

We perform the y-regularization in eq. (2.3.8) using eq. (2.3.10), which yields

$$I_{s+,\alpha} = -\frac{1}{2\varepsilon} \int d\Phi_n \frac{s^{1-\varepsilon}}{(4\pi)^{3-2\varepsilon}} d\Omega^{3-2\varepsilon} \lim_{\xi \to 0} \left[\xi^2 \mathcal{R}_\alpha\right]. \tag{2.3.22}$$

Here, in the factor $(1-y)\left(\frac{1}{1-y}\right)_+$ introduced by eq. (2.3.10), the numerator effectively cancels the denominator. This way, $I_{s+,\alpha}$ is identical to $I_{s,\alpha}$, from which it follows that

$$I_{s\delta,\alpha} = 0. \tag{2.3.23}$$

We want to emphasize that it can differ from zero in different regularization approaches, like the one used in resonance-aware FKS, cf. section 2.6. There it gives a contribution to the $\mathcal{Q}$-factor in eq. (2.3.1). In standard FKS, it is therefore

$$\mathcal{Q}_{j(f_b)} = \mathcal{Q}^{+\delta}_{j(fb)}. \tag{2.3.24}$$

Applying the soft limit of eq. (2.1.16) in $I_{s+,\alpha}$ is only well-defined in the sum over all singular regions with the same underlying Born flavor structure. We obtain

$$\begin{aligned}\sum_\alpha I_{s+,\alpha} &= -\frac{1}{2\varepsilon}\int d\Phi_B \int d\Omega^{3-2\varepsilon}\frac{s^{1-\varepsilon}}{(4\pi)^{2-2\varepsilon}}4\pi\alpha_s\mu^\varepsilon\xi^2\sum_{ij}\frac{k_i\cdot k_j}{(k_i\cdot k)(k_j\cdot k)}\mathcal{B}_{ij} \\ &= \int d\Phi_B \sum_{ij}\mathcal{B}_{ij}\underbrace{\left(\frac{-1}{2\varepsilon}\right)\left(\frac{\mu^2}{s}\right)^\varepsilon\int\frac{d\Omega^{3-2\varepsilon}}{\pi}\frac{s\xi^2}{4}\frac{k_i\cdot k_j}{(k_i\cdot k)(k_j\cdot k)}}_{\mathcal{E}_{ij,\rho}^{(m_i,m_j)}}\end{aligned} \tag{2.3.25}$$

The explicit formulas for the eikonal integrals $\mathcal{E}_{ij,\rho}^{(m_i,m_j)}$ are given in section B.3.1. Their finite part enters the master formula in eq. (2.3.1) as discussed in the beginning of the section.

2.4. Subtraction of initial-state divergences

Divergences induced by initial-state emissions are more intricate than final-state ones, due to their interaction with the beam structure functions. In this section, we focus on hadron collisions, because only here, NLO QCD corrections have an effect on the initial state. Photonic initial-state corrections on lepton beams are briefly discussed in sec. 2.7.

2.4.1. Divergences from PDF evolution

Given a beam constituent parton, the parton densities at the energy scales $x_{1,2} = E_{1,2}/\sqrt{s}$ evolve as

$$f(x_2) = \int_0^1\int_0^1 dx_1 dz f(x_1)\Gamma(z)\delta(x_2 - x_1 z). \tag{2.4.1}$$

Here Γ is the DGLAP evolution kernel. For a splitting of initial-state particles $a \to b$ it is given by

$$\Gamma_a^{(b)} = \delta_{ab}\delta(1-x) - \frac{\alpha_s}{2\pi}\left(\frac{1}{\varepsilon}P_{ab}(x,0) - K_{ab}(x)\right) + \mathcal{O}(\alpha_s^2). \tag{2.4.2}$$

P_{ab} is the **regularized Altarelli-Parisi splitting function**. The splitting functions defined in eq. (2.1.6) to eq. (2.1.8) contain divergences at $z = 1$, which can be regularized with plus-distributions, just as it has already been done for ξ and y. The connection between the regularized and the generalized splitting functions is [39]

$$P_{ab}(z,0) = \frac{(1-z)\hat{P}_{ab}(z,0)}{(1-z)_+} + \gamma_a\delta_{ab}\delta(1-z), \tag{2.4.3}$$

with γ_a as defined in table 2.1. K_{ab} is a renormalization scheme matching factor, which is exactly zero in $\overline{MS}$. The crucial point about eq. (2.4.2) is that it is a perturbative expansion itself, containing additional collinear divergences. In a consistent NLO calculation, the $\mathcal{O}(\alpha_s)$ contributions from the matrix elements have to be matched with the $\mathcal{O}(\alpha_s)$ contributions from the DGLAP evolution in eq. (2.4.2), leading to divergences which are not cancelled by the virtual contribution.

Let the leading-order hadronic cross section be given by

$$d\sigma^{(0)}(s) = \int dx_\oplus dx_\ominus f_\oplus(x_\oplus) f_\ominus(x_\ominus) \underbrace{d\tilde{\sigma}^{(0)}(x_\oplus x_\ominus s)}_{d\hat{\sigma}^{(0)}}, \tag{2.4.4}$$

then the NLO hadronic cross section is

$$d\sigma^{(1)}(s) = \int dx_\oplus dx_\ominus dz_\oplus dz_\ominus f_\oplus(x_\oplus) f_\ominus(x_\ominus) \underbrace{\Gamma_\oplus(z_\oplus)\Gamma_\ominus(z_\ominus) d\tilde{\sigma}^{(1)}(z_\oplus z_\ominus s)}_{d\hat{\sigma}^{(1)}}. \tag{2.4.5}$$

The subtracted partonic cross sections $d\hat{\sigma}^{(0,1)}$ are related to the partonic ones via

$$d\hat{\sigma}^{(0)}_{ab}(k_1, k_2) = d\tilde{\sigma}^{(0)}_{ab}(k_1, k_2) \tag{2.4.6}$$

and

$$\begin{aligned} d\hat{\sigma}^{(1)}_{ab}(k_1, k_2) &= d\tilde{\sigma}^{(1)}_{ab}(k_1, k_2) \\ &\quad + \frac{\alpha_s}{2\pi} \sum_d \int dx \left(\frac{1}{\varepsilon} P_{da}(x, 0) - K_{da}(x) \right) d\tilde{\sigma}^{(0)}_{db}(xk_1, k_2) \\ &\quad + \frac{\alpha_s}{2\pi} \sum_d \int \left(\frac{1}{\varepsilon} P_{db}(x, 0) - K_{db}(x) \right) d\tilde{\sigma}^{(0)}_{ad}(k_1, xk_2). \\ &= d\tilde{\sigma}^{(1)}_{ab} + d\tilde{\sigma}^{(\mathrm{cnt},+)}_{ab} + d\tilde{\sigma}^{(\mathrm{cnt},-)}_{ab}. \end{aligned} \tag{2.4.7}$$

We observe three terms. The first one, $d\tilde{\sigma}^{(1)}_{ab}$, is the partonic $\mathcal{O}(\alpha_s)$ cross section. Its divergences originate purely from the matrix element and the phase space. The other two are exclusive to hadron collisions. They are interference terms between the leading-order matrix elements and the $\mathcal{O}(\alpha_s)$-contributions to the PDF evolution. They introduce new singularities into the calculation, which cancel out with the divergences in the real matrix element, leading to additional subtraction terms. These singularities can be attributed to $y = 1$ for $d\tilde{\sigma}^{(\mathrm{cnt},+)}_{ab}$ and $y = -1$ for $d\tilde{\sigma}^{(\mathrm{cnt},-)}_{ab}$. Note that, in lepton collisions (and only for QCD corrections), $d\tilde{\sigma}^{(\mathrm{cnt},+)}_{ab} = d\tilde{\sigma}^{(\mathrm{cnt},-)}_{ab} = 0$, which removes the necessity of any additional subtraction terms. To account for collinear divergences both at $y = +1$ and

$y = -1$, eq. (2.2.17) is changed so that y^2 appears instead of y,

$$\mathcal{R} = \frac{1}{\xi^2}\frac{1}{1-y^2}\left(\xi^2(1-y^2)\mathcal{R}\right) = \frac{1}{\xi^2}\frac{1}{1-y^2}\tilde{\mathcal{R}}. \tag{2.4.8}$$

Since the divergences in eq. (2.4.7) are purely collinear, the soft-subtracted ξ-expansion of eq. (2.2.23) can be used throughout the following discussions. The master formula in eq. (2.2.19), taking into account the initial-state definition of $\tilde{\mathcal{R}}$ (2.4.8), yields

$$\mathcal{R}_\alpha^{(\mathrm{in})} = \left[\left(\frac{1}{\xi}\right)_+ - 2\varepsilon\left(\frac{\log\xi}{\xi}\right)_+\right]\left(1-y^2\right)^{-1-\varepsilon}\tilde{\mathcal{R}}_\alpha = \mathcal{P}_+(\xi)\left(1-y^2\right)^{-1-\varepsilon}\tilde{\mathcal{R}}_\alpha, \tag{2.4.9}$$

where $\mathcal{P}_+(\xi)$ has been defined in eq. (2.3.7). The collinear divergences are regularized using the identity,

$$\left(1-y^2\right)^{-1-\varepsilon} = -\frac{2^{-\varepsilon}}{\varepsilon}\left(\delta(1-y)+\delta(1+y)\right) + \frac{1}{2}\left[\left(\frac{1}{1-y}\right)_+ + \left(\frac{1}{1+y}\right)_+\right] + \mathcal{O}(\varepsilon), \tag{2.4.10}$$

similar to eq. (2.2.21). Note that the expansion only has to performed up to $\mathcal{O}(1)$ because there are no $1/\varepsilon$-poles in eq. (2.4.9). Equation (2.4.9) is split up further into

$$\mathcal{R}_\alpha^{(in)} = \mathcal{R}_\alpha^{(in,+)} + \mathcal{R}_\alpha^{(in,-)} + \mathcal{R}_\alpha^{(in,\mathrm{fin})} + \mathcal{O}(\varepsilon). \tag{2.4.11}$$

The last of the three summands,

$$\mathcal{R}_\alpha^{(\mathrm{in,fin})} = \frac{1}{2}\left[\left(\frac{1}{1-y}\right)_+ + \left(\frac{1}{1+y}\right)_+\right]\mathcal{P}_+(\xi)\tilde{\mathcal{R}}_\alpha, \tag{2.4.12}$$

is the initial-state analogon to eq. (2.2.25) and soft and collinear finite due to the plus-distributions. The other two summands,

$$\mathcal{R}^{(\mathrm{in},\pm)} = -\frac{2^{-\varepsilon}}{\varepsilon}\delta\left(1\mp y\right)\mathcal{P}_+(\xi)\tilde{\mathcal{R}}_\alpha, \tag{2.4.13}$$

are new and contain the DGLAP-structure of the full real matrix element. They are only present in the strict collinear limit $y = \pm 1$. Therefore, the conditions of the KLN theorem are not met. It requires an integration over the whole radiation phase space, which is clearly violated by the presence of the δ-function in eq. (2.4.13), which singles out the beam axis. Accordingly, instead of cancelling any poles, $\mathcal{R}^{(\mathrm{in},\pm)}$ just gives a finite contribution.

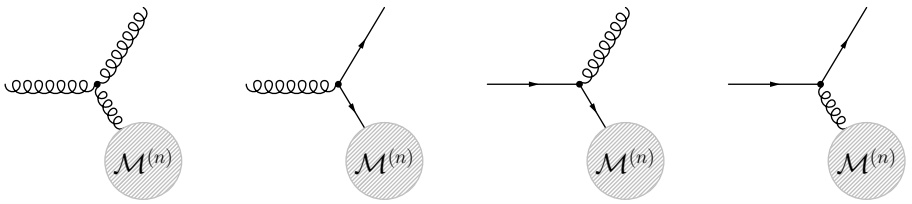

Figure 2.3. All factorized initial-state QCD splittings.

2.4.2. Initial-state real subtraction

Initial-state collinear singularities

The collinear limit in eq. (2.4.12) is the initial-state analogon to the third summand in eq. (2.2.25), whose treatment has been discussed in section 2.2.2 and most statements given there are also valid here. One difference is that in initial-state emission, $k^2_{\text{em}} < 0$, which has to be compensated by an additional minus sign. Also, there are in total four different splittings, depicted in fig. 2.3. The subtraction terms are

$$\mathcal{R}_C^{(g\to gg)} = \frac{8\pi\alpha_s C_A}{-k^2_{\text{em}}}\left[-2\left(\frac{z}{1-z}+z(1-z)\right)g^{\mu\nu}+\frac{4(1-z)}{z}\hat{k}_\perp^\mu\hat{k}_\perp^\nu\right]\mathcal{B}_{\mu\nu}, \tag{2.4.14}$$

$$\mathcal{R}_C^{(q\to gq)} = \frac{8\pi\alpha_s C_F}{-k^2_{\text{em}}}\frac{1+z^2}{1-z}\mathcal{B}, \tag{2.4.15}$$

$$\mathcal{R}_C^{(q\to qg)} = \frac{8\pi\alpha_s C_F}{-k^2_{\text{em}}}\left[-g^{\mu\nu}z+\frac{4(1-z)}{z}\hat{k}_\perp^\mu\hat{k}_\perp^\nu\right]\mathcal{B}_{\mu\nu}, \tag{2.4.16}$$

$$\mathcal{R}_C^{(g\to q\bar{q})} = \frac{8\pi\alpha_s T_F}{-k^2_{\text{em}}}\left(z^2+(1-z)^2\right)\mathcal{B}, \tag{2.4.17}$$

where now $z = 1-\xi$. In the soft limit, all equations are multiplied with ξ, cf. section 2.2.2, so that the factor of $1-z$ in the denominator of eq. (2.4.14) and eq. (2.4.15) vanishes, regularizing the soft-collinear limit $z = 1$.

Singular regions and $\mathcal{S}$-functions

To facilitate the evaluation of the $\mathcal{S}$-functions, the d_{ij} weights can be brought into a simpler form by fixing one of the momenta to be parallel to the beam axis. This way, in eq. (2.2.13), the scalar product $k_i \cdot k_j$ gives $E_iE_j(1 \pm y)$, where the + corresponds to emissions anti-parallel to the z-axis. Further, let j be the index of the emitted quark or gluon. Then, E_i equals the partonic beam energy. The ISR real-emission mapping ensures that $E_i > \overline{E}_i$, cf. eq. (A.2.3), so that the soft limit is entirely determined by $E_j \to 0$. In this limit, the denominator $(E_i + E_j)^2$ effectively cancels the E_j^2 factor in

the numerator. We can thus define

$$d_{(1,2)j} = 2E_j^2 \left(1 \mp y\right). \tag{2.4.18}$$

A further improvement can be made by introducing a 0-region, which contains singularities which are collinear to both the $\oplus$- and the $\ominus$- direction. In QCD, this is only the case for gluon emissions. The 0-region gets the phase-space weight,

$$d_{0j} = E_j^2 \left(1 - y^2\right), \tag{2.4.19}$$

which is the denominator of the sum $d_{1j}^{-1} + d_{2j}^{-1}$. As an illustration for that, consider the Drell-Yan process $q\bar{q} \to l^+l^-$ in NLO QCD. There are three initial-state singular regions, $\{(0,5),(1,5),(2,5)\}$. The first one corresponds to gluon emission from either the quark or the anti-quark. The second one contains the singularity associated with the $g \to q\bar{q}$-splitting, where q enters the hard interaction. Analogously, the $(2,5)$-region is associated with the same splitting and $\bar{q}$ entering the hard interaction. The $\mathcal{D}$-function from eq. (2.2.11) is given by

$$\mathcal{D} = \frac{1}{E_5^2(1-y^2)} + \frac{1}{2E_5^2(1-y)} + \frac{1}{2E_5^2(1+y)}, \tag{2.4.20}$$

so that

$$\mathcal{S}_{05} = \frac{1}{2}, \quad \mathcal{S}_{15} = \frac{1}{4}(1+y), \quad \mathcal{S}_{25} = \frac{1}{4}(1-y). \tag{2.4.21}$$

Note that $\mathcal{S}_{05}+\mathcal{S}_{15}+\mathcal{S}_{25} = 1$, which, however, is only valid if the factor of two is included in the definitions of eq. (2.4.18).

2.4.3. Subtraction of DGLAP remnants

We are left with $\mathcal{R}_\alpha^{(in,\pm)}$ in eq. (2.4.11) and its cross section $d\tilde{\sigma}^{(in,\pm)}$. It can be shown that, regularizing the splitting functions as in eq. (2.4.3) in eq. (2.4.7), the poles in $d\tilde{\sigma}^{(\mathrm{in},\pm)}$ and $d\tilde{\sigma}^{(\mathrm{cnt},\pm)}$ cancel in the sum

$$d\sigma^{(\mathrm{in},\pm)} = d\tilde{\sigma}^{(\mathrm{in},\pm)} + \frac{1}{4} d\tilde{\sigma}^{(\mathrm{cnt},\pm)} \tag{2.4.22}$$

When expanding in ε, the ε–dependence of $\hat{P}$ has to be taken into account,

$$\hat{P}_{ab}(z,\varepsilon) = \hat{P}_{ab}(z,0) + \varepsilon \frac{\partial \hat{P}_{ab}(z,\varepsilon)}{\partial \varepsilon}|_{\varepsilon=0} + \mathcal{O}(\alpha_s^2). \tag{2.4.23}$$

In summary, the initial-state collinear remnants are given by [39, 59]

$$\begin{aligned} d\hat{\sigma}_{ab}^{(in,\pm)} &= \frac{\alpha_s}{2\pi}\frac{1}{\varepsilon}\gamma_a(\mathcal{RS}_\alpha) \\ &+ \frac{\alpha_s}{2\pi}\sum_d \left\{(1-z)\hat{P}_{ad}(z,0)\left[\left(\frac{1}{1-z}\right)_+ \log\frac{s}{\mu^2} + 2\left(\frac{\log(1-z)}{1-z}\right)_+\right]\right. \\ &\left. - \frac{\partial\hat{P}_{ad}(z,\varepsilon)}{\partial\varepsilon}|_{\varepsilon=0} - K_{ad}(z)\right\}\mathcal{B}_{db}. \end{aligned} \tag{2.4.24}$$

The first line contains a soft singularity, which cancels out with the corresponding expression in the soft-virtual terms. This leads to additional summands in eq. (2.3.21), given by

$$\mathcal{Q}_{\text{IS}} = -\log\frac{\mu_F^2}{Q^2}\left(\gamma_\oplus + \gamma_\ominus\right), \tag{2.4.25}$$

where Q^2 is the Ellis-Sexton scale. The second line in eq. (2.4.24) can be integrated as it is. It makes up another independent component of the complete NLO calculation, next to the Born, real and virtual contributions. Its kinematics are essentially Born-like, with one additional degree of freedom due to the parton energy fraction z.

2.5. Phase space constructions

The first element of an FKS pair, given the redundancy-free definition of $\mathcal{P}_{\text{FKS}}$ in eq. (2.2.3), specifies the emitter of a singular region. An essential part of the subtraction procedure is to ensure that the phase-space point a real matrix element is evaluated with for a given α correctly reproduces the soft and collinear limits of this region. In other words, for each α, there is a mapping $\bar{\Phi}_n \to \Phi_{n+1}(\alpha_r)$ of Born kinematics to real-emission kinematics. This makes FKS especially suited for a combination with POWHEG matching, in contrast to dipole-based subtraction schemes like CS, where the mapping proceeds in the different direction. Here, one single $n+1$-particle phase-space configuration is mapped onto several Born configurations.

In original FKS works, the phase-space construction was hand-tailored for the processes involved. In the wake of the development of the POWHEG BOX [44], a general algorithm has been developed, first for massless particles. The first publication to discuss a phase-space construction for massive emitters is ref. [60] in the context of electroweak corrections to single W production. A special algorithm is used for resonance-aware FKS [61]. The details of real-emission phase space generation are vital for a correct implementation of an NLO event generator, but not relevant for the general picture. Their discussion is therefore deferred to appendix A. In the context of this thesis, we have developed two new phase-space construction procedures. The first one deals with

initial-state emissions for decay processes, which is discussed in section 4.1. The second is on-shell phase-space generation for the $e^+e^- \to t\bar{t}$ threshold treatment, cf. section 6.2.2.

2.6. Resonance-aware FKS Subtraction

In this section, we give an overview over the resonance-aware FKS subtraction, developed in ref. [61]. It was recently applied to NLO parton shower matching in off-shell $t\bar{t}$ and Wt production at a hadron collider by ref. [78]. It has also been applied in combination with an FSR/ISR matrix-element separation to Drell-Yan in ref. [79]. Its implementation and validation in WHIZARD is briefly outlined in section 4.2 for the process $e^+e^- \to b\bar{b}\mu^+\mu^-$. Especially, it plays an important role in the study of top production discussed in chapter 5 [2].

2.6.1. Narrow resonances and real-emission mappings

The standard FKS approach turns out to be very inefficient in the presence of resonances which decay into particles which participate in real emissions. For example in the process $e^+e^- \to bW^+\bar{b}W^-$ studied later in this thesis, there is a contribution of $H \to b\bar{b}$ decays in a Higgsstrahlung diagram, with a very narrow resonance $\Gamma_H = \mathcal{O}(1\,\mathrm{MeV})$. The real correction to this process generates emissions from either the bottom or anti-bottom quark. This moves the invariant mass of the Higgs boson away from its Born value by the amount Δ^2_{bbg}, given by

$$p^2_{bbg} = \bar{p}^2_{bb} + \Delta^2_{bbg}. \tag{2.6.1}$$

$\sigma^{\mathrm{Real}}_{\mathrm{NLO}}$ is made up of both Born and real-emission kinematics, the latter one existing for each possible emitter. For an effective cancellation of singularities, the real matrix element must strictly factorize into a kinematical factor and the Born matrix element. However, the shift in the Higgs virtuality induced by eq. (2.6.1) leads to a disagreement of the Higgs propagator so that this requirement is not met. More explicitly, consider the Higgs propagator in the Born and color-correlated matrix elements

$$D^{\mathrm{Born}}_H = \left[(\bar{p}^2_{bb} - m^2_H)^2 + m^2_H\Gamma^2_H\right]^{-1}, \tag{2.6.2}$$

and the corresponding one in the real matrix element,

$$D^{\mathrm{Real}}_H = \left[(p^2_{bbg} - m^2_H)^2 + m^2_H\Gamma^2_H\right]^{-1}. \tag{2.6.3}$$

For a perfect cancellation of divergences, these two quantities should be equal, or at least close to. Let $\varepsilon = \bar{p}^2_{bb} - m^2_H$ be the deviation of the Higgs virtuality from its Born

value. Then,

$$\mathcal{D} := \frac{D_H^{\text{Born}}}{D_H^{\text{Real}}} = 1 + \frac{\Delta_{bbg}^4 + 2\Delta_{bbg}^2\varepsilon}{\varepsilon^2 + m_H^2\Gamma_H^2} \overset{\varepsilon\to 0}{=} 1 + \frac{\Delta_{bbg}^4}{m_H^2\Gamma_H^2} \tag{2.6.4}$$

gives the propagator discrepancy at threshold. It clearly shows the problem involved for real emission, as $\mathcal{D}$ is proportional to the fourth power of the gluon emission energy and the inverse square of the Higgs width. $D \approx 1$ thus requires $\Delta_{bbg}^4 \ll m_H^2\Gamma_H^2$. In the standard final-state emission phase space construction, the gluon momentum is first aligned along the emitter momentum. Both are then separated by a rotation corresponding to the radiation variables y and ϕ. The gluon emission reshuffles energy from the recoiling system to the radiation system. To account for that, the real momenta in the recoiling system are obtained by boosting the Born-level momenta. This boost especially affects the momentum of the emitter's resonance partner. For example, in $H \to b\bar{b}$, for a gluon emission from the bottom quark, the momentum of the anti-bottom quark is boosted. This way, the Higgs virtuality is shifted as indicated in eq. (2.6.1) with $\Delta_{bbg}^2 > 0$. The mismatch is most distinct for collinear emissions, since Δ_{bbg}^4 can take arbitrarily large values, but also soft emissions can fall below this limit, especially for $H \to b\bar{b}$ where $m_H^2\Gamma_H^2 = (0.720\,\text{GeV})^4$. The mismatch is milder for $t \to Wb$, since $m_t^2\Gamma_t^2 = (15.4\,\text{GeV})^4$, but still of relevance. Note that the issue of the $H \to b\bar{b}$ subprocess is only present in the off-shell $t\bar{t}$ process at a lepton collider, because here the production process is $\mathcal{O}(\alpha^2)$, instead of $\mathcal{O}(\alpha_s^2)$ at a hadron collider. In the so-called resonance-aware FKS approach, first presented in ref. [61], the problem is solved by fixing $\Delta_{bbg} = 0$, so that $\mathcal{D}$ is always perfectly one and the soft and collinear approximations match the real matrix element in its respective limits. To fixate $\Delta_{bbg}^2 = 0$, the real emission is generated in the resonance rest frame. In contrast to the default approach, the mapping is completely insensitive to all particles not associated with the resonance. Their momenta are just kept at their Born value. The gluon and emitter momenta are constructed as usual, and all recoiling particles which belong to the resonance are boosted. This way, $\bar{p}_{bb}^2 = p_{bbg}^2$, which solves the problem of propagator mismatch. Processes can be made up of diagrams in which the final-state particles emerge from different resonances. For example, in four-jet production at a lepton collider, the process $e^+e^- \to u\bar{u}d\bar{d}$ consists of diagrams with Z resonances, in which $ZZ \to (u\bar{u})(d\bar{d})$ and of diagrams with W resonances, in which $WW \to (u\bar{d})(d\bar{u})$. These different **resonance histories** f_r interfere in the total matrix element, and it is thus necessary to separate the cross section into well-defined contributions, each of them dominating in a single resonance history. This leads to a modification of the FKS mappings, discussed in section 2.6.3.

2.6.2. Soft mismatch

Moving from the total CMS frame to the resonance rest frame requires careful replacement of $\sqrt{s}$ by the resonance virtuality $\sqrt{k_{\text{res}}^2}$ at the appropriate places. Because the momenta not associated with the emitter of a given resonance history are fixed at their Born values, the effective reference energy of the gluon emission is now given by the resonance momentum. Thus, there is the modified expression for the gluon energy

$$\xi = \frac{2k_{n+1}^0}{\sqrt{k_{\text{res}}^2}}, \tag{2.6.5}$$

with its upper limit given by

$$\xi_{\text{max}} = \frac{2\bar{k}_{\text{em}} \cdot k_{\text{res}}}{k_{\text{res}}^2}. \tag{2.6.6}$$

This trivial replacement has strong consequences for the soft integrals, because ξ differs between reference frames. This non-globality implies a phase-space factorization which is different from eq. (2.2.18), i.e.

$$d\Phi_{n+1} = \frac{\left(k_{\text{res}}^2\right)^{1-\varepsilon}}{(4\pi)^{3-2\varepsilon}} \xi^{1-2\varepsilon} d\xi d\Omega^{3-2\varepsilon} d\Phi_n. \tag{2.6.7}$$

Therefore, the soft-virtual integral in eq. (2.3.8) changes to

$$I_{s,\alpha} = -\frac{1}{2\varepsilon} \int d\Phi_n \frac{\left(k_{\text{res}}^2\right)^{1-\varepsilon}}{(4\pi)^{3-2\varepsilon}} d\Omega^{3-2\varepsilon} \lim_{\xi\to 0} \left[\xi^2 \mathcal{R}_\alpha\right]. \tag{2.6.8}$$

The collinear-virtual integral in eq. (2.3.9) on the other hand is not modified, because it does not use real phase-space factorization explicitly. The virtual subtraction terms in section 2.3 are obtained by summing over all $I_{s,\alpha}$ (the summation is actually always implicit there). The common factor s in the numerator of eq. (2.3.8) appears as a global logarithm in the final result. In eq. (2.6.8), k_{res}^2 depends on the reference frame of the resonance history f_r, so that the summation cannot be carried out in the standard way. In fact, the full $\mathcal{R}$ is not recovered that way, i.e. there is a mismatch between $\mathcal{R}$ and the sum over all α. This mismatch has to be included in the resonance-aware FKS computation as an additional component. The goal is to make the non Lorentz-invariant part of eq. (2.6.8) explicit. For this we rewrite eq. (2.6.5) to

$$\xi = \frac{2k_i \cdot k_{\text{res}}}{k_{\text{res}}^2}, \tag{2.6.9}$$

which is possible because ξ is defined in the rest frame of k_{res}. Note that eq. (2.6.9) is not Lorentz-invariant, because k_i belongs to the common radiation phase space. The

ε-pole in eq. (2.6.8) can be transformed into an integral by artificially extending ξ to the interval $(0, \xi)$,

$$\int_0^\infty d\xi \xi^{-1-2\varepsilon} e^{-\varepsilon} = \frac{\Gamma(1-2\varepsilon)}{-2\varepsilon}. \tag{2.6.10}$$

This continuation might seem problematic at first glance, because arbitrarily large values of ξ lead to arbitrarily large emission energies, which would violate momentum conservation. Yet, the soft mismatch has effectively Born kinematics and all radiation variables are inclusive in the integrals. Therefore, no explicit real-emission phase space has to be generated, avoiding a violation of momentum conservation[12] Vice versa, the replacement

$$\xi^{-1-2\varepsilon} e^{-\xi} \Rightarrow \frac{\Gamma(1-2\varepsilon)}{-2\varepsilon} \delta(\xi) \tag{2.6.11}$$

undoes eq. (2.6.9). Inserting eq. (2.6.10) into eq. (2.6.8) yields

$$\begin{aligned} I_{s,\alpha} &= \frac{1}{\Gamma(1-2\varepsilon)} \int d\Phi_n \int_0^\infty d\xi \xi^{-1-2\varepsilon} e^{-\varepsilon} \frac{\left(k_{\text{res}}^2\right)^{1-\varepsilon}}{(4\pi)^{3-2\varepsilon}} d\Omega^{3-2\varepsilon} \lim_{\xi\to 0} \left[\xi^2 \mathcal{R}_\alpha\right] \\ &= \frac{1}{\Gamma(1-2\varepsilon)} \int d\Phi_n \int d\Phi_i e^{\frac{-2k_i\cdot k_{\text{res}}}{k_{\text{res}}^2}} \left\{ \frac{1}{\xi^2} \lim_{\xi\to 0} \left[\xi^2 \mathcal{R}_\alpha\right] \right\}, \end{aligned} \tag{2.6.12}$$

where in the second line we have restored the Lorentz-invariant radiation phase space $d\Phi_i$. Moreover, ξ has been replaced in the exponent by eq. (2.6.9). In eq. (2.6.12), the only quantity which depends on the resonance frame is the exponential. Defining

$$\hat{\mathcal{R}}_\alpha = \frac{1}{\xi^2} \lim_{\xi\to 0} \left[\xi^2 \mathcal{R}_\alpha\right], \tag{2.6.13}$$

we split up $I_{s,\alpha}$ into an IR-finite and divergent part by subtracting and adding an exponential with the same singular behavior with respect to a reference momentum q,

$$I_{s,\alpha} = I_{s,\alpha}^{(0)} + I_{s,\alpha}^{(\varepsilon)}, \tag{2.6.14}$$

$$I_{s,\alpha}^{(0)} = \frac{1}{\Gamma(1-2\varepsilon)} \int d\Phi_n \int d\Phi_i \hat{\mathcal{R}}_\alpha \left\{ \exp\left[-\frac{2k_i\cdot k_{\text{res}}}{k_{\text{res}}^2}\right] - \exp\left[-\frac{2k_i\cdot q}{q^2}\right] \right\}, \tag{2.6.15}$$

$$I_{s,\alpha}^{(\varepsilon)} = \frac{1}{\Gamma(1-2\varepsilon)} \int d\Phi_n \int d\Phi_i \hat{\mathcal{R}}_\alpha \left[\frac{-2k_i\cdot q}{q^2}\right]. \tag{2.6.16}$$

In the soft limit $k_i \to 0$, eq. (2.6.15) behaves as $e^{-0} - e^{-0}$, causing the divergences in $\hat{\mathcal{R}}_\alpha$ to vanish. Most commonly, q is the total four-momentum of all final-state particles,

[12] A subtlety occurs for the evaluation of the soft subtraction, given by eq. (2.2.26), which is required by eq. (2.6.18). There, the gluon momentum occurs, contrary to the statement made here. Yet, the gluon energy cancels out in the full expression cf. eq. (2.2.17). Therefore, one can use a unit vector for k in eq. (2.2.26), which only depends on y and ϕ.

so that $q^2 = s$. This way, $q^2 > 0$, which damps contributions of large gluon energies k_i in eq. (2.6.16). The crucial point is that $I^{(\varepsilon)}_{s,\alpha}$ does not depend on the resonance frame. Therefore, the sum over all singular regions like in eq. (2.2.26) can be performed, and the exponential $\exp\left[-\frac{2k_i\cdot q}{q^2}\right]$ factors out. This leaves the sum over all $\hat{\mathcal{R}}_\alpha$ with the same Born flavor structure, in which, per construction $\sum_\alpha \hat{\mathcal{R}}_\alpha = \hat{\mathcal{R}}$, i.e. the full soft limit as in eq. (2.2.26). For this reason, $I^{(\varepsilon)}_{s,\alpha}$ is the same as in eq. (2.3.8) and does not introduce any new contributions. The $I^{(0)}_{s,\alpha}$ term has no soft, but collinear divergences. It is split up into a regularized and divergent part as depicted in fig. 2.2, using eq. (2.3.10). As before,

$$I^{(0)}_{s,\alpha} = I^{(0)}_{s\delta,\alpha} + I^{(0)}_{s+,\alpha}. \tag{2.6.17}$$

with

$$\begin{aligned} I^{(0)}_{s+,\alpha} \equiv I_{\text{mism},\alpha} = \int d\Phi_n \int_0^\infty d\xi \int_{-1}^1 dy \int_0^{2\pi} d\phi \frac{s\xi}{(4\pi)^3} \times \Bigg\{ \mathcal{R}_{s,\alpha} \left[e^{-\frac{2k\cdot k_{\text{res}}}{k^2_{\text{res}}}} - e^{-\xi} \right]_\alpha \\ - \frac{32\pi\alpha_s C_{j(f_b)}}{s\xi^2} \mathcal{B}_{f_b} (1-y)^{-1} \left[e^{-\frac{2k\cdot k_{\text{res}}}{k^2_{\text{res}}}\frac{k_i^0}{k_j^0}} - e^{-\xi} \right]_\alpha \Bigg\}, \end{aligned} \tag{2.6.18}$$

The second summand subtracts collinear divergences and is therefore only required in singular regions with massless emitters. $\mathcal{B}$ is the usual Born matrix element and $\mathcal{R}_{s,\alpha}$ the soft approximation of the real matrix element as given in eq. (2.2.26). k is the gluon momentum associated with the emitter of the singular region α. Note that the integration range is technically extended to infinity, as already pointed out in relation to eq. (2.6.10). Further, contributions with very large ξ are damped by the negative sign in the exponential. Equation (2.6.18) constitutes the so-called **soft mismatch**, an integration component exclusive to the resonance-aware FKS framework. In standard FKS, the integral $I_{s\delta}$ equals zero, cf. eq. (2.3.23). This is not the case here, where it is given by

$$\begin{aligned} I^{(0)}_{s\delta,\alpha} = -\frac{1}{\Gamma(1-2\varepsilon)} \int d\Phi_B \int_0^\infty d\xi \int_{-1}^1 dy \int_0^{2\pi} d\phi \frac{s^{1-\varepsilon}}{(4\pi)^{3-2\varepsilon}} \xi^{1-2\varepsilon} \\ \times \frac{2^{-2\varepsilon}}{\varepsilon} \delta(1-y) d\xi dy d\Omega^{2-2\varepsilon} \lim_{y\to 1}[(1-y)\mathcal{R}_{s,\alpha}] \left\{ e^{-\frac{2k_i\cdot k_{\text{res}}}{k^2_{\text{res}}}} - e^{-\xi} \right\}. \end{aligned} \tag{2.6.19}$$

It contributes as $\mathcal{Q}^{s\delta}$ to the collinear virtual subtraction term $\mathcal{Q}$ in eq. (2.3.1) in addition to the expression $\mathcal{Q}^{+\delta}$ of eq. (2.3.21). The evaluation of eq. (2.6.19) is similar to the computation of I_{s+} in section 2.3 and can be found in ref. [61]. The result for the finite

part is

$$Q_i^{s\delta} = 2\left(\log\frac{\sqrt{s}}{2\bar{k}_j^0} + \log\xi_{\max}\right)\left(\log\frac{\sqrt{s}}{2\bar{k}_j^0} + \log\xi_{\max} + \log\frac{Q^2}{s}\right)C_{i(f_b)}, \tag{2.6.20}$$

where $\bar{k}_j^0$ is the energy of the emitter in the Born phase space.

2.6.3. Modified FKS regions

The usual FKS regions discussed in section 2.2.1 are modified in order to separate different resonance histories[13]. Every resonance of f_r, collected in the set Nd , is associated with a Breit-Wigner factor, giving the weight

$$P^{f_r} = \prod_{i\in\mathrm{Nd}(f_r)} \frac{M_i^4}{(s_i - M_i^2)^2 + \Gamma_i^2 M_i^2}, \tag{2.6.21}$$

with $s_i = k_{\mathrm{res},i}^2$. This is used to extend the $\mathcal{S}$-functions of eq. (2.2.10). They should not only approach one only if the kinematics match the soft and collinear characteristics of α, but also only if the invariant masses s_i of the decay products of the resonances are close to threshold. Additionally, they have to vanish if the kinematics match a different resonance history. This requirements are fulfilled by

$$\mathcal{S}_\alpha = \frac{P^{f_r(\alpha)} d^{-1}(\alpha)}{\sum_{f_r'\in T(F_r(\alpha))} P^{f_r'}\left[\sum_{\alpha'\in\mathcal{P}_{\mathrm{FKS}}(f_r')} d^{-1}(\alpha')\right]}, \tag{2.6.22}$$

where T denotes the set of all resonance histories induced by the bare flavor structure F_r. For the d_{ij} terms, the same expressions as in e.g. eq. (2.2.13) can be used, but they need to be evaluated in the resonance rest frames. This can be achieved by the formal replacement $E_i \to k_i \cdot k_{\mathrm{res}}$. The resonance-aware extension of the $\mathcal{S}$-functions increases the number of singular regions. It is at most the number of emitters times the number of resonance histories, but can be less because not every emitter need to belong to all resonance histories. We indicate the additional resonance information in the FKS pairs by an additional index, $(i, j; k)$. An example is given for $e^+e^- \to b\bar{b}\mu^+\mu^-$ in section B.1 in table B.3.

[13] The approach for the Born phase space discussed ref. [61] is at leading order in principle the same as the phase-space mappings applied in the WHIZARD multi-channel setup. For this reason, WHIZARD only has resonance mappings for real matrix elements, and we constrain our discussion to those.

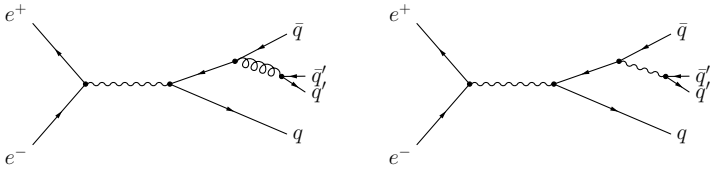

Figure 2.4. An $\mathcal{O}(\alpha^2\alpha_s^2)$ and an $\mathcal{O}(\alpha^4)$ contribution to $e^+e^- \to jjjj$. If taken as a real-emission correction to three-jet production, only the left diagram has a valid underlying Born flavor structure.

2.7. Remarks on electroweak and mixed corrections

Discussing the subtraction approach, we have implicitly assumed that the subtraction terms to the real amplitude can be unambiguously created. The factorization formulas in section 2.1.2 and section 2.1.1 connect real amplitudes with only one Born amplitude.

However, this assumption turns out to be too simple for most processes. The complete matrix element usually contains different mixed-coupling contributions. For example, the process $e^+e^- \to jjjj$ is made up of Feynman diagrams of $\mathcal{O}(\alpha_s\alpha)$ and $\mathcal{O}(\alpha^2)$, cf fig. 2.4. In a gauge-invariant calculation, the squared matrix element contains interference terms, so that $|\mathcal{M}|^2$ has contributions proportional to $\alpha_s^2\alpha^2$, $\alpha_s\alpha^3$ and α^4. Figure 2.5 shows the systematics of mixed-coupling corrections. It shows that the same combination of coupling powers can be reached by a different type of corrections to different LO terms. Therefore, the $\mathcal{O}(\alpha_s^2\alpha^3)$ and $\mathcal{O}(\alpha_s\alpha^4)$ amplitudes contain both divergences from QCD and QED splittings (apart from those already present at LO). If only pure QCD corrections are considered, these divergences do not cancel. This shows that to capture the full physical picture, both QED and QCD corrections have to be taken into account. In many studies, it is common to only take the coupling combinations at the left (QCD) or right (QED) border of fig. 2.5 into account. This approach has to be taken with a grain of salt, since in general, selecting diagrams can violate gauge invariance [80]. However, if the coupling powers and selected consistently, no such problem arises. The question arises in how far the calculations in this chapter can be transferred to QED and electroweak corrections. As far as final-state corrections are concerned, this is straightforward. The construction of soft and collinear limits in this domain is mostly a kinematical problem. In the collinear limit, color is conserved, and the results from section 2.1.1 and section 2.2.2 can be adopted for electroweak radiative corrections, with the trivial replacement of α_s by α. Moreover, because there is no $\gamma \to \gamma\gamma$ splitting in the standard model, eq. (2.2.34) can be dropped. However, soft subtraction terms have been composed with the explicit assumption of colored particles, leading to color-correlated Born matrix elements in eq. (2.2.26). In QED, matrix elements factorize perfectly in the soft photon limit. Nevertheless, charge-correlations occur because of the fermion-photon vertex. As briefly outlined in ref. [81], to conserve overall charge conservation,

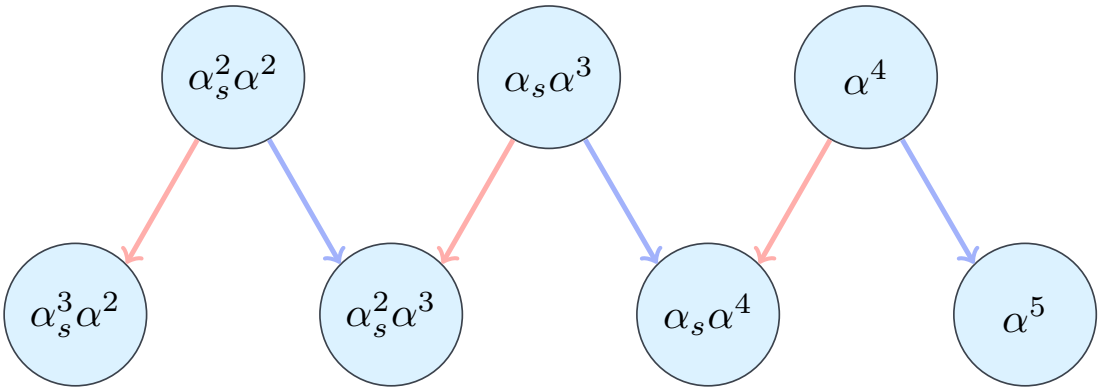

Figure 2.5. Visualization of the interference between combined QCD and QED NLO corrections at the example of the process $e^+e^- \to jjjj$. Red arrows denote QCD, blue arrows QED corrections. Only the circles at the left and right borders have one single associated leading-order contribution. For the other two, a separate QCD treatment is not possible and electroweak corrections are essential.

charge-flow sign factors $\sigma_f = \pm 1$ can be introduced such that

$$\sum_f Q_f \sigma_f = 0, \tag{2.7.1}$$

where Q_f is the positive or negative charge of particle f. σ_f is defined so that $\sigma_f = +1$ for incoming fermions or outgoing anti-fermions, and $\sigma_f = -1$ for incoming anti-fermions or outgoing anti-fermions. With these conventions, the charge-correlated Born matrix element simply takes the form

$$\mathcal{B}_{ij} = \sigma_{f_i}\sigma_{f_j}Q_{f_i}Q_{f_j}\mathcal{B}, \tag{2.7.2}$$

to be used in the soft subtraction term in eq. (2.2.26) as well as in the corresponding virtual expressions in eq. (2.3.1).

As far as initial-state radiative corrections are concerned, results cannot be taken directly from the QCD treatment. The discussion in section 2.4 deeply relies on the DGLAP evolution of QCD partons. Here, a completely new approach has to be made for photonic corrections, replacing the PDF evolution by the structure function of the lepton beam. A simpler approach would be to augment the initial-state real-emission mapping used for decays as described in section 4.1 to scattering processes.

3. The WHIZARD Event Generator

WHIZARD is a multi-purpose event generator for lepton and hadron colliders [1]. Historically, it emerged from works on electroweak physics at a 1.6 TeV lepton-collider [82] and in the TESLA technical design [83]. Especially important processes like vector-boson scattering with six particles (fermions and bosons) in the final state could not be treated by the available tools at that time. Hence the name of the program: **W**, **Hi**ggs, **Z** **A**nd **R**espective **D**ecays. WHIZARD has since grown far beyond that original purpose and is nowadays considered the major multi-purpose event generator in lepton-collider physics, which is most importantly achieved by its generic treatment of non-trivial lepton beam structures.

WHIZARD does not contain a fixed library of processes, like for example the POWHEG BOX, but instead is able to generate arbitrary matrix elements using O'MEGA [84, 85]. The algorithm is based on helicity amplitudes by using recursion relations and is designed to do this in the most efficient way. Another distinguishing feature of WHIZARD is the script language SINDARIN[2]. This is a striking difference to other programs, which use static input files to control the simulation. SINDARIN allows, apart from e.g. selecting physics models, making beam specifications, setting parameters and declaring processes, for a dynamic analysis using scans, cuts, histograms and plots. Every process in WHIZARD is associated with a specific physics model. The support of these models relies on its implementation both in O'MEGA and WHIZARD. At the time of writing, the incorporation of particles with spin 0, $\frac{1}{2}$ (Dirac/Majorana), 1, $\frac{3}{2}$ and 2 is supported. Interfaces to SARAH [86], FEYNRULES [87] and UFO [88] increase the flexibility of WHIZARD's BSM-support at tree-level.

From the technical point of view, WHIZARD is an object-oriented and modular program. Its main components, i.e. the WHIZARD core, O'MEGA and the multi-channel integrator VAMP [89], are written in programming languages most suited for their specific task. O'MEGA uses a recursive approach to generate matrix element code. This is the domain where function programming languages work best, and `O'Caml` was chosen for this task (which is also object oriented). The generated code purely consists of numerical

[1] The WHIZARD homepage is `http://whizard.hepforge.org`, where download and installation information can be found.

[2] The name is taken from the Lord of the Rings books, where Sindarin is an ancient language spoken by elves. It is an acronym for "**S**cripting **in**tegration, **d**ata **a**nalysis, **r**esults display and **in**terfaces".

expressions, where `Fortran` works best. In the following, when talking about `Fortran`, we always imply the modern `Fortran2008` standard. Also, VAMP is a mostly numeric code and is therefore also implemented in `Fortran`. The WHIZARD core functions as a facilitator between the matrix elements and the integrator. It creates the phase space and computes the matrix elements which are stored in special data structures. These dynamic data structures allow to compute in principle arbitrary traces of the matrix elements. Finally, it manages the interface to the multi-channel integrator. For these tasks, a modular and object-oriented programming language with an additional focus on numerics works best. Thus, also the WHIZARD core is written in `Fortran`. This also allows to interface various third-party programs to WHIZARD using `Fortran`'s native C-interface.

In the context of this thesis, WHIZARD has been augmented to automatically perform next-to-leading order QCD calculations. In the rest of this chapter, we discuss selected aspects of WHIZARD relevant for the NLO framework and also for the studies presented later in this thesis. We refrain from discussing giving any examples of source code or SINDARIN files. The reader should be aware that software is continuously changing, disrupting the current relationship between different components. A module, object or subroutine existing at the moment can e.g. be integrated into another, factored up into smaller entities or be removed entirely as the project advances. The first NLO calculation performed with WHIZARD was for chargino production at the ILC in refs. [90, 91], where both fixed-order QED corrections and soft-photon resummation have been studied. NLO QCD effects were first studied for the process $pp \to b\bar{b}b\bar{b}$ in refs. [92, 93] using Catani-Seymour subtraction. Independently from that, the ongoing WHIZARD+NLO project was started with the aim to create a fully-automated NLO framework using the FKS subtraction scheme discussed in detail in the previous chapter. It puts a first focus on lepton collisions, where NLO QCD corrections only affect final-state particles. It was first mentioned in ref. [8], from which point on the progress was continuously documented in refs. [1, 3–7]. Its most advanced application is the study of the off-shell top-quark continuum at a lepton collider in ref. [2] and the resummed and continuum-matched top-quark production at threshold in ref. [57].

3.1. Matrix elements and interactions

Data structures which allow for a flexible setup of the process computation are a crucial part of a multi-purpose event generator. The O'MEGA amplitudes are in general a function of the process flavors f_i, the color flow indices c_i [94], the helicities h_i and the momenta $\{p\}_i$. The first three are referred to as quantum numbers within WHIZARD. The quantum number structure of amplitudes is stored in state matrices of the dimension

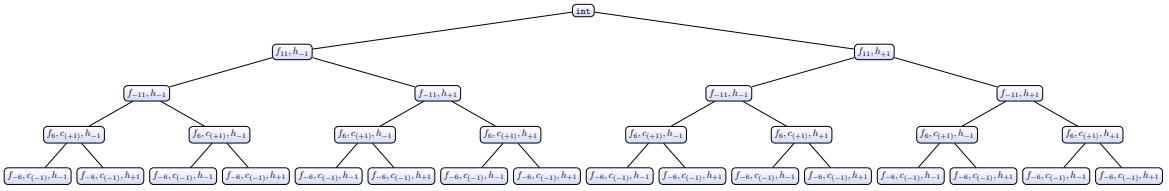

Figure 3.1. Fully-exclusive tree representation of the process $e^+e^- \to t\bar{t}$. The nodes carry the quantum numbers $\{f, c, h\}$, where the color is not indicated for the initial-state leptons. The final ones are also associated with amplitudes (not indicated in the picture).

$n_f \cdot n_c \cdot n_h$. They are represented by trees, with each node denoting one configuration of quantum numbers. In contrast to a multi-dimensional array, tree data structures allow for a dynamic data representation and, moreover, for the use of well-known optimized algorithms, such as searches, on them [3]. An example for such a state matrix is given in fig. 3.1 for the process $e^+e^- \to t\bar{t}$. Starting from the root, each quantum-number configuration can be traversed. Numerical values for amplitudes are stored on the final nodes. State matrices are combined with phase-space and particle information to an interaction. An evaluator is an interaction which receives two input interactions and performs manipulations on them, such as computing the appropriate helicity- and color-averaged sum of amplitudes. The evaluator is the final data structure in the WHIZARD amplitude chain, performing the appropriate summation or averaging over specified quantum numbers. Structure functions are also represented by a state matrix on initial-state particles. This state matrix is combined with the so-called isolated state, which contains the hard interaction of the partons.

3.1.1. External one-loop providers

WHIZARD's standard matrix element provider O'MEGA is only able to compute tree-level matrix elements. Moreover, the computation of color- and spin-correlated matrix elements, which are essential for soft and collinear approximations to real and virtual matrix elements (cf. eq. (2.1.17) and e.g. eq. (2.1.4)), is currently not accessible. The recent years have seen a tremendous development of automated one-loop calculations, which can be considered to have reached their final stage. Additionally, the Binoth Les Houches Accord (BLHA) [75, 76] has been developed as a standard interface between one-loop providers (OLP) and Monte Carlo programs. It prescribes both `C++` interfaces and keywords for configuration files. Among this is also the requirement for the OLP to

[3] To be more precise, matrix elements are represented in a trie. This is a tree in which the position of a node determines the key associated with it. An example application for tries is a dictionary. Here, each node of the trie is associated with a letter of the alphabet and every path inside the trie represents a word.

compute color- and spin-correlated squared amplitudes, thus making all building blocks of a complete NLO calculation accessible. WHIZARD, in its version 2.4.1 supports three one-loop providers: GOSAM [95, 96], OPENLOOPS [97, 98] and RECOLA [99, 100]. Besides loop amplitudes, all of these programs also can compute color- and spin-correlated squared amplitudes. It is possible to use each of them for every component of the NLO calculation, i.e. additionally also tree-level n- and $n+1$-particle matrix elements, as a matrix element provider. This builds upon the modular structure of WHIZARD, where all matrix element interfaces inherit from an abstract base class. The inclusion of any other OLP therefore is quite straightforward. GOSAM and OPENLOOPS use the BLHA interface, whereas the RECOLA code is included as an external module in WHIZARD[4]. OLPs which are BLHA-compatible are dynamically linked to WHIZARD. The BLHA configuration file, also called `.olp`–file, is automatically generated by WHIZARD. It contains specifications such as the desired correction type (QCD or QED) or the coupling powers of α and α_s, further referred to by n_{EW} and n_{QCD}. This is followed by a list of processes, each associated with an amplitude type which specifies if a tree, loop or color- or spin-correlated matrix element shall be computed. The one-loop-provider reads in the `.olp`–file and creates an answer file, or `.olc`–file. It is basically the same one as the `.olp`–file, but contains confirmation that the given processes have been found under the specifications. Moreover, each confirmed process is associated with an internal index, with which the amplitude can be accessed in the BLHA-interface. Different reasons might lead to the non-confirmation of a process, the most common one being unsuited coupling powers. For example, matrix elements for the process $e^+e^- \to jjj$ cannot be accessed with the default choices of $n_{EW} = 2$ and $n_{QCD} = 0$, but instead requires $n_{QCD} = 1$. In this case, WHIZARD just terminates the program and advises the user to check his or her settings. It is slightly more involved for processes with mixed contributions, such as $e^+e^- \to jjjj$. Here, there are diagrams with $n_{EW} = 2$ and $n_{QCD} = 2$, and such with $n_{EW} = 4$ and $n_{QCD} = 0$. This distinction is not made by O'MEGA, from which the PDG arrays used to create BLHA flavor structures are obtained, and therefore, not all but some processes match the coupling specification. In the given example with $n_{EW} = 2$ and $n_{QCD} = 2$, contributions of flavor combinations such as $e^+e^- \to u\bar{d}s\bar{c}$, which has $n_{EW} = 4$ and $n_{QCD} = 0$, are automatically set to zero by WHIZARD. In the following, each of the currently supported one-loop providers will be described in further detail.

GoSam GOSAM is based on an algebraic approach to the evaluation of loop amplitudes. Basically, it works as one would on paper: It creates Feynman diagrams with the corresponding analytical expressions and then uses dedicated algorithms to break

[4] If RECOLA is not enabled or available, dummy interfaces are used.

down the integrals to master integrals. Within GoSam, the first step is achieved by Qgraf [101] in combination with Form [102, 103]. The algebraic expressions are then translated to `Fortran90` code by the multi-purpose code generator `haggies` [104]. Integrals are then simplified by integral reduction [105, 106], using Samurai [107] or Ninja [108, 109]. Alternatively, Golem95C [110–112] can be used for tensorial reduction [113] [5]. Both methods yield master integrals, which can be looked up in an integral library such as OneLoop [114]. Whizard controls the GoSam workflow as described above. It checks whether compiled code for the current process already exists in the working directory and automatically calls all the steps of GoSam code generation if this is not the case. Once the code is generated, Amplitudes can be evaluated via the BLHA interface. Recently, a first application of GoSam to a two-loop calculation has been presented in ref. [115].

OpenLoops The OpenLoops algorithm is numerical, which means that in contrast to GoSam, it does not perform any analytical computations. Instead, it uses a hybrid approach of tensor integrals and OPP recursion relations [105, 116, 117], this way achieving good automation properties in terms of small code sizes, as well as a high amplitude evaluation speed. OpenLoops uses a public amplitude repository from which libraries for each process have to be downloaded. It contains all relevant matrix elements to compute NLO QCD corrections, both for hadron and lepton colliders. Many libraries for LHC processes can also be employed for leptonic initial states, as any crossing of external particles is automatically done when a library is loaded. For example, the one-loop library to be used for $e^+e^- \to jj$ is `ppll`. On the other hand, top quarks are not included in the proton, so that for $e^+e^- \to t\bar{t}$ the dedicated library `eett` has to be used. On top of that, there are also amplitudes for $1 \to n$ processes, which are used to compute NLO corrections to top-quark, Z and W decays, cf. section 4.1 and section 5.3.1. Furthermore, at the time of writing, amplitudes for electroweak corrections are obtainable from private repositories. The communication between Whizard and OpenLoops is based on the BLHA standard. A modification of this standard allows for the computation of polarized amplitudes by the addition of `(+)` or `(-)` after the particle identifier in the contract file, which obtains one process definition for each (not necessarily non-zero) initial-state helicity configuration. Whizard then performs the helicity-averaged sum automatically via its state-matrix structure (cf. section 3.1.2 below).

RECOLA Like OpenLoops, RECOLA is a numerical program based on recursion relations. It is, however, the only program on the market so far which has completely realized the recursive approach. To evaluate one-loop scalar and tensor integrals, it

[5] The name GoSam originated from the combination of both Golem and Samurai

relies on the COLLIER library [118, 119]. It has been successfully applied to various processes, e.g. the $\mathcal{O}(\alpha^2\alpha_s^2 \times \alpha)$-contribution to $pp \to l^+l^-jj$ [120] and fully off-shell $t\bar{t}H$-production at the LHC [121]. Together with SHERPA, it is used to provide automated NLO QCD and EW corrections as recently validated in ref. [122].

Discussion of the different OLPs

The three one-loop providers currently supported all have strengths and weaknesses. From the software development point of view, dynamically linked packages like GOSAM and OPENLOOPS are more convenient, as they avoid problems associated with different, possibly unsupported compilers, and are generally faster to implement once the standard interface exists. On the other hand, applications show that the BLHA interface is limited and the need for modifications arises beyond the application to inclusive, spin-averaged cross sections. For most analyses in this thesis, especially those in chapter 4,chapter 5 and chapter 6, OPENLOOPS has been used.

The on-the-fly code generation and compilation is definitely a drawback of GOSAM, because it can take a large amount of time and computing power. In principle, the building time of the library can be made arbitrarily short by distributing the compilations of code for different helicity configurations on several machines. Obviously, this requires user intervention and is therefore less suited to the fully-automated approach of WHIZARD+NLO. Nevertheless, the user could create the process library before starting WHIZARD. The advantage of GOSAM is its flexibility. The user is not constrained to a fixed number of processes and specific correction types. Even loops for BSM processes are possible, using FEYNRULES [87] and UFO [88], which has for example been successfully applied to the two-Higgs-doublet model in ref. [123].

RECOLA can be considered as the most powerful tool in this list. Its capabilities go beyond the computation of squared matrix elements. Unfortunately, at the time of writing, the RECOLA support in WHIZARD can only exploit a fraction of these features, but should be an integral part of the future WHIZARD+NLO development.

3.1.2. Organization of NLO matrix elements

In the following, we discuss the design of WHIZARD to accommodate additional matrix elements not present in the historically where leading-order matrix elements were the only components supported out of the box. The design choices are motivated by the different components entering the subtraction approach in eq. (2.0.1). These are

- The tree-level, N-particle Born matrix element,
- The tree-level, $N+1$-particle real radiation matrix element,

- The interference term of the Born and the loop amplitude (more precisely, its finite part),
- Color-correlated matrix elements as in eq. (2.1.16),
- Spin-correlated matrix elements as in eq. (2.1.4).

All of these objects can be computed interchangeably with different matrix-element generators, described in the previous section. Moreover, distinct components can be associated with different kinematics, like it is the case for the real-emission matrix element. Other examples are subtraction components for DGLAP remnants (cf. section 2.4), where WHIZARD must integrate over initial-state degrees of freedom, or the pseudo-radiation generated for the soft mismatch (cf. section 2.6). Additionally, WHIZARD+NLO can be run in two integration modes, separate and combined. In the separate mode, an individual integration is set up for each distinct summand of eq. (2.0.1). This allows for the distribution of integration and event generation to different jobs, increasing performance. Also, the number of integration calls can be tuned to each component. Real-subtracted matrix elements, for example, need significantly more integration calls to reach the same accuracy as components with Born-like kinematics, due to the larger phase-space dimension. On the other hand, the integration of the virtual part might still be the most time-consuming, because the evaluation of the loop matrix elements can be far more complex. The combined integration mode integrates the sum of all subtracted matrix elements and therefore hides details of the NLO calculation from the user. It is less efficient as the separate integration approach, but some applications, e.g. POWHEG matching (cf. section 4.5), require the combined integration, where the underlying Born phase-space point obtains a weight equal to the total NLO contribution. The stated design requirements are met by the following structure of WHIZARD as implemented by us from version number 2.4 and onwards.

A process is split up into components and terms [6]. Additionally, there is the core manager, which stores the interfaces to the different matrix-element generators. A component corresponds to one of the summands in the subtracted NLO cross section (Born, Real, Virtual, etc.). It is associated with several terms, which contain kinematics and parton states. This way, e.g. the real-subtracted component is connected to $n + 1$ terms, where n is the number of independent kinematical real-emission configurations in the FKS approach. The additional last term is reserved for the subtraction terms with Born kinematics. When the matrix element is evaluated, the process sums over all terms. Each term has a flag which indicates if it is active. This way, different integration components can be selected. In the combined integration mode, all allocated terms are

[6] For ease of notation, we do not use the distinction between `process` and `process_instance` or `term` and `term_instance`, as in the source code, since there is no major conceptual difference.

active. Active terms compute matrix elements. To do so, they set a pointer to a core in the core manager. If the term is for the real subtraction, it sets an additional pointer to the core used for correlated matrix elements. The matrix elements returned by each term are stored in the appropriate interactions, on which traces are evaluated which are transferred to the integrator at the end of the iteration. A schematic overview over this setup is given in fig. 3.2.

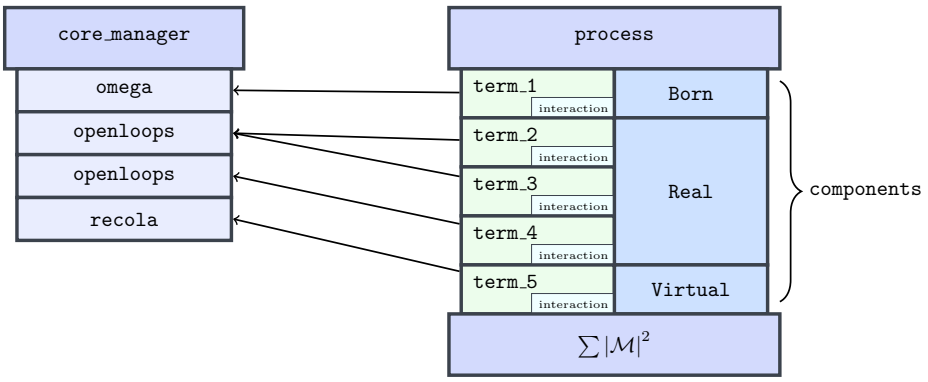

Figure 3.2. The organization of components, terms and cores for the example of $e^+e^- \to q\bar{q}$. Here, there are three components, Born, Real and Virtual, each of which is associated with a certain number of terms. Since the Born and virtual component consist of only one kinematical structure, they both have only one term. The real component has three terms, one for each emitter in $q\bar{q}$, and a third one for the calculation of the subtracted contribution, which has Born kinematics. The information about the kinematics and the state matrices is represented by the interaction object (white). Each term has a pointer to exactly one matrix-element core, collected in the core manager. It can have different matrix-element methods for each core. The list of process components can take additional components for more sophisticated types of corrections, e.g. `real_finite`, `soft_mismatch` or `dglap_remnant`.

The interactions in the parton states of each term are organized to flexibly accommodate NLO matrix elements. In WHIZARD versions prior to 2.4, they were stored in separate lists. Moreover, structure functions, especially beam polarizations, had to be extracted from the initial-state state matrices and applied to the matrix elements with separate subroutines. Version 2.4 introduced a better organization of the NLO matrix elements, embedded in the tree structure described above. This was especially motivated by the requirement to generically combine structure functions with (squared) BLHA matrix elements and subtraction terms. State matrices in their fully-differential form as they are used with O'MEGA matrix elements, cf. fig. 3.1, have been designed with the assumption that the matrix-element provider returns amplitudes differential in

all quantum numbers. This is not the case for most third-party tools such as GoSam or OpenLoops. Also, there are applications where also hand-tailored O'Mega matrix elements return already summed and averaged amplitudes, such as e.g. in the treatment of the top-quark threshold, cf. chapter 6. The inclusion of squared matrix elements in the state matrix tree relies on so-called quantum number masks, to make them inclusive in the corresponding quantum numbers. They are applied on the color and helicity indices, and the whole state matrix is contracted so that it only includes the quantum numbers specified in the mask. Polarization is included generically this way by setting up the quantum number mask in such a way that only final-state helicities are averaged.

Integrating subtraction terms in the standard state matrices requires the introduction of an additional (pseudo-) quantum number σ. Its internal role is to allocate additional entries to hold possibly polarized tree-level and color-correlated Born matrix elements in real-subtraction, virtual and DGLAP components. The book-keeping about which σ corresponds to which element in the amplitude array has to be done outside of the state matrices. Figure 3.3 depicts a state matrix tree for the interaction of a virtual component which deals with polarized $t\bar{t}$ production. There are two domains with the pseudo quantum numbers σ_0 and σ_1, corresponding to the virtual matrix element and the Born amplitude used in the associated subtraction terms, cf. eq. (2.3.1). The upper two node levels in fig. 3.3 additionally carry a helicity index. Note that this setup implies that internal color correlations are used, i.e. the Born matrix element stored in the σ_1 domain is multiplied by a color factor computed inside of Whizard. For color-correlations for a process with n final-state particles, there are $n \cdot (n-1)/2$ independent (off-diagonal) matrix as explained in the context of eq. (2.2.27). Thus, if an external matrix-element provider is used, the state matrix tree is continued straightforwardly by additional $n \cdot (n-1)/2$ σ domains. Similarly, there are 15 additional σ domains for spin-correlated matrix elements, cf. the discussion around eq. (2.2.36), independent of the process. Therefore, if the calculation requires spin correlations, 15 additional σ domains have to be included.

3.2. Phase space generation

The integration dimension for complicated multi-leg processes without structure functions typically is between 10 ($2 \to 6$) and 26 ($2 \to 10$). Initial-state structure functions can increase this number even further. As the evaluation of tree-level matrix elements is optimized (and that of one-loop amplitudes close to it), the phase-space sampling of the Monte-Carlo integrator nowadays is the bottleneck of high-multiplicity calculations. The kinematical structure of a process depends on the underlying Feynman diagrams. Resonances, radiation peaks and numerous other kinematical effects thus lead to a com-

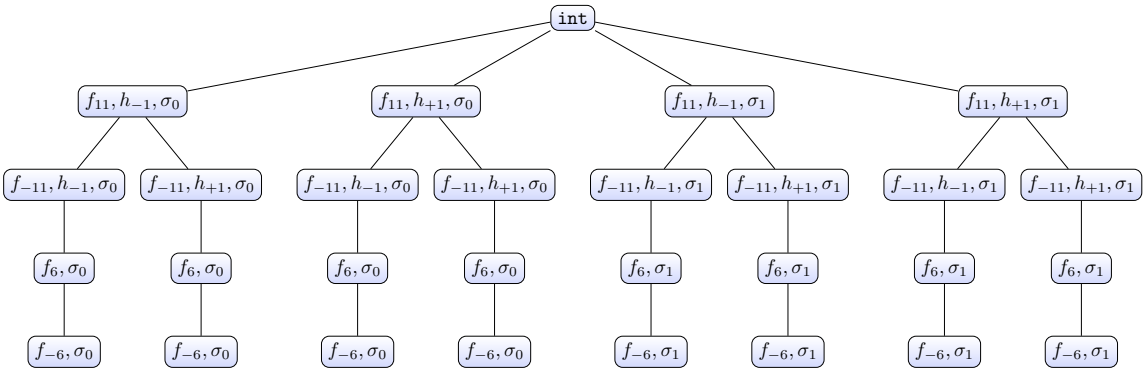

Figure 3.3. Tree representation of the process $e^+e^- \to t\bar{t}$ including polarization and subtraction terms. A summation over colors is implied, so that the quantum number $c_{(\pm 1)}$ does not appear. Instead, a subtraction pseudo quantum number σ_i is associated with each node.

plicated phase-space structure, which a naive, equally-distributed sampling mechanism can only deal with inefficiently. In theory, the sampling can be optimized with a mapping which transforms the actual kinematical dependence of the matrix element into a smooth, ideally constant distribution on the hypercube. For the phase-space parameterization, WHIZARD creates Feynman graph-like tree structures and keeps track of kinematically non-trivial regions like resonances within them. It creates a pre-selection of the most important configurations, dropping those irrelevant for sampling optimization. From these, WHIZARD constructs phase-space trees which are representations of realisations of momentum flow for a process. A tree is made up of branches, each of which can have two or no daughters (children). Associated with a mapping on each of its branches, a tree makes up an integration channel. Channels with similar kinematical mappings are collected in groves, which allows to connect channels with similar behavior during integration, thus yielding a better performance.

To make the most out of the multi-channel approach, WHIZARD is equipped with its own integration package, VAMP [89]. The VAMP algorithm is an extension of the VEGAS algorithm [124], in so far as it provides for each channel its individual (VEGAS–) integration grid [125]. The estimator for the integral is the weighted sum of the estimators of each channel. In each iteration, these weights are adapted to fit the multi-channel structure of the phase space, in addition to the usual rebinning of the integration grids. Moreover, VAMP identifies channels with vanishing contribution and drops them entirely to further increase the sampling efficiency.

The implementation of phase spaces in WHIZARD is modular. All concrete phase-space realizations inherit from the same abstract base type. The multi-channel approach is already realized in the organization of this data type. This structure allows for a sim-

ple exchange of different phase-space sampling approaches, suited for studies of special processes. The default phase space in WHIZARD is the so-called wood phase space (`phs_wood`). A phase space point is completely defined when an invariant mass m, an azimuthal angle $\cos\theta$ and a polar angle ϕ is associated to each of its internal branches. Neglecting structure functions such as parton densities or beam spectra, all external branches, i.e. initial- and final-state momenta, can be constructed using the tree structure. Internally, there are only $1 \to 2$ splittings in the trees, so that consequently for n final-state momenta, the number of internal branches is $(n-1)$. Each branch requires three random numbers. An exception is the first (initial) branch, which has a fixed invariant mass $m^2 = s$. Thus, the dimensionality of the integration is

$$d = 3 \cdot (n-1) - 1 = 3n - 4. \tag{3.2.1}$$

In the complete NLO calculation, the integration dimensionality of the different components in fig. 3.2 is not identical. Especially the real-subtracted component is evaluated on a phase space containing three additional degrees of freedom, i.e. the radiation variables of eq. (2.1.20) and eq. (2.1.22) and the azimuthal angle ϕ. These require three additional random variables. Other situation in which a non-Bornlike integrator setup is required is the subtraction of initial-state singularities, cf. eq. (2.4.24), which has n-particle kinematics but an additional degree of freedom through the parton energy fraction z. Explicitly, the integral dimension for each component is given by

$$d = 3n - 4 + \begin{cases} 0 & \text{Born, Virtual} \\ 3 & \text{Real, Soft mismatch} \\ 1 & \text{DGLAP} \end{cases}. \tag{3.2.2}$$

The real-emission phase space has to correctly map the singular behavior of the α-region it is constructed for, cf. section 2.5. In principle, this can be achieved by using a `phs_wood` phase space with a dedicated mapping on the emitter's leg which performs the real emission. In our implementation, we do not follow this approach. It would essentially multiply the number of channels at Born level by the number of distinct emitters, which is undesirable for performance optimization. Moreover, the real emission is located at one branch of the tree, but the FKS phase-space mapping works on the entire tree by boosting the recoiling momenta. Instead, WHIZARD+NLO uses an extension of the standard `phs_wood` phase space module to generate real radiation on top of the Born phase space, thus realizing directly the mapping $\Phi_n \to \Phi_{n+1}$. The real momenta generated this way are then stored generically in the associated term's interaction. The number of different real-emission phase spaces determines the number of terms attributed to the real component. It does in general not equal the number of singular regions,

because different singular regions can be associated with the same kinematics, e.g. if they have different underlying splittings ($g \to gg$ vs. $g \to q\bar{q}$), or if they differ in their resonance histories. We therefore define two phase spaces as being equivalent if they have the same emitter and the same resonance index. The mapping $\Phi_n \to \Phi_{n+1}$ is then performed for each non-equivalent real phase space using the algorithms outlined in chapter A.

3.3. Event generation

Parton shower simulations can be performed with an internal interface to PYTHIA 6 [33] or to WHIZARD's own analytical initial-state parton shower [126]. The latter efficiently keeps track of the entire shower history, allowing to reweight event samples, removing the requirement to start new simulation runs for different parameter settings. Real-subtracted, virtual and various other additional components have to be incorporated into event generation at next-to-leading order. Born-like kinematics, like virtual corrections, are trivial to implement, since they just add up to the Born event weight. Real corrections, on the other hand, are more difficult. First, they have to resemble the radiation kinematics. In the FKS framework, this means that as many events with an additional particle have to be produced as there are distinct real phase-spaces, their number determined by the conditions above. Second, subtraction terms have to be included to cancel large weights of soft or collinear phase-space points. Their kinematics is essentially Born-like, so pure real and subtraction events have to be treated on a different footing. Another problem is that both real-subtracted and virtual-subtracted matrix elements can be negative. This makes it impossible to re-weight the events. With this standard approach, NLO events are therefore only supported in weighted mode. Here, an event with Born kinematics is generated with its weight equal to the sum of the Born, virtual and subtraction contributions. In the presence of a soft mismatch or DGLAP component, also their weights are added. To each Born-like event, real-emission events are generated for each emitter with their weight equal to the pure non-subtraction real matrix element.

An alternative is event generation according to the POWHEG scheme [43, 59]. It is an NLO parton shower matching approach, which generates positive-weighted events (at least in relatively well-behaved regions of phase space), which can thus be unweighted. Moreover, POWHEG keeps next-to-leading order accuracy for the first emission while resumming large logarithms in the subsequent parton shower using modified Sudakov form factors. A more detailed description of POWHEG matching as well as predictions for $e^+e^- \to t\bar{t}$ are given in section 4.5 and chapter E. In distinction to NLO-matched events, the previously described approach is referred to as fixed-order NLO events, which

emphasizes the fact that large logarithms in parton-shower matching are not resummed in contrast to a matching procedure like POWHEG. Both POWHEG and fixed-order events can be written to an event file, .e.g. `hepmc` [127], or piped directly into an analysis tool like `Rivet` [128].

4. Validation of the WHIZARD NLO setup and example applications

In this chapter we give a brief overview over several applications of the NLO QCD extension of WHIZARD, thus combining the results from the two previous chapters. The presented studies also serve as a validation of our setup. We start by discussing the treatment of particle widths at NLO QCD with WHIZARD in section 4.1, a feature which is also of crucial importance in the top-quark studies of chapter 5 and chapter 6. Section 4.2 presents a brief study of the process $e^+e^- \to b\bar{b}\mu^+\mu^-$ as a validation of the resonance-aware FKS implementation and demonstrate the improvement of the integration it causes. Then, in section 4.3, we present a cross-check with various results from MG5_aMC@NLO for lepton-collider processes. In section 4.4, we elaborate a bit further on an improvement of the real subtraction by the introduction of damping factors, which we applied with WHIZARD to the process $e^+e^- \to t\bar{t}j$. We finish the chapter with a brief study of POWHEG matching for the processes $e^+e^- \to t\bar{t}$ and $e^+e^- \to t\bar{t}H$ in section 4.5.

4.1. NLO gauge boson and top-quark widths

WHIZARD is capable of computing gauge-boson and top-quark widths at NLO QCD. This feature is an essential part of every consistent NLO calculation involving resonant particles. Here, all widths have to be used at next-to-leading order. Especially, the employed NLO width has to be consistent with the input parameters used in the scattering process, which is best ensured by using the same program to compute them. All major WHIZARD+NLO studies [2, 57] compute NLO particle widths internally. Using FKS subtraction for decays is a straightforward task once scattering processes can be treated. The most striking difference however is the existence of an initial-state singularity from gluon emission from the top quark. Such a divergence is not present in lepton collider processes. Moreover, due to the top-quark mass, it is a purely soft divergence. For a $1 \to n$ decay, it enters the calculation as an initial-state singular region $(1, n+1)$. For this region, the ISR FKS weight in eq. (2.4.18) is used. Further, it has to be evaluated in its own dedicated real-emission phase space. In contrast to FSR singular regions,

where gluon emission can be created as outlined in appendix A.1, the standard ISR constructions can not directly be used. The algorithm, as described in appendix A.2, relies on the rearrangement of parton energy fractions, which is valid for processes with structure functions. But the decay has to be evaluated in the rest frame, i.e. the incoming momentum is fixed at $\bar{p}_0 = (m_0, 0, 0, 0)$, which renders this approach unsuitable. Instead, we implemented a different phase-space construction algorithm, mirroring the standard creation of phase-space trees in WHIZARD. It generates an $n+1$-particle phase space for a $1 \to n$ decay with a gluon emission occurring from the top quark. It does so recursively, i.e. it uses a basic $1 \to 2$ mapping to go through all the momenta in the final state. We first describe the basic $1 \to 2$ construction. The gluon four-momentum is created as for ISR in scattering processes,

$$k_{n+1} = \frac{\sqrt{s}}{2}\xi \left(1, \sqrt{1-y^2}\sin\phi, \sqrt{1-y^2}\cos\phi, y\right). \tag{4.1.1}$$

This gluon emission puts the decaying particle off its mass-shell to the momentum $\bar{p}_V = \bar{p} - k_{n+1}$. This intermediate off-shell momentum can be straightforwardly transformed into its rest frame using a boost Λ. In this frame of reference, the two decaying particles with masses m_1 and m_2, which originate from $\bar{p}_V$ move back-to-back, and their momentum is given by

$$p = \frac{\lambda^{1/2}(m^2, m_1^2, m_2^2)}{2m}. \tag{4.1.2}$$

Here m is the mass of the decaying particle and $\lambda(x, y, z) = (x - y - z)^2 - 4yz$ is the Källén function. To construct the decay momenta, their momenta are first set parallel to their corresponding Born momenta in the rest frame of $\bar{p}_V$, $\bar{p}_i^{\text{rest}}$. Thus, the decay momenta in the rest frame are given by

$$p_i^{\text{rest}} = \left(E_i, p \cdot \frac{\hat{\mathbf{p}}_i^{\text{rest}}}{|\hat{\mathbf{p}}_i^{\text{rest}}|}\right). \tag{4.1.3}$$

where $E_i^2 = m_i^2 + p^2$. Applying the inverse boost Λ^{-1} generates the momenta of the real-emission phase space in the lab frame p_i. The general case of a $1 \to n$ decay is treated by recursively applying this elemental construction on the momenta $\bar{p}_1' = \bar{p}_j$ and $\bar{p}_2' = \sum_{i=j+1}^{N} \bar{p}_i$. Here, j denotes the recursion depth and starts at one. In each step, we set $\bar{p}_V = \bar{p}_2'$ and increment j by one. The setup of NLO particle widths is checked for the decay $t \to bW$ against analytical results for massive bottom quarks [129, 130], the explicit expression of which is given in chapter D together with all input parameters. We find, at NLO QCD

$$\Gamma_t^{\text{whizard}} = 1.4078768(615)\,\text{GeV}, \quad \Gamma_t^{\text{analytical}} = 1.40787091\,\text{GeV}. \tag{4.1.4}$$

These values agree up to the sixth digit. Integration results for gauge boson decays and higher-multiplicity final states can be found in the context of the top-quark continuum in section 5.3.1. The role of Γ_t in the NLO-matched threshold computation is discussed in chapter 6.

4.2. The process $e^+e^- \to b\bar{b}\mu^+\mu^-$ with resonance-aware FKS subtraction

The resonance-aware FKS subtraction discussed in section 2.6 is implemented in WHIZARD. The soft mismatch in eq. (2.6.18) is realized as an integration component additional to the Born, real and virtual ones. It uses a dedicated phase space in which $\{\xi, y, \phi\}$ are generated, especially taking into account $\xi \in (0, \infty)$, but not used to generate real-emission momenta. Resonance histories are taken from the data structures already existent for the standard phase space. In the presence of resonances, the FKS pairs obtain an additional index r which denotes the index of the associated resonance history. Its purpose is twofold. First, it specifies which reference momentum is chosen when the real-emission phase space is constructed. Second, it determines which mapping $P^{f_r(\alpha)}$ is inserted into the numerator of $\mathcal{S}_\alpha$ in eq. (2.6.22). An example is discussed further below. In the approach of ref. [61], resonance mappings are also applied to Born-like kinematics. This is not done by us, as they are similar to the mappings applied by the multi-channel integrator VAMP.

We have checked our implementation of resonance-aware FKS subtraction using the production of two massive quarks in association with two muons as a benchmark process, i.e. $e^+e^- \to b\bar{b}\mu^+\mu^-$. This process has two different resonance histories, $Z \to b\bar{b}$ and $H \to b\bar{b}$, comprising both Z pair production and Higgsstrahlung. In the context of extended FKS regions, these then correspond to $r = 1$ and $r = 2$. Within both resonance histories, the bottom and anti-bottom quark can act as an emitter. For this reason, there are four effective singular regions, as shown in table B.3. Setting the fictitious mass $m_\mu = 20\,\text{GeV}$, we avoid an overly large rise of the cross section due to small muon invariant masses. This way, no cuts are required. Additionally, using $m_b = 4.2\,\text{GeV}$, we avoid collinear singularities and also the requirement for cuts on the bottom invariant mass. This way, we can focus on the pure testing of the resonance implementation. Note that due to the absence of collinear singularities, only the validity of the first summand of the soft mismatch component in eq. (2.6.18) is checked this way, the second being zero. We compare the resonance-aware FKS results with the integration of the same process in the standard approach. To ensure its convergence, we set the Higgs width to $\Gamma_H = 1000\,\text{GeV}$. This way, the standard subtraction can be compared to the improved one, see table 4.1, where σ_{real} denotes the full real-subtracted cross section

and σ_{mism} the result of the integration of the soft mismatch component. Adding the real and soft-mismatch component for the resonance-aware FKS subtraction, perfect agreement with the real radiation component of the standard approach is found. We want to emphasize the significantly higher number of integration calls required with standard FKS subtraction to reach the same accuracy as with the resonance-aware one. This improvement is even more distinctly visible on the right-hand side of fig. 4.1. It shows the ratio of the real matrix element and its soft limit in a selected singular region α for small gluon energies E_g. For this, a fixed number of phase-space points has been generated in the interval $0.0001 \cdot [0, \xi_{\text{max}}]$ at $\sqrt{s} = 500\,\text{GeV}$. The physical Higgs width and muon masses are used. In the resonance-aware approach (blue dots), the ratio $R_\alpha / R_\alpha^{\text{soft}}$ is almost exactly one on the whole interval, leading to the perfect convergence observed in table 4.1. In contrast, in the standard approach (red dots), $R_\alpha / R_\alpha^{\text{soft}}$ varies over two orders of magnitude and converges only unsatisfactory for very small values of E_g. This fluctuation is an effect of the small Higgs width for which already small emission energies can cause large numerical deviations in the Higgs propagator, as discussed in section 2.6.1.

The left-hand side of fig. 4.1 shows a scan of the total cross section. For this scan, we again used the physical muon mass and Higgs width. There are two distinct peaks at m_Z and $m_Z + 2m_b$, as well as two less pronounced enhancements at $m_Z + m_H$ and $2m_Z$. NLO QCD corrections are in the range of $+5\%$ for $\sqrt{s} > 2m_Z$ and approximately -4% for $m_Z + 2m_b < \sqrt{s} < m_Z$. Below $\sqrt{s} = m_Z$, the K-factor is significantly smaller than one.

Table 4.1. Real-subtracted integration component and, in the case of resonance-aware subtraction, soft mismatch, for $\Gamma_H = 1000\,\text{GeV}$. A fictitious muon mass $m_\mu = 20\,\text{GeV}$ has been used to avoid cuts.

	σ_{real}[fb]	σ_{mism}[fb]	n_{calls}
standard	$-1.90485 \pm 0.99\%$	n/a	5×100000
resonances	$-0.915077 \pm 0.52\%$	$-0.97930 \pm 0.94\%$	$5 \times 20000(\text{real}) + 5 \times 20000(\text{mism})$

4.3. Comparison with MG5_aMC@NLO

We put the NLO QCD implementation of WHIZARD to a test by comparing cross sections for various lepton collider processes computed by the MADGRAPH group, given

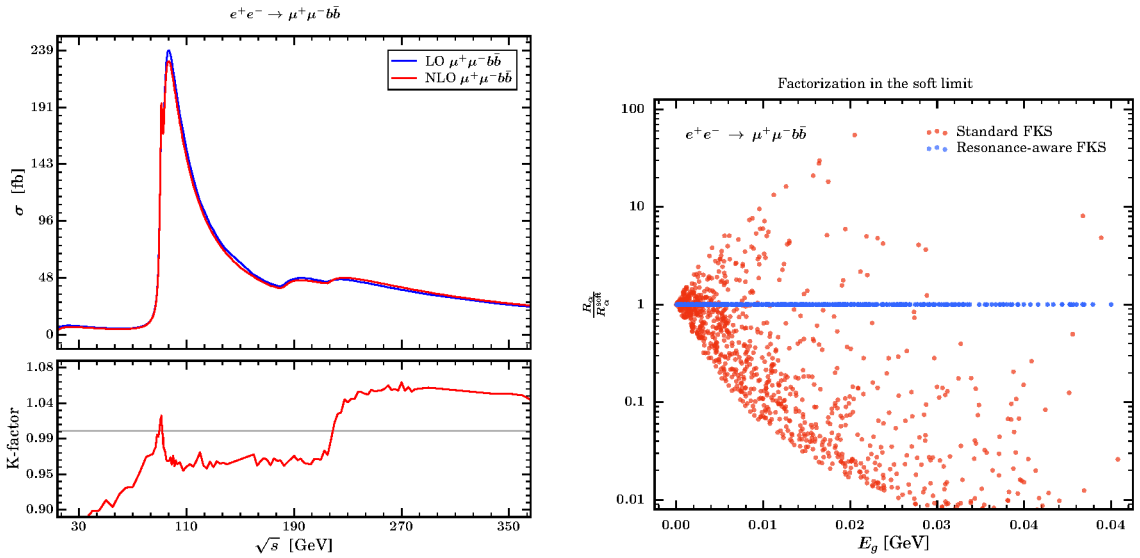

Figure 4.1. Left: Total cross section of the process $e^+e^- \to \mu^-\mu^+b\bar{b}$ at LO and NLO using resonance-aware FKS subtraction. In contrast to the validation results shown in table 4.1, here the physical muon mass and Higgs width have been used. Note that we accept the fluctuations in the K-factor as this plot only serves validation purposes. Right: Validation of the convergence of the real matrix element and its soft limit in both approaches.

in tables 10 and 11 of ref. [62]. The corresponding program, MG5_aMC@NLO, also uses the FKS subtraction scheme and is therefore suited for an in-depth comparison. MG5_aMC@NLO automatically selects the matrix elements with the strong and electroweak coupling powers belonging to a consistent NLO QCD calculation, i.e. the leftmost circle in fig. 2.5. We emphasize that for this reason, the numbers presented here do not necessarily mirror the correct physical situation and are only produced for cross-checking Whizard against MG5_aMC@NLO. Especially processes with many jets yield strong deviations of the QCD-selected from the full result. For example, the cross section for $e^+e^- \to t\bar{t}t\bar{t}$ is dominated by the electroweak background diagrams, giving a physical cross section about four times larger than the $\mathcal{O}(\alpha_s^2\alpha_e^2)$-selected one. To further facilitate the calculation, the widths of the top quark and of the $W^\pm$, Z and Higgs boson are set to zero. This way, no complex mass scheme is required. Moreover, the subtraction complications implied by narrow resonances discussed in section 2.6 and in the previous section do not arise, so that standard FKS can be used. As we need to select coupling powers, we use OpenLoops as matrix element generator for all NLO components. MG5_aMC@NLO uses MadLoop5 [26] for one-loop matrix elements. The results are summarized for $\sqrt{s} = 1\,\text{TeV}$ in table 4.2 and table 4.3. The MG5_aMC@NLO numbers are taken from ref. [62], if not specified further by asterisks. All input parameters and cuts are the same as in the Madgraph parameter and run card, available at

`http://amcatnlo.cern.ch/cards_paper.htm`. Especially, for process without explicit bottom quarks in the final state definition, bottom quarks are massless and included in the jet definition. The central scale choice is $\mu_0 = H_T/2$, with

$$H_T = \sum_i \sqrt{p_{T,i}^2 + m_i^2}, \tag{4.3.1}$$

where the sum runs over all final-state particles. We do not compare scale variations. Jets are clustered using an anti-k_T algorithm [131] with $R = 0.5$, which in WHIZARD is realised via the interface to FASTJET [132]. On the clustered jets, we apply an additional cut on the transverse momentum $p_T(j) > 30\,\text{GeV}$. Finally, on this selection, the cut $|\eta(j)| < 4$ is imposed. The phase-space point is discarded if the number of remaining jets is smaller than the number of jets in the Born process definition. In processes with photons, we use the cuts $p_T(\gamma) > 20\,\text{GeV}$ and $|\eta(\gamma)| < 2$. In the presence of jets, additionally Frixione isolation [133] is used in ref. [62]. In that approach, the separation measure $R_{i\gamma} = \sqrt{(\eta_i - \eta_\gamma)^2 + (\varphi_i - \varphi_\gamma)^2}$ is used to isolate photons from jets. Starting from all jets which are inside a cone of radius δ_0, the cumulative sum of the p_T-ordered jets must fulfill the condition

$$\sum_i p_{T,i}\theta\left(\delta - R_{i\gamma}\right) \leq p_{T,\gamma}\frac{1-\cos\delta}{1-\cos\delta_0}. \tag{4.3.2}$$

Otherwise, the whole event is rejected. This poses a problem, because the current SINDARIN implementation in WHIZARD only supports unary and binary operators. But, eq. (4.3.2) requires an n-ary operator for arbitrary jet multiplicities [1]. This could be achieved by additional `Fortran` code, which has not been done, however. Also, to our knowledge, there is no implementation of Frixione isolation in FASTJET. Therefore, no numbers are provided for processes with a light jet and at least one photon. Processes without a light jet but at least one photon have been recomputed without specifying Frixione isolation in the MADGRAPH run card. In processes with explicit bottom quarks, the four-flavor scheme is used and $m_b = 4.75\,\text{GeV}$. Further, MG5_aMC@NLO requires the number of b-jets to be conserved after clustering. Again, this is not possible with the current SINDARIN setup in WHIZARD because bottom quarks and jets cannot be separated in the cluster interface. For this reason, we do not provide numbers for processes with bottom quarks and at least one jet. The numbers presented here are computed in the separate NLO integration mode cf. section 3.3.

Despite these restrictions, the presented results are exhaustive enough to test all

[1] Another example of such an observable not available in SINDARIN is thrust, $T = \max_{\hat{n}} \sum_i |\hat{p}_i \cdot \hat{n}| \,/\, \sum_i |\hat{p}_i|$. This issue is supposed to be solved by a forseen major SINDARIN revision in the future.

relevant aspects of the NLO-integration in WHIZARD for lepton collisions and QCD corrections. The dijet process $e^+e^- \to jj$ validates the basic functionality as well as the correct treatment of multi-flavor particle definitions. The corresponding process with two top quarks in the final state checks the same setup but for the more complicated case of massive emitters. We see in table 4.2 good agreement between the two event generators for the jj, $b\bar{b}$ and $t\bar{t}$ final state. We also get agreeing results for all processes with a $t\bar{t}$ final state associated with at least one electroweak gauge boson (γ, W, Z, H). They are insensitive to QCD corrections, so that in the real-emission phase space, they just act as a recoiler. Nevertheless, they introduce more complicated loop diagrams (e.g. for $t\bar{t}HH$ up to pentagon diagrams). The $t\bar{t}t\bar{t}$, $b\bar{b}b\bar{b}$ and $t\bar{t}b\bar{b}$ final-state processes also show a good agreement with MADGRAPH. This probes non-trivial color correlations, which are treated correctly. Moreover, it is a test of the combinatorics involved in the setup of FKS regions, because the quarks need to be tagged in order not to be considered as identical particles.

Having established the validity of the $e^+e^- \to t\bar{t}$ process, the process $e^+e^- \to t\bar{t}j$ is the next simplest one to test. In contrast to $3j$-production, it has trivial FKS combinatorics because there is only one Born flavor structure. Yet, there are three aspects new to this process. First, it requires jet clustering. Second, it involves $g \to q\bar{q}$ and $g \to gg$ splittings which require spin-correlated matrix elements, cf. eq. (2.2.33) and eq. (2.2.34). Lastly, the eikonal correlation terms of the virtual-subtracted component in eq. (2.3.1) include in addition to massive-massive integrals also massive-massless integrals. The results for this process are shown in table 4.2. We observe an agreement of the leading-order numbers, but a clear discrepancy between the NLO cross sections. The agreement at LO validates that the same running of α_s is used and also that the clustering works. The NLO-deviation can have its origin in all of the three points mentioned above. A mismatch in the virtual integrals is excluded by the agreement for the process $e^+e^- \to t\bar{t}W^\pm jj$. Here, the jet can only consists out of quarks to counterbalance the charge of the W boson. Therefore, no gluon splittings appear in the real-subtracted part of the calculation. Yet, massive-massless eikonal integrals are present. A misimplementation of gluon splittings, either into a quark-antiquark pair or into two other gluons, in the real-subtracted matrix element could lead to disagreeing results. In fact, we observe a cross section mismatch in all processes with at least one gluon in the final state at Born level, cf. table 4.3. This effect, if existent, definitely also contributes to the disagreement in three- and four-jet production shown in table 4.2. Here, in addition, wrong combinatorics of FKS regions could be a source of errors. Yet, as long as the mismatch in the single-jet processes is not resolved, a discussion of these is pointless. For the same reason, we refrain from presenting numbers for processes with two light jets and gauge bosons or top quarks, as they are given in the corresponding tables in ref. [62]. The soft, collinear and soft-collinear limits in WHIZARD have been checked

numerically for each individual α region and found to have no inconsistency. To have comparable results, it is crucial to understand how the clustering and cutting procedures exactly work both in MG5_aMC@NLO and WHIZARD. It has been observed that in WHIZARD, a significant difference exists between results obtained in the separate and combined integration mode. For the process $e^+e^- \to t\bar{t}j$, we obtain a result of 51.0(3)fb in the latter case, which is much closer to the MADGRAPH value, yet still not within the respective error bounds. In the combined integration setup, when a real-emission phase space point fails the cuts after clustering, also the Born and virtual weights are discarded. This interplay between the integration components is not present in the separate integration mode, leading to the observed difference. Although with these settings we observe an almost perfect agreement between MADGRAPH and WHIZARD, other processes do not show the same improvement. For example the NLO cross section of the process $e^+e^- \to jjj$ falls off below 300 fb. It is therefore not clear whether the only source of the observed discrepancies can be found in the application of the wrong integration mode. We have observed that MG5_aMC@NLO treats scales and cuts significantly differently from WHIZARD in the calculation of the real-subtracted cross section. Whereas WHIZARD per default uses the same scale for the real-emission and the subtraction event, MG5_aMC@NLO does not. Also, an event is discarded in WHIZARD if any of the emitter regions or the Born phase space does not pass the cuts. MG5_aMC@NLO, on the other hand, keeps the event weights separately. We have implemented these different scale and cut choices in WHIZARD, but do not observe a significant agreement of the numbers. Note that the validity of $e^+e^- \to t\bar{t}W^\pm jj$ also hints to a correct treatment of cuts and scales, although the discrepancy might just not be noticeable in the result [2] There are several ways one can approach a solution to this problem. Analytical NLO QCD calculations for $e^+e^- \to t\bar{t}j$ are available in the literature [134–137], yet none of them is directly applicable to a comparison with a total cross section. A comparison with a third event generator, like SHERPA or HERWIG, might give a hint, especially with respect to the fact that the MADGRAPH e^+e^-–results have not yet been cross-checked against analytical results or any other event genertor than WHIZARD [138]. Further, a separation of the integration in MG5_aMC@NLO into Born, real and virtual contributions would help to narrow down the problem, although this has to be considered with care as both programs probably use different conventions for the arrangement of singularities and subtraction terms. Also, switching off or singling out FKS regions with gluon splittings in MG5_aMC@NLO could tell whether these actually are the source of the problem. However, this task could not be achieved before the completion of this thesis.

[2] MG5_aMC@NLO per default uses the FKS tuning parameters with ξ_c and δ_0 with values different from one and two, i.e. $\xi_c = 1/2$ and $\delta_0 = 1$. Per construction, this should not influence the total cross section, which has been verified both in WHIZARD and MG5_aMC@NLO.

Table 4.2. Comparison of MG5_aMC@NLO and WHIZARD+NLO for lepton collider processes involving jets and top quarks. Cuts and input values are as given in section 4.3. Processes marked with an asterisk have been recomputed with $m_b = 0$ to match the WHIZARD number, so the numbers presented here differ from ref. [62].

	MG5_aMC			WHIZARD		
Final state	σ^{LO}[fb]	σ^{NLO}[fb]	K	σ^{LO}[fb]	σ^{NLO}[fb]	K
jj	622.3(5)	639(1)	1.02684	622.73(4)	639.7(2)	1.02725
$b\bar{b}^*$	92.73(6)	94.89(1)	1.0233	92.32(1)	94.78(7)	1.02664
$t\bar{t}$	166.2(2)	174.5(6)	1.04994	166.4(1)	175.1(1)	1.05228
$t\bar{t}t\bar{t}$	$6.45(1) \cdot 10^{-4}$	$12.21(5) \cdot 10^{-4}$	1.89302	$6.463(2) \cdot 10^{-4}$	$12.16(2) \cdot 10^{-4}$	1.88147
$b\bar{b}b\bar{b}$	$1.644(3) \cdot 10^{-1}$	$3.60(1) \cdot 10^{-1}$	2.1897	$1.64(2) \cdot 10^{-1}$	$3.67(4) \cdot 10^{-1}$	2.2378
$t\bar{t}b\bar{b}$	$1.819(3) \cdot 10^{-1}$	$2.92(1) \cdot 10^{-1}$	1.6052	$1.86(1) \cdot 10^{-1}$	$2.93(2) \cdot 10^{-1}$	1.5752
$t\bar{t}j$	48.13(5)	52.7(2)	1.09496	48.3(2)	61.8(5)	1.27951
jjj	340.1(2)	316(2)	0.92914	342.4(5)	319(1)	0.93166
$jjjj$	104.7(1)	109.0(6)	1.04106	105.1(4)	118(1)	1.12274
$t\bar{t}t\bar{t}j$	$2.719(5) \cdot 10^{-5}$	$5.34(3) \cdot 10^{-5}$	1.96394	$2.722(1) \cdot 10^{-5}$	$4.471(5) \cdot 10^{-5}$	1.64253

Table 4.3. Comparison of MG5_aMC@NLO and WHIZARD+NLO for lepton collider processes with two top quarks and at least one electroweak gauge boson in the final state. Cuts and input values are as given in section 4.3. The value given for the $t\bar{t}W^{\pm}$ final state corresponds to the sum of the two identified final states. Processes marked with an asterisk have been recomputed without Frixione isolation to match the WHIZARD number, so the numbers presented here differ from ref. [62].

	MG5_aMC			WHIZARD		
Final State	σ^{LO}[fb]	σ^{NLO}[fb]	K	σ^{LO}[fb]	σ^{NLO}[fb]	K
$t\bar{t}H$	2.018(3)	1.911(6)	0.9461	2.022(3)	1.913(3)	0.9461
$t\bar{t}\gamma$	12.7(2)	13.3(4)	1.04726	12.71(4)	13.78(4)	1.08418
$t\bar{t}Z$	4.642(6)	4.95(1)	1.06636	4.64(1)	4.94(1)	1.06467
$t\bar{t}HZ$	$3.600(6)\cdot 10^{-2}$	$3.58(1)\cdot 10^{-2}$	0.99445	$3.596(1)\cdot 10^{-2}$	$3.581(2)\cdot 10^{-2}$	0.99571
$t\bar{t}\gamma Z$	0.2212(3)	0.2364(6)	1.06873	0.220(1)	0.240(2)	1.09094
$t\bar{t}\gamma H$	$9.75(1)\cdot 10^{-2}$	$9.42(3)\cdot 10^{-2}$	0.96614	$9.748(6)\cdot 10^{-2}$	$9.58(7)\cdot 10^{-2}$	0.98277
$t\bar{t}\gamma\gamma^{*}$	0.383(5)	0.416(2)	1.08618	0.382(3)	0.420(3)	1.09952
$t\bar{t}ZZ$	$3.788(4)\cdot 10^{-2}$	$4.00(1)\cdot 10^{-2}$	1.05597	$3.756(4)\cdot 10^{-2}$	$4.005(2)\cdot 10^{-2}$	1.06621
$t\bar{t}HH$	$1.358(1)\cdot 10^{-2}$	$1.206(3)\cdot 10^{-2}$	0.888	$1.367(1)\cdot 10^{-2}$	$1.218(1)\cdot 10^{-2}$	0.8909
$t\bar{t}W^{+}W^{-}$	0.1372(3)	0.1540(6)	1.1225	0.1370(4)	0.1538(4)	1.12257
$t\bar{t}W^{\pm}jj$	$2.400(4)\cdot 10^{-4}$	$3.72(1)\cdot 10^{-4}$	1.541	$2.41(1)\cdot 10^{-4}$	$3.74(2)\cdot 10^{-4}$	1.55186
$t\bar{t}Hj$	0.2533(3)	0.2658(9)	1.04935	0.254(1)	0.307(1)	1.20874
$t\bar{t}\gamma j$	2.355(2)	2.62(1)	1.11253	2.47(1)	3.14(2)	1.27124
$t\bar{t}Zj$	0.6059(6)	0.694(3)	1.14548	0.610(4)	0.666(5)	1.09187

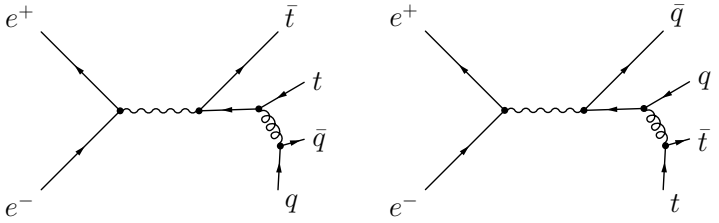

Figure 4.2. The Born-associated signal diagram (left) and a background diagram (right). Only the left one gives a correct Born process if the gluon splitting is undone.

4.4. Improving the integration by partitioning the real matrix element

The process $e^+e^- \to t\bar{t}j$ discussed in the previous section is an example par-excellence for the improvement which can be obtained by separating the real matrix element into a real and a finite part. The real corrections to this process are made up by final states which contain one additional gluon and those in which the gluon is replaced by a light quark pair. Two Feynman diagrams for the latter case are shown in fig. 4.2. Upon removing the quarks the gluon splits into, only one of them corresponds to the underlying Born flavor structure $e^+e^- \to t\bar{t}g$. The other one, i.e. that with the $g \to t\bar{t}$ splitting, gives rise to the different Born topology $e^+e^- \to t\bar{t}\gamma$. In a fully gauge-invariant calculation, all diagrams have to be summed up, including the pure squared contribution of the non-associated background diagrams. They are finite, because the collinear singularity is regularized by the top quark mass. Therefore, in regions in which these diagrams dominate, adding subtraction terms actually decreases integration performance. An example output, clearly showing the poor convergence in the $g \to q\bar{q}$-regions, is shown on the left-hand side of table 4.4. This problem does not arise in other multi-jet processes, given that the flavors of the jet definition of the Born process matches the flavors allowed for gluon splittings in the real correction.

To solve this problem, WHIZARD can separate the integration of the real-subtracted matrix element by partitioning the real phase space Φ such that

$$R^\alpha = R_s^\alpha + R_f^\alpha. \tag{4.4.1}$$

Here, R_s^α is the singular part of R^α, constrained to the subset $\Phi_s \subset \Phi$ dominated by the singularity of region α. Subtraction is performed only on this part of R^α. Accordingly, R_f^α is the finite part of R^α, defined on $\Phi_f = \Phi \setminus \Phi_s$. With the basic ideas similar to phase-space slicing methods, the partition of R has first been discussed in the context of Born-zero damping in the POWHEG approach [139, 140], which is discussed further below in section 4.5. To achieve the desired behavior of R as in eq. (4.4.1), the suppression

factor $F(\Phi)$ is introduced so that

$$R_s^\alpha = R^\alpha F(\Phi), \quad R_f^\alpha = R^\alpha \left(1 - F(\Phi)\right). \tag{4.4.2}$$

The standard suppression factor in WHIZARD is given by

$$F(\Phi) = 1 - \prod_{(i,j)\in\mathcal{P}_{\text{FKS}}} \theta\left[\sqrt{p_i^2} + \sqrt{p_j^2} + h - \sqrt{(p_i + p_j)^2}\right], \tag{4.4.3}$$

which uses the resonance information present in the $\mathcal{P}_{\text{FKS}}$ (cf. eq. (2.2.2)) to sample potential singularities. Ergo, a phase-space point is regular ($F = 0$), if the invariant masses of all momentum combinations given by $\mathcal{P}_{\text{FKS}}$ are larger than the sum of a hard scale h and the virtualities of the individual particles. If at least one FKS pair falls below this threshold, divergent matrix elements can arise and $F = 1$. The integration of R_f^α can be performed using the standard WHIZARD setup with a `phs_wood` phase space. It is allocated as a separate component, along with the Born, (singular-)real and virtual integral summands, cf. fig. 3.2 [3]. The significant improvement of the integration can be seen very clearly on the right-hand side of table 4.4, which shows the integration history if only R_s^α is used. The FKS regions have been constrained to one single FKS region α with only one FKS pair corresponding to a $g \to q\bar{q}$-splitting. This way, the inefficient integration becomes most visible. In the complete calculation, the sum over all α is performed, where the contribution of $g \to q\bar{q}$-splittings is small compared to that of the other ones. The $e^+e^- \to t\bar{t}gg$ regions make up about 90% of the entire real-subtracted cross section. Nevertheless, also in the full calculation applying damping factors to the real matrix elements shows an improvement in the integration convergence. Note that the integration results in table 4.4 are not identical because the contribution of R_f^α is missing, because it cannot be constrained to one single α region. It has been checked that, with a sufficient amount of integration calls, $\sigma_{\text{real}} = \sigma_{\text{real,sing}} + \sigma_{\text{real,fin}}$ in the sum over all singular regions. Another choice of the suppression factor has been introduced by ref. [141] and ref. [142] as

$$F = 1 - \theta\left(R^\alpha - n \cdot R^\alpha_{\text{soft}}\right)\theta\left(R^\alpha - n \cdot R^\alpha_{\text{coll}}\right), \tag{4.4.4}$$

i.e. an event is considered as finite if the real matrix element is n times larger than its soft and/or collinear approximation. Commonly, $n = 5$ is chosen. It is currently not implemented in WHIZARD, but a future study should reveal how approach (4.4.4) compares to eq. (4.4.3).

[3] This is also the anchor point for possible other finite real contributions, e.g. those with real electroweak radiation.

Table 4.4. Integration histories for $\sigma^{e^+e^-\to t\bar{t}j}_{\alpha,\text{real}}$ (left) and $\sigma^{e^+e^-\to t\bar{t}j}_{\alpha,\text{real,sing.}}$ (right) for the same number of calls per iteration and constrained to one singular region in which only a $g \to q\bar{q}$-splitting contributes. The last line shows the average over all iterations. The improved convergence is obvious. The associated finite result $\sigma^{e^+e^-\to t\bar{t}j}_{\text{real,fin.}}$ is not shown here, because it cannot be constrained to one single singular region.

Iter.	Int. – standard [fb]	Err.[fb]	Err.[%]	Int. – R_s [fb]	Err.[fb]	Err.[%]
1	$3.16 \cdot 10^{-1}$	$1.88 \cdot 10^{-1}$	59.39	-0.85	$2.44 \cdot 10^{-1}$	28.71
2	$-3.3 \cdot 10^{-1}$	$2.70 \cdot 10^{-1}$	81.35	-1.23	$1.37 \cdot 10^{-1}$	11.08
3	$1.24 \cdot 10^{-2}$	$7.03 \cdot 10^{-2}$	565.45	-1.02	$1.02 \cdot 10^{-1}$	9.96
4	$3.73 \cdot 10^{-2}$	$2.78 \cdot 10^{-2}$	74.29	-1.05	$4.02 \cdot 10^{-2}$	3.82
5	$1.02 \cdot 10^{-2}$	$1.64 \cdot 10^{-2}$	160.42	-1.05	$1.94 \cdot 10^{-2}$	1.84
	$1.77 \cdot 10^{-2}$	$1.38 \cdot 10^{-2}$	77.67	-1.05	$1.70 \cdot 10^{-2}$	1.61

4.5. POWHEG matching in $t\bar{t}$ and $t\bar{t}H$ production in WHIZARD

The matching of NLO event generation with parton showers requires a matching procedure to resum large logarithms and restore the correct order of α_s. Multiple approaches have been developed to address this problem, most notably MC@NLO [62] and POWHEG[4][43]. In the following, we very briefly outline the POWHEG procedure and discuss its implementation in WHIZARD. A more detailed description of POWHEG matching can be found in appendix app:ch:powheg-veto.

4.5.1. The Powheg PS+NLO matching approach

The essence of the POWHEG approach is that events are generated according to the following distribution

$$d\sigma = \sum_{f_b} \bar{B}^{f_b}(\Phi_n) d\Phi_n \left\{ \Delta^{\text{NLO}}_{f_b}(\Phi_n, p_{\text{T}}^{\text{min}}) + \sum_{\alpha \in \mathcal{P}_{\text{FKS}}(f_b)} \frac{\left[d\Phi_{\text{rad}} \theta(k_T - p_{\text{T}}^{\text{min}}) \Delta^{\text{NLO}}_{f_b}(\Phi_n, k_T) R(\Phi_{n+1}) \right]^{\bar{\Phi}^\alpha_n = \Phi_n}_\alpha}{B^{f_b}(\Phi_n)} \right\}, \tag{4.5.1}$$

[4] POWHEG stands for **Po**sitive **we**ight **h**ardest **e**mission **g**enerator, which points out the two major features of the procedure: The generation of events with positive weights (in contrast to e.g. MC@NLO and the resummation of large logarithms in the parton shower by the explicit generation of the hardest emission.

where

$$\bar{B}^{f_b}(\Phi_n) = B^{f_b}(\Phi_n) + V^{f_b}(\Phi_n) + \sum_{\alpha \in \mathcal{P}_{\mathrm{FKS}}(f_b)} \int \left[d\Phi_{\mathrm{rad}} \left(R(\Phi_{n+1}) - C(\Phi_{n+1}) \right) \right]_{\alpha}^{\bar{\Phi}_n^{\alpha} = \Phi_n} \quad (4.5.2)$$

is the fully inclusive NLO matrix element including subtraction terms (which are implicitly present in V) for an individual Born flavor structure f_b. Δ^{NLO} is the probability that no emission occurs between a high scale $p_{\mathrm{T}}^{\mathrm{max}}$ and any $p_{\mathrm{T}}^{\mathrm{max}} > k_T > p_{\mathrm{T}}^{\mathrm{min}}$. Equation (4.5.1) has an intuitive interpretation. The first summand is the probability that no emission harder than p_T^{min} happens at all, in which case an event with n-parton kinematics is generated. The second summand is the probability that an emission happens exactly at k_T with a splitting probability of R/B. In this case no emission must have happened for $p_T > k_T$, which is ensured by the factor $\Delta^{\mathrm{NLO}}(k_T)$. All contributions below the cut-off $p_{\mathrm{T}}^{\mathrm{min}}$ are discarded due to the θ-function. With this interpretation, it can be easily understood that eq. (4.5.1) conserves the NLO cross section (up to the small cut-off $p_{\mathrm{T}}^{\mathrm{min}}$) and only changes the spectrum of differential distributions. We stress the contraint $\bar{\Phi}_n^{\alpha} = \Phi_n^{\alpha}$ in eq. (4.5.1) and eq. (4.5.2). All matrix elements have to be evaluated with the same Born phase space in all singular regions. This has consequences for the application of POWHEG matching with Catani-Seymour subtraction, as briefly discussed further below. The non-splitting probability is given by the modified Sudakov form factor

$$\Delta_{f_b}^{\mathrm{NLO}}(\Phi_n, p_T) = \exp\left\{ - \sum_{\alpha \in \mathcal{P}_{\mathrm{FKS}}(f_b)} \int \frac{\left[d\Phi_{\mathrm{rad}} R(\Phi_{n+1}) \theta(k_T(\Phi_{n+1}) - p_T) \right]_{\alpha}^{\bar{\Phi}_n^{\alpha} = \Phi_n}}{B^{f_b}(\Phi_n)} \right\}, \quad (4.5.3)$$

which differs from the usual one by the replacement of the splitting functions by R/B as well as the inclusion of the θ-function. It therefore also covers non-singular regions. In fact, it damps soft and collinear radiation in eq. (4.5.1) since $\lim(p_T \to \infty)\Delta^{\mathrm{NLO}} = 0$.

There are two main approaches to cope with the integral in the exponent of the modified Sudakov form factor in eq. (4.5.3). The most straight-forward, but technically intense, one is to evaluate the integral numerically, as it is done in EXSAMPLE [143]. WHIZARD, like most other POWHEG implementations, uses a veto method. Here, the soft and collinear divergence structure is used to construct an over-estimator, or upper bounding function (UBF), U, such that

$$\frac{\mathcal{J}^{a_r}(\xi, y) R^{a_r}(\xi, y)}{B^{f_b}} \leq N_{f_b}^{a_r}(\xi, y) U^{a_r}(\xi, y). \quad (4.5.4)$$

Here, we stress the inclusion of the real jacobian $\mathcal{J}$ which is implicitly present in eq. (4.5.3). N is a normalization factor, to be determined by sampling the phase space

and determine the maxima of the ratio $\mathcal{J} \cdot R/(B \cdot U)$. Equation (4.5.4) has to be evaluated for every distinct combination of emitter and resonance history, collected in the multi-index rr. The UBF should be constructed in such a way that it is easy to integrate analytically. Also, to reproduce the correct collinear limits, there are different functional forms of U for initial- and final-state radiation. The explicit formulas used in WHIZARD can be found in appendix E.2. Also there, a detailed description of the veto procedure can be found. Finally, we want to emphasize the nice interplay between FKS and POWHEG, where only one Born phase space exists, so that the requirement $\bar{\Phi}_n^\alpha = \Phi_n$ is met automatically. This is in contrast to Catani-Seymour subtraction. Here, one single real-emission phase space is mapped onto several n-particle ones, thereby requiring an explicit implementation of the above projection. This can be done in several ways, e.g. by mimicking FKS mappings as weighted ratios of CS dipoles [144, 145].

4.5.2. Differential distributions

The automated POWHEG matching procedure in WHIZARD+NLO has been applied to quark production at lepton colliders, especially top quarks. The study has been presented in ref. [5, 6], which are recapitulated in the following. We consider the process $e^+e^- \to t\bar{t}$ at NLO QCD. Events are generated both at fixed-order and in the POWHEG scheme, cf. section 3.3, but no parton shower is applied. This allows to analyze the differences between the two approaches already at parton level. It has been checked, though, that processing the POWHEG events produced by WHIZARD with the p_T-ordered shower of PYTHIA8 [146] in the corresponding veto mode delivers reasonable physical results. In this setup, the top mass is set to $m_t = 172\,\mathrm{GeV}$. We chose $\mu_r = m_t$ as renormalization scale. The coupling constants are $\alpha_e^{-1} = 132.160$ with no running and $\alpha_S(M_Z) = 0.118$ with an NLL running and five active flavors. LO and POWHEG events are unweighted during generation. Polarization and beamstrahlung effects as well as lepton ISR are neglected. In total, we generate 500K (unweighted) LO events and POWHEG events as well as 1500K (weighted) fixed-order NLO events. We denote as jets all possible combinations of the occurring quarks and gluons, clustered with FASTJET according to an anti-k_T algorithm that uses energies and spherical coordinates instead of transverse momentum and rapidities as distance measure with $R = 1.0$. Figure 4.3 shows gluon and jet energy distributions at $\sqrt{s} = 500\,\mathrm{GeV}$. The soft gluon divergence can be seen in the NLO event samples either directly in the (unphysical) energy distribution of the gluon or indirectly in the distribution of the hardest jet, which peaks around the Born value due to mostly soft gluons. The POWHEG events have the expected suppression of this divergence, originating from the application of the Sudakov form factor. Due to the unitarity-conserving nature of the POWHEG procedure, this leads to an increase of the differential cross section in the remaining part of the spectrum, a well known feature of

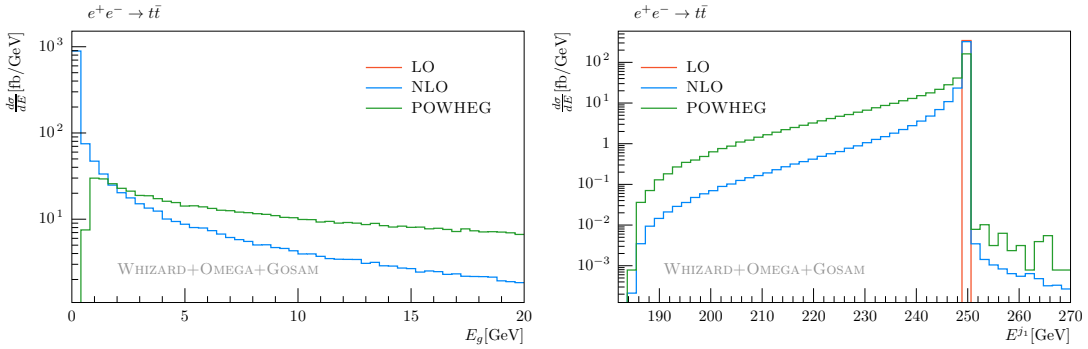

Figure 4.3. Energy distributions of the emitted gluon and of the hardest jet in the process $e^+e^- \to t\bar{t}$.

pure POWHEG distributions.

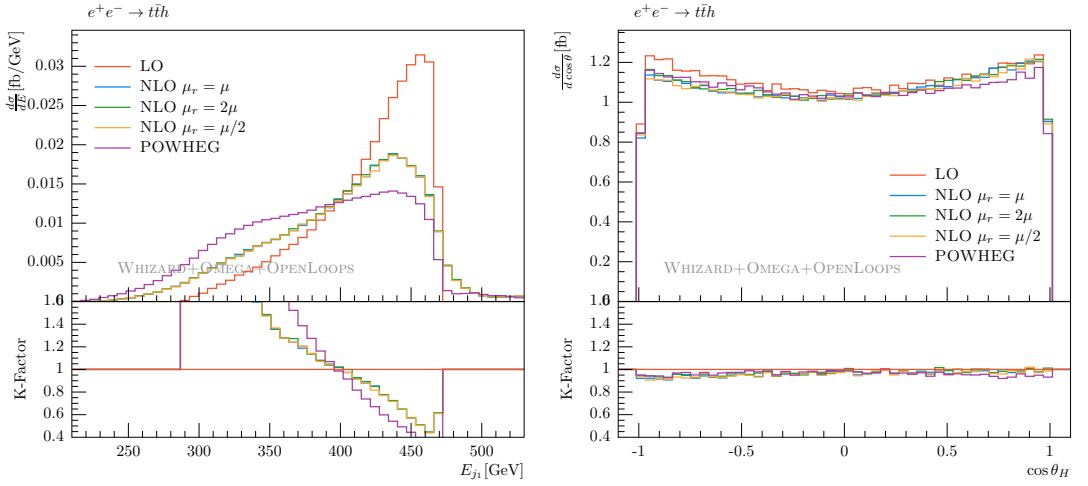

Figure 4.4. The energy distribution of the hardest jet and the angular distribution of the Higgs boson in the process $e^+e^- \to t\bar{t}H$.

Next we address the process $e^+e^- \to t\bar{t}H$ with the same setup at $\sqrt{s} = 1000\,\text{GeV}$. Apart from that, all other settings are identical to before. The left-hand side of fig. 4.4 shows the distribution of the energy of the hardest jet. The effect of Sudakov suppression is clearly visible when compared to the same observable in the fixed-order approach. Scale variations, also shown in the plot, cannot account for this difference. On the other hand, we observe that in inclusive quantities like the angular distribution of the Higgs boson, shown on the right-hand side of fig. 4.4, the POWHEG matching has no significant effect, which confirms that inclusive quantities remain correct to NLO accuracy. We want to emphasize that the total K-factor at this value of $\sqrt{s}$ is close to 1, yet distributions of observables that are sensitive to QCD radiation change drastically in both approaches. The treatment of POWHEG matching presented here is definitely not exhaustive. At the time of writing, NLO+PS matching in WHIZARD is considered an experimental feature,

with the above discussions showing its basic validity. The application to more elaborate processes, e.g. off-shell top production described at fixed-order in detail in chapter 5, in combination with increased efficiency through damping methods, might be the scope of future works within WHIZARD+NLO.

Optimizing real radiation

A well-known problem of the event generation using the modified Sudakov factor in eq. (4.5.3) is the existence of so-called Born zeroes [139]. These are configurations in which B (nearly) vanishes, but $\bar{B}$ does not [5]. In this case, a radiation event is generated which has a very large ratio R/B in the Sudakov exponent. This is a significant challenge for the upper bounding function to adapt to, leading to inefficient grids $N(\xi, y)$.

The solution, first implemented by ref. [140], is the partition of the real matrix element into a singular and a finite part as already discussed in section 4.4. The POWHEG event generation is then performed using only R_s^α. The R_f^α-contribution is finite and can be treated separately in the standard fixed-order approach.

In contrast to eq. (4.4.3), for POWHEG events a different suppression factor is commonly used [139],

$$F = \frac{Z}{Z+H}, \quad Z = B\frac{k_{T,\text{max}}^2}{B_\text{max}}, \quad H = k_T^2, \tag{4.5.5}$$

where B_max is an upper estimator of the Born matrix element. To see how this damps the Born zeroes, consider

$$R_s^\alpha = R^\alpha \frac{Bk_{T,\text{max}}^2}{Bk_{T,\text{max}}^2 + B_\text{max}k_T^2}. \tag{4.5.6}$$

Here, the ratio R/B is well-behaved, because the damping factor vanishes as fast as the Born matrix element. POWHEG damping is implemented in WHIZARD using the same setup described in section 4.4. However, we refrain from discussing its effect on the event generation here.

[5] In the case of ref. [139], which studies two-lepton production at a hadron collider (i.e. $q\bar{q}' \to W/Z \to ll'$), the vanishing Born configurations occur for leptons close to the beam axis.

Part II.

Higher-order effects in top-quark physics

5. Off-shell $t\bar{t}$ and $t\bar{t}H$ production at a linear collider

In this chapter, we investigate NLO QCD perturbative corrections in top-quark pair production at lepton colliders modeling off-shell and interference effects at increasing levels of precision. At a future lepton collider like the ILC or CLIC, a scan of this process including the production threshold allows for a measurement of the top-quark mass at a precision of 100 MeV or less. Moreover, the associated Higgs process gives the best access to a measurement of the top Yukawa coupling at the per cent level [45, 52, 147–150]. The top quark produced in the collision of the electrons decays almost immediately into a W boson and a bottom quark. The W boson then further decays either leptonically into a lepton-neutrino pair or hadronically into two quarks. In this study, we focus on the leptonic decay channels, with the related $2 \to 2$, $2 \to 4$ and $2 \to 6$ processes,

$$e^+e^- \to t\bar{t}\,, \tag{5.0.1}$$

$$e^+e^- \to bW^+\bar{b}W^-\,, \tag{5.0.2}$$

$$e^+e^- \to \mu^+\nu_\mu e^-\bar{\nu}_e b\bar{b}\,. \tag{5.0.3}$$

The highest QCD precision for on-shell $t\bar{t}$ production is currently N^{3}LO [151] at the inclusive level. Fully differential results have been obtained at NNLO QCD in ref. [152] using antenna subtraction and before that by ref. [153] using phase-space slicing methods. Both come to the conclusion that NNLO QCD corrections have sizeable effects on top of the already large NLO corrections. For electroweak corrections, NLO is still state of the art [154, 155]. An NLO QCD calculation for the off-shell process in eq. (5.0.2) has first been presented in ref. [156] and reevaluated in ref. [157] with the aim of extracting the top-quark width using ratios of single- and double-resonant signal regions. Off-shell NLO QCD predictions for top-quark production at a hadron collider have been studied in ref. [158, 159] for the $bW^+\bar{b}W^-$ final state and in ref. [78, 160–163] with leptonic decays. Notably, in ref. [78] resonance-aware FKS subtraction (cf. section 2.6) as well as POWHEG matching (cf. section 4.5) are applied. Electroweak corrections are available since recently [164].

Similar to top-quark pair production, we consider the following related $2 \to 3, 2 \to 5$

and $2 \to 7$ processes for the associated production of a Higgs boson together with a top-quark pair with increasing level of precision with respect to off-shell, non-resonant and interference effects,

$$e^+e^- \to t\bar{t}H\,, \tag{5.0.4}$$
$$e^+e^- \to bW^+\bar{b}W^-H\,, \tag{5.0.5}$$
$$e^+e^- \to \mu^+\nu_\mu e^-\bar{\nu}_e b\bar{b}H\,. \tag{5.0.6}$$

The on-shell process has been computed up to NLO QCD [165], which is also the highest currently available precision. Combined electroweak and QCD corrections are available in ref. [166] and ref. [167].

Our study is the first in-depth analysis of the processes in eq. (5.0.3) and eq. (5.0.6). It has been published in ref. [2], on which the following discussions in this chapter are based. We start by discussing the effect of the top-quark width on predictions for off-shell processes, introducing the complex mass scheme. We then give an in-depth overview of the phenomenology of the different processes. We encounter a problem of resonance-aware FKS subtraction in the presence of gluon emissions from internal tops and discuss a possible solution. After discussing our setup, we proceed by presenting integrated cross sections. The NLO integration setup is then used to investigate the dependence of σ_{tot} on the top Yukawa coupling and the effect of polarized beams at NLO QCD. The section concludes with the presentation of differential results in the off-shell processes for various observables, especially the top forward-backward asymmetry.

5.1. The top-quark width

The top quark is unstable with a lifetime τ_t inaccessible to direct measurements [1]. Nevertheless, τ_t can be obtained from the SM prediction for the top-quark width, given in eq. (4.1.4). Apart from that, Γ_t is of fundamental importance in every perturbative calculation involving top quarks. It enters the denominator of the top-quark propagator as a result of the resummation of self-energy diagrams. The bare propagator $\sim \frac{1}{k^2-m^2}$ has a pole at $k^2 = m^2$, which is regularized by the resummation of 1PI vacuum insertions $\Sigma(k^2)$,

$$D(k) = \frac{1}{k^2-m^2}\left\{1 + \sum_{n=1}^{\infty}\left[\frac{\Sigma(k^2)}{k^2-m^2}\right]^n\right\} = \frac{1}{k^2-m^2-\Sigma(k)}. \tag{5.1.1}$$

This procedure is well-known and leads to the on-shell renormalization scheme, which imposes $\text{Re}\left(\Sigma(k^2)\right)|_{k^2=m^2} = 0$ and $\text{Re}\left(\frac{\partial\Sigma(k^2)}{\partial k^2}\right)|_{k^2=m^2} = 0$. This renormalization con-

[1] The CDF collaboration attempted a direct determination of the top lifetime and obtained an upper limit of $\tau_t < 2.7 \cdot 10^{-13} s$ [168].

dition allows for the use of the standard propagator, because the resummed quantity $\Sigma(k^2)/(k^2 - m^2)$ vanishes and the pole is regularized with a running top mass.

Standard on-shell renormalization works for theories without CP-violation. However, the resummed diagram clearly contains CP-violating terms due to γ_5 matrices. An explicit calculation shows that the Ward identity is not fulfilled for the top-quark self energy diagram induced by a virtual W-boson, 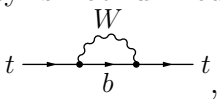

, which means that the standard on-shell scheme is not gauge-invariant. The solution to this problem is to extend the on-shell renormalization conditions to the entire complex plane, so that

$$\Sigma(k^2)|_{k^2=\mu^2} = 0, \tag{5.1.2}$$

$$\frac{\partial\Sigma(k^2)}{\partial k^2}|_{k^2=\mu^2} = 0, \tag{5.1.3}$$

where $\mu^2 = m^2 - im\Gamma$. The renormalization conditions (5.1.2) and (5.1.3) define the **complex mass scheme** [169, 170]. It is the gauge-invariant modification of the usual on-shell renormalization scheme for resonant particles and also guarantees unitarity [171]. In section 5.3.1, we will further discuss its practical application and its consequences on the electroweak parameter scheme.

A common approach to intermediate resonant particles is the so-called narrow-width approximation (NWA), where the matrix element is factorized into production and decay contributions. The NWA is usually employed to enable the computation of high-multiplicity final states where the full matrix element or the full phase space is too expensive to compute. This comes at the cost of the neglection of spin- and color correlations as well as non-resonant background contributions and interference terms. While the correlations can technically be restored [172], the contributions of non-resonant diagrams can be large and indeed are in WHIZARD's factorized approach. In general, the broader the resonance peak is, the more significant these contributions become. The NWA therefore works best with Higgs decays, but should be used with caution when applied to top quarks and weak gauge bosons. Further, for loop diagrams, non-factorizable propagators cannot consistently be taken into account. For all these reasons, it is desirable to have predictions which do not require the NWA, which is achieved in this study.

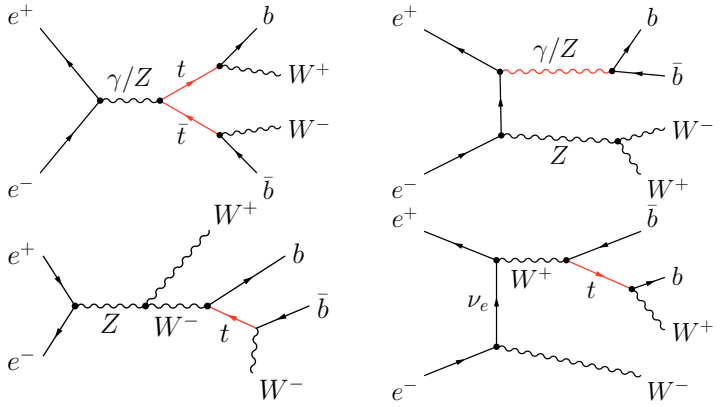

Figure 5.1. The double-resonant signal diagram (top left) besides example non-resonant (top right) and s- and t-channel single-top diagrams (bottom left and right, respectively) of the process $e^+e^- \to bW^+\bar{b}W^-$.

5.2. Phenomenology of $t\bar{t}$ and $t\bar{t}H$ production and decay

5.2.1. The $t\bar{t}$ final state

Top quarks almost exclusively decay via $t \to bW^+$, so the process in eq. (5.0.1) directly leads to the final state of eq. (5.0.2). In the NWA this is the only diagram which makes up the process in eq. (5.0.2). However, beyond the NWA, i.e. for completely off-shell top production, the process contains besides this doubly-resonant (signal) top-quark diagrams also contributions from non-resonant and single-resonant (background) diagrams together with their interference terms. Example diagrams for all three production mechanisms are shown in fig. 5.1. The sub-dominant single-top diagrams always occur via a fermion line between the two external bottom quarks. Using the full matrix element, all NLO interference effects with single-resonant and non-resonant contributions as well as spin correlations in the top decay are consistently taken into account. Diagrams like the one in the top right of fig. 5.1 include potentially divergent photon propagators from a $\gamma \to b\bar{b}$ splitting. In general, this evokes the necessity of an invariant-mass cut, which in our setup is avoided due to a finite bottom-quark mass. W bosons are unstable and decay either into a (charged) lepton-neutrino pair or a quark anti-quark pair. The hadronic decay modes account for about two third of the total decay rate, leaving about 10 % for each leptonic decay mode. Taking decays of the W boson, which is also the particle in the standard model with the largest width, into account therefore is essential to make contact with experimental signatures. From the leading-order calculational perspective, the hadronic decay modes do not yield any substantial complexities compared to the leptonic ones. However, this changes significantly at NLO QCD. The complexity

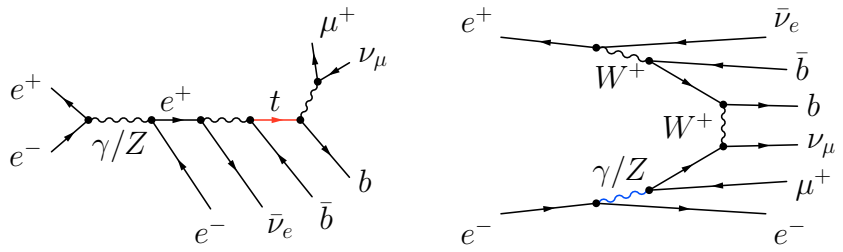

Figure 5.2. Possible topologies of the full process. The blue line indicates a potentially soft photon that gives rise to a leading-order singularity.

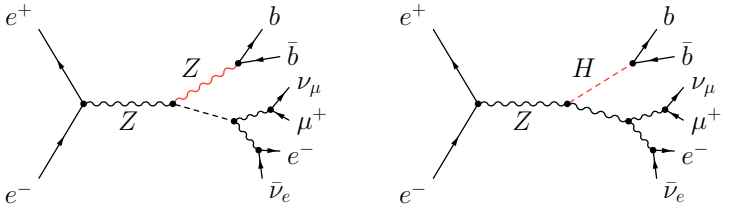

Figure 5.3. Contributions to the process $e^+e^- \to \mu^+\nu_\mu e^-\bar{\nu}_e b\bar{b}$ involving a Z or H resonance, treated via the resonance-aware FKS subtraction.

of the loop diagrams increases drastically with the additional four colored particles in the final state. Moreover, the subtraction of divergences includes collinear contributions and non-trivial color-correlations. On the phenomenological side, the clustering is much more involved and the most suitable scale choice is harder to determine. For this reasons we focus in this first study on the leptonic decay channels. Radiation only occurs from massive b-quarks, so that no collinear singularities arise. We use $2 \to 6$ matrix elements, including all off-shell and background contributions as well as spin correlations. Due to the purely electroweak nature of the leptonic W-boson decays, from a perturbative point of view these additional decays do not increase the computational complexity compared to the process with on-shell W-bosons, i.e. the one of eq. (5.0.2). However, besides the more involved phase space integration, the number of contributing diagrams increases substantially due to additional single- and non-resonant contributions, examples of which are shown in fig. 5.2. Diagrams like the one on the right of fig. 5.2 show a singularity due to photon emission from a continuous initial-final lepton line (blue photon line). Therefore, the process in eq. (5.0.3) can not be integrated over the whole phase space without cuts. Further, we focus on the different lepton-flavor case. No additional phenomenological aspects are introduced in the same-flavor case, so the description of off-shell top-quark production is detailed enough with this simplification. The different-flavor case also has a smaller number of diagrams and requires less cuts than the same-flavor process.

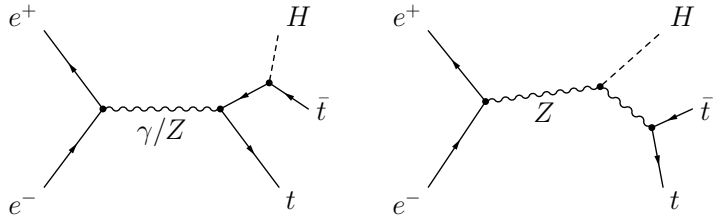

Figure 5.4. Contributing diagrams to $t\bar{t}H$ production: associated production of a Higgs boson and a top quark pair and Higgsstrahlung with an off-shell $Z^* \to t\bar{t}$ splitting.

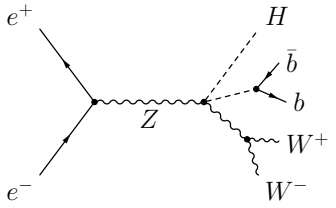

Figure 5.5. A representative non-resonant diagram contributing to $bW^+\bar{b}W^-H$ production via a quartic $ZZHH$-coupling.

5.2.2. The $t\bar{t}H$ final state

The diagrams involved in Higgs-associated top-pair production are very similar to those of the corresponding $t\bar{t}$ production processes, apart form the additional Higgs boson that couples to all massive internal or external particles $(t, b, W^\pm, Z, H)$. Already on the level of the on-shell processes of eq. (5.0.4) this results in two competing contributions, as depicted in fig. 5.4. The diagram on the left of fig. 5.4 is proportional to the top Yukawa coupling y_t and will be referred to as the $t\bar{t}H$ signal contribution, while the diagram on the right can be considered as irreducible Higgsstrahlung background in the ZH channel with an off-shell $Z^* \to t\bar{t}$ splitting. Furthermore, at the level of the off-shell processes of eq. (5.0.5) and eq. (5.0.6), besides topologies already present for the corresponding $t\bar{t}$ processes with an additional attached Higgs boson, new contributions arise from quartic EW couplings as illustrated in fig. 5.5. Note that a non-vanishing Higgs width is inconsistent with an external on-shell Higgs boson, especially concerning gauge invariance. We accept this slight inconsistency to be able to provide results independent of a specific Higgs decay channel. A completely consistent approach to this process would require the inclusion of the non-factorized Higgs decay into its dominant decay mode $H \to b\bar{b}$, similar to what is done in this study for the top quarks and the W bosons. This is in reach of Whizard, OpenLoops and other automated tools, but beyond the scope of this thesis. The resulting inconsistency is very small with contributions from $H \to b\bar{b}$ for off-shell $t\bar{t}$ as well as $t\bar{t}H$ production being at the percent level.

5.2.3. Resonance-aware subtraction and its limitations for top-quark decay

The off-shell processes, i.e. those with $bW^+\bar{b}W^-(H)$ and $\mu^+\nu_\mu e^-\bar{\nu}_e b\bar{b}(H)$ final states, contain diagrams with $Z/H \to b\bar{b}$ splittings, for example as depicted in fig. 5.3. Due to the small intermediate widths, the integration of such contributions benefit strongly from the extended resonance-aware FKS subtraction, described in section 2.6. Moreover, there are double- and single-top resonances involved, as depicted in fig. 5.1. Therefore, the whole process contains three distinct resonance topologies. The Z/H-topologies have been discussed for the process $e^+e^- \to b\bar{b}\mu^+\mu^-$ in section 4.2 and do not pose any additional problems for top production. Top resonances, on the other hand, lead to complications involving gluon emissions from internal resonant top quarks. There is no standard resonance history associated with gluon emissions from top quarks directly before they decay, yet they can be clearly separated from bottom-quark emissions for gluon emissions with $E_g > \Gamma_t$. In other words, for bottom-associated gluon emissions, it is $m_{W^+bg} \approx m_{W^-\bar{b}} \approx m_t$ or $m_{W^+b} \approx m_{W^-\bar{b}g} \approx m_t$, while in top-associated ones $m_{W^+b} \approx m_{W^-\bar{b}} \approx m_t$, independent of the gluon energy. The standard resonance mapping, which fixes either m_{W^+bg} or $m_{W^-\bar{b}g}$ therefore does not suitably conserve the top-quark virtuality. It becomes thus obvious that there should be additional resonance histories for internal gluon emissions. The corresponding phase-space mapping needs to keep m_{W^+b} and $m_{W^-\bar{b}}$ at a fixed value, which can be achieved by boosting the entire final state without the gluon. However, this naive boost violates momentum conservation. In a hadron collision process, the missing momentum could easily compensated by adapting the hadron energy fractions of the colliding partons (which then also involves the adaption of PDFs). This makes clear that in the naive setup where the lepton beams are considered structureless, such a mapping cannot be realized. A complete resonance-aware treatment therefore requires the inclusion of structure functions into the analysis. While this issue certainly deserves a more detailed treatment, we defer it to future projects. In this study, we omit top-quark resonance histories, i.e. the only resonances the subtraction is aware of are Z and H. We want to emphasize that this choice does not influence the NLO accuracy of the final result, but is only a performance issue.

5.2.4. Virtual matrix elements

In this study, all tree-level amplitudes, including color correlated ones, as well as one-loop amplitudes are obtained using OpenLoops[2]. We observe a well-known feature of

[2]The required libraries are `eett`, `eevvjj` and `eellllbb` for the $t\bar{t}$ and `eehtt`, `eehvvjj` and `eehllllbb` for the $t\bar{t}H$ processes. Note that, if the OpenLoops configuration file the setting `compile_extra = 1` is set, all these libraries also include the necessary matrix elements for the associated real amplitude with one additional gluon, so no additional installation of these processes is required.

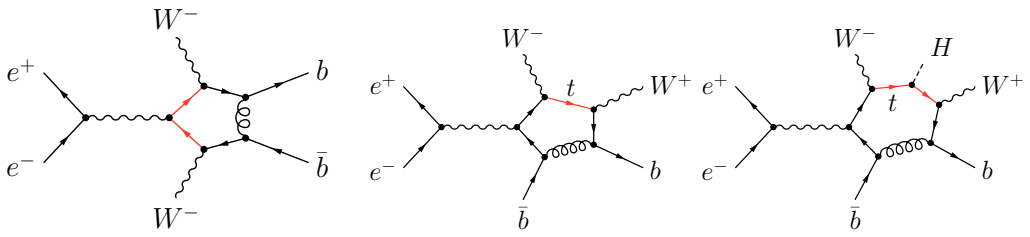

Figure 5.6. Example pentagon diagrams contributing to the $bW^+\bar{b}W^-$ final-state process containing one or two (leftmost diagram) top resonances and a hexagon diagram contributing for $bW^+\bar{b}W^-H$ production.

OpenLoops: The total number of diagrams is not decisive for the computational effort in the recursion formalism. Instead, the crucial point is the maximal number of n-point functions involved. For the $bb(W \to l\nu)(W \to l\nu)$ processes discussed here, the most complex integrals originate from pentagon diagrams, examples for which are depicted in fig. 5.6. Also shown in fig. 5.6 is a hexagon diagram contributing to the associated Higgs production process. Table 5.1 lists information about the computational complexity with respect to the one-loop amplitudes of all processes. Concerning the complexity of the amplitudes, due to the reduced number of contributing helicity structures the calculation of the off-shell processes including leptonic decays are even less involved compared to the corresponding processes with on-shell W-bosons, despite the increased number of diagrams, particularly due to the fixed neutrino chirality.

Table 5.1. Overview of loop matrix elements at NLO QCD for the studied processes. Shown are the number of one-loop diagrams, the maximal number of loop propagators and the number of helicity structures (assuming charged leptons to be massless).

$e^+e^- \to$	$n_{\text{loop diags}}$	Max. prop.	n_{hel}
$t\bar{t}$	2	3	16
$bW^+\bar{b}W^-$	157	5	144
$b\bar{b}\bar{\nu}_e e^-\nu_\mu\mu^+$	830	5	16
$t\bar{t}H$	17	4	16
$bW^+\bar{b}W^-H$	1548	6	144
$b\bar{b}\bar{\nu}_e e^-\nu_\mu\mu^+H$	7436	6	16

5.3. Setup and validation

The results presented in this chapter are very computationally intense. To achieve good statistics in differential distributions, both well-adapted grids and a high number

of events are necessary. The latter issue is a well-known problem of weighted event generation, but unavoidable due to the existence of negative weighted events in the fixed-order approach cf. section 3.3. A good grid can take up to a week to be produced in a single-threaded WHIZARD integration. Since event generation can always be trivially parallelized by distributing the total number of events to a large number of small batches, the integration constitutes the bottleneck of the event generation for high-multiplicity processes [3]. For this reason, all scans have only be performed up to four(five)-particle final states, whereas differential distributions are available for the full processes, since here only one integration is required for each scale. The events used for the differential distributions in the subsequent sections are generated using several thousand CPU cores by additionally splitting up the simulation into separate runs for Born, real, virtual and soft-mismatch components. The weights are then added in the final analysis. This way, several hundreds of millions of events have been produced for both $e^+e^- \to \mu^+\nu_\mu e^-\bar{\nu}_e b\bar{b}$ and $e^+e^- \to \mu^+\nu_\mu e^-\bar{\nu}_e b\bar{b}H$. The analysis is directly linked to the event generation in WHIZARD by piping the `hepmc` [127] output into `Rivet` [128], which continuously adapts YODA-files [4]. In the final step, the YODA-files are merged into one single object for each scale and can easily be plotted.

5.3.1. Input parameters, scale choices and phase-space cuts

We use the following gauge-boson, quark and Higgs masses [173],

$$\begin{aligned} m_Z &= 91.1876\,\text{GeV}\,, & m_W &= 80.385\,\text{GeV}\,, \\ m_b &= 4.2\,\text{GeV}\,, & m_t &= 173.2\,\text{GeV}\,, \\ m_H &= 125\,\text{GeV}\,, \end{aligned}$$

which enter the calculation as independent input parameters. The electroweak couplings are derived from the gauge-boson masses and the Fermi constant, $G_\mu = 1.1663787 \times 10^{-5}\,\text{GeV}^{-2}$, in the G_μ-scheme. The CKM matrix is assumed to be trivial, i.e. diagonal with entries equal to one[5]. Its most relevant element in our computation is V_{tb}, for which the trivial value is consistent with the measured value (1.021 ± 0.032 [173]). Furthermore, using the precisely measured value of G_μ automatically absorbs important electroweak corrections into the top decay [174]. For the strong coupling constant we use $\alpha_s(m_Z) = 0.1185$ and a two-loop running including $n_f = 5$ active flavors. The massive

[3] This might change in a well-tested parallelized version of VAMP, which at the time of writing is in the validation and testing phase.

[4] YODA is a set of C++ classes especially suited for histogramming, `https://yoda.hepforge.org`.

[5] Note that off-diagonal entries in the CKM matrix give additional contributions in the computation of $1 \to 3$ decay widths. However, to be consistent with the scattering matrix element, we also there use a trivial CKM matrix.

bottom quark is renormalized in the on-shell scheme, which is valid here because we assume $\Gamma_b = 0$, and, since α_s does not enter at LO, no renormalization of the strong coupling is necessary. Further, we use constant ttH and bbH Yukawa couplings.

With this setup, the gauge boson and top widths are computed directly with WHIZARD at LO and NLO, using massive b-quarks, cf. section 4.1. In the NLO computation, we use the mass of the decaying particle as renormalization scale. This way, the following LO and NLO gauge boson widths are obtained:

$$\Gamma_Z^{\mathrm{LO}} = 2.4409\,\mathrm{GeV}, \qquad \Gamma_Z^{\mathrm{NLO}} = 2.5060\,\mathrm{GeV}, \tag{5.3.1}$$

$$\Gamma_W^{\mathrm{LO}} = 2.0454\,\mathrm{GeV}, \qquad \Gamma_W^{\mathrm{NLO}} = 2.0978\,\mathrm{GeV}. \tag{5.3.2}$$

In our calculation we use Γ_Z and Γ_W at NLO throughout, i.e. also for off-shell cross sections at LO. This ensures that the effective W and Z leptonic branching ratios that result from $e^+e^- \to b\bar{b}4f(H)$ matrix elements are always NLO accurate. In contrast, in order to guarantee that $t \to Wb$ branching ratios remain consistently equal to one at LO and NLO, off-shell matrix elements and the top-decay width need to be evaluated at the same perturbative order. For the top-quark width we employ two distinct sets of values: one for the on-shell decay $t \to W^+b$ and one for the off-sell decay $t \to f\bar{f}b$, as also detailed in ref. [175]. The value used for the off-shell top-quark decay includes decays into three lepton generations and two quark generations. It also involves the W width, for which we use the previously computed NLO value. The numerical values are

$$\Gamma_{t\to Wb}^{\mathrm{LO}} = 1.4986\,\mathrm{GeV}, \qquad \Gamma_{t\to Wb}^{\mathrm{NLO}} = 1.3681\,\mathrm{GeV}, \tag{5.3.3}$$

$$\Gamma_{t\to f\bar{f}b}^{\mathrm{LO}} = 1.4757\,\mathrm{GeV}, \qquad \Gamma_{t\to f\bar{f}b}^{\mathrm{NLO}} = 1.3475\,\mathrm{GeV}. \tag{5.3.4}$$

The Higgs width is set to $\Gamma_H = 4.143\,\mathrm{MeV}$. For the reasons mentioned in section 5.1, we apply the complex mass scheme by moving to complex-valued masses

$$\mu_i^2 = M_i^2 - \mathrm{i}\Gamma_i M_i \qquad \text{for } i = \mathrm{W}, \mathrm{Z}, \mathrm{t}, \mathrm{H}\,, \tag{5.3.5}$$

that imply a complex-valued weak mixing angle

$$s_w^2 = 1 - c_w^2 = 1 - \frac{\mu_{\mathrm{W}}^2}{\mu_{\mathrm{Z}}^2}\,. \tag{5.3.6}$$

The electromagnetic coupling in the G_μ is computed as

$$\alpha_e = \frac{\sqrt{2}}{\pi} G_\mu \left|\mu_W^2 s_w^2\right|, \tag{5.3.7}$$

which gives $\alpha_e^{-1} = 132.16916$. For the on- and off-shell $t\bar{t}$ and $t\bar{t}H$ processes (i.e. in

contrast to the decays), the renormalization scale μ_R is set to

$$\mu_R = \xi_R \cdot m_t \tag{5.3.8}$$

for $t\bar{t}$ processes and

$$\mu_R = \xi_R \cdot (m_t + m_H) \tag{5.3.9}$$

for $t\bar{t}H$ processes. The parameter ξ_R specifies the scale variation, which is chosen to be

$$\xi_R \in \left[\frac{1}{2}, 2\right]. \tag{5.3.10}$$

The scale choices in eq. (5.3.8) and eq. (5.3.9) are different to most works on NLO processes at hadron colliders, where dynamical scales are used. At a lepton collider, fixed values μ_R can be used without significant loss of accuracy, because pure QCD corrections do not comprise initial-state radiation. Thus, the hard scattering process happens at fixed energy, which is not the case for the corresponding processes at hadron colliders. This assumption is confirmed by the very good perturbative description presented in the following sections, cf. fig. 5.7. Still, different dynamical scale choices might be appropriate for the description of some differential observables.

To avoid singularities at Born-level arising from small photon energy transfers, such as on the right-hand side of fig. 5.2, for processes with final-state electrons or positrons we apply a mild phase-space cut

$$\sqrt{\left(k_{e^\pm}^{\text{in}} - k_{e^\pm}^{\text{out}}\right)^2} > 20\,\text{GeV}. \tag{5.3.11}$$

Possible other sources for Born-level divergences are photon splittings into final-state b-quarks. These are regulated by our choice of $m_b \neq 0$. Therefore, no other cuts are imposed, although to provide realistic simulations for an experimental setup, a feasible study has to take into account jet clustering. We define a separate jet by the generalized k_T-algorithm [131, 132] with $R = 0.4$ and $p = -1$, corresponding to an anti-k_T clustering. The jet clustering is performed by `Rivet`, which has an interface to FastJet[6], on the partonic events from Whizard, before the filling of histograms occurs. We tag $b/\bar{b}$-jets according to their partonic content and denote them as j_b and $j_{\bar{b}}$. Similarly, in the on-shell processes $e^+e^- \to t\bar{t}$ and $e^+e^- \to t\bar{t}H$, we identify the top quark with the jet containing a top quark. In the discussion of differential cross sections in section 5.7 we always require at least two b-tagged jets.[7] No further phase-space restrictions are applied.

[6] The k_T-algorithm corresponds to `ee-genkt` in FastJet.

[7] Since we do not impose any kinematical restriction on b-jets, requiring two b-jets amounts to a lower bound for their ΔR separation.

5.3.2. Validation

Validations of the automated subtraction in WHIZARD+NLO have been discussed extensively in chapter 4. Especially the top-quark width has been checked against the value used in ref. [175] and the analytical formulas [129, 176, 177], cf. section 4.1. Also, the resonance-aware NLO calculation was shown to work in section 4.2. For the scope of the continuum study, we have performed additional dedicated checks and validations. They have been performed at the permille level and differences are all within two standard deviations of the MC integration. For the $e^+e^- \to bW^+\bar{b}W^-$ process, we have performed an in-depth cross check with various other results and generators. The total cross section corresponding to the study of ref. [157], therein computed with MADGRAPH5_AMC@NLO, has been reproduced. Moreover, we find excellent agreement between WHIZARD, SHERPA [30] and MUNICH [8] for the parameter set given in section 5.3.1, as can be recapitulated in tab. 5.2. Note, that both SHERPA and MUNICH use Catani-Seymour subtraction, while MADGRAPH5_AMC@NLO and WHIZARD use FKS subtraction.

Table 5.2. LO and NLO inclusive cross sections for $e^+e^- \to t\bar{t}$ and $e^+e^- \to bW^+\bar{b}W^-$ at $\sqrt{s} = 800\,\text{GeV}$, using the settings of section 5.3.1. For the NLO results, the integration errors are shown.

	WHIZARD+NLO		SHERPA		MUNICH	
Process	σ^{LO}[fb]	σ^{NLO}[fb]	σ^{LO}[fb]	σ^{NLO}[fb]	σ^{LO}[fb]	σ^{NLO}[fb]
$e^+e^- \to t\bar{t}$	253.5	271.16(2)	253.6	271.15(2)	253.8	271.369(3)
$e^+e^- \to bW^+\bar{b}W^-$	301.8	321(1)	301.3	323.4(3)	302.1	323.8(4)

5.4. Integrated cross sections and scale variation

We start our discussion of numerical results with an investigation of the NLO QCD corrections to inclusive top quark pair-production cross sections as a function of $\sqrt{s}$. In the left plot of fig. 5.7 we show inclusive LO and NLO cross sections for the on-shell process $e^+e^- \to t\bar{t}$ and the off-shell process $e^+e^- \to bW^+\bar{b}W^-$ together with the corresponding K-factors.

[8] MUNICH is the abbreviation of "MUlti-chaNnel Integrator at Swiss (CH) precision"—an automated parton level NLO generator by Stefan Kallweit. In preparation.

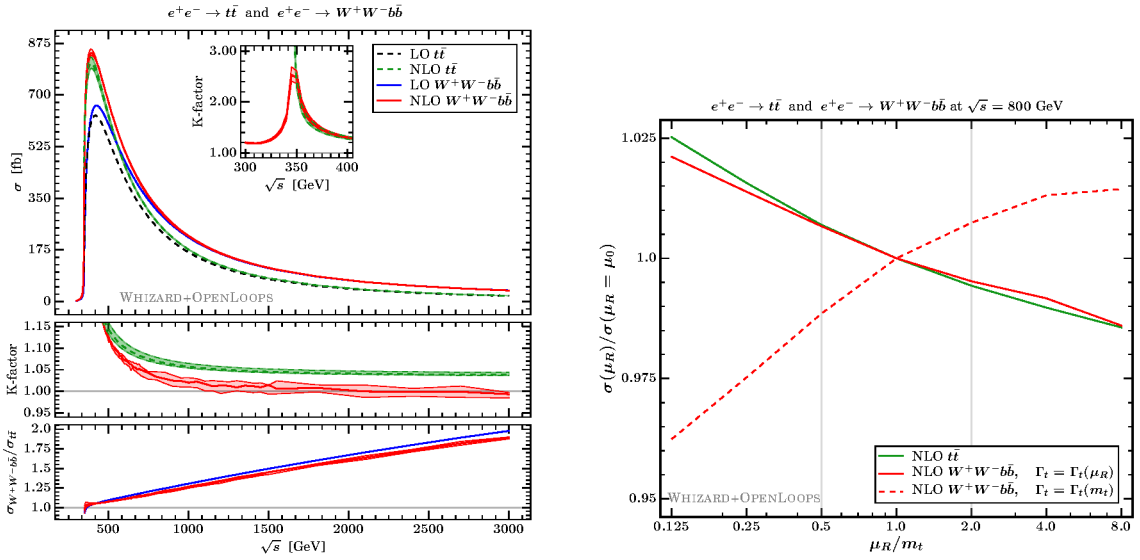

Figure 5.7. Total cross section for on-shell and off-shell $t\bar{t}$ production as a function of $\sqrt{s}$ and μ_R. In the lower panels of the left plot, we show the K-factor for $t\bar{t}$ and $bW^+\bar{b}W^-$ in green and red, respectively, as well as the ratio of off-shell to on-shell results for LO and NLO in blue and red.

Right above the production threshold at $\sqrt{s} = 2m_t$, both LO and NLO cross sections are strongly enhanced. This is the result of non-relativistic threshold corrections, which manifest themselves as large logarithmic contributions to the virtual one-loop matrix element, as discussed in chapter 6. This Coulomb divergence is not present in the off-shell process $e^+e^- \to bW^+\bar{b}W^-$, but is instead regularized by the finite top-quark width, so that the NLO corrections remain finite. But still, the non-relativistic threshold corrections introduce a distinct peak in the ratio plot at $\sqrt{s} = 2m_t$ with a maximum K-factor of about 2.5. Below threshold the cross section drops sharply, but QCD corrections remain significant. Far above threshold the NLO corrections are rather small for both the on-shell and the off-shell processes. For $e^+e^- \to t\bar{t}$, the corrections remain positive for all values of $\sqrt{s}$. In fact, for large center-of-mass energies, the effect of the top quark mass becomes negligible and the corrections approach the universal leptonic massless quark pair-production correction factor α_s/π. In contrast, the NLO corrections to $e^+e^- \to bW^+\bar{b}W^-$ decrease significantly faster for large center-of-mass energies, are at the percent level for $\sqrt{s} = 1500\,\text{GeV}$, and come close to zero at $\sqrt{s} = 3000\,\text{GeV}$. This corresponds to the fact that the non-resonant irreducible background and interference contributions grow with energy relative to the $t\bar{t}$ signal contribution, which receives purely positive corrections. Our results suggest that at a CMS energy of $\sqrt{s} = 800\,\text{GeV}$, positive corrections to the signal process and negative corrections to the background are of the same order of magnitude and partially cancel each other. This leads to very small NLO QCD corrections. However, at this level the currently unknown and possibly large

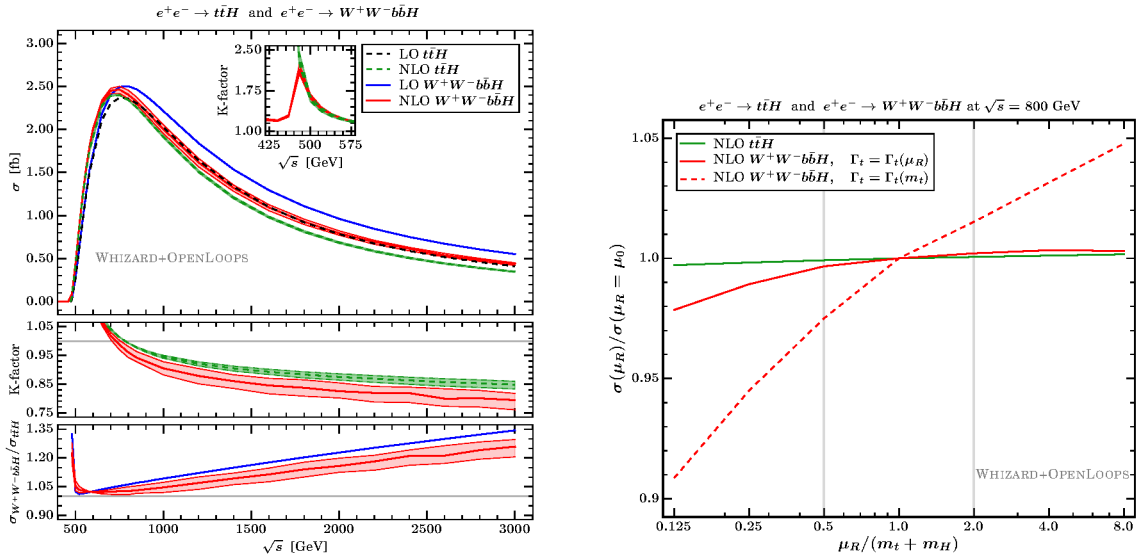

Figure 5.8. Total cross section of on-shell and off-shell $t\bar{t}H$ production subject to $\sqrt{s}$ and μ_R. Extra panels as in fig. 5.7.

NLO EW corrections to $e^+e^- \to bW^+\bar{b}W^-$ have to be included as well for reliable predictions. Comparing off-shell to on-shell cross sections, we see that they are about equal at threshold, but at $\sqrt{s} = 800\,\text{GeV}$ the off-shell prediction is about 20% larger. The right panel of fig. 5.7 shows the variation for $\sqrt{s} = 800\,\text{GeV}$ of the $e^+e^- \to t\bar{t}$ and $e^+e^- \to bW^+\bar{b}W^-$ NLO predictions with respect to the renormalization scale μ_R in the interval $\mu_\text{R} = [1/8, 8] \cdot m_t$. Within the error band $[m_t/2, 2m_t]$ predictions for $t\bar{t}$ and $bW^+\bar{b}W^-$ with fixed top-quark width, $\Gamma_t = \Gamma_t(\mu_\text{R} = m_t)$, vary at the level of a few per cent, however with an opposite slope. To understand this behavior, we show the scale variation of the off-shell process additionally with a scale-dependent width, $\Gamma_t(\mu_\text{R})$. With such a consistent setting of the width according to the input parameters, including μ_R, scale variations in the off-shell process are very similar to the on-shell one. We note that the scale dependence in the top width is in principle a higher-order effect, such that both approaches are valid to estimate missing higher order effects by means of scale variations. However, in order to properly recover the narrow width limit the parameter settings for the width in the propagator and the decay part of the matrix element have to match, including the scale setting.

Inclusive cross sections for Higgs associated top-pair production are shown in the left panel of fig. 5.8. Also here we observe a rise of the cross sections with a maximum located at around $\sqrt{s} = 800\,\text{GeV}$, i.e. far above the production threshold at $2m_t + m_H \approx 471\,\text{GeV}$, where $\sigma_\text{incl.}(\sqrt{s} = 800\,\text{GeV}) \approx 2.4\,\text{fb}$. Again, NLO QCD corrections are sizeable due to non-relativistic Coulomb enhancements close to the production threshold. For the off-shell process $e^+e^- \to bW^+\bar{b}W^-H$ the corrections reach +100%

Table 5.3. LO and NLO inclusive cross sections and K-factors for $e^+e^- \to t\bar{t}$ and $e^+e^- \to bW^+\bar{b}W^-$ for various center-of-mass energies targeted by future linear collider experiments. Uncertainties at NLO are due to scale variation.

	$e^+e^- \to t\bar{t}$			$e^+e^- \to bW^+\bar{b}W^-$		
$\sqrt{s}$ [GeV]	σ^{LO}[fb]	σ^{NLO}[fb]	K-factor	σ^{LO}[fb]	σ^{NLO}[fb]	K-factor
500	548.4	$627.4^{+1.4\%}_{-0.9\%}$	1.14	600.7	$675.1^{+0.4\%}_{-0.8\%}$	1.12
800	253.1	$270.9^{+0.8\%}_{-0.4\%}$	1.07	310.2	$320.7^{+1.1\%}_{-0.7\%}$	1.03
1000	166.4	$175.9^{+0.7\%}_{-0.3\%}$	1.06	217.2	$221.6^{+1.1\%}_{-1.0\%}$	1.02
1400	86.62	$90.66^{+0.6\%}_{-0.2\%}$	1.05	126.4	$127.9^{+0.7\%}_{-1.5\%}$	1.01
3000	19.14	$19.87^{+0.5\%}_{-0.2\%}$	1.04	37.89	$37.63^{+0.4\%}_{-0.9\%}$	0.993

and remain large but finite below threshold, while for the on-shell process they diverge close to threshold. Around the maximum of the cross sections, NLO corrections vanish for both the on-shell and the off-shell process. Above this maximum, the NLO corrections turn negative, yielding corrections at the maximal CLIC energy of $\sqrt{s} = 3000\,\text{GeV}$ of up to -15% for the on-shell process $e^+e^- \to t\bar{t}H$ and up to -20% for the off-shell process $e^+e^- \to bW^+\bar{b}W^-H$. Again one should also consider how the off-shell cross sections behave relative to their on-shell counterparts. While at LO the $e^+e^- \to bW^+\bar{b}W^-H$ cross section decreases considerably slower with energy compared to the on-shell process $e^+e^- \to t\bar{t}H$, at NLO the corrections to the off-shell process are more sizeable and negative with respect to the on-shell case, yielding comparable inclusive cross sections for the on-shell and off-shell process. Still, at 3000 GeV the off-shell inclusive cross section is about 20% smaller then the on-shell one. In the right panel of fig. 5.8, we display renormalization scale variations at $\sqrt{s} = 800\,\text{GeV}$ for Higgs associated top-pair production. For this center-of-mass energy scale variation uncertainties in $e^+e^- \to t\bar{t}H$ are negligible (induced by vanishing NLO QCD corrections), while in $e^+e^- \to bW^+\bar{b}W^-H$ with the standard choice $\Gamma_t = \Gamma_t(\mu_{\text{R}} = m_t)$ they amount to several per cent in the considered variation band. Similar to the $t\bar{t}$ case, we also show scale variations taking consistently into account the scale dependence in the top-quark width. Here, the behavior of the off-shell process is very similar to the on-shell one. The small scale variation of this process a posteriori confirms our assumptions about fixed scales made in eq. (5.3.8) and eq. (5.3.9), improving the reliability of differential predictions in the following sections.

Finally, in table 5.3 and table 5.4 we list inclusive cross sections for $t\bar{t}$ and $t\bar{t}H$ (both on- and off-shell) processes, respectively, for several representative center-of-mass energies.

Table 5.4. LO and NLO inclusive cross sections and K-factors for $e^+e^- \to t\bar{t}H$ and $e^+e^- \to bW^+\bar{b}W^-H$ for various center-of-mass energies targeted by future linear collider experiments. Uncertainties at NLO are due to scale variation.

	$e^+e^- \to t\bar{t}H$			$e^+e^- \to bW^+\bar{b}W^-H$		
$\sqrt{s}$ [GeV]	σ^{LO}[fb]	σ^{NLO}[fb]	K-factor	σ^{LO}[fb]	σ^{NLO}[fb]	K-factor
500	0.26	$0.42^{+3.6\%}_{-3.1\%}$	1.60	0.27	$0.44^{+2.6\%}_{-2.4\%}$	1.63
800	2.36	$2.34^{+0.1\%}_{-0.1\%}$	0.99	2.50	$2.40^{+2.1\%}_{-1.9\%}$	0.96
1000	2.02	$1.91^{+0.5\%}_{-0.5\%}$	0.95	2.21	$2.00^{+2.5\%}_{-2.5\%}$	0.90
1400	1.33	$1.21^{+0.9\%}_{-1.0\%}$	0.90	1.53	$1.32^{+2.6\%}_{-3.0\%}$	0.86
3000	0.41	$0.35^{+1.4\%}_{-1.8\%}$	0.84	0.55	$0.44^{+2.9\%}_{-4.3\%}$	0.79

Listed uncertainties are due to scale variations, where we employ the fixed top-width, $\Gamma_t = \Gamma_t(\mu_{\mathrm{R}} = m_t)$. In section 5.7.1 we will continue our discussion of NLO corrections for top-pair and Higgs associated top-pair production at the differential level. There we will focus on $\sqrt{s} = 800\,\mathrm{GeV}$, as here cross sections are largest for $t\bar{t}H$ production, which should offer the best condition for a precise determination of the top Yukawa coupling, as discussed in the following section. While this can be considered a viable running scenario for a precision measurement, one should keep in mind that for other energies, the NLO QCD corrections will be larger in general, at least at the inclusive level.

5.5. Determination of the top Yukawa coupling

Being the largest of all Yukawa couplings, the tth coupling y_t is a crucial quantity in many BSM modes, such as the MSSM, 2HDM, composite Higgs or Little Higgs models. A precise measurement of Higgs associated top-pair production allows for the direct determination of y_t at the per cent level [178, 179], thus probing a wide range of new physics models. Such a measurement is feasible at a future high-energy lepton collider. In the following, we will study the sensitivity of the $t\bar{t}H$ and $bW^+\bar{b}W^-H$ cross sections to y_t and investigate the effects of NLO QCD corrections. The sensitivity of the $t\bar{t}H$ process on y_t is commonly expressed in terms of [179, 180]

$$\frac{\Delta y_t}{y_t} = \kappa \frac{\Delta\sigma}{\sigma}, \tag{5.5.1}$$

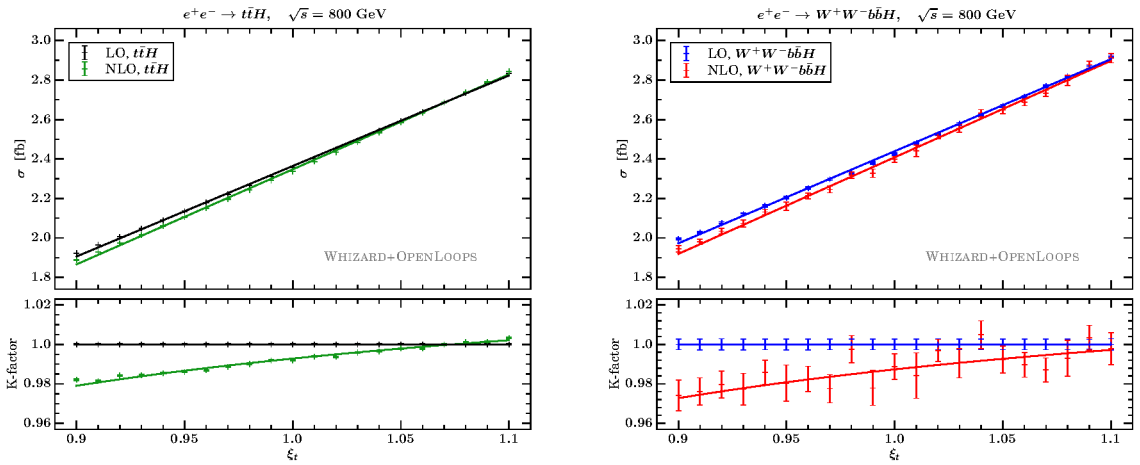

Figure 5.9. The $e^+e^- \to t\bar{t}H$ and $e^+e^- \to bW^+\bar{b}W^-H$ LO and NLO cross sections as a function of the top Yukawa coupling modifier $\xi_t = y_t/y_t^{\mathrm{SM}}$, as well as a linear fit used to determine the coefficient κ as described in the text, (5.5.1).

directly relating the relative accuracy on the measured cross section to the relative accuracy on the top Yukawa coupling.

The amplitude for Higgs-associated processes is made up of a signal diagram, containing one power of y_t, and background diagrams with no Yukawa coupling. Therefore, the cross section can be written as

$$\sigma(y_t) = y_t^2 \cdot S + y_t \cdot I + B. \tag{5.5.2}$$

Here, S denotes the contribution of the $t\bar{t}H$ signal diagram depicted on the left-hand side of fig. 5.4. The background Higgsstrahlung contribution is contained in B. I denotes the interference terms between the two diagrams. Assuming that the signal diagram dominates the cross section σ, (5.5.1) implies $\kappa \approx \kappa_0 = 0.5$. Thus, the ratio κ_0/κ quantifies the contribution of background and interference terms to the total cross section. We investigate the dependence of the total cross section on deviations of the top Yukawa coupling from the standard model value. This deviation is parameterized by $y_t = \xi_t \cdot y_t^{\mathrm{SM}}$, such that $\sigma(\xi_t) = \xi_t^2 \cdot S + \xi_t \cdot I + B$. Figure 5.9 shows a scan of $\sigma(\xi_t)$ at LO and NLO in the interval $[0.9, 1.1]$. From this, the slope κ can be determined, as listed in table 5.5. As expected, all listed κ-values are close to 0.5. For $e^+e^- \to t\bar{t}H$ at LO the Higgsstrahlung contribution induces a value $\kappa > 0.5$. For the off-shell process $e^+e^- \to bW^+\bar{b}W^-H$ we observe a slightly larger value compared to the on-shell process, originating from additional irreducible backgrounds. The NLO QCD corrections to κ turn out to be significant. They decrease κ by 6.0% and 4.6% compared to LO for the on- and off-shell case, respectively. This can be understood from a different behavior of the signal and background contributions with respect to QCD corrections. The fact

that NLO QCD make κ drop below κ_0 suggests the assumption that interference and background diagrams are affected more by the corrections than the signal diagram. To quantify this, we use (5.5.1) and (5.5.2) to express κ in terms of S, I and B,

$$\kappa = \sigma(\xi_t)\left[\frac{\sigma(\xi_t)}{d\xi_t}\right]^{-1}\Bigg|_{\xi_t=1} = \frac{S+I+B}{2S+I} = \frac{I}{2} + \frac{I/2+B}{2S+I}, \tag{5.5.3}$$

Note that, in the above formula, the additional factor of ξ_t from (5.5.2) is already set to one. While B and S are strictly positive, I can take either sign. As can be inferred from eq. (5.5.3), for κ to drop below 0.5, the interference contribution must be negative. Assuming that the signal contribution dominates over the interference, i.e. $-I < 2S$, it is clear that $\kappa < \kappa_0$ can only be realized via sufficiently large and negative interference terms. It can therefore be concluded that the decrease of κ is due to large negative corrections on I, which can be attributed to subtraction terms dominating this subset of the overall result. Negative contributions to I could also be created by BSM effects at tree level. The study above shows that the discrimination of perturbative corrections from new physics signals plays an important role in future experimental studies of the top Yukawa coupling.

Finally, we want to mention that the results from this section are already used by CLIC to determine their true sensitivity on the top Yukawa coupling [181].

Table 5.5. The parameter κ as defined in eq. (5.5.3) for $e^+e^- \to t\bar{t}H$ and $e^+e^- \to bW^+\bar{b}W^-H$ at LO and NLO for $\sqrt{s} = 800\,\text{GeV}$.

$e^+e^- \to$	κ^{LO}	κ^{NLO}	$\kappa^{\text{NLO}}/\kappa^{\text{LO}}$
$t\bar{t}H$	0.514	0.485	0.943
$bW^+\bar{b}W^-H$	0.520	0.497	0.956

5.6. Polarization Effects

We complete our study of inclusive cross sections for leptonic top-pair and Higgs associated top-pair production with an investigation of possible beam polarization effects on these processes. Beam polarization is a powerful tool at linear colliders to disentangle contributing couplings and to reduce backgrounds [182, 183], or e.g. improve the measurement of the top Yukawa coupling [179]. In table 5.6 and table 5.7 inclusive LO and NLO cross sections with different polarization settings as suggested by the favored

ILC running scenarios [184] and two different collider energies are listed for the on-shell processes $e^+e^- \to t\bar{t}$ and $e^+e^- \to t\bar{t}H$, respectively. While cross sections vary strongly with the beam polarization, the K-factors are unaffected. These results confirm the naive expectation that NLO QCD corrections fully factorize with respect to the beam polarization due to the uncolored initial state. On the other hand, one can view the constant K-factors in table 5.6 and table 5.7 as validation of the polarization dependent WHIZARD-OPENLOOPS-interface via the BLHA extension described in section 3.1.1. The factorization also holds when top-quark decays are considered and we refrain from showing polarized cross sections for off-shell production processes.

Table 5.6. LO and NLO inclusive cross sections for $e^+e^- \to t\bar{t}$ with possible ILC beam polarization settings at $\sqrt{s} = 800\,\text{GeV}$ and $1500\,\text{GeV}$.

		$\sqrt{s} = 800\,\text{GeV}$			$\sqrt{s} = 1500\,\text{GeV}$		
$P(e^-)$	$P(e^+)$	σ^{LO}[fb]	σ^{NLO}[fb]	K-factor	σ^{LO}[fb]	σ^{NLO}[fb]	K-factor
0%	0%	253.7	272.8	1.075	75.8	79.4	1.049
−80%	0%	176.5	190.0	1.077	98.3	103.1	1.049
80%	0%	176.5	190.0	1.077	53.2	55.9	1.049
−80%	30%	420.8	452.2	1.074	124.9	131.0	1.048
−80%	60%	510.7	548.7	1.074	151.6	158.9	1.048
80%	−30%	208.4	224.5	1.077	63.0	66.1	1.049
80%	−60%	240.3	258.9	1.077	72.7	76.3	1.049

5.7. Differential distributions

5.7.1. Top-pair production and decay

We start our analysis of differential distributions for top-pair production and decay considering the top-quark transverse momentum distribution for the on-shell process $e^+e^- \to t\bar{t}$ and the corresponding off-shell process $e^+e^- \to \mu^+\nu_\mu e^-\bar{\nu}_e b\bar{b}$ including leptonic decays, shown in fig. 5.10. For the latter the top quark is reconstructed from its leptonic decay products at so-called Monte-Carlo truth level. This refers to the assumption that the neutrino momentum can be perfectly reconstructed, so that $p_{\text{T},W^+j_b} = p_{\text{T},\ell^+\nu j_b}$. Despite the different normalization of the two distributions, due to the fact that the on-shell process does not include leptonic branching ratios, the LO and NLO shapes are very similar below the Jacobian peak located at around 350 GeV. This peak with

Table 5.7. LO and NLO inclusive cross sections for $e^+e^- \to t\bar{t}H$ with possible ILC beam polarization settings at $\sqrt{s} = 800\,\text{GeV}$ and $\sqrt{s} = 1500\,\text{GeV}$.

		$\sqrt{s} = 800$ GeV			$\sqrt{s} = 1500$ GeV		
$P(e^-)$	$P(e^+)$	σ^{LO}[fb]	σ^{NLO}[fb]	K-factor	σ^{LO}[fb]	σ^{NLO}[fb]	K-factor
0%	0%	2.358	2.337	0.991	1.210	1.064	0.879
−80%	0%	1.583	1.571	0.992	1.576	1.381	0.876
80%	0%	1.584	1.571	0.992	0.843	0.746	0.885
−80%	30%	3.988	3.950	0.990	2.003	1.757	0.877
−80%	60%	4.840	4.795	0.991	2.429	2.128	0.876
80%	−30%	1.860	1.846	0.992	0.996	0.879	0.883
80%	−60%	2.134	2.120	0.993	1.148	1.018	0.886

its large event density is smeared out by the NLO corrections, in particular due to kinematical shifts induced by the real gluon radiation, yielding corrections at the level of −20% at the peak and around +20% below the peak. For the on-shell process the phase-space above the Jacobian peak is kinematically not allowed at LO and gets only sparsely populated at NLO. In contrast, for the off-shell process this kinematical regime is allowed already at LO. The observed sizeable corrections in the transverse momentum of the intermediate top quarks also translate into relevant corrections in the directly observable transverse momentum of the final state leptons, as shown in fig. 5.12. Namely, we find corrections up to −30% and up to −20% for the hardest and second hardest lepton, respectively. In a realistic setup, where experimental selection cuts have to be applied on the leptons, such effects become also relevant for the fiducial cross section in precision top physics. Experimentally, p_{T,W^+j_b} is not directly measurable, as in the considered leptonic decay mode the top quark cannot be exactly reconstructed due to the two invisibly escaping neutrinos. To model this constraint, we construct and measure the transverse momentum of the j_b–lepton system, p_{T,ℓ^+j_b}. Corresponding predictions for $e^+e^- \to \mu^+\nu_\mu e^-\bar{\nu}_e b\bar{b}$ are shown in fig. 5.11 (left). Here we observe a tilt of the NLO shape with respect to the LO one, yielding corrections up to 20% for small p_{T,ℓ^+j_b} and up to −40% for large p_{T,ℓ^+j_b}. In contrast, the transverse momentum distribution of the j_b–$j_{\bar{b}}$ system, as shown on the right of fig. 5.11, only receives mild QCD corrections at the level of 10%. The kinematical mass of the top resonance is one of the observables of especially large interest. On the left of fig. 5.13 we show the reconstructed invariant top-quark mass, $m_{W^+j_b} = m_{\ell^+\nu j_b}$, where the $\ell^+\nu j_b$ system is identified based on Monte Carlo truth. At LO and close to the peak, this distribution corresponds to the Breit-

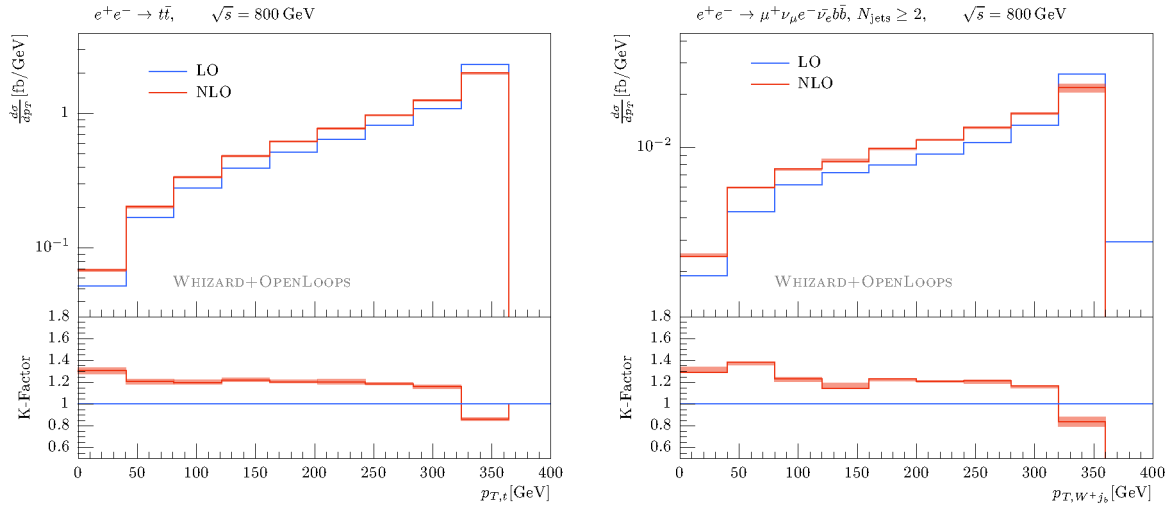

Figure 5.10. Differential distributions in the transverse momentum of the top quark in $e^+e^- \to t\bar{t}$ (left) and the reconstructed top quark in $e^+e^- \to \mu^+\nu_\mu e^-\bar{\nu}_e b\bar{b}$ (right). Shown are LO (blue) and NLO (red) predictions together with the corresponding K-factors and NLO scale uncertainties.

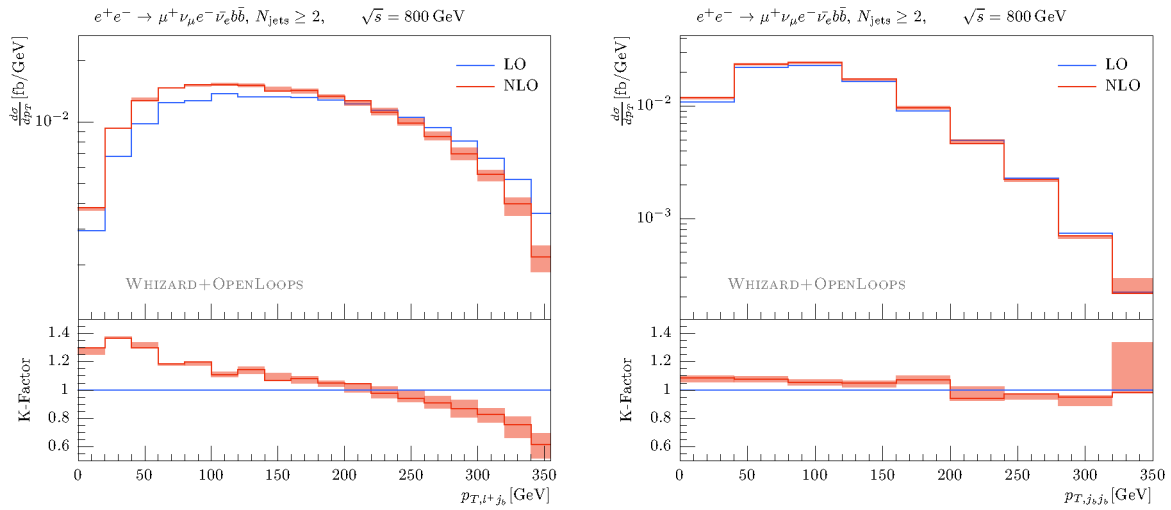

Figure 5.11. Transverse momentum distribution of the bottom-jet–lepton system (left), $p_{\text{T},\ell^+ j_b}$, and of the j_b–$j_{\bar{b}}$ system (right), $p_{\text{T},b\bar{b}}$, in $e^+e^- \to \mu^+\nu_\mu e^-\bar{\nu}_e b\bar{b}$. Curves and bands as in fig. 5.10.

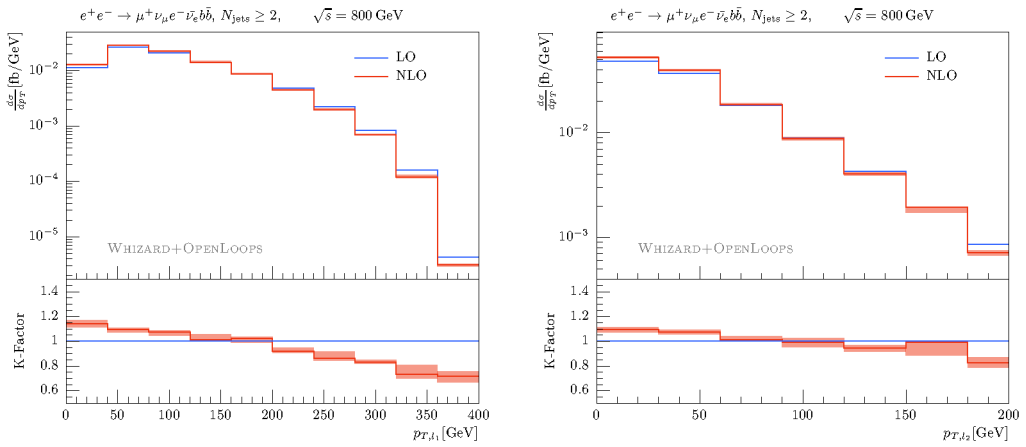

Figure 5.12. Transverse momentum distributions of the hardest and second hardest lepton in $e^+e^- \to \mu^+\nu_\mu e^-\bar{\nu}_e b\bar{b}$. Curves and bands as in fig. 5.10.

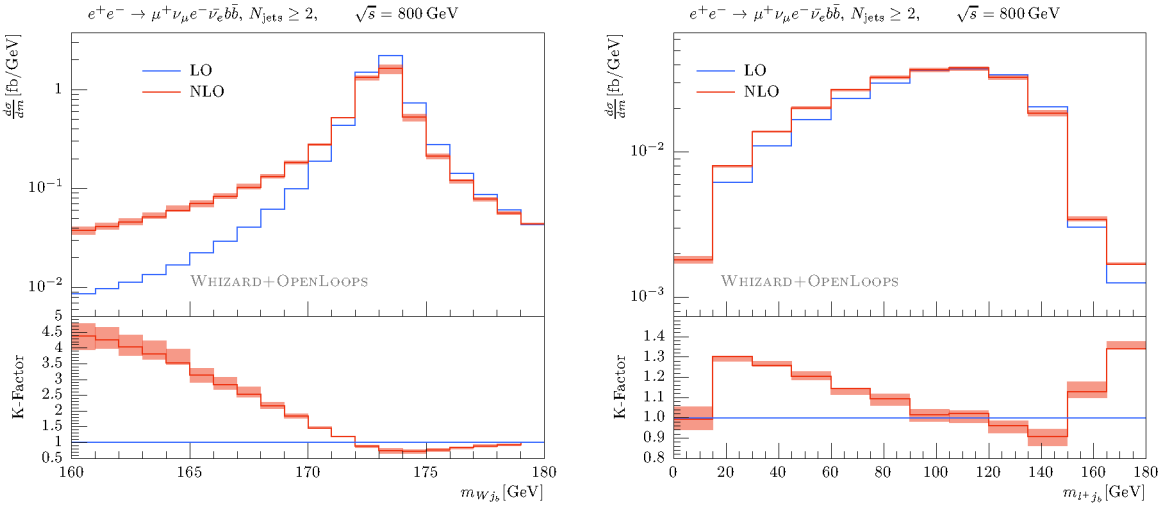

Figure 5.13. Reconstructed top invariant mass (left) and invariant mass of the b-jet–ℓ^+ system in $e^+e^- \to \mu^+\nu_\mu e^-\bar{\nu}_e b\bar{b}$. Curves and bands as in fig. 5.10.

Wigner peak that arises due to the top propagator. Off-shell effects and non-resonant contributions become visible a couple of GeV away from the pole and tend to increase the background. At NLO we observe a drastic shape distortion compared to LO, in particular below the resonance peak. These NLO shape distortions are very sensitive to the cone size of the employed jet algorithm. They can be attributed to gluon emissions that escape the b-jet forming either a separate light jet or being recombined with the other b-jet. The reconstructed invariant top-quark mass is thus on average significantly shifted compared to the top-quark resonance. Similar shape distortions have also been observed in ref. [157] as well as at the LHC [185, 186]. Again, the perfectly reconstructed top-quark mass is not directly measurable due to escaping neutrinos. However, it can

be computed by the relation [187–189]

$$m_t^2 = m_W^2 + \frac{2\langle m_{\ell j_b}^2 \rangle}{1 - \langle \cos\theta_{\ell j_b} \rangle}\,, \tag{5.7.1}$$

where $\langle m_{\ell j_b}^2 \rangle$ and $\langle \cos\theta_{\ell j_b} \rangle$ are the mean values of the corresponding invariant mass and angular distributions. Predictions for the $m_{\ell^+ j_b}$ invariant mass distribution are shown on the right of fig. 5.13. The position of the kinematical edge at around $m_{\ell^+ j_b} \approx 150\,\text{GeV}$ is unaffected by the NLO QCD corrections, however, below the edge we observe significant shape effects with corrections varying between -10% and $+30\%$. Finally, as shown in fig. 5.14, we want to note that QCD radiative corrections to the angular separation $\cos\theta_{\ell^+ j_b}$ entering the top-quark mass estimator of eq. (5.7.1) are negligible.

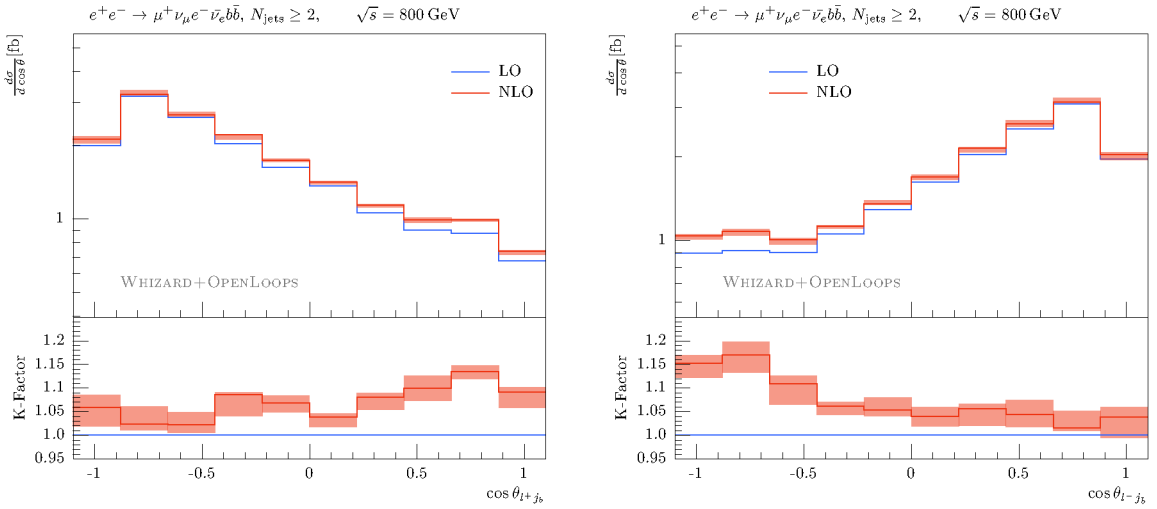

Figure 5.14. Differential distributions in the angular separations $\cos\theta_{\ell^+ j_b}$ (left) and $\cos\theta_{\ell^- j_{\bar{b}}}$ (right) for $e^+e^- \to \mu^+\nu_\mu e^-\bar{\nu}_e b\bar{b}$. Curves and bands as in fig. 5.10.

5.7.2. Forward-backward asymmetries

The top quark forward-backward asymmetry A_{FB} is defined as

$$A_{FB} = \frac{\sigma(\cos\theta_t > 0) - \sigma(\cos\theta_t < 0)}{\sigma(\cos\theta_t > 0) + \sigma(\cos\theta_t < 0)}\,, \tag{5.7.2}$$

where, at a lepton collider, θ_t is the angle between the positron beam axis and the outgoing top-quark. This asymmetry can be measured with a precision below 2% [182, 183]. The SM prediction for A_{FB} is non-zero due to interference contributions between s-channel Z- and γ^*-exchange in the dominant production process [190]. Various new physics models can substantially alter the SM prediction (for an overview cf. ref. [191])

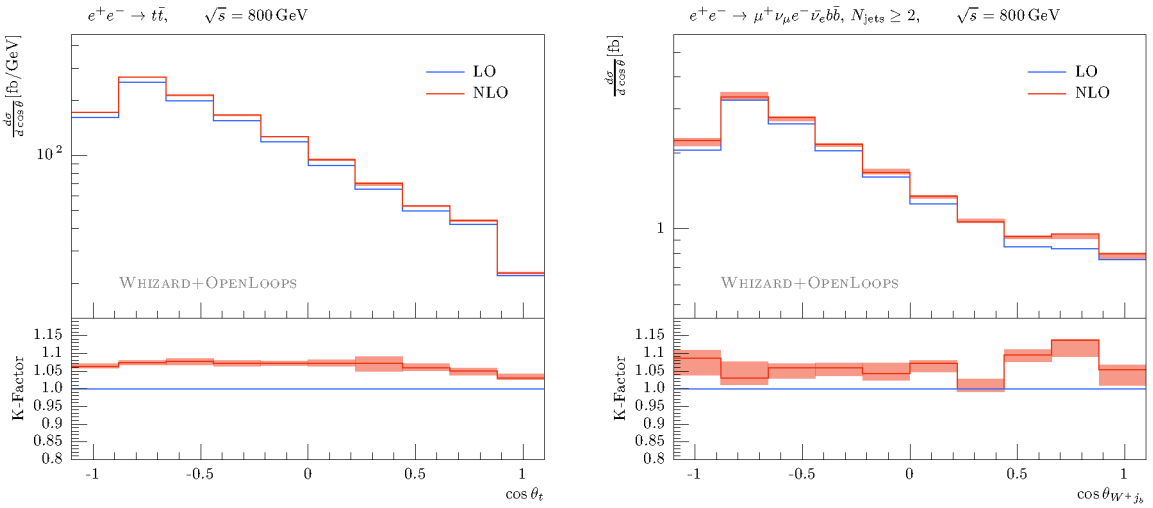

Figure 5.15. Differential distributions in the azimuthal angle of the top quark in $e^+e^- \to t\bar{t}$ (left) and $e^+e^- \to \mu^+\nu_\mu e^-\bar{\nu}_e b\bar{b}$ (right). Curves and bands as in fig. 5.10.

and thus, a precise determination of A_{FB} serves as a stringent probe for new physics. A similar asymmetry can also be defined and measured at hadron colliders, where the dominant top-production channels are of QCD type, such that within the standard model the LO forward-backward asymmetry is zero. At the Tevatron a non-vanishing A_{FB} was measured [15–17], posing a long-standing puzzle, which was finally resolved within the SM by taking QCD corrections up to NNLO [18] and NLO EW corrections [19] into account. In fig. 5.15 we show the underlying distribution in the angle of the (reconstructed) top quark with respect to the beam axis for on-shell top-pair production and the corresponding off-shell process $e^+e^- \to \mu^+\nu_\mu e^-\bar{\nu}_e b\bar{b}$. The prediction of a non-zero forward-backward asymmetry at lepton colliders is apparent in fig. 5.15 and the shape of this distribution is hardly affected by radiative corrections, which yield an almost constant K-factor of about 1.05. For $\cos\theta_{W^+j_b} \lesssim 0.75$, the angular distribution of the reconstructed top quark in $e^+e^- \to \mu^+\nu_\mu e^-\bar{\nu}_e b\bar{b}$ correlates with the on-shell prediction. However, for $\cos\theta_{W^+j_b} \gtrsim 0.75$, there is an enhancement of events, which can be attributed to single-top background diagrams. This has a significant effect on the reconstructed top forward-backward asymmetry, which is reduced by about 20%, see the $e^+e^- \to \mu^+\nu_\mu e^-\bar{\nu}_e b\bar{b}$ and $e^+e^- \to bW^+\bar{b}W^-$ predictions in table 5.8. In table 5.8 we list LO and NLO predictions for the forward-backward asymmetry A_{FB} (and the corresponding asymmetry for the anti-top quark), considering different treatments of the top-quark off-shellness. In $e^+e^- \to \mu^+\nu_\mu e^-\bar{\nu}_e b\bar{b}$, either the top quark is reconstructed at MC truth level or the information of the neutrino momenta is dropped. NLO QCD corrections to A_{FB} can be sizeable (up to a few percent), but are small compared to the changes associated with increasing the final-state multiplicity and taking into account all off-shell and non-resonant effects. Note that if the neutrino momenta are omitted,

Table 5.8. Forward-backward asymmetries of the top quark, A_{FB}, and the anti-top quark, $\bar{A}_{FB}$.

	$e^+e^- \to$	A_{FB}^{LO}	A_{FB}^{NLO}	$A_{FB}^{\text{NLO}}/A_{FB}^{\text{LO}}$
A_{FB}	$t\bar{t}$	-0.535	-0.539	1.013
	$bW^+\bar{b}W^-$	-0.428	-0.426	0.995
	$\mu^+e^-\nu_\mu\bar{\nu}_e b\bar{b}$	-0.415	-0.409	0.986
	$\mu^+e^-\nu_\mu\bar{\nu}_e b\bar{b}$, without neutrinos	-0.402	-0.387	0.964
$\bar{A}_{FB}$	$t\bar{t}$	0.535	0.539	1.013
	$bW^+\bar{b}W^-$	0.428	0.426	0.995
	$\mu^+e^-\nu_\mu\bar{\nu}_e b\bar{b}$	0.415	0.409	0.986
	$\mu^+e^-\nu_\mu\bar{\nu}_e b\bar{b}$, without neutrinos	0.377	0.350	0.928

the relation $A_{FB} = -\bar{A}_{FB}$ is not fulfilled any more, both at LO and NLO. This can also observed directly in the angular distribution of lj_b-pairs, cf. fig. 5.14, where there is a slightly more pronounced dip at the lower edge of $\cos\theta_{l^-j_{\bar{b}}}$ than at the one of $\cos\theta_{l^+j_b}$. The differences come from combinatorial issues in the event reconstruction, where the neutrino momentum in the MC truth information allows to determine the top helicity and hence the flight direction of the lepton (cf. e.g. ref. [192]). Such information is unavailable when the neutrino kinematics are omitted.

5.7.3. Higgs associated top-pair production and decay

We start our analysis of differential Higgs-associated top-pair production by again considering the on-shell process first. Figure 5.16 shows the energy of the Higgs boson, E_H, and top-pair invariant mass $m_{t\bar{t}}$. In the $e^+e^- \to t\bar{t}H$ process, the Higgs boson acts as a colorless recoiler, reducing the effective CMS energy for the $t\bar{t}$ system. Thus, as $m_{t\bar{t}}$ approaches the top production threshold at $m_{t\bar{t}} \approx 2m_t$, threshold enhancements become visible also in the E_H–distribution. The explicit kinematical connection between E_H and $m_{t\bar{t}}$ is

$$E_H = \frac{1}{2\sqrt{s}}\left(s + m_H^2 - m_{t\bar{t}}^2\right) . \tag{5.7.3}$$

For the on-shell process $e^+e^- \to t\bar{t}H$ the lower kinematical bound of the E_H distribution is given by $E_H^{\min} = m_H = 125\,\text{GeV}$ and its upper bound by $E_H^{\max} = 335\,\text{GeV}$, which follows from $m_{t\bar{t}}^{\min} = 2m_t$. The Higgs energy is thus a key observable in the identifica-

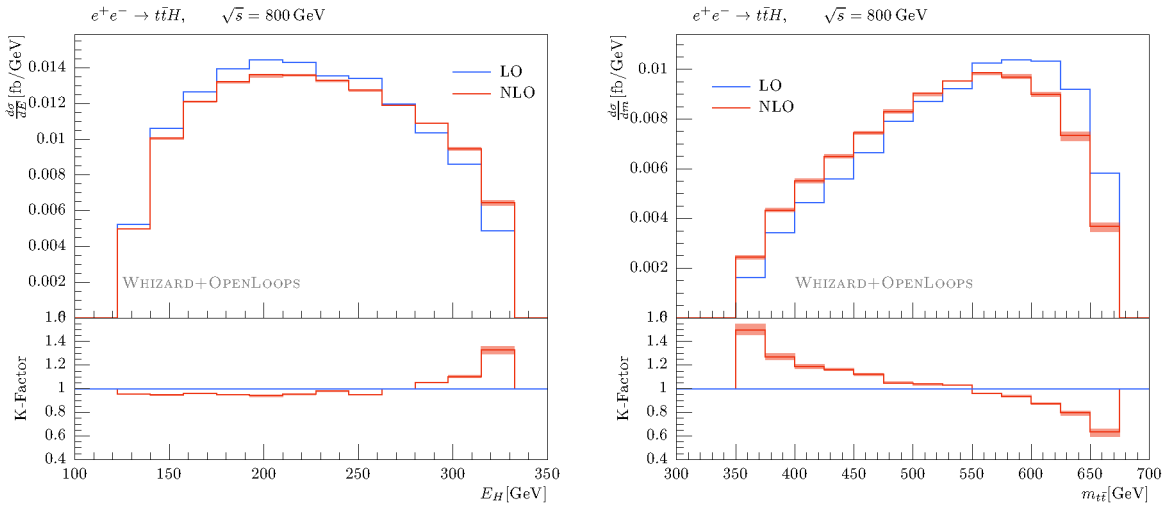

Figure 5.16. The energy of the Higgs boson, E_H, and the invariant mass of the top-quark pair, $m_{t\bar{t}}$, in $e^+e^- \to t\bar{t}H$. Curves and bands as in fig. 5.10.

tion of the top-quark threshold. The postulated threshold effects are directly visible in fig. 5.16, with a sizeable positive NLO QCD correction up to +35% for large values of E_H. The $m_{t\bar{t}}$–distribution next to it exhibits a threshold enhancement of about +50%. For small Higgs boson energies we observe an apparent mismatch of the NLO QCD corrections with respect to large $m_{t\bar{t}}$. While for small values of E_H the K-factor flattens out to an almost constant value of about 0.95, the K-factor for the top-pair invariant mass distribution monotonically decreases to a minimum value of about 0.60. This is due to the fact that the E_H distribution is a fully inclusive observable that is completely independent of the clustering applied to final state QCD radiation. On the other hand, the $m_{t\bar{t}}$ distribution does not include hard gluon radiation off the $t\bar{t}$ system, which takes energy away from it, while soft and collinear gluons are recombined with the top quarks. This systematically shifts the $m_{t\bar{t}}$–distribution towards lower values and results in the observed differences with respect to the E_H–distribution. The corresponding distributions for the off-shell process $e^+e^- \to \mu^+\nu_\mu e^-\bar{\nu}_e b\bar{b}H$ are shown in fig. 5.17. Again, we observe a strong enhancement for large Higgs boson energies and small reconstructed top-pair masses, together with a strong suppression for large reconstructed top-pair masses. In contrast to the on-shell process, already at LO kinematical boundaries are washed out due to off-shell and non-resonant contributions. In particular, the E_H distributions range to energies above 335 GeV, with strongly increasing NLO corrections. The $m_{W^+W^-j_bj_{\bar{b}}}$–distribution at LO falls off quickly below $m_{W^+W^-j_bj_{\bar{b}}} = 2m_t$, while at NLO it reaches to very small values. As already discussed in the context of fig. 5.13, this phase-space region is populated at NLO due to kinematical shifts of the reconstructed masses originating from the recombination of radiation from different stages of production and decay. In fig. 5.18 we show the transverse momentum distribution of the

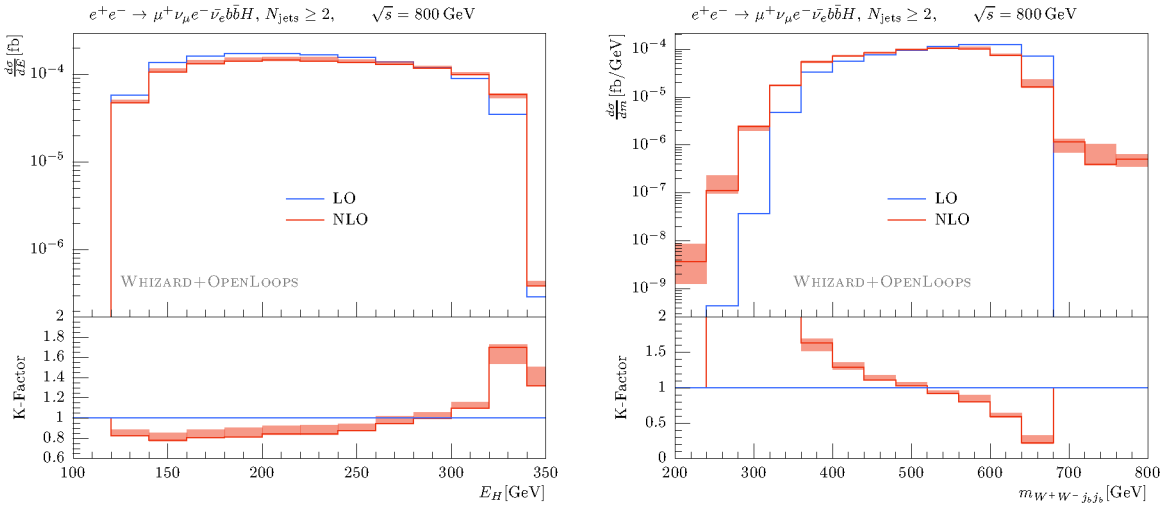

Figure 5.17. The energy of the Higgs boson, E_H, and the invariant mass of the reconstructed top-quark pair, $m_{W^+W^-j_b\bar{j}_b}$, in $e^+e^- \to \mu^+\nu_\mu e^-\bar{\nu}_e b\bar{b}H$. Curves and bands as in fig. 5.10.

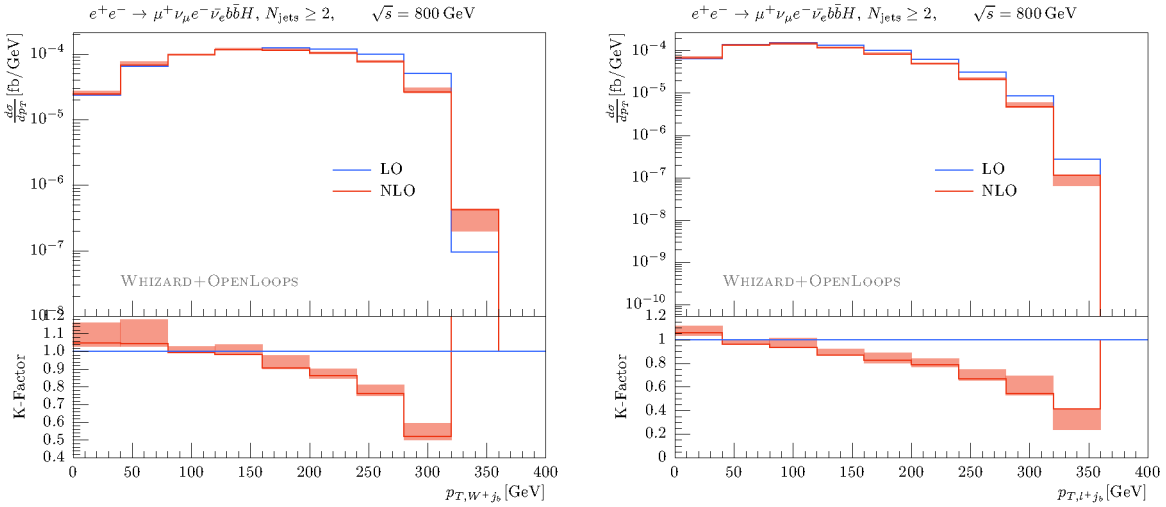

Figure 5.18. Transverse momentum distributions of the reconstructed top- quark (left) and of the bottom-jet–lepton system (right), p_{T,ℓ^+j_b}, in $e^+e^- \to \mu^+\nu_\mu e^-\bar{\nu}_e b\bar{b}H$. Curves and bands as in fig. 5.10.

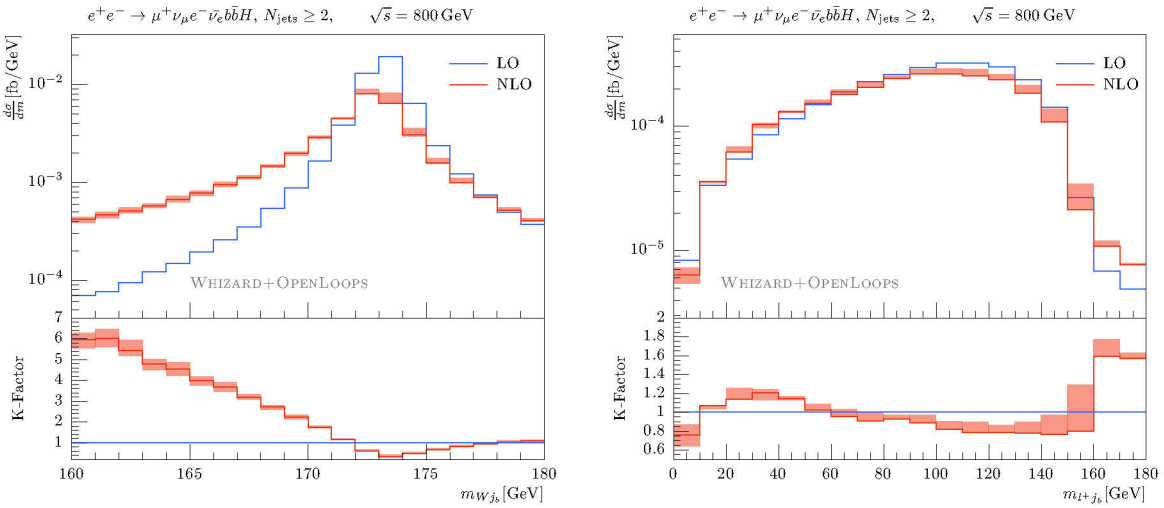

Figure 5.19. Reconstructed top-quark invariant mass (left) and invariant mass distribution of the b-jet–ℓ^+ system (right) in $e^+e^- \to \mu^+\nu_\mu e^-\bar{\nu}_e b\bar{b}H$. Curves and bands as in fig. 5.10.

reconstructed top quark and the directly observable j_b–lepton system in the off-shell process $e^+e^- \to \mu^+\nu_\mu e^-\bar{\nu}_e b\bar{b}H$. Comparing these distributions with the corresponding ones for top-pair production, shown in fig. 5.10 and fig. 5.11, we observe distinct shape differences already at leading order. Instead of a pronounced peak in the p_{T,W^+j_b} distribution, there is a plateau between about 100 GeV and 250 GeV. At larger transverse momenta, the distribution drops sharply to its kinematical bound at around 325 GeV. NLO QCD corrections shift both the p_{T,W^+j_b} and the p_{T,ℓ^+j_b} distribution towards smaller values inducing shape effects up to -50% at large p_{T,W^+j_b} and up to -40% at large p_{T,ℓ^+j_b}.

Finally, with fig. 5.19 we show the reconstructed kinematical top mass, $m_{W^+j_b}$, and its directly observable pendant, $m_{\ell^+j_b}$. We observe similar NLO shape distortions as already discussed in the case of the $\mu^+\nu_\mu e^-\bar{\nu}_e b\bar{b}$ final state, shown in fig. 5.13. For $m_{W^+j_b} < m_t$, i.e. below the top resonance, we observe a strong NLO enhancement which results in 20% shape corrections in the case of the $m_{\ell^+j_b}$ distribution. As already noted before, the size of these corrections strongly depends on the details of the employed jet clustering.

6. Matching the NLL threshold resummation with fixed-order QCD corrections for $e^+e^- \to bW^+\bar{b}W^-$

The study of top-quark production at threshold will be an integral part in the physics program of future lepton colliders, enabling a measurement of the top mass and width with unprecedented precision [45, 52, 147–150]. Moreover, also the top-quark couplings can be studied at threshold. In this chapter, we present the results of the combination of the NLL-resummed top threshold calculation using NRCQD and the WHIZARD NLO QCD implementation. We consider the off-shell process $e^+e^- \to bW^+\bar{b}W^-$, for which the first fully matched NLL + NLO QCD calculation is presented, which gives a coherent description of the transition region between the non-relativistic threshold regime and the top-quark continuum. As in chapter 5, we constrain ourselves to structureless beams. The convolution of theory predictions for the threshold with initial-state radiation and realistic beam spectra is studied in ref. [52, 148].

A detailed treatment of all aspects of the calculation, e.g. different summation prescriptions for intermediate top helicities or scale choices, is beyond the scope of this thesis. We concentrate on the relevant points in which fixed-order NLO corrections enter the calculation and how it affects the FKS subtraction in WHIZARD, based on original work by us. The full in-depth study is currently in preparation [57]. A summary of the current progress in validation at the time of writing is given in ref. [1].

6.1. Top-quark quasi-bound states and NRQCD

$Q\overline{Q}$ bound states constitute an essential window of probing non-perturbative QCD at collider experiments. Such a state, also called quarkonium, is non-relativistic, and can to a large extend be described with classical quantum mechanics. The challenge lies in properly transferring QCD, defined in the purely relativistic regime, to the non-relativistic one. Bound states of light quarks, such as the J/ψ (charmonium) or the Υ (bottomonium) exhibit a large spectrum of excitations. Like in atomic physics, they are referred to by their radial (excitation) and spin quantum numbers, e.g. $\Upsilon(1S)$. The

top bound state (toponium) is special because the formation time of the bound state is larger than the top life time, hence it is called a quasi-bound state. Nevertheless, at a lepton collider, it would be accessible because $\sqrt{s}$ can be set close to the threshold and the final state is clean enough to allow for a precise reconstruction of the top quarks. In a quantum field theoretical approach, bound states are produced by the divergences of a ladder summation of gluon-exchange diagrams,

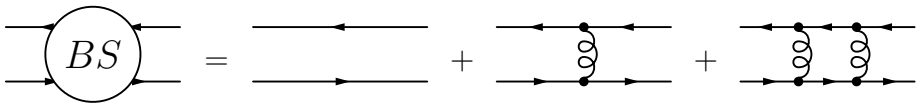

(6.1.1)

The reason for this is that bound states have to appear as poles of a Green function. Having the energy $E_B < 0$, it must be located at $s = 2m + E_B$. No single Feynman diagram can have this pole, therefore bound states are an interference effect between different loop diagrams. [1]. In the non-relativistic regime, the additional gluon propagators are enhanced, leading to factors of $(\alpha_s/v)^n$, where

$$v = \left[\frac{\sqrt{s} - 2m_t + i\Gamma_t}{m_t}\right]^{1/2} \tag{6.1.2}$$

is the non-relativistic top velocity [193]. These additional (large) terms need to be resummed, which is commonly done in the framework of non-relativistic QCD (NRQCD) [53–56], which describes the color-charged interactions of the quarks with an effective potential.

In general, the R-ratio to all orders takes the form

$$R = \frac{\sigma_{t\bar{t}}}{\sigma_{\mu^+\mu^-}} = v \sum_k \left(\frac{\alpha_s}{v}\right)^k \sum_i (\alpha_s \ln v)^i \times \Big\{1\,(\text{LL});\ \alpha_s, v\,(\text{NLL});\ \alpha_s^2,\ \alpha_s v,\ v^2\,(\text{NNLL}); \ldots\Big\}. \tag{6.1.3}$$

Currently, the state of the art is NNLL accuracy [194] and, without resumming logarithms of v, N^{3}LO [195, 196]. The resonance peak observed in top-quark pair production corresponds to the 1S-niveau numbers of the bound state. Other states do not exist due to the large value of the top-quark width. The position of the resonance peak does not correspond to the top-quark pole mass m_t which enters the propagator. Instead, it is shifted to a lower value due to the negative binding energy of the toponium system.

[1] The same effect leads to the emergence of repulsive and attractive forces in classical electrodynamics. The Born diagram for a $e^+e^- \to e^+e^-$ or $e^+e^+ \to e^+e^+$ interaction alone cannot explain the different sign of the electromagnetic potential, because the absolute square is insensitive to a replacement $e^+ \to e^-$. Only at the level of interference terms, the different signs of the processes turn out to be significant.

This resonance mass is denoted as M_t^{1S}. It is related to the pole mass via

$$m_t = M_t^{1S} \left[1 + \Delta M(\sqrt{s}, \alpha_s)\right]. \tag{6.1.4}$$

The explicit formulas for ΔM at LL and NLL accuracy are given in eq. (F.1.2). A similar relation exists for the relation between the pole mass and the $\overline{MS}$ mass of the top quark [197–199], but this is beyond the scope of this thesis.

6.1.1. The NRQCD form factor and scales

The resummation of the threshold logarithms is a multi-scale problem, which involves the mass, momentum and kinetic energy of the top quark. Close to the threshold, there is a strict scale hierarchy,

$$\Lambda_{\mathrm{QCD}} \ll m_t v^2 \ll m_t v \ll m_t. \tag{6.1.5}$$

Integrating out the second largest scale $m_t v$ leads to an effective field theory (EFT) called NRCQD. The three different scales in eq. (6.1.5) are called the hard, soft and ultra-soft scale. In consequence, they are associated with three different couplings, α_{H}, α_{S} and α_{US} (note the capital letter "S" in the soft strong coupling, opposed to the lower-case one when generally referring to α_s).

We are not giving an in-depth description of the whole resummation procedure. For the purpose of this work, it should be noted that in the EFT approach, a form factor enters the $t\gamma_\mu\bar{t}$ and $t\gamma_\mu\gamma_5\bar{t}$ vertices which contains loop integrals stemming from the resummation approach. At leading-log accuracy, it has an analytical formulation,

$$F_{\mathrm{LL}} = 1 + im\rho\Gamma(\epsilon)\Gamma(1+\epsilon)\Gamma(1-\rho)\frac{z_2 - z_1}{\rho\Gamma(1+\epsilon-\rho)}, \tag{6.1.6}$$

where $\epsilon > 0$ is a small parameter and $\rho = (C_F\alpha_s)/(2v)$. The parameters $z_{1,2}$ are given by the hypergeometric function

$$z_{1,2} =_2 F_2\left(\epsilon, 1+\epsilon, 1+\epsilon-\rho; \frac{mv \mp i(p \mp |p_0|)}{2mv}\right), \tag{6.1.7}$$

where p is the magnitude of the three-momentum of the top quark in the collision system. Such a relatively simple formula only exists at leading-log accuracy. Already at NLL, the form factor can only be computed numerically, with far-reaching consequences from the event generator point of view, since this leads to the requirement of additional numerical

codes for its computation. The form factor F_{LL} can be expanded in α_s to obtain

$$F_{\mathrm{LL}}^{\mathrm{exp}}(\alpha_s) = 1 + \alpha_s \left(\frac{iC_F m \log \frac{mv+p}{mv-p}}{2p} \right) + \mathcal{O}(\alpha_s^2). \tag{6.1.8}$$

The extension to NLL is quite simple

$$F_{\mathrm{NLL}}^{\mathrm{exp}}(\alpha_s) = F_{\mathrm{LL}}^{\mathrm{exp}}(\alpha_s) + \alpha_s \left(-\frac{2C_F}{\pi} \right) + \mathcal{O}(\alpha_s^2). \tag{6.1.9}$$

6.2. Factorized NLO decays for the top threshold treatment of $e^+e^- \to bW^+\bar{b}W^-$ in Whizard

The outlined resummed amplitudes are available in WHIZARD for the on-shell process $e^+e^- \to t\bar{t}$. The numerical NRQCD form factor is obtained from the third-party code TOPPIK [200] [2] and then included in the factorized computation using the O'MEGA library. This direct modification of the vertices fails for off-shell process, i.e. the process $e^+e^- \to bW^+\bar{b}W^-$. Here, modifying the vertices breaks gauge invariance, as can be seen by applying a suitable local gauge transformation $\Psi_t \to e^{-iQg\theta(x)}\Psi_t$ to the Lagrangian component containing the modified (covariant) derivative $\bar{\psi} i \not{D}_{NRQCD} \psi$. Moreover, the modified vertices lead to loop contributions with gluons connecting all colored particles. This means that integrals over the form factor have to be executed, which however is, if at all, only possible at LL, since at higher orders, there does not exist a simple analytic form. These issues are solved by using the factorized ansatz [201, 202], together with an **on-shell projection** for the top quark. In this projection, the final-state bottom and W momenta are transformed in such a way that the top momenta reconstructed from them are on-shell. The technical details are outlined in section F.2. The factorized matrix element is given by

$$\mathcal{M} = \underbrace{\left\langle e^+e^- \middle| \mathcal{T}_{\mathrm{NRQCD}} \middle| t\bar{t} \right\rangle}_{\equiv \mathcal{M}_{\mathrm{prod}}} \left\langle t\bar{t} \middle| \mathcal{T} \middle| bW^+\bar{b}W^- \right\rangle, \tag{6.2.1}$$

where the form factor only enters the production matrix element $\mathcal{M}_{\mathrm{prod}}$ and NLO QCD corrections to the decay can be computed separately. Decay matrix elements do not obtain large non-relativistic corrections, so that standard relativistic NLO corrections

[2] TOPPIK is a Fortran program by Thomas Teubner which is included in every recent WHIZARD distribution. To speed up the calculation, at the beginning of a threshold run, WHIZARD generates a grid of TOPPIK output in $\sqrt{s}$, the top-quark spatial momentum and the top-quark off-shellness. Within this grid, form factors are interpolated. Also, existing grids are saved to disk and reused if the parameters fit.

to them can be used. Moreover, the NLO width can be used in the corresponding parts of the matched computation, keeping NLO accuracy in observables sensitive to the decay kinematics. The leading-order $bW^+\bar{b}W^-$–contribution is simply the square of the sum of the tree-level amplitudes, including the interferences with all background processes,

$$\sigma_{\mathrm{LO}} = \left| \right|^2 \,. \tag{6.2.2}$$

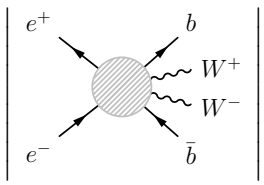

Note that, for ease of notation, we represent cross sections only by their diagrammatic kernels and omit other factors, especially the phase-space integration. Furthermore, in NLO diagrams, α_s stands for all possible QCD one-loop diagrams for this final state. Further, real parts of interference terms are denoted by $\left(a \int b\right) = 2\,\mathrm{Re}(a \cdot b^*)$, so that in this notation, the usual fixed-order NLO matrix element is given by

$$\sigma_{\mathrm{NLO}} = \sigma_{\mathrm{LO}} + \left(\right) \left(\right) + \left| \right|^2 \,, \tag{6.2.3}$$

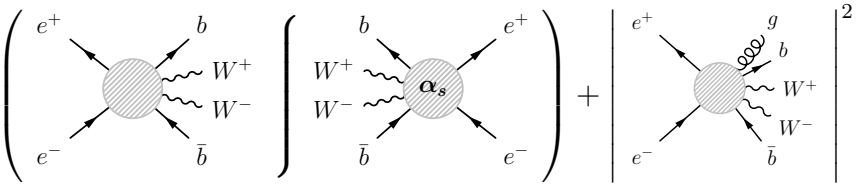

where the first summand is Born cross section evaluated using the NLO value for Γ_t. The second summand comprises the virtual and the third one the real contribution. In the factorized case, the LO matrix element is

$$\sigma_{\mathrm{LO}}^{\mathrm{fact}} = \left| \right|^2 \,. \tag{6.2.4}$$

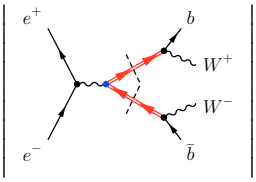

Double lines denote top propagators and a dashed line through them a factorized computation with an on-shell projection. The NLO corrections to the decay can then be

written as

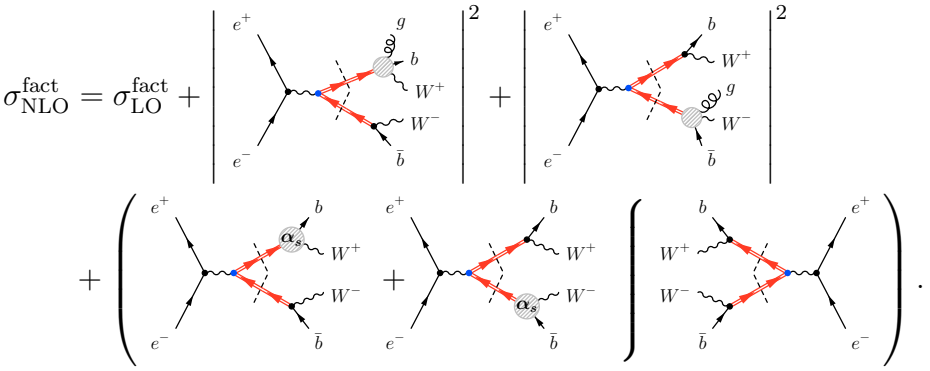

(6.2.5)

Here, the small gray blob  includes the same IR-divergent loops as in the calculation for an individual top decay, i.e. one diagram with a gluon exchange between t and b (the quark self-energies are IR-finite). Likewise, the gray blob in the real-emission contribution contains all diagrams with an additional final-state gluon. In this case, it contains two diagrams, one in which the gluon is emitted from the bottom quark, and one in which it is emitted from the top quark. It is important to note that we have omitted final-state interferences between different legs in the real-emission diagrams like

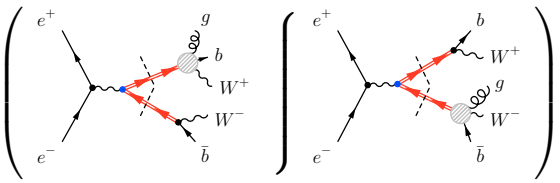

(6.2.6)

This is because the IR divergences of these diagrams only cancel when added to appropriate virtual corrections that connect final-state bottom quarks. But these require an integration over the form factor, which is unfeasible as outlined at the beginning of this section.

6.2.1. The full NLO-matched cross section

Finally, we combine the (N)LL cross sections σ_{NRQCD} with an $\mathcal{O}(\alpha_s)$-decay with the full, fixed-order NLO results σ_{QCD} for including all irreducible background processes and interferences of the $bW^+\bar{b}W^-$ final state. This results is the highest-precision description of the off-shell $t\bar{t}$–threshold as of today. Care has to be given about the correct power counting near the threshold, where $v \sim \alpha_s$. For this reason, the matrix element $\mathcal{M}_{\text{prod}}$ in eq. (6.2.1), which contains the NRQCD form factor of eq. (6.1.8) and eq. (6.1.9), is at leading logarithmic accuracy already an NLO contribution in α_s. Thus, the combination with the factorized $\mathcal{O}(\alpha_s)$-diagrams discussed in the previous section would count as NNLO corrections.

A central issue in the matching procedure is the introduction of a switch-off function f_s, which makes contributions including the form factor vanish well below threshold. Its argument is the velocity v_{1S}, which is obtained from eq. (B.3.13) by replacing m_t by M_t^{1S} and $\Gamma_t(m_t)$ by $\Gamma_t(M_t^{1S})$. The actual measure of proximity to threshold is $|v_{1s}|$, with the minimal value of $|v_{1s}|$ at $2M_t^{1S}$ being about $\sqrt{\Gamma_t\ M_t^{1S}} \approx 0.1\,\text{GeV}$. With $|v_{1S}|$ having its minimum at the 1S peak, $f_s = 1$ is guaranteed. Other choices of v would induce the switch-off to begin before or after the peak, thus affecting its shape. The switch-off function f_s enters the matrix element via multiplication to the couplings of the resummed computation. This way, it is ensured that the switch-off scales with the corresponding power of the particular coupling. In principle, one could also multiply the whole matrix element with f_s, but our approach leads to a smoother switch-off. The explicit form of the switch-off function is arbitrary, with the minimal requirements

$$f_s\left(v(\sqrt{s} = 2M_t^{1S})\right) = 1 \quad \text{and} \quad f_s(1) = 0. \tag{6.2.7}$$

Further, it should be continuously differentiable, which excludes simple linear realizations of f_s. Moreover, it has been experienced that switch-off functions that have a high curvature close to 0 and 1 introduce unphysical wiggles in cross section scans in the transition region. The most suited choice for f_s has been found to be

$$f_s(v) = \begin{cases} 1 & v < v_1 \\ 1 - 3\left(\frac{v-v_1}{v_2-v_1}\right)^2 - 2\left(\frac{v-v_1}{v_2-v_1}\right)^3 & v_1 \le v \le v_2 \\ 0 & v > v_2 \end{cases}. \tag{6.2.8}$$

For a more thorough discussion of switch-off functions, including the question whether the real or imaginary part or the magnitude of v should be taken, cf. ref. [57] and ref. [203]. The form factor contains different powers of α_s, c.f. eq. (6.1.8) and eq. (6.1.9). For this reason, naively adding $\sigma^{\text{full}}_{\text{NRQCD}}$ and the fixed-order NLO QCD cross section σ_{QCD} yields double counting of $\mathcal{O}(\alpha_s)$-terms. To solve this problem, we define with $\sigma^{\text{expanded}}_{\text{NRQCD}}$ the resummed cross section, but with the full form factor replaced by its $\mathcal{O}(\alpha_s)$-expansion. Thus, the master formula for the matched cross section is

$$\begin{aligned} \sigma_{\text{matched}} = \sigma_{\text{QCD}}(\alpha_{\text{H}}) &+ \sigma^{\text{full}}_{\text{NRQCD}}(f_s\,\alpha_{\text{H}},\ f_s\,\alpha_{\text{S}},\ f_s\,\alpha_{\text{US}}) \\ &- \sigma^{\text{expanded}}_{\text{NRQCD}}(f_s\,\alpha_{\text{H}}), \end{aligned} \tag{6.2.9}$$

where in the full NRCQD calculation, the strong coupling enters the total cross section at the hard (α_{H}), soft (α_{S}) and ultra-soft scale (α_{US}) as described in the context of eq. (6.1.5). To ensure the removal of double counting, $\sigma^{\text{expanded}}_{\text{NRQCD}}$ has to be evaluated at the same scale as σ_{QCD}, i.e. the hard scale. Note that in eq. (6.2.9), all couplings in

the NRCQD terms are already multiplied by f_s. We subtract hereby the leading α_s correction, which contains the dominating Coulomb singularity, evaluated at the hard scale α_H, which is also used in σ_QCD. Thus, we are removing the hard scale for the first order, as the soft scale in $\sigma^\mathrm{full}_\mathrm{NRQCD}$ is the more relevant one at threshold. From the fixed-order point of view both scales are valid choices. The switch-off function f_s guarantees that we keep only σ_QCD in the continuum. To better separate powers of α_s in the form factor and the matrix element, we separate the form factor into

$$F_\mathrm{(N)LL} = 1 + \tilde{F}_\mathrm{(N)LL}, \tag{6.2.10}$$

so that $\tilde{F}_\mathrm{NLL}$ only contains summands of $\mathcal{O}(\alpha_s)$ and higher. Using this, the final matching formula in a diagrammatic expression is

$\sigma_\mathrm{NLO+NLL} = \sigma_\mathrm{NLO} +$

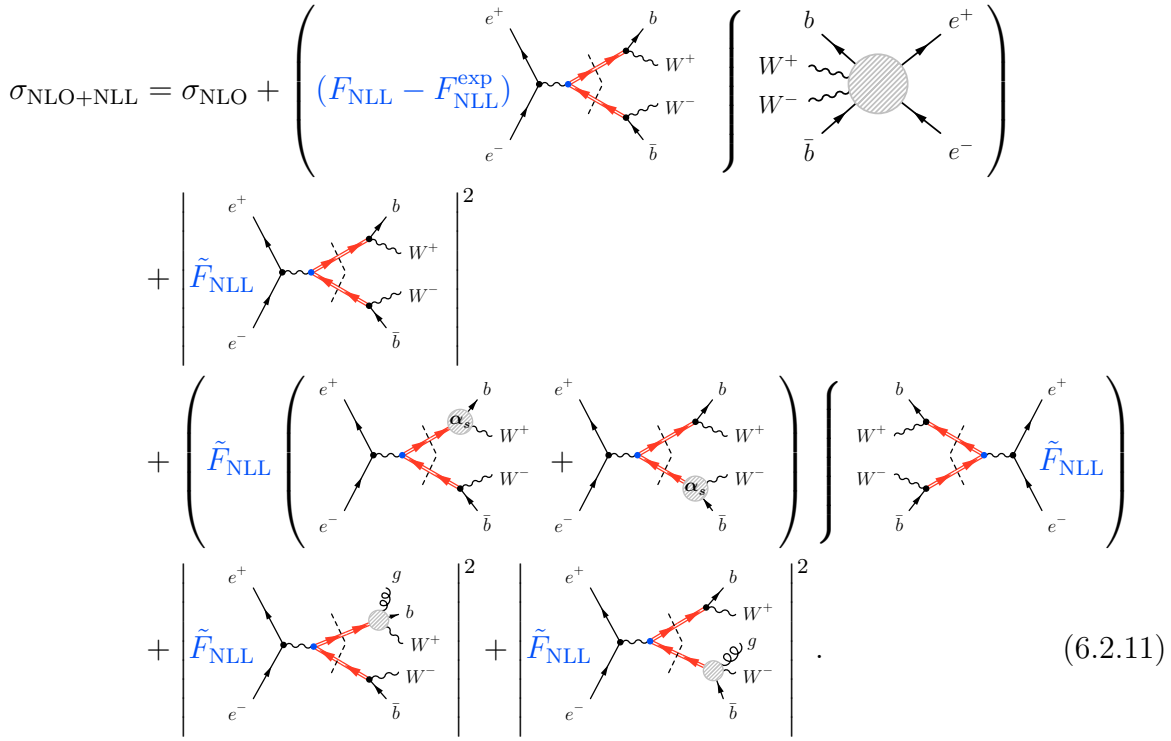

(6.2.11)

The first summand is the fixed-order continuum cross section. The second is the $\mathcal{O}(\alpha_s)$-contribution which is free of double-counting due to the subtraction of $\sigma^\mathrm{expanded}_\mathrm{NRQCD}$. The rest of the formula is the NLO contribution to the factorized NRQCD matrix element in eq. (6.2.1). Note that the last two lines formally constitute parts of the NNLO corrections to $bW^+\bar{b}W^-$ in non-relativistic power counting.

6.2.2. Modifications to standard FKS for factorized NLO

Equation 6.2.11 is evaluated using the standard WHIZARD FKS setup. The treatment of the fixed-order NLO cross section σ_{NLO} is identical to the one in the previous section and as in ref. [2]. Yet, technical modifications have to be made to the subtraction in order to deal with the rest of the formula. In the following, we describe these modifications to standard FKS developed by us. We focus on top-quark production but the statements also hold for general factorized NLO calculations without ISR.

On-shell generation of the real-emission phase space

Like the tree-level matrix element, the real matrix element has to be evaluated using on-shell momenta. To generate this phase space, we use the same mappings as in resonance-aware FKS [61], cf. section 2.6. In that approach, the real emission is generated in such a way that the invariant mass of the respective resonance is kept at its Born value, which removes mismatches between the real matrix-element and its soft approximation. Thus, starting from an already on-shell projected Born momentum configuration, we apply the same mapping to obtain an also on-shell projected real phase-space point. Note that, to ensure correct subtraction of soft divergences, also the real-emission FKS variables ξ and y need to be computed in the on-shell projected Born system. We stress that the on-shell momenta only enter the matrix-elements and their subtraction terms but not the phase-space Jacobian. For the latter as well as for event generation, the off-shell phase-space is used, which is generated alongside the on-shell case.

Decay subtraction

The divergences in the factorized calculation all originate from the $t \to bWg$ matrix element. It consists of two Feynman diagrams. One in which the gluon is emitted from the top quark and another one in which it is emitted from the bottom. Divergences can only occur in emissions from particles with on-shell momenta and zero width. Therefore, in the full $bW^+\bar{b}W^-$ matrix element, emissions from internal top quarks do not yield divergences, as they are regularized by Γ_t. However, in the pure real-emission decay amplitude, the gluon emission from the top quark is a singular contribution, which needs to be subtracted. We call this additional singular region a **pseudo-ISR** region. Pseudo, because the emitter is still associated with the final state, and so is the real-emission phase space. However, the FKS weight (cf. eq. (2.2.13))

$$d_{ij} = 2\,(p_i \cdot p_j)\,\frac{E_i E_j}{(E_i + E_j)^2} \tag{6.2.12}$$

is evaluated as though it belongs to an initial-state emission, i.e. it is evaluated with

$$p_i = p_{\text{top}} = p_b + p_W. \tag{6.2.13}$$

With this modification, the FKS pairs (b, g) and $(\bar{b}, g)$ associated with this process are extended by the pseudo-ISR tuples $(b, g)^*$ and $(\bar{b}, g)^*$, where the asterisk indicates that in this region the FKS weight in eq. (6.2.12) is evaluated with the reconstructed top momentum in eq. (6.2.13). In regions without an asterisk, $p_i = p_b$ is used.

Rearrangement of interference terms

In the square of the real matrix element, we omit interference terms between gluon emissions from different legs, cf. the term 6.2.6. In consequence, we must remove these interference contributions from the color-correlated Born matrix element used in the soft subtraction,

$$\sum_{i,j=1}^{n} \frac{k_i \cdot k_j}{(k_i \cdot k)(k_j \cdot k)} \mathcal{B}_{ij}, \tag{6.2.14}$$

cf. eq. (2.2.26). The same reasoning applies to the virtual part and its subtraction. Loop matrix elements do not include diagrams with gluon exchange between quarks on different legs since these contributions have already been resummed and are included in the form factor. Therefore, also in the soft part of the virtual subtraction terms, we leave out summands that correspond to gluon exchange between different legs. In addition to removing interference terms, tb–interferences have to be taken into account, using the bottom momentum and the reconstructed top momentum in eq. (6.2.13). The absence of interference terms allows to split up the FKS regions into two disjoint subsets, as shown on the right-hand side of table 6.1. Each subset contains a standard and a pseudo-ISR FKS pair. For $\alpha_r \in \{1, 2\}$, the contribution of color correlations take the form

$$- C_F \mathcal{B} \left[\frac{k_b^2}{(k \cdot k_b)^2} + \frac{(k_b + k_{W^-})^2}{(k \cdot (k_b + k_{W^-}))^2} - 2 \frac{k_b \cdot (k_b + k_{W^-})}{(k_b \cdot k)((k_b + k_{W^-}) \cdot k)} \right], \tag{6.2.15}$$

with an analogous expression for $\alpha_r \in \{3, 4\}$. Here, k is the gluon momentum generated with the emitter of the given α_r and we have already used the fact that for the top decay, color correlations between different legs are trivially given by a factor of C_F. The minus signs keep color conservation.

Table 6.1. Singular regions for the process $e^+e^- \to W^+W^-b\bar{b}$ in standard FKS (left) and in its modification devised for factorized processes (right), split up into a (final-state) interference-free subset and using pseudo-ISR regions.

α_r	emitter	FKS pairs
1	5	$\{(5,7),(6,7)\}$
2	6	$\{(5,7),(6,7)\}$

α_r	emitter	pseudo-ISR	FKS pairs
1	5	no	$\{(5,7),(5,7)^*\}$
2	5	yes	$\{(5,7),(5,7)^*\}$
3	6	no	$\{(6,7),(6,7)^*\}$
4	6	yes	$\{(6,7),(6,7)^*\}$

6.3. Results for the matched NLL + continuum cross section

We finally present the fully matched total cross section for the process $e^+e^- \to bW^+\bar{b}W^-$. The following masses enter the calculation as input parameters

$$m_Z = 91.1876\,\text{GeV}, \qquad m_W = 80.385\,\text{GeV},$$
$$m_b = 4.2\,\text{GeV}, \qquad m_H = 125\,\text{GeV},$$

with the corresponding (LO) widths

$$\Gamma_Z = 2.443\,\text{GeV}, \qquad \Gamma_W = 2.049\,\text{GeV},$$
$$\Gamma_b = 0\,\text{GeV}, \qquad \Gamma_H = 4.143\,\text{MeV}.$$

The electron is considered massless. The resonance mass M_t^{1S}, as defined in eq. (6.1.4), enters the calculation as an input parameter. We use $M_t^{1S} = 172\,\text{GeV}$. Therefore, using eq. (F.1.2), we obtain ${m_t}^{\text{LL}}(2M_t^{1S}) = 172.802\,\text{GeV}$ and ${m_t}^{\text{NLL}}(2M_t^{1S}) = 173.124\,\text{GeV}$.

As in the continuum study, cf. section 5.3.1, Γ_t is computed directly with WHIZARD both at LO and NLO, whereby M_t^{1S} is used as renormalization scale. Nevertheless, Γ_t depends on the pole mass m_t, and for this reason also on $\sqrt{s}$, cf. eq. (6.1.4), which is taken into account by the WHIZARD setup. At threshold, we obtain $\Gamma_t^{\text{LO}}(2M_t^{1S}) = 1.4866\,\text{GeV}$ and $\Gamma_t^{\text{NLO}}(2M_t^{1S}) = 1.3692\,\text{GeV}$. Also like in the continuum study, the electroweak coupling is derived in the G_μ-scheme using $G_\mu = 1.1663787 \times 10^{-5}\,\text{GeV}^{-2}$, keeping corrections to the top decay small [174]. The complex mass scheme is used. However in order to be consistent with the factorized computation, we do not use complex couplings like $\cos\theta_W$. Instead, the Weinberg angle and α_{em} are computed using the real part of

m_W and m_Z like in the usual Fermi scheme as

$$\alpha_{\mathrm{em}}(G_F) = \frac{\sqrt{2}}{\pi} m_W^2 \sin^2(\theta_W) G_F. \tag{6.3.1}$$

A running $\alpha_{\mathrm{em}}(\sqrt{s})$ might be more appropriate, but this can easily be achieved a posteriori by rescaling our predictions. The strong coupling, whose value at m_Z is set to $\alpha_s(m_Z) = 0.118$, has to be evaluated at the hard, soft and ultra-soft scale, cf. eq. (6.1.5). We use a three-loop running and $n_f = 5$ flavors to evolve α_s to $\alpha_{\mathrm{H}} = \alpha_s(M_t^{1S})$. From this value, the strong coupling at the soft scale $\mu_S = M_t^{1S}|v|$, i.e. α_{S}, is obtained by evolving from α_{H} with a two-loop or one-loop running at NLL or LL, respectively. v is given by eq. (B.3.13)[3]. Similarly, the strong coupling at the ultra-soft scale $\mu_{US} = M_t^{1S}|v|^2$, i.e. α_{US}, is obtained by a one-loop running from α_{H}. In fig. 6.1, we present cross sections of $e^+e^- \to bW^+\bar{b}W^-$ for various approaches to higher-order corrections as a function of $\sqrt{s}$ close to threshold. The green, violet and orange lines are fully matched results with different intervals $[v_1, v_2]$ on which the switch-off function of eq. (6.2.8) is active. For reference, also the pure fixed-order NLO cross section (blue curve) and the pure NLL cross section (red curve) are shown. It can be seen nicely that they fail in the regions where they are not a valid description of top-pair production. The red-dotted NLL resummation line clearly rises unphysically far above threshold. On the other hand, the blue fixed-order NLO curve does not even come close to a correct description of threshold effects. The matched results, as they should, reproduce both the pure NLL result close to the threshold, and then converge to the fixed-order line at about 360 GeV, whereby the exact value depends on the switch-off interval $[v_1, v_2]$. Far below threshold at about $\sqrt{s} < 335\,\mathrm{GeV}$, $|v_{1S}|$ increases again, so that the switch-off function becomes active. For this reason, like in the relativistic regime, the fixed-order NLO curve and the matched results agree nicely, whereas there is a significant gap to the pure NLL cross section. The black dotted line in fig. 6.1 shows the matched cross section without any switch-off, which is achieved technically by defining it only far away from threshold with $v_1 = 1000$ and $v_2 = 10000$. It is of particular interest because it shows the effects of the non-trivial construction of eq. (6.2.11). If $\sigma_{\mathrm{NLO+NLL}}$ would be obtained by simply interpolating the NLL and fixed-order result, e.g. via

$$\sigma^{\mathrm{naive}}_{\mathrm{NLO+NLL}} = f_s \sigma_{\mathrm{NLL}} + (1 - f_s)\sigma_{\mathrm{NLO}}, \tag{6.3.2}$$

it would be located strictly between these two. This is clearly not given for all $\sqrt{s}$. Instead, in the transition region at about 355 GeV to 365 GeV, it intersects the blue line.

We generate events at the $1S$–peak at $\sqrt{s} = 2M_t^{1S} = 344\,\mathrm{GeV}$, i.e. the position of

[3] To be precise, $\nu_* = 0.05 + |v|$ is used, but this detail is not relevant within the scope of this work.

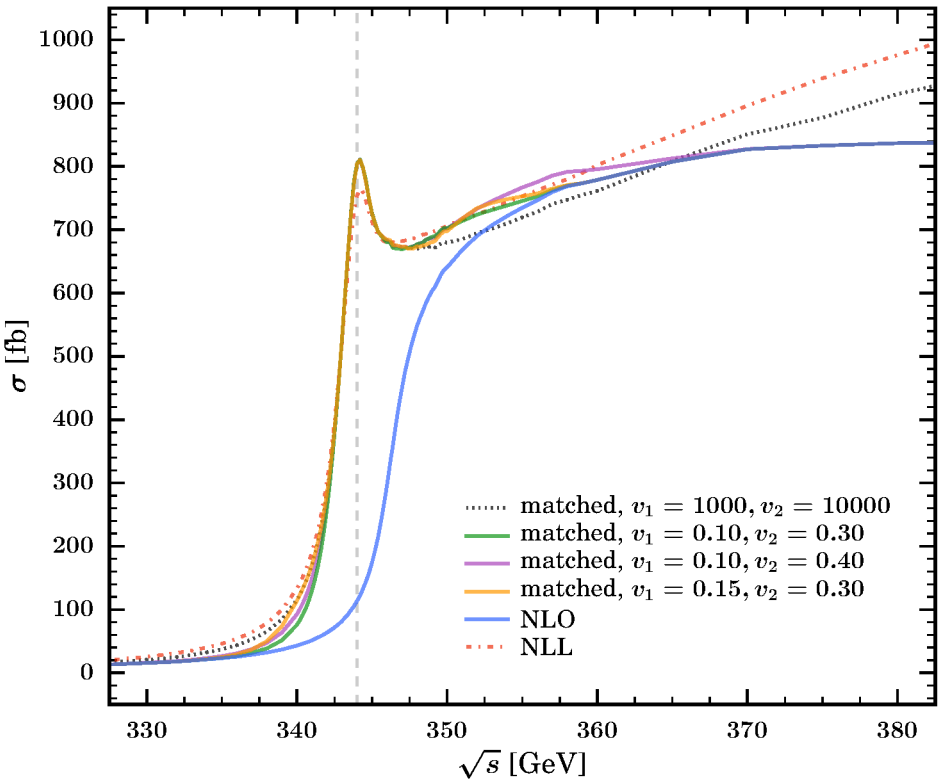

Figure 6.1. $\sqrt{s}$–scans of the $e^+e^- \to bW^+\bar{b}W^-$ process close to threshold using different switch-off intervals $[v_1, v_2]$. Also, the pure NLL resummed (red) and fixed-order NLO result (blue) are shown as reference. The black line emulates a matching approach without switch-off functions. The gray line indicates the peak-position at $\sqrt{s} = 2M_t^{1S}$.

the gray line in fig. 6.1. The setup of the simulation is identical to the one used in the continuum study, cf. section 5.3.1. We assume a perfect b-tag efficiency so that a b-jet (j_b or $j_{\bar{b}}$) denotes a jet containing a b ($\bar{b}$) quark. We use a custom `Rivet` analysis in which jets are clustered with the anti-k_T algorithm in FastJet with $R = 0.4$. Moreover, a minimal jet energy of 1 GeV is required. In all of the following figures, we present distributions according to the fixed-order NLO and the matched calculation. In the lower panels, the ratio $\sigma_{\text{matched}}/\sigma_{\text{NLO}}$ is shown. Note that this is not a K-factor and these ratios are expected to be large as can be inferred from the total cross section in fig. 6.1.

The choice of $\sqrt{s} = 2M_t^{1S}$ is slightly below the kinematical threshold $\sqrt{s} = 2m_t$, so that one top propagator can be assumed to be on-shell, while the other one is off-shell. The kinematics of the top decay products are mostly determined by the top-quark rest frame, in which the bottom and W-boson energy are

$$E_b^{\text{rest}} = \frac{m_t^2 - m_W^2 + m_b^2}{2m_t}, \quad E_W^{\text{rest}} = \frac{m_t^2 - m_b^2 + m_W^2}{2m_t}. \tag{6.3.3}$$

Upon boosting into the lab frame, the $E_{b,W}$–distribution will be localized around a peak at $E_{b,W}^{\text{rest}}$. This can be seen in fig. 6.2, which shows $d\sigma_{\text{matched}}/dE$ and $d\sigma_{\text{NLO}}/dE$, both for the b-jets and the W-bosons. In each plot, both histograms converge towards each other outside of a window of $\Delta E \approx 30\,\text{GeV}$ around the values given by eq. (6.3.3), i.e. $E_b \approx 68\,\text{GeV}$ and $E_W \approx 105\,\text{GeV}$, respectively. This is because the contribution of the factorized calculation, in which the decay kinematics are dominated by eq. (6.3.3), vanishes. Yet, for the E_W–distribution, the correction does not reach one but still has a considerable value of two, hinting towards less localized top-quark contributions. Inside the ΔE window, the correction is sizeable, with a maximum of about 14 in both distributions. As proposed in refs. [204–206], the position of the correction peak of the b-jets can be used to to measure m_t.

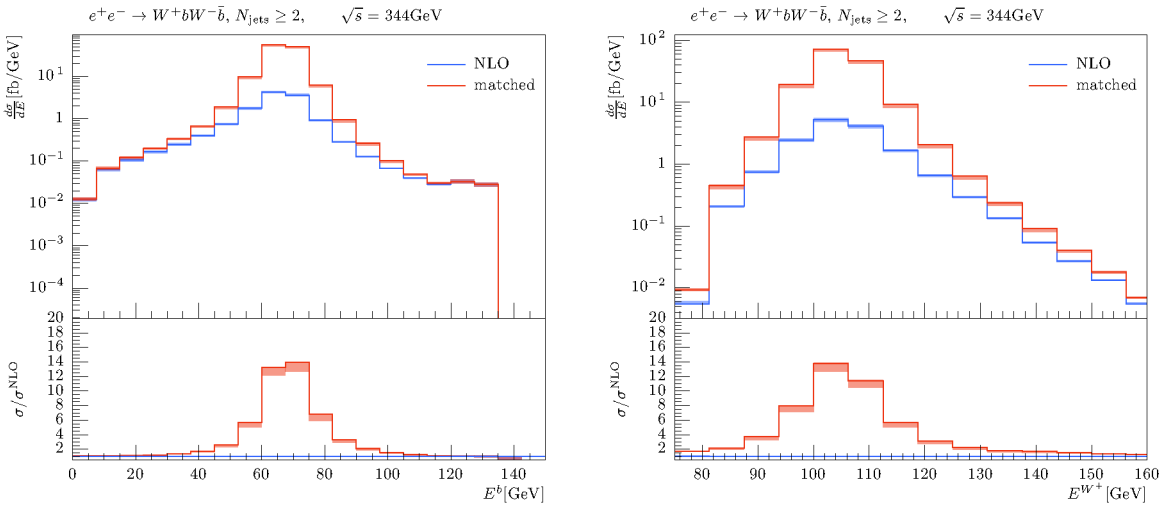

Figure 6.2. Differential distributions in the energy of the b-jet (left) and W-boson (right). The blue line describes the standard σ_{NLO} cross section, while the red one corresponds to the matched calculations as in eq. (6.2.11). Scale variations are as in section 5.7.

Next we consider direct top observables. Figure 6.3 shows the reconstructed top transverse momentum as well as the magnitude of its three-momentum, $|\mathbf{p}|^{W^+ j_b}$. The latter observable is of prime interest for understanding the dynamics at threshold. As expected, low $|\mathbf{p}|^{j_b W^+}$ and $p_T^{j_b W^+}$ are preferred both in the fixed-order simulation as well as in the matched description. Yet, large threshold corrections of almost 18 at $\sqrt{s} < 20\,\text{GeV}$ increase this preference even further. Finally, fig. 6.4 shows the reconstructed top-quark invariant mass in the interval $[80\,\text{GeV}, 260\,\text{GeV}]$ and localized around the threshold in the interval $[160\,\text{GeV}, 180\,\text{GeV}]$. As in fig. 6.2, there is a distinct peak at m_t with a width of about 30 GeV. Again, the matched curve approaches the pure NLO curve outside of this window, for a similar reason as in fig. 6.2. The kinematics away from the peak are dominated by off-shell top configurations which are mostly determined

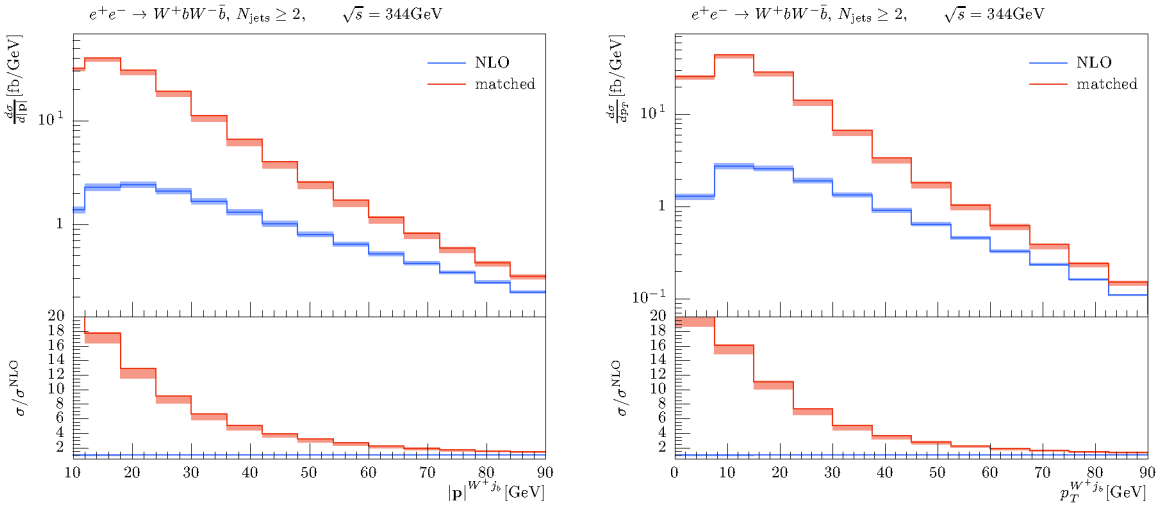

Figure 6.3. Differential distributions of the reconstructed top-quark three-momentum (left) and transverse momentum (right).

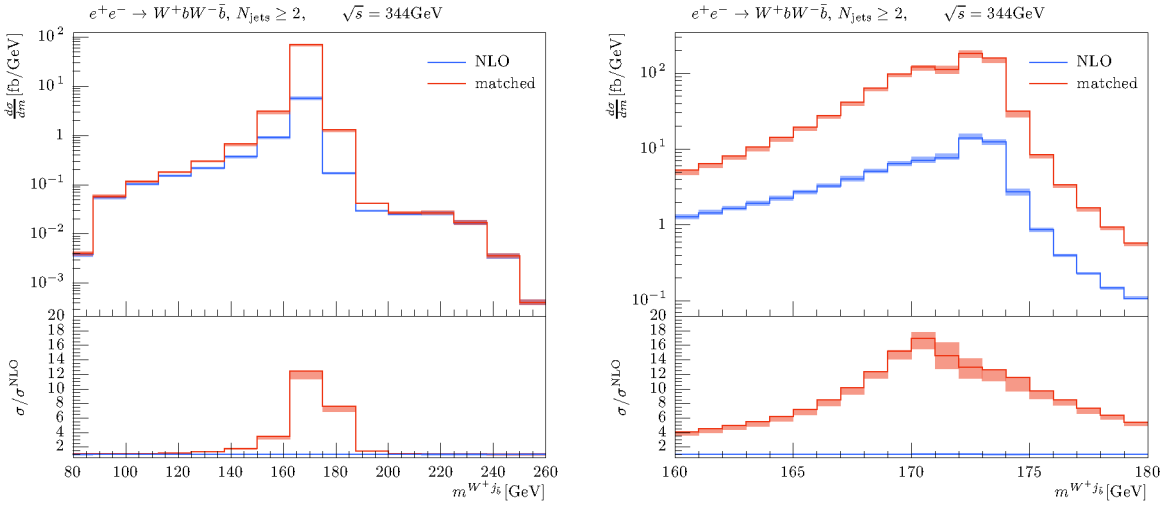

Figure 6.4. Fixed-order NLO and matched distributions for the top-quark invariant mass.

by background diagrams. Thus, the factorized contribution to the matched cross section vanishes, as this background is not included in it.

7. Summary & Outlook

The discovery of the Higgs boson completed the experimental verification of the standard model in terms of its particle content. Yet, a sizeable array of electroweak parameters has not been measured at all or at a satisfying accuracy, which is a prime task of a future lepton collider together with the search for new physics with electroweak quantum numbers. This thesis has given an outlook on important studies at such a machine, the WHIZARD event generator used for them and the theory behind NLO subtraction techniques. It has been shown that the control of NLO QCD corrections is of essential importance to match the precision of future experiments.

We started out by giving an in-depth description of the FKS subtraction scheme in chapter 2, which has become one of the standard approaches to numerical NLO calculations. It has been derived from first principles, and the numerous references on the topic have been put into one coherent description. We focused on QCD corrections in lepton collisions, but also outlined additional calculational aspects for hadron colliders emerging from the perturbative structure of PDFs and also gave a brief outlook on electroweak or QED corrections. Moreover, we have discussed the new resonance-aware FKS approach. Both the standard and the resonance-aware approach have been implemented in the WHIZARD event generator by us for general lepton-collider processes and QCD corrections.

The thesis continued by giving a brief overview of the WHIZARD event generator and especially the integration of FKS subtraction in chapter 3. WHIZARD is the most commonly used event generator in the lepton collider community, where studies at NLO accuracy will become increasingly important in the future. WHIZARD has an interface to the external programs GOSAM, OPENLOOPS and RECOLA for the calculation of one-loop matrix elements and color- and spin-correlated Born matrix elements. Subtracted amplitudes for all parts of the NLO calculation have been integrated in the dynamic data structures of WHIZARD, thus allowing for the convenient development of the program for future projects. Combining chapter 2 and chapter 3 then allowed us to present various validation checks and applications of WHIZARD in chapter 4. We have shown that WHIZARD is a reliable and well-performing tool for NLO QCD by means of the decay process $t \to bW$ and the scattering process $e^+e^- \to b\bar{b}\mu^+\mu^-$, where the new resonance-aware FKS framework has been used. However, we have also found discrepancies with MG5_aMC@NLO in section 4.3, the resolution of which should be the content of work

in the immediate future. WHIZARD and MADGRAPH agree for processes without gluons at Born-level. Also in chapter 4, we presented some distributions for events generated with the POWHEG NLO+PS matching scheme, implemented by us in WHIZARD.

The main physics part showed studies of top-quark production both in the continuum in chapter 5 and at threshold in chapter 6. In the continuum case, we have presented the first fully off-shell NLO QCD study of the $e^+e^- \to t\bar{t}(H)$ process at a lepton collider including leptonic decays. Apart from presenting the capabilities of both WHIZARD and OPENLOOPS to perform high-multiplicity calculations, we have shown that both off-shell as well as NLO QCD effects are essential in a complete description of this process. We focused on a CMS energy of $\sqrt{s} = 800\,\text{GeV}$, where the $t\bar{t}H$ cross section is largest, but K-factors for $e^+e^- \to t\bar{t}(H)$ and $e^+e^- \to bW^+\bar{b}W^-(H)$ coincidentally are almost one, as positive NLO corrections to signal diagrams counterbalance negative corrections from background and interference terms. However, the K-factor for $e^+e^- \to t\bar{t}H$ and its off-shell processes drops off much stronger than the one for top-quark production without Higgs, so that at a possible CLIC CMS energy of $\sqrt{s} = 3000\,\text{GeV}$ NLO QCD corrections are as large as -20%. Local K-factors can be even higher in some observables both for the $t\bar{t}$ and $t\bar{t}H$ final states. Further, we have analyzed the dependence of the cross section for the processes $e^+e^- \to t\bar{t}H$ and $e^+e^- \to bW^+\bar{b}W^-H$ on the top Yukawa coupling at leading and next-to-leading order. Suitably normalized, this dependence is linear with a slope which is determined by the contribution of background diagrams. We have found that NLO QCD corrections decrease this slope by about $+5\%$, thus showing that negative corrections to interference terms are sizeable. We have presented numerous observables for the complete off-shell processes $e^+e^- \to \mu^+\nu_\mu e^-\bar{\nu}_e b\bar{b}$ and $e^+e^- \to \mu^+\nu_\mu e^-\bar{\nu}_e b\bar{b}H$ in section 5.7. Local K-factors can be as large as six in the reconstructed top-quark invariant mass due to kinematical regions not accessible at LO and commonly range between 0.6 and 1.4. The events generated this way have been used to study NLO QCD effects on the top forward-backward asymmetry in section 5.7.2 for $e^+e^- \to \mu^+\nu_\mu e^-\bar{\nu}_e b\bar{b}$. Corrections increase with the off-shellness of the process, reaching to about -5%.

The top-quark continuum study was performed with the resonance-aware FKS approach, which avoids mismatches between real matrix elements and their soft and collinear approximations in emissions from particles with a non-vanishing width. Yet, we have encountered the limits of this approach in the naive setup with structureless lepton beams. As discussed in section 5.2.3, a coherent resonance treatment requires final-state boosts which can only be performed if energy can be transferred from the initial to the final state in the case of partonic scattering systems with variable collision energy.

In chapter 6, we presented an overview of the study of the top-quark threshold matched to the NLL resummed calculation. We provided the necessary modifications to the subtraction implementation required for the factorized approach used to describe the

matched matrix elements. These include the introduction of so-called pseudo-ISR regions as well as the treatment of the subtraction on an on-shell mapped phase space. The NLO framework has been successfully combined with the threshold resummation, which we have shown in section 6.3, where we have presented of the matched cross section around the threshold as well as some differential observables at $\sqrt{s} = 344\,\mathrm{GeV}$.

Finally, we collect some open aspects of the projects in this thesis, some of which are already work in progress. Concerning the continuum study of chapter 5, a complete NLO QCD study of top-quark production has to be performed with a realistic beam description. Further, an NLO+PS matching procedure like e.g. POWHEG should be applied so that the results can in principle directly be used for experimental studies involving parton showers and detector simulations. The current approach with fixed-order events both has the drawback that it produces large logarithms when interfaced to a parton shower and that it requires a very large number of weighted events to give reliable results. A treatment of this issue will definitely also play an important role in the studies of electroweak corrections in connection with beam structure functions.

NNLO QCD effects in $e^+e^- \to t\bar{t}$ are known to give additional corrections of several percent [152]. Performing this calculation is in the realm of the possible within WHIZARD, using well-known subtraction schemes like e.g. STRIPPER [207] or antenna subtraction [208]. Double-virtual, double-real and real-virtual contributions can be integrated into the WHIZARD architecture as additional components with associated terms, just like the pure NLO components (cf. fig. 3.2). All matrix elements except for the double-virtual ones can be obtained with an already interfaced one-loop provider. Since at the moment, there is no automated or semi-automated two-loop provider (and is still probably far away), the two-loop amplitudes would have to be implemented by hand. Considering $e^+e^- \to t\bar{t}H$, there is no conceptual difference to the $t\bar{t}$ final state from the NNLO perspective, except for more complicated loop integrals. Investigating NNLO effects here is still an open task and is particularly interesting if we can expect the relative corrections to be of the same order of magnitude as in the $t\bar{t}$ case, especially with respect to the study of the Yukawa coupling in section 5.5.

Notwithstanding the progress in NNLO computations, the work on NLO corrections is far from complete. As the LHC has not yet shown any significant excess, but several deviations in the range of two to three standard deviations, e.g. in rare b decays, reliably controlling both QCD and electroweak corrections becomes even more important. It is reasonable to assume that this will also be the case for a future lepton collider. Therefore, the work on the NLO framework of the WHIZARD event generator is a vital project. Besides the open questions of the validation with MG5_aMC@NLO in section 4.3, a complete validation of NLO QCD effects in hadron collisions is within the scope of future WHIZARD projects. Moreover, a reliable treatment of electroweak (photonic)

corrections is required for a complete description of real-world experiments. Here, the correct matching to beam structure functions is a special challenge which is only partly analogous to the treatment of PDFs at a hadron collider. We recently took up work in this field and progress can be expected in the coming years.

Acknowledgements

In my almost four-year journey through high-energy physics, I have encountered many people who made this work possible. First and foremost, I want to thank my supervisor Jürgen Reuter. Not only did he make this thesis possible, but also most of the time supplied the team with a good working atmosphere. Moreover, I am thankful for the freedom he provided for my work and the shaping thereof. I am also indebted for his time and effort invested into reviewing this thesis and making suggestions towards its improvement. Further, I want to thank Bernd Kniehl, who readily agreed to be the second supervisor of this thesis despite rather short notice.

Special thanks go to Wolfgang Kilian, who brought me into the WHIZARD team and thus opened up a large opportunity for me to learn and to achieve things. During the first year of my work, he functioned as the main supervisor of this thesis and was always available for skilled support. It was also a pleasure for me to participate in the general relativity course as exercise organizer at the university of Siegen in the summer term of 2014. It is therefore very gratifying for me to have Wolfgang Kilian as a member of the defense committee.

My thanks also go the other members of the promotion committee, Dieter Horns and Géraldine Servant.

Working in the WHIZARD group has always been a pleasant experience. I therefore want to thank all the other members who have been part of the collaboration during my time: Thorsten Ohl, Simon Brass, Christian Fleper, Zhijie Zhao, Fabian Bach and Vincent Rothe. Special thanks go to Bijan Chokoufé and Marco Sekulla. Bijan and I have become a very powerful team. Working together always was fun and educational. Marco was great help introducing me to the WHIZARD team and the project as a whole.

I want to thank all the people who have made my time in Siegen pleasant, especially my office colleagues Susanne Kränkl and Farnoush Shahriarian, who quietly endured my typing excesses. Other people are Denis Rosenthal, Patrick Gelhausen, Sanah Altenburg, Felix Huber, Florian Hartmann, Rebecca Klein, Philipp Böer, Sven Faller, Christian Hambrock, Claus Grupen, Isa Wagner and Flora Herzner. With all of these people I had very interesting and enlightening discussions not only about physics.

The physics group in Siegen has been largely build up by Thomas Mannel, who is also a great physics communicator. I am thankful for his participation in the organization of the Maria Laach school and for inviting me there.

For the cooperation in the SFB student council at DESY, I want to thank Peter Drechsel, Benedict Broy, Anne Ernst and Markus Ebert. The work in the council was a welcome change of scenery and I think that the organized events were big successes. For this, I also want to thank PIER and Manfred Fleischer for their support.

At DESY, I met many people from different countries, who made my stay here convenient. I want to thank my present and former office colleagues, Shruti Patel, Shireen Gangal, Julian Schweizer, Jonas Wittbrodt and Marco Scalisi, for discussions and distractions. Thanks go also to So Young Shim, Stefan Liebler, Pjotr Pietrulewicz, Lorena Rothen, Frank Tackmann and Markus Diehl from building 1b. Special thanks go to Markus Dierigl and Nayara Fonseca for organizing the Friday cookie breaks.

I shared many professional relationships with physicists from many places all over the world. The most fruitful one was that with Jonas Lindert with his support on OpenLoops and related topics. In the paper we published together, also the contributions by Stefano Pozzorini are indispensable. He always kept a clear head about the physics behind the technical issues. Moreover, our work on resonances and FKS subtraction, greatly benefited from the many fruitful discussions we had with Tomáš Ježo about that topic. We are also grateful for the various cross-checks of Whizard by Stefan Kallweit and Andrew Papanastasiou. Moreover, the cooperation with André Hoang and Maximilian Stahlofen has strongly enhanced the scope of this work and was very instructive.

Further thanks go to Jean-Nicolas Lang and Nico Greiner for their support on their respective programs and fruitful discussions about NLO calculations and collider physics.

Connecting with people from all over the world is an essential part of science. I made this experience by attending international conferences and exchange programs. Therefore, I want to thank all the people who gave me the opportunity to do so. These are Doreen Wackeroth for inviting me to the LoopFest in Buffalo and especially its organization. Lucy Linsen for inviting me to the CLIC dp workshop. Special thanks go to the DAAD for its exchange program with Zewail City in Egypt, and Shaaban Khalil and Suzy Naguib for hosting us there.

Scientific work would be much harder if nobody would take care of organizational issues. I therefore want to thank Arzu Ergüzel from TP1 in Siegen and the secretaries of theory group at DESY, Julia Herrmann, Cristina Guerrero and Inna Henning.

Finally, I want to mention some personal friends: Julia Sprenger, Volker Enzesberger, Ferdinand Eiteneuer, Sebastian Krämer, Knut Kiesel and Stephan Brüggemann. They helped to keep my head up and my eyes open during the almost four years of PhD work.

A. Details on the construction of the radiation phase space

This chapter documents the real-emission phase-space generation for final- and initial-state emissions. In the first case, it has to be distinguished between the massless and the massive case. We use the conventions from section 2.1.3. Further, we always assume that the momentum at position n is associated with the emitter and that k_{n+1} is the momentum of the radiated particle.

A.1. Real-emission phase space for final-state singularities

We use the conventions for momenta introduced in section 2.1.3. The construction of the real-emission phase space leaves the initial state completely unaffected, so that in all of the following constructions, $k_\oplus = \bar{k}_\oplus$ and $k_\ominus = \bar{k}_\ominus$. The construction of real emission can therefore be constrained to the set of final-state particles $\mathcal{F}$. We further denote by $\mathcal{F}_R \subseteq \mathcal{F}$ the set of final-state momenta which are modified by the real-emission algorithm. In default mappings, $\mathcal{F}_R = \mathcal{F}$, whereas in mappings which conserves invariant masses, such as resonance-aware or on-shell real-emission mappings, $\mathcal{F}_R \subsetneq \mathcal{F}$.

A.1.1. Basic final-state construction

The construction of the final-state real-emission phase space relies on a separation of the kinematics of the whole process into that of the emitter system $\mathcal{E} = \{k_n, k_{n+1}\}$ and the kinematics of the recoiling system $\mathcal{C}$, defined by $\mathcal{C} \cup \mathcal{E} = \mathcal{F}_R$. The radiation variables $\Xi = \{\xi, y, \phi\}$ determine the construction of the gluon momentum k_{n+1} in $\mathcal{E}$ (for simplicity, we assume that the radiated particle is a gluon, but the following discussions hold for any massless particle). Since the sum of the gluon and emitter momenta must equal the emitter momentum in the Born phase space, i.e. $\bar{k}_n = k_n + k_{n+1}$, this also fixes k_n. A boost is applied on $\mathcal{C}$ to restore total momentum conservation, after the construction in $\mathcal{E}$ is finished. In the following we explain in detail what we call the

basic construction, on which all FSR phase-space constructions rely. In summary, it is as follows:

1. The gluon energy is given by
$$E_g = \frac{q^0}{2}\xi, \tag{A.1.1}$$
with $\xi \in \Xi$. Here, q^0 is the energy entering the radiating system. In default constructions, where the radiating system is made up of all final-state particles, it is the partonic center-of-mass energy $\sqrt{\hat{s}}$. In general, it is the energy of a subset of all final-state particles. Especially, in the construction of a resonance-aware FSR phase-space, q^0 is the resonance energy of the associated resonance history.

   The magnitude $\underline{k}_{n+1}$ of the (massless) FKS parton momentum is trivially given by $\underline{k}_{n+1} = E_g$. This fixates k_{n+1} except for its polar and azimuthal angles.

2. The momenta magnitudes $\underline{k}$ and $\underline{k}_n$ are constructed, which determines $\mathbf{k}_n$ except for a rotation. The construction method differs for massless and massive particles as outlined below.

3. k_n and k_{n+1} are positioned parallel to the emitter momentum in the Born system,
$$\mathbf{k}'_n = \underline{k}_n \frac{\bar{\mathbf{k}}_n}{\underline{\bar{k}}_n}, \quad \mathbf{k}'_{n+1} = \underline{k}_n \frac{\bar{\mathbf{k}}_n}{\underline{\bar{k}}_n}. \tag{A.1.2}$$
   Then, a rotation is applied to both momenta,
$$\mathbf{k}_{n,n+1} = R\left(\psi_{n,n+1}, \mathbf{d}\right) \mathbf{k}'_{n,n+1}, \quad \cos\psi_{n,n+1} = \cos\angle\left(\mathbf{k}_{n,n+1}, \mathbf{k}\right) = \frac{\mathbf{k}_{n,n+1}\cdot\mathbf{k}}{\underline{k}_{n,n+1}\underline{k}}, \tag{A.1.3}$$
   around the unit vector $\mathbf{d}$ orthogonal to $\bar{\mathbf{k}}_n$,
$$\mathbf{d} = \frac{1}{\sqrt{\left(\bar{k}_n^1\right)^2 + \left(\bar{k}_n^2\right)^2}} \left(\bar{k}^2, -\bar{k}^1, 0\right)^T. \tag{A.1.4}$$
   The scalar product in the numerator of (A.1.3) can be obtained from momentum conservation, $\left(\mathbf{k} - \mathbf{k}_{n,n+1}\right)^2 = \mathbf{k}^2_{n+1,n}$, yielding
$$\cos\psi_{n,n+1} = \frac{\underline{k}^2_{n,n+1} + \underline{k}^2 - \underline{k}^2_{n+1,n}}{2\underline{k}_{n,n+1}\underline{k}}. \tag{A.1.5}$$

4. The rotation $R\left(\phi, \bar{\mathbf{k}}_n/\underline{\bar{k}}_n\right)$ is applied on $\mathcal{E}$ with $\phi \in \Xi$.

5. Finally, the recoiling system is boosted by a boost $\Lambda_{\text{rec}}(\beta)$ along the beam axis to

balance the momentum of the radiation system. The boost parameter β is given by the expressions in eq. (A.1.9) and eq. (A.1.13).

A.1.2. Details of the massless construction

In the default massless construction $\mathcal{F}_R = \mathcal{F}$. For a massless emitter, $y = \cos\theta$. This yields

$$\underline{k}^2 = \underline{k}_n^2 + \underline{k}_{n+1}^2 + 2\underline{k}_n\underline{k}_{n+1}y. \tag{A.1.6}$$

Moreover, $\underline{k}_n = k_n^0$, such that energy conservation gives

$$\underline{k}_n + \underline{k}_{n+1} + k_{\text{rec}}^0 = \underline{k}_n + \underline{k}_{n+1} + \sqrt{\underline{k}^2 + M_{\text{rec}}^2} = q^0, \tag{A.1.7}$$

where k_{rec} is the momentum of the recoiling system $\mathcal{C}$ and M_{rec} its associated invariant mass. Momentum conservation yields $\underline{k}_{\text{rec}} = \underline{k}$. Combining (A.1.6) and (A.1.7) yields

$$\underline{k}_n = \frac{q^2 - M_{\text{rec}}^2 - 2q^0\underline{k}_{n+1}}{2\left(q^0 - \underline{k}_{n+1}(1-y)\right)}. \tag{A.1.8}$$

The boost velocity of Λ_{rec} is found by considering the Lorentz-invariant quantity $\bar{k}_n^2 = \left(q - \bar{k}_{\text{rec}}\right)^2 = 0$. This must also be fulfilled in the real-emission phase space, so that $\left(q - \Lambda_{\text{rec}}k_{\text{rec}}\right)^2 = 0$, with the resulting boost parameter

$$\beta = \frac{q^2 - \left(k_{\text{rec}}^0 + \underline{k}_{\text{rec}}\right)^2}{q^2 + \left(k_{\text{rec}}^0 + \underline{k}_{\text{rec}}\right)}. \tag{A.1.9}$$

A.1.3. Details of the massive construction

The construction of a real emission from a massive particle is treated in ref. [60] with a Dalitz plot analysis of the (k_n^0, k_{n+1}^0)–space. The parameter $z > 0$ defines the Dalitz domain

$$k_n^0 = \bar{k}_n^0 - zk_{n+1}^0, \tag{A.1.10}$$

with its two boundaries z_1 and z_2. In this treatment, the real radiation variable y changes its meaning from the emission angle $\cos\theta$ to the slope of the tangent in the Dalitz plot. It enters the parameterization in eq. (A.1.10) via

$$z = z_2 - \frac{1+y}{2}\left(z_2 - z_1\right). \tag{A.1.11}$$

As discussed in ref. [60], the limits z_1 and z_2 are given by the boundaries of specific Dalitz regions,

$$z_{1/2} = \left(\bar{k}^0_{\text{rec}} \pm \sqrt{\left(\bar{k}^0_{\text{rec}}\right)^2 - M^2_{\text{rec}}}\right) / q^0. \tag{A.1.12}$$

Noteworthy to say, this also determines $\xi_{\max}$ and $k^0_{n,\max}$. Knowing z and the upper limit of the emitter energy, k^0_n can be constructed according to eq. (A.1.10). The same argumentation that leads to eq. (A.1.9) yields

$$\beta = \frac{1-\alpha^2}{1+\alpha^2}, \quad \text{with} \quad \alpha = \frac{k^0_{\text{rec}} + \underline{k}_{\text{rec}}}{k^0_{\text{rec}} - \underline{k}_{\text{rec}}}. \tag{A.1.13}$$

A.2. Real-emission phase space for initial-state divergences

The construction of initial-state emissions is more involved than that of final-state emissions because in general, the kinematics of the beam momenta are determined by structure functions. Here, it is generally assumed that the beam partons move fast enough that radiative effects do not significantly alter their direction. The direction of their momentum is essentially fixed to be parallel to the beam axis, with parton branchings only affecting the energy. The construction of a real phase space in an initial-state singular region therefore relies on the manipulation of the energies of the colliding partons and a subsequent boost of final-state momenta. The gluon momentum can simply be constructed as

$$k_{n+1} = \frac{\sqrt{s}}{2}\xi \left(1, \sqrt{1-y^2}\sin\phi, \sqrt{1-y^2}\cos\phi, y\right) \tag{A.2.1}$$

The momenta entering the hard process $k_\oplus$ and $k_\ominus$ are written in terms of the beam momenta $K_\oplus$ and $K_\ominus$,

$$k_\oplus = x_\oplus K_\oplus, \quad \text{and} \quad k_\ominus = x_\ominus K_\ominus. \tag{A.2.2}$$

The same notation also applies for the Born momenta $\bar{k}_i$. The parton energy fractions of the real-emission and Born phase space are related through the equation [59, 209]

$$x_\oplus = \frac{\bar{x}_\oplus}{\sqrt{1-\xi}}\sqrt{\frac{2-\xi(1-y)}{2-\xi(1+y)}}, \quad x_\ominus = \frac{\bar{x}_\ominus}{\sqrt{1-\xi}}\sqrt{\frac{2-\xi(1+y)}{2-\xi(1-y)}}. \tag{A.2.3}$$

The total final-state momentum in the Born phase space is $\bar{k}_{\text{tot}} = \sum_{i=1}^n \bar{k}_i$. Analogously, we define $k_{\text{tot}} = \sum_{i=1}^n k_i$. Obviously, $\bar{k}_{\text{tot}}$ is parallel to the beam axis. Due to the gluon emission, this is not the case for k_{tot}, which has a transversal component. Nevertheless, both quantities are connected through a boost, $k_{\text{tot}} = \Lambda \bar{k}_{\text{tot}}$, and so are the individual

final-state momenta k_i and $\bar{k}_i$. Further, Λ is split up into boosts into systems with no longitudinal component, Λ_L, and no transversal component, Λ_T, which are easier to construct. Thus,

$$k_i = \Lambda_L^{-1}\Lambda_T^{-1}\Lambda_L\bar{k}_i, \quad i = 1, \dots n. \tag{A.2.4}$$

The Lorentz transformation Λ_L is achieved by boosting by the amount

$$\beta_{L,i} = \frac{\bar{k}^i_{\text{tot}}}{\bar{k}^0_{\text{tot}}} = \frac{\bar{k}^i_{\oplus} + \bar{k}^i_{\ominus}}{\bar{k}^0_{\oplus} + \bar{k}^0_{\ominus}}, \tag{A.2.5}$$

whereas the boost into the frame with no transversal component is

$$\beta_T = \left[1 + \frac{\hat{s}(1-\xi)}{p_T^2}\right]^{-1/2}, \tag{A.2.6}$$

where p_T is the radiated particle's transverse momentum with respect to the z-axis

A.3. Upper limits for real radiation energy

FSR, $m = 0$ For a massless final-state emitter, the maximal radiation energy is trivially given by the emitter's energy at Born level,

$$\xi_{\max} = \frac{2\bar{k}_n}{q^0}. \tag{A.3.1}$$

FSR, $m > 0$ The derivation of $\xi_{\max}$ has already been outlined in the discussion of the emitter momentum in section A.1.3. We divide $k^0_{n,\max}$ by $\sqrt{s}/2$ to obtain

$$\xi_{\max} = \frac{2}{q^0} \cdot \frac{2q^0 z\bar{k}^0_{\text{rec}} - q^2z^2 - M^2_{\text{rec}}}{2q^0 z(1-z)}. \tag{A.3.2}$$

ISR The beam momentum fractions in the Born and real emission phase space are connected by eq. (A.2.3) which can be used to determine an upper bound on ξ by imposing the conditions $x_\oplus \leq 1$ and $x_\ominus \leq 1$. Solving for ξ in eq. (A.2.3) gives two upper bounds, out of which the smaller one is taken, i.e.

$$\xi_{\max} = 1 - \max\left[\frac{2(1+y)\bar{x}^2_{\oplus}}{\sqrt{(1+\bar{x}^2_{\oplus})^2(1-y)^2 + 16y\bar{x}^2_{\oplus} + (1-y)(1-\bar{x}^2_{\oplus})}}, \frac{2(1-y)\bar{x}^2_{\ominus}}{\sqrt{(1+\bar{x}^2_{\ominus})^2(1+y)^2 + 16y\bar{x}^2_{\ominus} + (1+y)(1-\bar{x}^2_{\ominus})}}\right]. \tag{A.3.3}$$

B. Further details on FKS subtraction

B.1. Example singular regions

To get a deeper understanding of the set of singular regions $\mathcal{P}_{\text{FKS}}$ as introduced in eq. (2.2.3), we present information about the singular regions for the example processes $e^+e^- \to jjj$ and $e^+e^- \to t\bar{t}t\bar{t}$ as well as $e^+e^- \to b\bar{b}\mu^+\mu^-$, using the resonance-aware approach for the latter.

$\boldsymbol{e^+e^- \to jjj}$ We consider only two flavors and the gluon in the jet, i.e. $j = u, \bar{u}, d, \bar{d}, g$. This way, the process still contains all relevant singular configurations with the least amount of combinatorial complexity. Table B.1 gives a summary of all real-emission and Born flavor structures, emitters, multiplicities and the set $\mathcal{P}_{\text{FKS}}$. The real corrections to this process contain all possible final-state splittings of QCD. The $q \to qg$ and $g \to gg$ splittings yield real configurations with two gluons in the final state ($\alpha_r = 2, 3, 4, 8, 9, 10$), whereas the $g \to q\bar{q}$ splittings lead to flavor structures with two, either identical ($\alpha_r = 1, 7$) or different ($\alpha_r = 5, 6$) quark pairs. Here, for simplicity, we have only considered two possible quark flavors for the gluon to split into, matching the jet definition. The real flavor arrays in the second column are organized in such a way that the radiated particle is on the last position. The preceeding entries are permuted in such a way that they match the underlying Born flavor structure in the last column. The emitter ε defines the phase space the real matrix element is evaluated with for this α_r. The regions in $\{1, 4, 5, 6, 7, 10\}$, $\{2, 8\}$ and $\{3, 9\}$ have identical emitters. The $g \to q\bar{q}$–regions $\alpha_r = 1$ and $\alpha_r = 7$ have multipicity $\varsigma = 4$, corresponding to each combinatorial possibility the final-state quarks can be combined to form a gluon with a correct underlying Born. Treating them seperately does not reproduce the correct collinear limit, because all the combinatorical contributions are also present in the real matrix element. Likewise, the $q \to qg$-regions ($\alpha_r = 2, 3, 8, 9$) have $\varsigma = 2$ for each possible assignment of the two gluons to the emitted particle. Note that this can easily be deduced from the existence of two FKS-pairs with the first index matching the region's emitter (i.e. $(3, 5)$ and $(3, 6)$ in regions 2 and 8).

Table B.1. A list of singular FKS regions for the process $e^+e^- \to jjj$ with $n_f = 2$. ε denotes the position of the emitter in the flavor array f_r. The indices i_b and i_r label the Born and real flavor structures, respectively. an associated index i_r. ς denotes the region's multiplicity. $\mathcal{P}_{\text{FKS}}$ is defined in eq. (2.2.3). Table automatically produced by WHIZARD.

α_r	f_r	i_r	ε	ς	$\mathcal{P}_{\text{FKS}}$	i_b	f_b
1	[-11,11,-2,2,-2,2]	1	5	4	$\{(4,5),(5,6),(3,4),(3,6)\}$	1	[-11,11,-2,2,21]
2	[-11,11,-2,2,21,21]	2	3	2	$\{(3,5),(3,6),(4,5),(4,6),(5,6)\}$	1	[-11,11,-2,2,21]
3	[-11,11,-2,2,21,21]	2	4	2	$\{(3,5),(3,6),(4,5),(4,6),(5,6)\}$	1	[-11,11,-2,2,21]
4	[-11,11,-2,2,21,21]	2	5	1	$\{(3,5),(3,6),(4,5),(4,6),(5,6)\}$	1	[-11,11,-2,2,21]
5	[-11,11,-2,2,-1,1]	3	5	1	$\{(5,6)\}$	1	[-11,11,-2,2,21]
6	[-11,11,-1,1,-2,2]	4	5	1	$\{(5,6)\}$	2	[-11,11,-1,1,21]
7	[-11,11,-1,1,-1,1]	5	5	4	$\{(4,5),(5,6),(3,4),(3,6)\}$	2	[-11,11,-1,1,21]
8	[-11,11,-1,1,21,21]	6	3	2	$\{(3,5),(3,6),(4,5),(4,6),(5,6)\}$	2	[-11,11,-1,1,21]
9	[-11,11,-1,1,21,21]	6	4	2	$\{(3,5),(3,6),(4,5),(4,6),(5,6)\}$	2	[-11,11,-1,1,21]
10	[-11,11,-1,1,21,21]	6	5	1	$\{(3,5),(3,6),(4,5),(4,6),(5,6)\}$	2	[-11,11,-1,1,21]

Table B.2. A list of singular FKS regions for the process $e^+e^- \to t\bar{t}t\bar{t}$. All quantities as described in tab. B.1. Table automatically produced by WHIZARD.

α_r	f_r	i_r	ε	ς	$\mathcal{P}_{\text{FKS}}$	i_b	f_b
1	[-11,11,6,-6,6,-6,21]	1	3	1	$\{(3,7),(4,7),(5,7),(6,7)\}$	1	[-11,11,6,-6,6,-6]
2	[-11,11,6,-6,6,-6,21]	1	4	1	$\{(3,7),(4,7),(5,7),(6,7)\}$	1	[-11,11,6,-6,6,-6]
3	[-11,11,6,-6,6,-6,21]	1	5	1	$\{(3,7),(4,7),(5,7),(6,7)\}$	1	[-11,11,6,-6,6,-6]
4	[-11,11,6,-6,6,-6,21]	1	6	1	$\{(3,7),(4,7),(5,7),(6,7)\}$	1	[-11,11,6,-6,6,-6]

$e^+e^- \to t\bar{t}t\bar{t}$ Identical particles in real flavor structures can pose an additional complication for $q \to qg$ - splittings, as is shown for the example $e^+e^- \to t\bar{t}t\bar{t}$. We treat this process at NLO in section 4.3 and find excellent agreement to MADGRAPH. Table B.2 lists singular regions for this process. There are four distinct regions, corresponding to the four different emitters involved in this process, each with $\varsigma = 1$.

$e^+e^- \to b\bar{b}\mu^+\mu^-$ with resonance mappings In this process, there are two resonance histories, $Z \to b\bar{b}$ and $H \to b\bar{b}$. As outlined in section 2.6.3, these two resonance histories appear as an additional index of the FKS region. For example, in $\{\ldots;1\}$ regions, as shown in table B.3, the Z mass and width is inserted in the numerator of the $\mathcal{S}$ function in eq. (2.6.22). Likewise, $\{\ldots;2\}$ regions employ the Higgs mass and width. Note that,

Table B.3. A list of singular regions for the process $e^+e^- \to b\bar{b}\mu^+\mu^-$ in resonance-aware FKS. All quantities as described in table B.1.

α_r	f_r	i_r	ε	ς	$\mathcal{P}_{\text{FKS}}$	i_b	f_b
1	[11,-11,5,-5,13,-13,21]	1	3	1	$\{(3,7;1),(4,7;1),(3,7;2),(4,7;2)\}$	1	[11,-11,5,-5,13,-13]
1	[11,-11,5,-5,13,-13,21]	1	3	1	$\{(3,7;1),(4,7;1),(3,7;2),(4,7;2)\}$	1	[11,-11,5,-5,13,-13]
2	[11,-11,5,-5,13,-13,21]	1	4	1	$\{(3,7;1),(4,7;1),(3,7;2),(4,7;2)\}$	1	[11,-11,5,-5,13,-13]
2	[11,-11,5,-5,13,-13,21]	1	4	1	$\{(3,7;1),(4,7;1),(3,7;2),(4,7;2)\}$	1	[11,-11,5,-5,13,-13]

however, in this case the resonance index does not influence the generation of the real-emission phase space, because in both cases the radiation system comprises the two bottom quarks. Table B.3 depicts the entirety if singular regions for this process.

B.2. Rescaling the real integration for $\xi_{\max} < 1$

The FKS variable ξ is kinematically limited to a value $\xi_{\max} \leq 1$, because simply put, the radiated particle cannot have more energy than its emitter. This limit in general depends on the angular separation y, e.g. in emissions from massive particles, cf. eq. (A.3.2). Both the fact that $\xi_{\max} \leq 1$ and its dependence on y slightly complicates the integration in eq. (2.2.25). The upper integration limit 1 is restored by rescaling the ξ-integral with the transformation

$$\xi = \xi_{\max}(y)\tilde{\xi}, \tag{B.2.1}$$

with $\tilde{\xi}$ as the new integration variable. Rescaling the plus-distribution in eq. (2.2.24) leads to

$$\int_0^{\xi_{\max}(y)} d\xi \left(\frac{1}{\xi}\right)_+ \tilde{\mathcal{R}}_\alpha(\xi) = \int_0^1 d\tilde{\xi} \left[\left(\frac{1}{\tilde{\xi}}\right)_+ + \log \xi_{\max}(y)\delta(\tilde{\xi})\right] \tilde{\mathcal{R}}_\alpha(\tilde{\xi}), \tag{B.2.2}$$

which results in additional finite terms due to the delta function. The pole structure is not affected, so that no modifications for virtual subtraction terms have to be done.

Upon executing the $\delta(\tilde{\xi})$ function, eq. (2.2.25) becomes

$$\int d\Phi_{\text{rad}} \mathcal{R}_\alpha^{\text{fin}} = \int_0^{2\pi} d\phi \int_{-1}^{1} \frac{dy}{1-y} \Bigg\{ \Big[\overbrace{\log \xi_{\max}(y) \mathcal{R}_\alpha(\tilde{0}, y) - \log \xi_{\max}(1) \mathcal{R}_\alpha(\tilde{0}, 1)}^{I_{\text{remn}}^{\text{FSR}}} \Big] + \int_0^1 \frac{d\tilde{\xi}}{\tilde{\xi}} \Big[\tilde{\mathcal{R}}_\alpha(\tilde{\xi}\xi_{\max}(y), y) - \tilde{\mathcal{R}}_\alpha(0, y) - \tilde{\mathcal{R}}_\alpha(\tilde{\xi}\xi_{\max}(1), 1) + \tilde{\mathcal{R}}_\alpha(0, 1) \Big] \Bigg\}, \tag{B.2.3}$$

which differs from eq. (2.2.25) by the additional remnant logarithms $I_{\text{remn}}^{\text{FSR}}$. Note that here, the only collinear limit is $y = 1$. In the presence of initial-state singularities, additional remnant terms appear, given by

$$I_{\text{remn}}^{\text{ISR}} = \log(\xi_{\max}) \tilde{\mathcal{R}}_\alpha(0, y) - \log(1 - x_\oplus) \tilde{\mathcal{R}}_\alpha(\xi, 1) - \log(1 - x_\ominus) \tilde{\mathcal{R}}_\alpha(\xi, -1). \tag{B.2.4}$$

Here, $x_\oplus$ and $x_\ominus$ are the parton energy fractions as defined in eq. (A.2.3).

B.3. Formulas for the virtual-subtracted contribution

B.3.1. Eikonal integrals

We give a list of the explicit expressions for the divergent and finite part of the eikonal integrals introduced in eq. (2.3.1) and eq. (2.3.2) [40]. k_i and k_j denote the Born momenta of the ith and jth particle, respectively. s is the partonic center-of-mass energy, which in the resonance-aware approach discussed in section 2.6 has to be replaced by k_{res}^2. Q^2 is the Ellis-Sexton scale, as discussed in section 2.3 in the context the normalization factor $\mathcal{N}(\varepsilon)$ in eq. (2.3.3). Also in this normalization factor, the renormalization scale μ^2 is included. m_i and m_j are the corresponding particle masses.

- $m_i = 0, i = j$

$$\hat{\mathcal{E}}_{ii}^{(0,0)} = 0, \qquad \mathcal{E}_{ii}^{(0,0)} = 0. \tag{B.3.1}$$

  This follows directly from $k_i^2 = 0$ in $\frac{k_i^2}{(k_i \cdot k_j)^2}$.

- $m_i = 0, m_j = 0, i \neq j$

$$\hat{\mathcal{E}}_{ij}^{(0,0)} = \mathcal{N}(\varepsilon)\left[\frac{1}{\varepsilon^2} - \frac{1}{\varepsilon}\left(\log\frac{2k_i\cdot k_j}{Q^2} - \log\frac{4E_iE_j}{s}\right)\right], \tag{B.3.2}$$

$$\begin{aligned}\mathcal{E}_{ij}^{(0,0)} &= \frac{1}{2}\log^2\frac{s}{Q^2} + \log\frac{s}{Q^2}\log\frac{k_i\cdot k_j}{2E_iE_j} - \mathrm{Li}_2\frac{k_i\cdot k_j}{2E_iE_j} \\ &\quad + \frac{1}{2}\log^2\frac{k_i\cdot k_j}{2E_iE_j} - \log\left(1 - \frac{k_i\cdot k_j}{2E_iE_j}\right)\log\frac{k_i\cdot k_j}{2E_iE_j}.\end{aligned} \tag{B.3.3}$$

In the second line, $\varepsilon = 0$, so that $\mathcal{N} = 1$. Further, Li_2 is the dilogarithm,

$$\mathrm{Li}_2(x) = -\int_0^x dz \frac{\log(1-z)}{z}. \tag{B.3.4}$$

- $m_i = 0, m_j \neq 0$

$$\hat{\mathcal{E}}_{ij}^{(0,m_j)} = \mathcal{N}(\varepsilon)\left[\frac{1}{2\varepsilon^2} - \frac{1}{\varepsilon}\left(\log\frac{2k_i\cdot k_j}{Q^2} - \frac{1}{2}\log\frac{4m_j^2E_j^2}{sQ^2}\right)\right], \tag{B.3.5}$$

$$\begin{aligned}\mathcal{E}_{ij}^{(0,m_j)} &= -\frac{\pi^2}{12} + \frac{1}{4}\log^2\frac{s}{Q^2} - \frac{1}{4}\log^2\frac{1+\beta_j}{1-\beta_j} \\ &\quad + \frac{1}{2}\log^2\frac{k_i\cdot k_j}{(1-\beta_j)E_iE_j} + \log\frac{s}{Q^2}\log\frac{k_i\cdot k_j}{m_jE_i} \\ &\quad - \mathrm{Li}_2\left(1 - \frac{(1+\beta_j)E_iE_j}{k_i\cdot k_j}\right) + \mathrm{Li}_2\left(1 - \frac{k_i\cdot k_j}{(1-\beta_j)E_iE_j}\right),\end{aligned} \tag{B.3.6}$$

where

$$\beta_i = \sqrt{1 - \frac{m_i^2}{E_i^2}}. \tag{B.3.7}$$

- $m_i \neq 0, i = j$

$$\hat{\mathcal{E}}_{ii}^{(m_i,m_i)} = \mathcal{N}(\varepsilon)\left(-\frac{1}{\varepsilon}\right), \tag{B.3.8}$$

$$\mathcal{E}_{ii}^{(m_i,m_i)} = \log\frac{s}{Q^2} - \frac{1}{\beta_i}\frac{1+\beta_i}{1-\beta_i}, \tag{B.3.9}$$

with β as in eq. (B.3.7).

- $m_i \neq 0, m_j \neq 0, i \neq j$

$$\hat{\mathcal{E}}_{ij}^{(m_i,m_j)} = \mathcal{N}(\varepsilon)\left(-\frac{1}{2\varepsilon}\frac{1}{v_{ij}}\log\frac{1+v_{ij}}{1-v_{kl}}\right), \tag{B.3.10}$$

$$\mathcal{E}_{ij}^{(m_i,m_j)} = \frac{1}{2v_{ij}}\log\frac{1+v_{ij}}{1-v_{ij}}\log\frac{s}{Q^2} + \frac{(1+v_{ij})(k_i\cdot k_j)^2}{2m_i^2}\left(J(\alpha_{ij}E_i, \alpha_{ij}\beta_i E_i) - J(E_j, \beta_j E_j)\right), \tag{B.3.11}$$

with β as in eq. (B.3.7). The function J is defined as

$$J(x,y) = \frac{1}{2\lambda\nu}\left[\log^2\frac{x-y}{x+y} + 4\mathrm{Li}_2\left(1-\frac{x+y}{\nu}\right) + 4\mathrm{Li}_2\left(1-\frac{x-y}{\nu}\right)\right]. \tag{B.3.12}$$

The other parameters are given by

$$v_{ij} = \sqrt{1-\left(\frac{m_i m_j}{k_i\cdot k_j}\right)^2}, \tag{B.3.13}$$

$$\alpha_{ij} = \frac{1+v_{ij}}{m_i^2}k_i\cdot k_j, \tag{B.3.14}$$

$$\lambda = \alpha_{ij}E_i - E_j, \tag{B.3.15}$$

$$\nu = \frac{\alpha_{ij}^2 m_i^2 - m_j^2}{2\lambda}. \tag{B.3.16}$$

B.3.2. Collinear integrals

The integral of the collinear splittings with an ab final state, as encountered in eq. (2.3.18), is given by,

$$I_{ab} = \int_0^1 dz z^{-2\varepsilon}(1-z)^{-2\varepsilon}\langle\hat{P}_{ab}\rangle(z,\varepsilon). \tag{B.3.17}$$

Here, space-averaged Altarelli-Parisi splitting functions are used. They are obtained by using the collinear parameterization in eq. (2.1.2). E.g. for the $g \to q\bar{q}$-splitting in eq. (2.1.7), we obtain

$$\langle\hat{P}_{q\bar{q}}\rangle(z,\varepsilon) = \frac{T_F}{d-2}\left(-g_{\mu\nu} + \frac{p_\mu n_\nu + p_\nu n_\mu}{p\cdot n}\right)\left(-g^{\mu\nu} + 4z(1-z)\frac{k_\perp^\mu k_\perp^\nu}{k_\perp^2}\right), \tag{B.3.18}$$

which, using $n\cdot k_\perp = 0$ and $d = 4-2\varepsilon$ yields

$$\langle\hat{P}_{q\bar{q}}\rangle(z,\varepsilon) = \frac{T_F}{2-2\varepsilon}(2-2\varepsilon-4z(1-z)). \tag{B.3.19}$$

In total, all $\langle \hat{P}_{ab} \rangle(z, \varepsilon)$ are given by

$$\langle \hat{P}_{qg} \rangle(z, \varepsilon) = C_F \left(\frac{1+z^2}{1-z} - \varepsilon(1-z) \right), \tag{B.3.20}$$

$$\langle \hat{P}_{q\bar{q}} \rangle(z, \varepsilon) = T_F \frac{(1-z)^2 + z^2 - \varepsilon}{1-\varepsilon}, \tag{B.3.21}$$

$$\langle \hat{P}_{gg} \rangle(z, \varepsilon) = 2C_A \left(\frac{z}{1-z} + \frac{1-z}{z} + z(1-z) \right). \tag{B.3.22}$$

Inserting them into eq. (B.3.17) leads to the results [61]

$$I_{gg} = -\frac{1}{\varepsilon} C_A - \frac{11}{6} C_A - \varepsilon \left(\frac{67}{9} - \frac{2\pi^2}{3} \right), \tag{B.3.23}$$

$$I_{qg} = -\frac{1}{\varepsilon} C_F - \frac{3}{2} C_F - \varepsilon \left(\frac{13}{2} - \frac{2\pi^2}{3} \right), \tag{B.3.24}$$

$$I_{qq} = \frac{2}{3} T_F + \varepsilon \frac{23}{9} T_F. \tag{B.3.25}$$

C. The BLHA interface in WHIZARD

Below is an example of a BLHA [75, 76] contract file (or `.olc`–file) for the process $e^+e^- \to t\bar{t}$ with polarized electron beams. It is produced by the one-loop provider by reading in the `.olp`–file, which is generated automatically by WHIZARD. The `.olp`– and `.olc`–file differ only in the additional `OK` and index tags, which indicate that the OLP has successfully linked the given process to a library and has given it the specified internal index.

```
 # BLHA order written by WHIZARD 2.4.2
 # BLHA interface mode: OpenLoops
 # process: openloops_2_p1_LOOP
 # model: SM
InterfaceVersion          BLHA2       | Ok
CorrectionType            QCD       | OK
Extra AnswerFile          openloops_2_p1_LOOP.olc       | OK
IRregularisation          CDR       | OK
CouplingPower QCD         0      | OK
CouplingPower QED         2      | OK
extra use_cms             1       | OK
extra me_cache            0       | OK
extra psp_tolerance       10e-7       | OK
 # Process definitions
AmplitudeType             Loop       | OK
 11(-1) -11(-1) ->   6  -6 | 1    1
AmplitudeType             Loop       | OK
 11(-1) -11(1)  ->   6  -6 | 1    2
AmplitudeType             Loop       | OK
 11(1)  -11(-1) ->   6  -6 | 1    3
AmplitudeType             Loop       | OK
 11(1)  -11(1)  ->   6  -6 | 1    4
AmplitudeType             ccTree       | OK
 11(-1) -11(-1) ->   6  -6 | 1    5
AmplitudeType             ccTree       | OK
 11(-1) -11(1)  ->   6  -6 | 1    6
AmplitudeType             ccTree       | OK
 11(1)  -11(-1) ->   6  -6 | 1    7
AmplitudeType             ccTree       | OK
 11(1)  -11(1)  ->   6  -6 | 1    8
```

The contract file consists of two major blocks. The first one gives general informations like the powers of α_e and α_s at leading order or the employed IR regularization scheme. Entries starting with `extra` are special to OpenLoops and allow to interface additional settings into the program. For example, `extra use_cms 1` switches on the complex mass scheme in OpenLoops. Processes are registered in the second major block using first the `AmplitudeType` specifier, which can be either `Tree`, `Loop`, `ccTree` or `scTree`, followed by the explicit flavor content. These tags correspond to a tree-level, loop, color- or spin-correlated matrix element, respectively. In the given example, the helicity-aware extension of OpenLoops is used in which polarized beams can be accessed by specifying the helicity index values $(-1, 0, 1)$ behind the flavor index. Here, we have one entry for each combination of initial-state electron helicities. After the process definition, the first number signals that the loading of the library was successful by the tag 1. The second number is the OLP-internal index of the process to be used in the `EvalSubProcess2`-call. Here, the internal index is identical with its position in the contract file. However, the indices can occur in an arbitrary order.

Note on a software development issue The creation of quantum numbers from the processes specified in Sindarin at the time of writing requires the O'Mega–libraries have to be linked to Whizard even when all matrix element are computed by external matrix element providers. For example, a real-subtraction component requires PDG arrays of all real flavor structures to set up the region data. Thereby, it also manipulates these flavor structures by performing permutations suitable for the combinatorics of the process. Therefore, the flavor strings written into the `.olp`–file are not necessarily identical to the ones produced by O'Mega. Yet, an exact agreement is relevant in order to avoid mismatches between the phase-space and the flavor definitions. Moreover, a lot of overhead code is generated, whose compilation can take up a significant amount of time for complicated processes. In a possible refactoring of Whizard and O'Mega, the two tasks performed by O'Mega– quantum number generation and matrix element computation – should be separated from each other. In a setup that only uses third-party matrix element providers, only the first functionality would be used.

D. The top quark width at NLO QCD

The following is the analytic expression for the top-quark width with massive b-quarks originally given in ref. [129]. Defining $\xi = m_t^2/m_W^2$ and $\varepsilon = m_b/m_t$, it is

$$\Gamma = \frac{G_F m_t^2}{16\sqrt{2}\pi}\left[\mathcal{F}_0\left(\varepsilon, \xi^{-1/2}\right) - \frac{2\alpha_s}{3\pi}\mathcal{F}_1\left(\varepsilon, \xi^{-1/2}\right)\right]. \tag{D.0.1}$$

The leading-corder contribution is

$$\mathcal{F}_0(\varepsilon, w^2) = \frac{\sqrt{\lambda(\varepsilon, w^2)}}{2} f_0(\varepsilon, w^2) \tag{D.0.2}$$

with

$$f_0(\varepsilon, w^2) = 4\left[(1-\varepsilon^2)^2 + w^2(1+\varepsilon^2) - 2w^4\right] \tag{D.0.3}$$

and

$$\lambda(\varepsilon, w^2) = 1 + w^4 + \varepsilon^4 - 2(w^2 + \varepsilon^2 + w^2\varepsilon^2). \tag{D.0.4}$$

Note that the auxilliary variable w^2 equals $\xi^{-1/2}$ as in eq. (D.0.1). Further, using the definitions

$$u_q = \frac{1 + \varepsilon^2 - w^2 - \lambda^{1/2}}{1 + \varepsilon^2 - w^2 + \lambda^{1/2}} \tag{D.0.5}$$

and

$$u_w = \frac{1 - \varepsilon^2 + w^2 - \lambda^{1/2}}{1 - \varepsilon^2 + w^2 + \lambda^{1/2}}, \tag{D.0.6}$$

the pure next-to-leading-order contribution to eq. (D.0.1) is given by

$$\begin{aligned}\mathcal{F}_1 = \frac{1}{2} f_0 \cdot (1+\varepsilon^2-w^2)\Big\{ & \pi^2 + 2\mathrm{Li}_2(u_w) - 2\mathrm{Li}_2(1-u_w) - 4\mathrm{Li}_2(u_q) \\ & - 4\mathrm{Li}_2(u_q u_w) + \log\left(\frac{1-u_q}{w^2}\right)\log(1-u_q) - \log^2(1-u_q u_w) \\ & + \frac{1}{4}\log^2\left(\frac{w^2}{u_w}\right) - \log(u_w)\log\left[\frac{(1-u_q u_w)^2}{1-u_q}\right] \\ & - 2\log(u_q)\log\left[(1-u_q)(1-u_q u_w)\right]\Big\} \\ & - \sqrt{\lambda} f_0 \cdot (2\log(w) + 3\log(\varepsilon) - 2\log(\lambda)) \\ & + 4(1-\varepsilon^2)\left[(1-\varepsilon^2)^2 + w^2(1+\varepsilon^2) - 4w^4\right]\log(u_w) \\ & + \left[(3-\varepsilon^2+11\varepsilon^4-\varepsilon^6) + w^2(6-12\varepsilon^2+2\varepsilon^4) - w^4(21+5\varepsilon^2) + 12w^6\right]\log(u_q) \\ & + 6\sqrt{\lambda}(1-\varepsilon^2)(1+\varepsilon^2-w^2)\log(\varepsilon) \\ & + \sqrt{\lambda}\left[-5+22\varepsilon^2-5\varepsilon^4-9w^2(1+\varepsilon^2)+6w^4\right].\end{aligned} \tag{D.0.7}$$

Note that we have omitted the functional dependence of f_0 and λ on w^2 and ε for ease of notation. The above formula was checked against the numerical WHIZARD results as discussed in section 4.1 where we find an agreement with the numbers $\Gamma_t^{\text{whizard}} = 1.4078768(615)\,\text{GeV}$ and $\Gamma_t^{\text{analytical}} = 1.40787091\,\text{GeV}$. The input parameters used for this comparison are given below. Top and bottom quarks are massive,

$$m_b = 4.2\,\text{GeV}, \quad m_t = 172.0\,\text{GeV}. \tag{D.0.8}$$

Further, their width, as well as the W-boson width are set to zero. We use $m_W = 80.419\,\text{GeV}$, $m_Z = 91.188\,\text{GeV}$ and $\alpha_e^{-1} = 125.924$, from which G_F and the electroweak mixing angles are computed. The renormalization scale in the NLO part of the calculation is set to the top mass.

E. The Powheg veto procedure

We outline the POWHEG veto algorithm briefly addressed in section 4.5. To avoid the direct evaluation of the integral in the exponent of eq. (4.5.3), the corresponding p_T–distribution is produced by a reweighting procedure instead.

E.1. The algorithm

The probability distribution as a function of the FKS variables ξ, y (and ϕ, which is irrelevant here) we want to sample is

$$P(\xi, y) = \frac{R(\xi, y)}{B} \exp\left[- \int d\Phi'_{\text{rad}} \frac{R(\xi', y')}{B} \theta(k_T(\xi', y') - p_T) \right], \tag{E.1.1}$$

where k_T is a function parameterizing the transverse momentum of the radiation. The transverse momentum p_T is the value which is generated by the algorithm. In the full event generation, it is used to construct the real-emission event and also enters the subsequent vetoed parton shower. For this reason, it is advisable to transform eq. (E.1.1) into an expression with explicit p_T–dependence, i.e. we want to trade y for p_T. To do so, we can make use of an identity for variable transformations in probability densities. For a random variable x with distribution $f(x)$, and another variable $y = g(x)$, the probability density $\tilde{f}(y)$ is given by

$$\tilde{f}(y) = \int dx f(x) \delta(y - g(x)). \tag{E.1.2}$$

With this identity, eq. (E.1.1) can be rewritten to, using $\hat{R} = R/B$,

$$\begin{aligned} P(\xi, p_T) &= \int d\Phi_{\text{rad}} \delta(p_T - k_T(\xi, y)) \hat{R}(\xi, y) e^{-\int d\Phi'_{\text{rad}} \hat{R}(\xi', y') \theta(k_T(\xi', y') - p_T)} \\ &= \frac{d}{dp_T} e^{-\int d\Phi'_{\text{rad}} \hat{R}(\xi', y') \theta(k_T(\xi', y') - p_T)} = \frac{d}{dp_T} \Delta(p_T). \end{aligned} \tag{E.1.3}$$

The last line emphasizes that $P(\xi, p_T)$ is uniform in $\Delta(p_T)$. Therefore, the correct p_T–distribution according to eq. (E.1.1) can be reproduced by solving $\Delta(p_T) = r$ for p_T with a random number $r \in [0, 1]$. Solving this equation nevertheless requires the evaluation

of the integral in the exponent. To facilitate the generation of p_T, an upper bounding function (UBF) is introduced which is analytically easy to integrate and fulfills the condition

$$\frac{\mathcal{J}(\Phi_{n+1})R(\Phi_{n+1})}{B(\Phi_n)} \leq NU(\xi, y). \tag{E.1.4}$$

For an explanation of the normalization N, cf. section 4.5. Explicit examples of UBFs are discussed in the next section. The Sudakov factor where the expression on the left-hand side of eq. (E.1.4) is replaced by its right-hand side is denoted by $\Delta^U(p_T)$.

The veto algorithm, a graphical representation of which is given in fig. E.1, proceeds as follows. First, p_T is generated uniformly in the interval $[p_T, p_T^{\max}]$, i.e. the equation

$$\frac{\Delta^U(p_T)}{\Delta^U(p_T^{\max})} = r \tag{E.1.5}$$

is solved for p_T. The denominator ensures that p_T is only generated in the interval $[0, p_T^{\max}]$. If the obtained value is below the lower bound $p_T^{\min}$, the radiation is vetoed and a Born event is generated (note that the Born kinematics are already present at this point). Else, real kinematics are created. To undo the upper estimate of eq. (E.1.4), a second veto is performed using a second random number $r' \in [0, 1]$. The real-emission event is accepted if $r' < \mathcal{J}RB/(NU)$, otherwise the upper bound $p_T^{\max}$ is set to the value of p_T generated in this iteration. The vetoes are repeated until either p_T falls below $p_T^{\min}$ or the UBF-veto is passed.

E.2. Upper bounding functions

In most applications, the logarithm is taken on both sides of eq. (E.1.5) to avoid the exponential function of the standard expression for the UBF in eq. (E.1.4). This gives the integral

$$-\log \Delta^{\mathrm{U}}(p_T) = -\int d\xi dy d\phi U(\xi, y)\theta\left(k_T - p_T\right). \tag{E.2.1}$$

The explicit form of $U(\xi, y)$ differs between FSR and ISR regions. First, because divergences arise differently and this has to be represented in the UBF. Second, different parametirzations of k_T^2 in terms of y have to be employed for initial- and final-state emissions. Here, we give examples for ISR and FSR UBFs. In the latter case, we distinguish between massless and massive emitters. Further, since in QED the running of α_{em} is usually neglected, we consider the case of a non-running coupling constant, which leads to a simpler UBF which can be used for photon emissions.

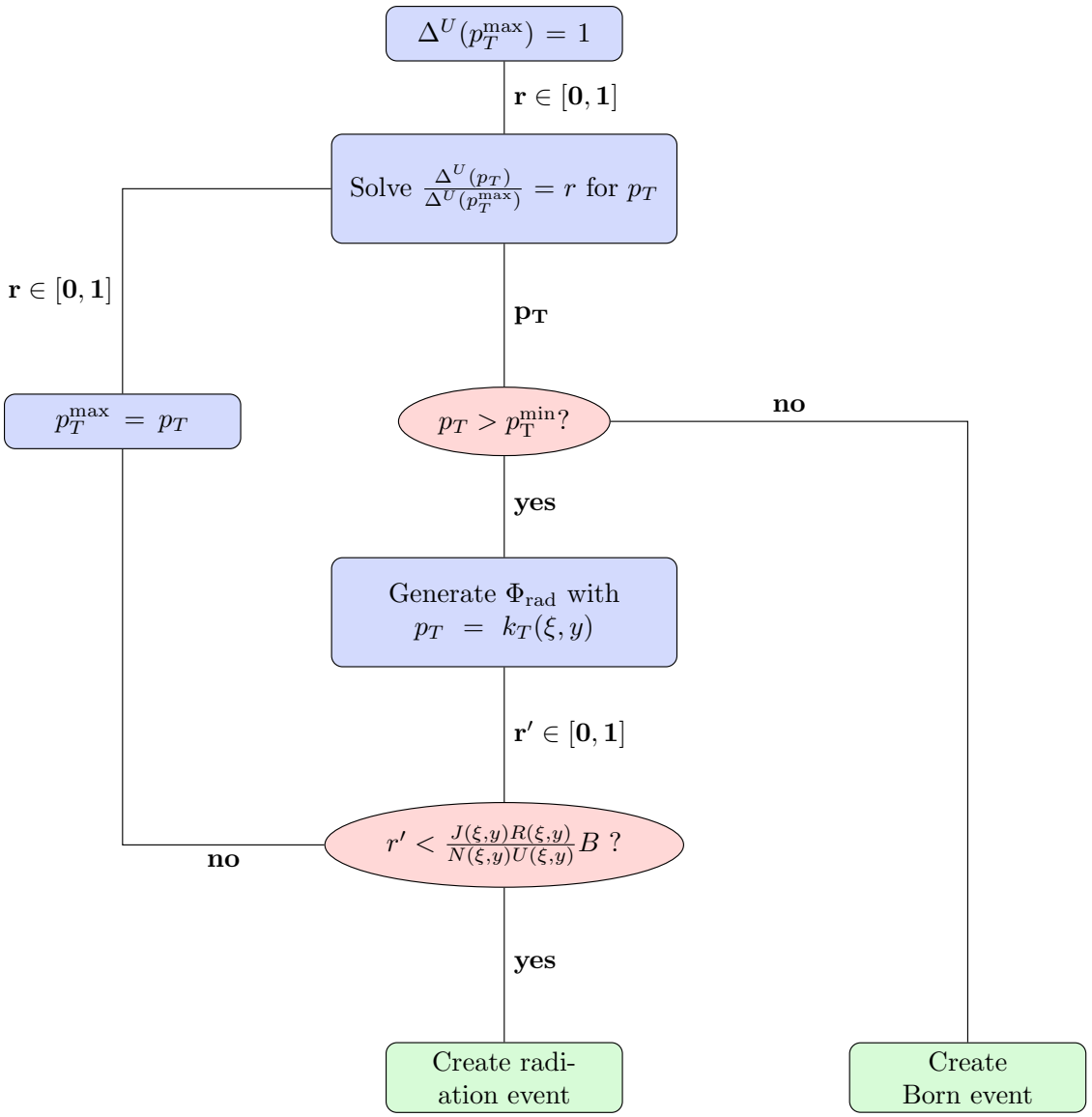

Figure E.1. Outline of the POWHEG veto procedure

E.2.1. Final-state emissions – massless emitters

The standard upper bounding function for FSR is given by

$$U(\xi, y) = N \frac{\alpha_s(k_T^2)}{\xi(1-y)}. \tag{E.2.2}$$

The strong coupling in the numerator is essential for an effective sampling of the real matrix element. It depends on k_T^2,

$$\alpha_s(k_T^2) = \frac{1}{b_0 \log\left(k_T^2/\Lambda^2\right)}. \tag{E.2.3}$$

We therefore trade y for k_T^2 in eq. (E.2.1), using the parameterization

$$k_T^2 = \frac{s}{2}\xi^2(1-y). \tag{E.2.4}$$

Note that this is not necessarily the correct kinematical relation between y and k_T^2, which is not a problem as long as the singular behavior is the same. With this definitions, we find from eq. (E.2.1)

$$\begin{aligned} -\log \Delta^{\mathrm{U}}(p_T) &= 2\pi N \int_0^{\xi_{\max}} \frac{d\xi}{\xi} \int_{p_T^2}^{\xi^2 s} \frac{dk_T^2}{k_T^2} \alpha_s(k_T^2) \\ &= \frac{\pi N}{b_0} \theta\left(\xi_{\max}^2 - \frac{p_T^2}{s}\right) \left[\log \frac{\xi_{\max}^2 s}{\Lambda^2} \log \frac{\log(\xi_{\max}^2 s/\Lambda^2)}{\log(p_T^2/\Lambda^2)} - \log \frac{\xi_{\max}^2 s}{p_T^2}\right]. \end{aligned} \tag{E.2.5}$$

Here, we have inserted the kinematical bound for ξ as upper integration bound of the integration [1].

The integrated UBF takes a much simpler form if no running coupling is considered in eq. (E.2.2), e.g. for photon emissions, where α_e can be assumed to be constant. In this case, we find

$$-\log \Delta^{\mathrm{U}}_{\mathrm{QED}}(p_T) = \frac{\pi}{2} \alpha_e N \theta\left(\xi_{\max}^2 - \frac{p_T^2}{s}\right) \log^2\left(\frac{\xi_{\max}^2 s}{p_T^2}\right). \tag{E.2.6}$$

E.2.2. Final-state emissions – massive emitters

The upper bounding function for emissions from massive partons is more involved. It has been discussed for the first time in ref. [60], where it is derived from eikonal approx-

[1] Due to eq. (E.2.3), the reference scale Λ appears in eq. (E.2.5). WHIZARD commonly evolves α_s from M_Z, so Λ is not obtainable from the model setup. Instead, it is obtained by first computing $\alpha_s(p_{\mathrm{T}}^{\min})$ as usual and then solving eq. (E.2.3) for Λ.

imations to the real amplitude. It is

$$U_{\text{massive}}(\xi, y) = \frac{\sqrt{s}}{\bar{p}_{\text{em}}} \frac{1}{\xi(1-z)}, \tag{E.2.7}$$

using the notation of section A.1.3, i.e. $\bar{p}_{\text{em}}$ is the emitter momentum in the Born phase space and z is as defined in the context of Dalitz plot variables in the generation of FSR from massive emitters, cf. eq. (A.1.11). Note that there is no strong coupling in this choice of Δ^{U}. Integrating eq. (E.2.1) with this UBF, using $t = p_T^2$, gives

$$\begin{aligned} -\log \Delta^{\text{U}}(t) = \frac{\sqrt{s}}{\bar{p}_{\text{em}}} \Bigg[& \log \xi \cdot \log \left[(1-z_2) \frac{\sqrt{s}}{t} \right] + \frac{1}{2} \log^2 \xi \\ & + G(-t, q^2, \xi) - G(2\bar{p}_{\text{em}}^2, -\sqrt{s}, \xi) \Bigg]_{\xi_{\min}}^{\min(\xi_1(t), \xi_{\max})} \\ & + \frac{\sqrt{s}}{\bar{p}_{\text{em}}} \theta(\xi_{\max} - \xi_1(t)) \log \frac{\xi_{\max}}{\xi_1(t)} \log \frac{1-z_2}{1-z_1}. \end{aligned} \tag{E.2.8}$$

The Dalitz variables z_1 and z_2 are as defined in eq. (A.1.12). $\xi_{\min}$ is the minimal value of ξ compatible with the given scale t,

$$\xi_{\min}(t) = \frac{\sqrt{t\left(t z_2^2 + 8 \bar{p}_{\text{em}}^0 \sqrt{s}(1-z_2)\right)} - t z_2}{2s(1-z_1)}. \tag{E.2.9}$$

Moreover, $\xi_1(t) = \xi_{\min}(t)$ with $z_2 = z_1$ and

$$\begin{aligned} G(a, b, \xi) &= \log(a + b\xi) \log \left(1 - \frac{a + b\xi}{a} \right) + \text{Li}_2 \left(\frac{a + b\xi}{a} \right) \quad \text{for} a < 0, \\ G(a, b, \xi) &= \log \left| \frac{b\xi}{a} \right| \log a - \text{Li}_2 \left(-\frac{b\xi}{a} \right) + \frac{\pi^2}{6} \quad \text{for} a > 0, \end{aligned} \tag{E.2.10}$$

which is the antiderivative of $\log(a + b\xi)/\xi$.

E.2.3. Initial-state emissions

The simplest UBF for initial-state radiation is the same as in eq. (E.2.2), but taking into account the additional collinear limit $y \to -1$,

$$U(\xi, y) = N \frac{\alpha_s(k_T^2)}{\xi(1-y^2)}, \tag{E.2.11}$$

with the corresponding parameterization of the radiation hardness

$$k_T^2 = \frac{s}{4(1-\xi)} \xi^2 (1-y^2). \tag{E.2.12}$$

Note that in contrast to eq. (E.2.4), the CMS energy which actually enters the hard interaction has to be used.

Performing the integration of the UBF yields [44, 210]

$$\begin{aligned}
-\log\Delta^U(p_T) = \theta(s-p_T^2)\frac{\pi N}{b_0}\Bigg\{&\theta(k_{T,\max}^2-s)\Big[\log\frac{2s}{\Lambda^2}\log\frac{\log(s/\Lambda^2)}{\log(p_T^2/\Lambda^2)}-\log\frac{s}{p_T^2}\\
&+\log(2)\log\frac{\log(k_{T,\max}^2)}{\log(s/\Lambda^2)}\Big]\\
&+\theta(s-k_{T,\max}^2)\left[\log\frac{2s}{\Lambda^2}\log\frac{\log(k_{T,\max}^2/\Lambda^2)}{\log(p_T^2/\Lambda^2)}-\log\frac{k_{T,\max}^2}{p_T^2}\right]\Bigg\}\\
&+\theta(p_T^2-s)\frac{\pi N}{b_0}\log(2)\log\frac{\log(k_{T,\max}^2/\Lambda^2)}{\log(p_T^2/\Lambda^2)}.
\end{aligned} \tag{E.2.13}$$

Again, most of the complexity arises from the running of the strong coupling. For a fixed electroweak coupling, we find [9]

$$\begin{aligned}
-\log\Delta^U_{\mathrm{QED}}(p_T) = \pi\alpha_e N\Bigg[&2\theta(p_T^2-s)\log(2)\log\frac{k_{T,\max}^2}{p_T^2}\\
&+\theta(s-k_{T,\max}^2)\theta(s-p_T^2)\left(\log^2\frac{2s}{p_T^2}-\log^2\frac{2s}{k_{T,\max}^2}\right)\\
&+\theta(s-p_T^2)\theta(k_{T,\max}^2-s)\left(\log^2\frac{2s}{p_T^2}-\log^2(2)+2\log(2)\log\frac{k_{T,\max}^2}{s}\right)\Bigg].
\end{aligned} \tag{E.2.14}$$

F. Technical details of the top-quark threshold matching

F.1. Relation between the top-quark pole mass and M_t^{1S}

The top-quark pole mass m_t and the resonance mass M_t^{1S} are related via

$$m_t = M_t^{1S}\left[1 + \Delta M(\sqrt{s}, \alpha_s)\right]. \tag{F.1.1}$$

The shift $\Delta M_{(\mathrm{N})\mathrm{LL}}$ is given by

$$\begin{aligned} \Delta M_{\mathrm{LL}} &= \frac{(C_F\alpha_{\mathrm{S}})^2}{8}, \\ \Delta M_{\mathrm{NLL}} &= \Delta M_{\mathrm{LL}} + \frac{(C_F\alpha_{\mathrm{S}})^3}{8\pi C_F}\left\{B_0 \cdot \left(1 + \log\frac{hf\nu_*}{C_F\alpha_{\mathrm{S}}}\right) + \frac{A_1}{2}\right\} \end{aligned} \tag{F.1.2}$$

where

$$B_0 = \frac{11C_A - 2N_F}{3}, \tag{F.1.3}$$

$$A_1 = \frac{31}{9}C_A - \frac{20}{9}T_R \cdot N_F. \tag{F.1.4}$$

The factors h and f are scale factors which we are not interested in this work so we can assume $h = f = 1$. The velocity ν_* is mostly identically to v in eq. (B.3.13), but evaluated at M_t^{1S} instead of m_t and shifted by 0.05 [194],

$$\nu_*(\sqrt{s}) = 0.05 + \left|\sqrt{\frac{\sqrt{s} - 2M_t^{1S} + i\Gamma_t(M_t^{1S})}{M_t^{1S}}}\right|. \tag{F.1.5}$$

F.2. On-shell projection

The on-shell projection performed to keep gauge invariance in section 6.2 assumes that the reconstructed top momenta can be written as

$$\hat{p}_t = \frac{1}{2}\left(\sqrt{s}, \beta \cdot \mathbf{e}_t\right), \tag{F.2.1}$$

where $\mathbf{e}_t = \mathbf{p}_t/|\mathbf{p}_t|$ is a unit vector parallel to the top momentum in the original phase space. This way, the projection transitions smoothly into the case where the momenta are already on-shell and also maintain spatial correlations, e.g. the forward-backward asymmetry. The scale factor β is above the threshold, i.e. for $\sqrt{s} > 2m_t$, given by the mass-shell relation as $\beta = \sqrt{s - 4m_t^2}$. In the full process $e^+e^- \to bW^+\bar{b}W^-$, the top-quark invariant mass can fall below $2m_t$, so that this choice is not possible. Here, the top quark is essentially at rest. Therefore, below threshold for $\sqrt{<}2m_t$, the scale factor is set to an arbitrary small number ε. Setting $\varepsilon = 0$ leads to numerical instabilities in the matrix elements, so in WHIZARD we choose $\varepsilon = 10^{-10}$.

The bottom and W momenta can be constructed in the rest frame according to

$$|\hat{\mathbf{p}}_W| = |\hat{\mathbf{p}}_b| = \frac{\lambda^{1/2}(m_t^2, m_W^2, m_b^2)}{2m_t}, \tag{F.2.2}$$

and

$$E_W = \frac{m_t^2 + m_W^2 - m_b^2}{2m_t}, \quad E_b = \frac{m_t^2 - m_W^2 + m_b^2}{2m_t}, \tag{F.2.3}$$

which are identical for each event. The reference direction is chosen to be given by the W-boson momentum in the non-projected phase space, so that $\hat{\mathbf{p}}_W = |\hat{\mathbf{p}}_W| \cdot \mathbf{e}_W$, which also fixes the bottom-quark momentum. The final-state momenta can then be straightforwardly boosted into the lab frame, which concludes the on-shell projection.

Bibliography

[1] J. Reuter, B. Chokoufe Nejad, and C. Weiss. "NLO QCD Corrections to Off-shell $t\,\bar{t}$ and $t\,\bar{t}\,H$ at the ILC". *International Workshop on Future Linear Colliders 2016 (LCWS2016) Morioka, Iwate, Japan, December 5-9, 2016*. 2017. [1703.05791].

[2] B. Chokouf Nejad, W. Kilian, J. M. Lindert, et al. *NLO QCD predictions for off-shell $t\bar{t}$ and $t\bar{t}H$ production and decay at a linear collider*. JHEP, **12** (2016), p. 075. [1609.03390].

[3] J. Reuter, F. Bach, B. Chokoufe Nejad, et al. "Top Physics in WHIZARD". *Proceedings, International Workshop on Future Linear Colliders (LCWS15): Whistler, B.C., Canada, November 02-06, 2015*. 2016. [1602.08035].

[4] J. Reuter, B. Chokoufe, A. Hoang, et al. *Automation of NLO processes and decays and POWHEG matching in WHIZARD*. J. Phys. Conf. Ser., **762**.1 (2016), p. 012059. [1602.06270].

[5] J. Reuter, F. Bach, B. Chokoufe Nejad, et al. *QCD NLO with Powheg matching and top threshold matching in WHIZARD*. PoS, **RADCOR2015** (2015), p. 088. [1601.02459].

[6] B. Chokoufe Nejad, W. Kilian, J. Reuter, and C. Weiss. *Matching NLO QCD Corrections in WHIZARD with the POWHEG scheme*. PoS, **EPS-HEP2015** (2015), p. 317. [1510.02739].

[7] C. Weiss, B. C. Nejad, W. Kilian, and J. Reuter. *Automated NLO QCD Corrections with WHIZARD*. PoS(EPS-HEP2015)466, **466**.July 2015 (2015), p. 9. [1510.02666].

[8] J. Reuter, F. Bach, B. Chokoufe, et al. *Modern Particle Physics Event Generation with WHIZARD*. J. Phys. Conf. Ser., **608**.1 (2015), p. 012063. [1410.4505].

[9] C. Weiss. Electroweak Corrections in the POWHEG BOX. MA thesis. RWTH Aachen University, 2013.

[10] W. E. Lamb and R. C. Retherford. *Fine Structure of the Hydrogen Atom by a Microwave Method*. Phys. Rev., **72** (1947), pp. 241–243.

[11] H. A. Bethe. *The Electromagnetic shift of energy levels*. Phys. Rev., **72** (1947), pp. 339–341.

[12] J. S. Schwinger. *On Quantum electrodynamics and the magnetic moment of the electron.* Phys. Rev., **73** (1948), pp. 416–417.

[13] P. Kusch and H. M. Foley. *The Magnetic Moment of the Electron.* Phys. Rev., **74**.3 (1948), p. 250.

[14] R. K. Ellis, W. J. Stirling, and B. R. Webber. *QCD and collider physics.* Camb. Monogr. Part. Phys. Nucl. Phys. Cosmol., **8** (1996), pp. 1–435.

[15] T. Aaltonen et al. *Forward-Backward Asymmetry in Top Quark Production in $p\bar{p}$ Collisions at $\sqrt{s} = 1.96$ TeV.* Phys. Rev. Lett., **101** (2008), p. 202001. [0806.2472].

[16] T. Aaltonen et al. *Evidence for a Mass Dependent Forward-Backward Asymmetry in Top Quark Pair Production.* Phys. Rev., **D83** (2011), p. 112003. [1101.0034].

[17] V. M. Abazov et al. *Forward-backward asymmetry in top quark-antiquark production.* Phys. Rev., **D84** (2011), p. 112005. [1107.4995].

[18] M. Czakon, P. Fiedler, and A. Mitov. *Resolving the Tevatron Top Quark Forward-Backward Asymmetry Puzzle: Fully Differential Next-to-Next-to-Leading-Order Calculation.* Phys. Rev. Lett., **115**.5 (2015), p. 052001. [1411.3007].

[19] W. Hollik and D. Pagani. *The electroweak contribution to the top quark forward-backward asymmetry at the Tevatron.* Phys. Rev., **D84** (2011), p. 093003. [1107.2606].

[20] G. 't Hooft and M. J. G. Veltman. *Regularization and Renormalization of Gauge Fields.* Nucl. Phys., **B44** (1972), pp. 189–213.

[21] F. Bloch and A. Nordsieck. *Note on the Radiation Field of the electron.* Phys. Rev., **52** (1937), pp. 54–59.

[22] D. R. Yennie, S. C. Frautschi, and H. Suura. *The infrared divergence phenomena and high-energy processes.* Annals Phys., **13** (1961), pp. 379–452.

[23] T. Kinoshita. *Mass singularities of Feynman amplitudes.* J. Math. Phys., **3** (1962), pp. 650–677.

[24] T. D. Lee and M. Nauenberg. *Degenerate Systems and Mass Singularities.* Phys. Rev., **133** (1964). [,25(1964)], B1549–B1562.

[25] A. Kanaki and C. G. Papadopoulos. *HELAC: A Package to compute electroweak helicity amplitudes.* Comput. Phys. Commun., **132** (2000), pp. 306–315. [hep-ph/0002082].

[26] V. Hirschi, R. Frederix, S. Frixione, et al. *Automation of one-loop QCD corrections.* JHEP, **05** (2011), p. 044. [1103.0621].

[27] J. Alwall, M. Herquet, F. Maltoni, O. Mattelaer, and T. Stelzer. *MadGraph 5 : Going Beyond.* JHEP, **06** (2011), p. 128. [1106.0522].

[28] J. M. Campbell, R. K. Ellis, and W. T. Giele. *A Multi-Threaded Version of MCFM.* Eur. Phys. J., **C75**.6 (2015), p. 246. [1503.06182].

[29] R. Boughezal, J. M. Campbell, R. K. Ellis, et al. *Color singlet production at NNLO in MCFM.* Eur. Phys. J., **C77**.1 (2017), p. 7. [1605.08011].

[30] T Gleisberg, S Höche, F Krauss, et al. *Event generation with SHERPA 1.1.* Journal of High Energy Physics, **2009**.02 (2009), pp. 007–007. [0811.4622].

[31] K. Arnold et al. *VBFNLO: A Parton level Monte Carlo for processes with electroweak bosons.* Comput. Phys. Commun., **180** (2009), pp. 1661–1670. [0811.4559].

[32] W. Kilian, T. Ohl, and J. Reuter. *WHIZARD - simulating multi-particle processes at LHC and ILC.* The European Physical Journal C, **71**.9 (2011), p. 1742. [0708.4233].

[33] T. Sjostrand, S. Mrenna, and P. Z. Skands. *PYTHIA 6.4 Physics and Manual.* JHEP, **05** (2006), p. 026. [hep-ph/0603175].

[34] T. Sjostrand, S. Mrenna, and P. Z. Skands. *A Brief Introduction to PYTHIA 8.1.* Comput. Phys. Commun., **178** (2008), pp. 852–867. [0710.3820].

[35] J. Bellm, S. Gieseke, D. Grellscheid, et al. *Herwig 7.0 / Herwig++ 3.0 Release Note* (2015). [1512.01178].

[36] M. Bahr et al. *Herwig++ Physics and Manual.* Eur. Phys. J., **C58** (2008), pp. 639–707. [0803.0883].

[37] S. Frixione, F. Stoeckli, P. Torrielli, and B. R. Webber. *NLO QCD corrections in Herwig++ with MC@NLO.* JHEP, **01** (2011), p. 053. [1010.0568].

[38] S. Catani and M. Seymour. *A general algorithm for calculating jet cross sections in NLO QCD.* Nuclear Physics B, **485**.1-2 (1997), pp. 291–419. [9605323].

[39] S. Frixione, Z. Kunszt, and A. Signer. *Three-jet cross sections to next-to-leading order.* Nuclear Physics B, **467**.3 (1996), pp. 399–442. [9512328].

[40] R. Frederix, S. Frixione, F. Maltoni, and T. Stelzer. *Automation of next-to-leading order computations in QCD: the FKS subtraction.* Journal of High Energy Physics, **2009**.10 (2009), pp. 003–003. [0908.4272].

[41] S. Frixione and B. R. Webber. *Matching NLO QCD computations and parton shower simulations.* JHEP, **06** (2002), p. 029. [hep-ph/0204244].

[42] S. Frixione, P. Nason, and B. R. Webber. *Matching NLO QCD and parton showers in heavy flavor production.* JHEP, **08** (2003), p. 007. [hep-ph/0305252].

[43] P. Nason. *A New Method for Combining NLO QCD with Shower Monte Carlo Algorithms.* Journal of High Energy Physics, **2004**.11 (2004), pp. 040–040. [hep-ph/0409146].

[44] S. Alioli, P. Nason, C. Oleari, and E. Re. *A general framework for implementing NLO calculations in shower Monte Carlo programs: the POWHEG BOX*. JHEP, **06** (2010), p. 043. [1002.2581].

[45] H. Baer, T. Barklow, K. Fujii, et al. *The International Linear Collider Technical Design Report - Volume 2: Physics* (2013). [1306.6352].

[46] H. Abramowicz et al. *The International Linear Collider Technical Design Report - Volume 4: Detectors* (2013). Ed. by T. Behnke, J. E. Brau, P. N. Burrows, et al. [1306.6329].

[47] L. Linssen, A. Miyamoto, M. Stanitzki, and H. Weerts. *Physics and Detectors at CLIC: CLIC Conceptual Design Report* (2012). [1202.5940].

[48] J. Ellis, J. R. Espinosa, G. F. Giudice, A. Hoecker, and A. Riotto. *The Probable Fate of the Standard Model*. Phys. Lett., **B679** (2009), pp. 369–375. [0906.0954].

[49] G. Degrassi, S. Di Vita, J. Elias-Miro, et al. *Higgs mass and vacuum stability in the Standard Model at NNLO*. JHEP, **08** (2012), p. 098. [1205.6497].

[50] A. V. Bednyakov, B. A. Kniehl, A. F. Pikelner, and O. L. Veretin. *Stability of the Electroweak Vacuum: Gauge Independence and Advanced Precision*. Phys. Rev. Lett., **115**.20 (2015), p. 201802. [1507.08833].

[51] M. Martinez and R. Miquel. *Multiparameter fits to the t anti-t threshold observables at a future e+ e- linear collider*. Eur. Phys. J., **C27** (2003), pp. 49–55. [hep-ph/0207315].

[52] K. Seidel, F. Simon, M. Tesar, and S. Poss. *Top quark mass measurements at and above threshold at CLIC*. Eur. Phys. J., **C73**.8 (2013), p. 2530. [1303.3758].

[53] G. T. Bodwin, E. Braaten, and G. P. Lepage. *Rigorous QCD analysis of inclusive annihilation and production of heavy quarkonium*. Phys. Rev., **D51** (1995). [Erratum: Phys. Rev.D55,5853(1997)], pp. 1125–1171. [hep-ph/9407339].

[54] M. E. Luke, A. V. Manohar, and I. Z. Rothstein. *Renormalization group scaling in nonrelativistic QCD*. Phys. Rev., **D61** (2000), p. 074025. [hep-ph/9910209].

[55] A. V. Manohar and I. W. Stewart. *The QCD heavy quark potential to order v**2: One loop matching conditions*. Phys. Rev., **D62** (2000), p. 074015. [hep-ph/0003032].

[56] A. H. Hoang and I. W. Stewart. *Ultrasoft renormalization in nonrelativistic QCD*. Phys. Rev., **D67** (2003), p. 114020. [hep-ph/0209340].

[57] B. Chokoufe Nejad, F. Bach, A. Hoang, et al. *Matching NLL threshold resummation with fixed-order QCD for differential top-pair production (working title)*. To be published, ().

[58] S. Frixione. *A General approach to jet cross-sections in QCD*. Nucl. Phys., **B507** (1997), pp. 295–314. [hep-ph/9706545].

[59] S. Frixione, P. Nason, and C. Oleari. *Matching NLO QCD computations with parton shower simulations: the POWHEG method*. Journal of High Energy Physics, **2007**.11 (2007), p. 70. [0709.2092].

[60] L. Barze, G. Montagna, P. Nason, O. Nicrosini, and F. Piccinini. *Implementation of electroweak corrections in the POWHEG BOX: single W production*. JHEP, **04** (2012), p. 037. [1202.0465].

[61] T. Ježo and P. Nason. *On the treatment of resonances in next-to-leading order calculations matched to a parton shower*. Journal of High Energy Physics, **2015**.12 (2015), p. 65. [1509.09071].

[62] J Alwall, R Frederix, S Frixione, et al. *The automated computation of tree-level and next-to-leading order differential cross sections, and their matching to parton shower simulations*. Journal of High Energy Physics, **2014**.7 (2014), p. 79. [1405.0301].

[63] C. H. Chung, M. Kramer, and T. Robens. *An alternative subtraction scheme for next-to-leading order QCD calculations*. JHEP, **06** (2011), p. 144. [1012.4948].

[64] T. Gleisberg and F. Krauss. *Automating dipole subtraction for QCD NLO calculations*. Eur. Phys. J., **C53** (2008), pp. 501–523. [0709.2881].

[65] C.-H. Chung and T. Robens. *Nagy-Soper subtraction scheme for multiparton final states*. Phys. Rev., **D87** (2013), p. 074032. [1209.1569].

[66] G. Bevilacqua, M. Czakon, M. Kubocz, and M. Worek. *Complete Nagy-Soper subtraction for next-to-leading order calculations in QCD*. JHEP, **10** (2013), p. 204. [1308.5605].

[67] T. Robens. *Nagy-Soper Subtraction: A Review*. Mod. Phys. Lett., **A28** (2013), p. 1330020. [1306.1946].

[68] Z. Nagy and D. E. Soper. *Parton showers with quantum interference*. JHEP, **09** (2007), p. 114. [0706.0017].

[69] Z. Nagy and D. E. Soper. *Parton showers with quantum interference: Leading color, with spin*. JHEP, **07** (2008), p. 025. [0805.0216].

[70] M. Czakon, H. B. Hartanto, M. Kraus, and M. Worek. *Matching the Nagy-Soper parton shower at next-to-leading order*. JHEP, **06** (2015), p. 033. [1502.00925].

[71] S. Frixione, E. Laenen, P. Motylinski, and B. R. Webber. *Single-top production in MC@NLO*. JHEP, **03** (2006), p. 092. [hep-ph/0512250].

[72] G. Altarelli and G. Parisi. *Asymptotic Freedom in Parton Language*. Nucl. Phys., **B126** (1977), pp. 298–318.

[73] M. E. Peskin and D. V. Schroeder. *An Introduction to quantum field theory*. 1995.

[74] S. Catani and M. Grazzini. *The soft gluon current at one loop order*. Nucl. Phys., **B591** (2000), pp. 435–454. [hep-ph/0007142].

[75] T. Binoth et al. *A Proposal for a standard interface between Monte Carlo tools and one-loop programs*. Comput. Phys. Commun., **181** (2010). [,1(2010)], pp. 1612–1622. [1001.1307].

[76] S. Alioli, S. Badger, J. Bellm, B. Biedermann, F. Boudjema, et al. *Update of the Binoth Les Houches Accord for a standard interface between Monte Carlo tools and one-loop programs*. Comput.Phys.Commun., **185** (2014), pp. 560–571. [1308.3462].

[77] R. K. Ellis and J. C. Sexton. *QCD Radiative Corrections to Parton Parton Scattering*. Nucl. Phys., **B269** (1986), pp. 445–484.

[78] T. Jeo, J. M. Lindert, P. Nason, C. Oleari, and S. Pozzorini. *An NLO+PS generator for $t\bar{t}$ and Wt production and decay including non-resonant and interference effects*. Eur. Phys. J., **C76**.12 (2016), p. 691. [1607.04538].

[79] A. Mück and L. Oymanns. *Resonance-improved parton-shower matching for the Drell-Yan process including electroweak corrections* (2016). [1612.04292].

[80] E. Boos and T. Ohl. "Forests and groves: Minimal gauge invariant classes of tree diagrams in gauge theories". *Physics and experiments with future linear e+ e- colliders. Proceedings, 4th Workshop, LCWS'99, Sitges, Spain, April 28-May 5, 1999. Vol. 1: Physics at linear colliders*. 1999, pp. 467–471. [hep-ph/9909487].

[81] S. Dittmaier. *A General approach to photon radiation off fermions*. Nucl. Phys., **B565** (2000), pp. 69–122. [hep-ph/9904440].

[82] E. Boos, H. J. He, W. Kilian, et al. *Strongly interacting vector bosons at TeV e+ e- linear colliders*. Phys. Rev., **D57** (1998), p. 1553. [hep-ph/9708310].

[83] R. Chierici, S. Rosati, and M. Kobel. "Strong electroweak symmetry breaking signals in w w scattering at tesla". *Physics and Experiments with Future Linear e+ e- Colliders: Proceedings, 5th International Linear Collider Workshop (LCWS 2000) Batavia, Illinois, October 24-28, 2000*. [,1906(2001)]. 2001, pp. 544–549.

[84] T. Ohl. *O'Mega & WHIZARD: Monte Carlo event generator generation for future colliders* (2000). [AIP Conf. Proc.578,638(2001)], pp. 638–641. [hep-ph/0011287].

[85] M. Moretti, T. Ohl, and J. Reuter. *O'Mega: An Optimizing Matrix Element Generator. I: Basic Algorithms.* IKDA-2001-06, LC-TOOL-2001-040, (2001), p. 29. [hep-ph/0102195].

[86] F. Staub. *Exploring new models in all detail with SARAH.* Adv. High Energy Phys., **2015** (2015), p. 840780. [1503.04200].

[87] A. Alloul, N. D. Christensen, C. Degrande, C. Duhr, and B. Fuks. *FeynRules 2.0 - A complete toolbox for tree-level phenomenology.* Comput. Phys. Commun., **185** (2014), pp. 2250–2300. [1310.1921].

[88] C. Degrande, C. Duhr, B. Fuks, et al. *UFO - The Universal FeynRules Output.* Comput. Phys. Commun., **183** (2012), pp. 1201–1214. [1108.2040].

[89] T. Ohl. *Vegas revisited: Adaptive Monte Carlo integration beyond factorization.* Computer Physics Communications, **120**.1 (1999), pp. 13–19. [hep-ph/9806432].

[90] W. Kilian, J. Reuter, and T. Robens. *NLO Event Generation for Chargino Production at the ILC.* Eur. Phys. J., **C48** (2006), pp. 389–400. [hep-ph/0607127].

[91] T. Robens, J. Kalinowski, K. Rolbiecki, W. Kilian, and J. Reuter. *(N)LO Simulation of Chargino Production and Decay.* Acta Phys. Polon., **B39** (2008), pp. 1705–1714. [0803.4161].

[92] T. Binoth, N. Greiner, A. Guffanti, et al. *Next-to-leading order QCD corrections to pp –¿ b anti-b b anti-b + X at the LHC: the quark induced case.* Phys. Lett., **B685** (2010), pp. 293–296. [0910.4379].

[93] N. Greiner, A. Guffanti, T. Reiter, and J. Reuter. *NLO QCD corrections to the production of two bottom-antibottom pairs at the LHC.* Phys. Rev. Lett., **107** (2011), p. 102002. [1105.3624].

[94] W. Kilian, T. Ohl, J. Reuter, and C. Speckner. *QCD in the Color-Flow Representation.* JHEP, **10** (2012), p. 022. [1206.3700].

[95] G. Cullen, N. Greiner, G. Heinrich, et al. *Automated One-Loop Calculations with GoSam.* Eur. Phys. J., **C72** (2012), p. 1889. [1111.2034].

[96] G. Cullen, H. van Deurzen, N. Greiner, et al. *GoSam-2.0: a tool for automated one-loop calculations within the Standard Model and beyond.* The European Physical Journal C, **74**.8 (2014), p. 3001. [1404.7096].

[97] F. Cascioli, P. Maierhöfer, and S. Pozzorini. *Scattering Amplitudes with Open Loops.* Phys.Rev.Lett., **108** (2012), p. 111601. [1111.5206].

[98] The OpenLoops one-loop generator by F. Cascioli, J. Lindert, P. Maierhöfer and S. Pozzorini is publicly available at `http://openloops.hepforge.org`.

[99] S. Actis, A. Denner, L. Hofer, A. Scharf, and S. Uccirati. *Recursive generation of one-loop amplitudes in the Standard Model.* JHEP, **04** (2013), p. 037. [1211.6316].

[100] S. Actis, A. Denner, L. Hofer, et al. *RECOLA: REcursive Computation of One-Loop Amplitudes* (2016). [1605.01090].

[101] P. Nogueira. *Automatic Feynman graph generation.* J. Comput. Phys., **105** (1993), pp. 279–289.

[102] J. A. M. Vermaseren. *New features of FORM* (2000). [math-ph/0010025].

[103] J. Kuipers, T. Ueda, J. A. M. Vermaseren, and J. Vollinga. *FORM version 4.0.* Comput. Phys. Commun., **184** (2013), pp. 1453–1467. [1203.6543].

[104] T. Reiter. *Optimising Code Generation with haggies.* Comput. Phys. Commun., **181** (2010), pp. 1301–1331. [0907.3714].

[105] G. Ossola, C. G. Papadopoulos, and R. Pittau. *Reducing full one-loop amplitudes to scalar integrals at the integrand level.* Nucl.Phys., **B763** (2007), pp. 147–169. [hep-ph/0609007].

[106] P. Mastrolia, G. Ossola, C. G. Papadopoulos, and R. Pittau. *Optimizing the Reduction of One-Loop Amplitudes.* JHEP, **06** (2008), p. 030. [0803.3964].

[107] P. Mastrolia, G. Ossola, T. Reiter, and F. Tramontano. *Scattering AMplitudes from Unitarity-based Reduction Algorithm at the Integrand-level.* JHEP, **08** (2010), p. 080. [1006.0710].

[108] H. van Deurzen, G. Luisoni, P. Mastrolia, et al. *Multi-leg One-loop Massive Amplitudes from Integrand Reduction via Laurent Expansion.* JHEP, **03** (2014), p. 115. [1312.6678].

[109] P. Mastrolia, E. Mirabella, and T. Peraro. *Integrand reduction of one-loop scattering amplitudes through Laurent series expansion.* JHEP, **06** (2012). [Erratum: JHEP11,128(2012)], p. 095. [1203.0291].

[110] G. Cullen, J. P. Guillet, G. Heinrich, et al. *Golem95C: A library for one-loop integrals with complex masses.* Comput. Phys. Commun., **182** (2011), pp. 2276–2284. [1101.5595].

[111] T. Binoth, J. P. Guillet, G. Heinrich, E. Pilon, and T. Reiter. *Golem95: A Numerical program to calculate one-loop tensor integrals with up to six external legs.* Comput. Phys. Commun., **180** (2009), pp. 2317–2330. [0810.0992].

[112] J. P. Guillet, G. Heinrich, and J. F. von Soden-Fraunhofen. *Tools for NLO automation: extension of the golem95C integral library.* Comput. Phys. Commun., **185** (2014), pp. 1828–1834. [1312.3887].

[113] G. Heinrich, G. Ossola, T. Reiter, and F. Tramontano. *Tensorial Reconstruction at the Integrand Level*. JHEP, **10** (2010), p. 105. [1008.2441].

[114] A. van Hameren. *OneLOop: For the evaluation of one-loop scalar functions*. Comput.Phys.Commun., **182** (2011), pp. 2427–2438. [1007.4716].

[115] S. Borowka, N. Greiner, G. Heinrich, et al. *Higgs Boson Pair Production in Gluon Fusion at Next-to-Leading Order with Full Top-Quark Mass Dependence*. Phys. Rev. Lett., **117**.1 (2016). [Erratum: Phys. Rev. Lett.117,no.7,079901(2016)], p. 012001. [1604.06447].

[116] W. T. Giele, Z. Kunszt, and K. Melnikov. *Full one-loop amplitudes from tree amplitudes*. JHEP, **04** (2008), p. 049. [0801.2237].

[117] C. F. Berger, Z. Bern, L. J. Dixon, et al. *An Automated Implementation of On-Shell Methods for One-Loop Amplitudes*. Phys. Rev., **D78** (2008), p. 036003. [0803.4180].

[118] A. Denner, S. Dittmaier, and L. Hofer. *COLLIER - A fortran-library for one-loop integrals*. PoS, **LL2014** (2014), p. 071. [1407.0087].

[119] A. Denner, S. Dittmaier, and L. Hofer. *Collier: a fortran-based Complex One-Loop LIbrary in Extended Regularizations*. Comput. Phys. Commun., **212** (2017), pp. 220–238. [1604.06792].

[120] A. Denner, L. Hofer, A. Scharf, and S. Uccirati. *Electroweak corrections to lepton pair production in association with two hard jets at the LHC*. JHEP, **01** (2015), p. 094. [1411.0916].

[121] A. Denner, R. Feger, and A. Scharf. *Irreducible background and interference effects for Higgs-boson production in association with a top-quark pair*. JHEP, **04** (2015), p. 008. [1412.5290].

[122] B. Biedermann, S. Bruer, A. Denner, et al. *Automation of NLO QCD and EW corrections with Sherpa and Recola* (2017). [1704.05783].

[123] N. Greiner, S. Liebler, and G. Weiglein. *Interference contributions to gluon initiated heavy Higgs production in the Two-Higgs-Doublet Model*. Eur. Phys. J., **C76**.3 (2016), p. 118. [1512.07232].

[124] G. P. Lepage. *A New Algorithm for Adaptive Multidimensional Integration*. J. Comput. Phys., **27** (1978), p. 192.

[125] R. Kleiss and R. Pittau. *Weight optimization in multichannel Monte Carlo*. Comput. Phys. Commun., **83** (1994), pp. 141–146. [hep-ph/9405257].

[126] W. Kilian, J. Reuter, S. Schmidt, and D. Wiesler. *An Analytic Initial-State Parton Shower*. JHEP, **04** (2012), p. 013. [1112.1039].

[127] M. Dobbs and J. B. Hansen. *The HepMC C++ Monte Carlo event record for High Energy Physics*. Comput. Phys. Commun., **134** (2001), pp. 41–46.

[128] A. Buckley, J. Butterworth, D. Grellscheid, et al. *Rivet user manual*. Computer Physics Communications, **184**.12 (2013), pp. 2803–2819. [1003.0694].

[129] M. Jezabek and J. H. Kuhn. *QCD Corrections to Semileptonic Decays of Heavy Quarks*. Nucl. Phys., **B314** (1989), pp. 1–6.

[130] J. M. Campbell and R. K. Ellis. *Top-Quark Processes at NLO in Production and Decay*. J. Phys., **G42**.1 (2015), p. 015005. [1204.1513].

[131] M. Cacciari, G. P. Salam, and G. Soyez. *The Anti-k(t) jet clustering algorithm*. JHEP, **04** (2008), p. 063. [0802.1189].

[132] M. Cacciari, G. P. Salam, and G. Soyez. *FastJet user manual*. The European Physical Journal C, **72**.3 (2012), p. 1896. [1111.6097].

[133] S. Frixione. "Isolated photons without fragmentation contribution". *High-energy physics. Proceedings, 29th International Conference, ICHEP'98, Vancouver, Canada, July 23-29, 1998. Vol. 1, 2*. 1998, pp. 790–794. [hep-ph/9809397].

[134] P. Nason and C. Oleari. *Next-to-leading order corrections to the production of heavy flavor jets in e+ e- collisions*. Nucl. Phys., **B521** (1998), pp. 237–273. [hep-ph/9709360].

[135] W. Bernreuther, A. Brandenburg, and P. Uwer. *Next-to-leading order QCD corrections to three jet cross-sections with massive quarks*. Phys. Rev. Lett., **79** (1997), pp. 189–192. [hep-ph/9703305].

[136] A. Brandenburg and P. Uwer. *Next-to-leading order QCD corrections and massive quarks in e+ e- —¿ three jets*. Nucl. Phys., **B515** (1998), pp. 279–320. [hep-ph/9708350].

[137] A. Brandenburg. "The Reaction e+ e- —¿ t anti-t g at next-to-leading order in alpha(s)". *Physics and experiments with future linear e+ e- colliders. Proceedings, 4th Workshop, LCWS'99, Sitges, Spain, April 28-May 5, 1999. Vol. 1: Physics at linear colliders*. [,253(1999)]. 1999, pp. 222–225. [hep-ph/9908383].

[138] R. Frederix. *Private Communication* ().

[139] S. Alioli, P. Nason, C. Oleari, and E. Re. *NLO vector-boson production matched with shower in POWHEG*. JHEP, **07** (2008), p. 060. [0805.4802].

[140] S. Alioli, P. Nason, C. Oleari, and E. Re. *NLO Higgs boson production via gluon fusion matched with shower in POWHEG*. JHEP, **04** (2009), p. 002. [0812.0578].

[141] S. Alioli, P. Nason, C. Oleari, and E. Re. *Vector boson plus one jet production in POWHEG*. JHEP, **01** (2011), p. 095. [1009.5594].

[142] P. Nason and C. Oleari. *NLO Higgs boson production via vector-boson fusion matched with shower in POWHEG.* JHEP, **02** (2010), p. 037. [0911.5299].

[143] S. Platzer. *ExSample: A Library for Sampling Sudakov-Type Distributions.* Eur. Phys. J., **C72** (2012), p. 1929. [1108.6182].

[144] M. Kraus. The POWHEG method using Catani-Seymour subtraction for electroweak corrections. MA thesis. RWTH Aachen University, 2013.

[145] A. Mück. *Parton-shower matching for electroweak corrections.* Nucl. Part. Phys. Proc., **261-262** (2015), pp. 308–310.

[146] T. Sjöstrand, S. Ask, J. R. Christiansen, et al. *An introduction to PYTHIA 8.2.* Computer Physics Communications, **191** (2015), pp. 159–177. [1410.3012].

[147] T. Horiguchi, A. Ishikawa, T. Suehara, et al. *Study of top quark pair production near threshold at the ILC* (2013). [1310.0563].

[148] F. Simon. "A First Look at the Impact of NNNLO Theory Uncertainties on Top Mass Measurements at the ILC". *Proceedings, International Workshop on Future Linear Colliders (LCWS15): Whistler, B.C., Canada, November 02-06, 2015.* 2016. [1603.04764].

[149] M. Vos et al. *Top physics at high-energy lepton colliders* (2016). [1604.08122].

[150] K. Fujii et al. *The Potential of the ILC for Discovering New Particles* (2017). [1702.05333].

[151] Y. Kiyo, A. Maier, P. Maierhofer, and P. Marquard. *Reconstruction of heavy quark current correlators at O(alpha(s)**3).* Nucl. Phys., **B823** (2009), pp. 269–287. [0907.2120].

[152] L. Chen, O. Dekkers, D. Heisler, W. Bernreuther, and Z.-G. Si. *Top-quark pair production at next-to-next-to-leading order QCD in electron positron collisions.* JHEP, **12** (2016), p. 098. [1610.07897].

[153] J. Gao and H. X. Zhu. *Top Quark Forward-Backward Asymmetry in e^+e^- Annihilation at Next-to-Next-to-Leading Order in QCD.* Phys. Rev. Lett., **113**.26 (2014), p. 262001. [1410.3165].

[154] J. Fleischer, A. Leike, T. Riemann, and A. Werthenbach. *Electroweak one loop corrections for e+ e- annihilation into t anti-top including hard bremsstrahlung.* Eur. Phys. J., **C31** (2003), pp. 37–56. [hep-ph/0302259].

[155] T. Hahn, W. Hollik, A. Lorca, T. Riemann, and A. Werthenbach. "O(alpha) electroweak corrections to the processes e+ e- —¿ tau- tau+, c anti-c, b anti-b, t anti-t: A Comparison". *Proceedings, 4th ECFA / DESY Workshop on Physics and Detectors for a 90-GeV to 800-GeV Linear e^+e^- Collider: Amsterdam, Netherlands, April 1-4, 2003*. 2003. [hep-ph/0307132].

[156] L. Guo, W.-G. Ma, R.-Y. Zhang, and S.-M. Wang. *One-loop QCD corrections to the $e^+e^- \to W^+W^-b\bar{b}$ process at the ILC*. Physics Letters B, **662**.2 (2008), pp. 150–157. [0802.4124].

[157] S. Liebler, G. Moortgat-Pick, and A. S. Papanastasiou. *Probing the top-quark width through ratios of resonance contributions of $e^+e^- \to W^+W^-b\bar{b}$* (2015). [1511.02350].

[158] A. Denner, S. Dittmaier, S. Kallweit, and S. Pozzorini. *NLO QCD corrections to WWbb production at hadron colliders*. Phys. Rev. Lett., **106** (2011), p. 052001. [1012.3975].

[159] G. Heinrich, A. Maier, R. Nisius, J. Schlenk, and J. Winter. *NLO QCD corrections to $W^+W^-b\bar{b}$ production with leptonic decays in the light of top quark mass and asymmetry measurements*. JHEP, **06** (2014), p. 158. [1312.6659].

[160] G. Bevilacqua, M. Czakon, A. van Hameren, C. G. Papadopoulos, and M. Worek. *Complete off-shell effects in top quark pair hadroproduction with leptonic decay at next-to-leading order*. JHEP, **02** (2011), p. 083. [1012.4230].

[161] A. Denner, S. Dittmaier, S. Kallweit, and S. Pozzorini. *NLO QCD corrections to off-shell top-antitop production with leptonic decays at hadron colliders*. JHEP, **10** (2012), p. 110. [1207.5018].

[162] R. Frederix. *Top Quark Induced Backgrounds to Higgs Production in the $WW^{(*)} \to ll\nu\nu$ Decay Channel at Next-to-Leading-Order in QCD*. Phys. Rev. Lett., **112**.8 (2014), p. 082002. [1311.4893].

[163] F. Cascioli, S. Kallweit, P. Maierhfer, and S. Pozzorini. *A unified NLO description of top-pair and associated Wt production*. Eur. Phys. J., **C74**.3 (2014), p. 2783. [1312.0546].

[164] A. Denner and M. Pellen. *NLO electroweak corrections to off-shell top-antitop production with leptonic decays at the LHC*. JHEP, **08** (2016), p. 155. [1607.05571].

[165] S. Dittmaier, M. Kramer, Y. Liao, M. Spira, and P. M. Zerwas. *Higgs radiation off top quarks in e+ e- collisions*. Phys. Lett., **B441** (1998), pp. 383–388. [hep-ph/9808433].

[166] G. Belanger, F. Boudjema, J. Fujimoto, et al. *Full O(alpha) electroweak and O(alpha(s)) corrections to e+ e- —¿ t anti-t H.* Phys. Lett., **B571** (2003), pp. 163–172. [hep-ph/0307029].

[167] A. Denner, S. Dittmaier, M. Roth, and M. Weber. *Electroweak radiative corrections to $e^+e^- \to t\bar{t}H$.* Physics Letters B, **575**.3-4 (2003), pp. 290–299. [0307193].

[168] J. Leveque. "Measurement of top quark properties at the Tevatron". *Proceedings, 41st Rencontres de Moriond, 2006 QCD and High Energy Hadronic Interactions: La Thuile, Val d'Aoste, Italy, Mar 18-25, 2006.* 2006, pp. 161–164. [hep-ex/0607005].

[169] A. Denner et al. *Electroweak corrections to charged-current $e^+e^- \to$ 4 fermion processes: Technical detail results.* Nucl.Phys., **B724** (2005), pp. 247–294. [hep-ph/0505042].

[170] A. Denner and S. Dittmaier. *The Complex-mass scheme for perturbative calculations with unstable particles.* Nucl. Phys. Proc. Suppl., **160** (2006). [,22(2006)], pp. 22–26. [hep-ph/0605312].

[171] A. Denner and J.-N. Lang. *The complex-mass scheme and unitarity in perturbative quantum field theory.* The European Physical Journal C, **75**.8 (2015), p. 377. [1406.6280].

[172] E. Fuchs, S. Thewes, and G. Weiglein. *Interference effects in BSM processes with a generalised narrow-width approximation.* Eur. Phys. J., **C75** (2015), p. 254. [1411.4652].

[173] K. A. Olive et al. *Review of Particle Physics.* Chin. Phys., **C38** (2014), p. 090001.

[174] A. Denner and T. Sack. *The Top width.* Nucl. Phys., **B358** (1991), pp. 46–58.

[175] A. Denner, S. Dittmaier, S. Kallweit, and S. Pozzorini. *NLO QCD corrections to off-shell top-antitop production with leptonic decays at hadron colliders.* Journal of High Energy Physics, **2012**.10 (2012), p. 110. [arXiv:1207.5018v1].

[176] M. Jezabek and J. H. Kuhn. *Semileptonic Decays of Top Quarks.* Phys. Lett., **B207** (1988), pp. 91–96.

[177] M. Jezabek and J. H. Kuhn. *Lepton Spectra from Heavy Quark Decay.* Nucl. Phys., **B320** (1989), pp. 20–44.

[178] K. Agashe et al. "Working Group Report: Top Quark". *Proceedings, Community Summer Study 2013: Snowmass on the Mississippi (CSS2013): Minneapolis, MN, USA, July 29-August 6, 2013.* 2013. [1311.2028].

[179] T. Price, P. Roloff, J. Strube, and T. Tanabe. *Full simulation study of the top Yukawa coupling at the ILC at $\sqrt{s} = 1$ TeV*. Eur. Phys. J., **C75**.7 (2015), p. 309. [1409.7157].

[180] P. Roloff and J. Strube. *Measurement of the top Yukawa Coupling at a 1 TeV International Linear Collider using the SiD detector* (2013). [1307.7644].

[181] P. Roloff. *Private Communication* ().

[182] M. S. Amjad, M. Boronat, T. Frisson, et al. *A precise determination of top quark electro-weak couplings at the ILC operating at $\sqrt{s} = 500$ GeV* (2013). [1307.8102].

[183] M. S. Amjad et al. *A precise characterisation of the top quark electro-weak vertices at the ILC*. Eur. Phys. J., **C75**.10 (2015), p. 512. [1505.06020].

[184] T. Barklow, J. Brau, K. Fujii, et al. *ILC Operating Scenarios* (2015). [1506.07830].

[185] R. Frederix, S. Frixione, A. S. Papanastasiou, S. Prestel, and P. Torrielli. *Off-shell single-top production at NLO matched to parton showers*. JHEP, **06** (2016), p. 027. [1603.01178].

[186] M. Kraus. "NLO QCD off-shell effects for top pair production with a jet in the dilepton channel". *4th Large Hadron Collider Physics Conference (LHCP 2016) Lund, Sweden, June 13-18, 2016*. 2016. [1608.05296].

[187] A. Kharchilava. *Top mass determination in leptonic final states with J/ψ*. Phys. Lett., **B476** (2000), pp. 73–78. [hep-ph/9912320].

[188] M. Beneke et al. "Top quark physics". *1999 CERN Workshop on standard model physics (and more) at the LHC, CERN, Geneva, Switzerland, 25-26 May: Proceedings*. 2000. [hep-ph/0003033].

[189] S. Biswas, K. Melnikov, and M. Schulze. *Next-to-leading order QCD effects and the top quark mass measurements at the LHC*. JHEP, **08** (2010), p. 048. [1006.0910].

[190] W. Bernreuther, R. Bonciani, T. Gehrmann, et al. *Two-Parton Contribution to the Heavy-Quark Forward-Backward Asymmetry in NNLO QCD*. Nucl. Phys., **B750** (2006), pp. 83–107. [0604031].

[191] F. Richard. *Present and future constraints on top EW couplings* (2014). [1403.2893].

[192] I. Garcia, E. Ros, J. Trenado, and M. Vos. "The potential of the $t\bar{t}$ charge asymmetry measurement at a Linear Collider with $\sqrt{s}$ in the range 500 GeV - 1 TeV". *Helmholtz Alliance Linear Collider Forum: Proceedings of the Workshops Hamburg, Munich, Hamburg 2010-2012, Germany*. DESY. Hamburg: DESY, 2013, pp. 93–99.

[193] A. H. Hoang, A. V. Manohar, I. W. Stewart, and T. Teubner. *The Threshold t anti-t cross-section at NNLL order.* Phys. Rev., **D65** (2002), p. 014014. [hep-ph/0107144].

[194] A. H. Hoang and M. Stahlhofen. *The Top-Antitop Threshold at the ILC: NNLL QCD Uncertainties.* JHEP, **05** (2014), p. 121. [1309.6323].

[195] M. Beneke, Y. Kiyo, P. Marquard, et al. *Next-to-Next-to-Next-to-Leading Order QCD Prediction for the Top Antitop S-Wave Pair Production Cross Section Near Threshold in e^+e^- Annihilation.* Phys. Rev. Lett., **115**.19 (2015), p. 192001. [1506.06864].

[196] M. Beneke, A. Maier, J. Piclum, and T. Rauh. *Non-QCD contributions to top-pair production near threshold.* PoS, **EPS-HEP2015** (2015), p. 315. [1511.00801].

[197] B. A. Kniehl and O. L. Veretin. *Two-loop electroweak threshold corrections to the bottom and top Yukawa couplings.* Nucl. Phys., **B885** (2014). [Erratum: Nucl. Phys.B894,56(2015)], pp. 459–480. [1401.1844].

[198] F. Jegerlehner, M. Yu. Kalmykov, and B. A. Kniehl. *On the difference between the pole and the $\overline{MS}$ masses of the top quark at the electroweak scale.* Phys. Lett., **B722** (2013), pp. 123–129. [1212.4319].

[199] P. Marquard, A. V. Smirnov, V. A. Smirnov, M. Steinhauser, and D. Wellmann. $\overline{\text{MS}}$*-on-shell quark mass relation up to four loops in QCD and a general SU(N) gauge group.* Phys. Rev., **D94**.7 (2016), p. 074025. [1606.06754].

[200] A. H. Hoang and T. Teubner. *Top quark pair production close to threshold: Top mass, width and momentum distribution.* Phys. Rev., **D60** (1999), p. 114027. [hep-ph/9904468].

[201] W. Beenakker, F. A. Berends, and A. P. Chapovsky. *Radiative corrections to pair production of unstable particles: results for e+ e- —¿ four fermions.* Nucl. Phys., **B548** (1999), pp. 3–59. [hep-ph/9811481].

[202] A. Denner, S. Dittmaier, M. Roth, and D. Wackeroth. *O(alpha) corrections to e+ e- —¿ W W —¿ four fermions (+ gamma): First numerical results from RACOON W W.* Phys. Lett., **B475** (2000), pp. 127–134. [hep-ph/9912261].

[203] B. Chokoufé. Scrutinizing the Top Quark at Lepton Colliders with Higher Orders. PhD thesis. University of Hamburg, 2017.

[204] K. Agashe, R. Franceschini, and D. Kim. *Simple invariance of two-body decay kinematics.* Phys. Rev., **D88**.5 (2013), p. 057701. [1209.0772].

[205] K. Agashe, R. Franceschini, S. Hong, and D. Kim. *Energy spectra of massive two-body decay products and mass measurement.* JHEP, **04** (2016), p. 151. [1512.02265].

[206] K. Agashe, R. Franceschini, D. Kim, and M. Schulze. *Top quark mass determination from the energy peaks of b-jets and B-hadrons at NLO QCD.* Eur. Phys. J., **C76**.11 (2016), p. 636. [1603.03445].

[207] M. Czakon. *A novel subtraction scheme for double-real radiation at NNLO.* Phys. Lett., **B693** (2010), pp. 259–268. [1005.0274].

[208] A. Gehrmann-De Ridder, T. Gehrmann, and E. W. N. Glover. *Antenna subtraction at NNLO.* JHEP, **09** (2005), p. 056. [hep-ph/0505111].

[209] S. Alioli, P. Nason, C. Oleari, and E. Re. *NLO single-top production matched with shower in POWHEG: s- and t-channel contributions.* JHEP, **09** (2009). [Erratum: JHEP02,011(2010)], p. 111. [0907.4076].

[210] P. Nason and G. Ridolfi. *A Positive-weight next-to-leading-order Monte Carlo for Z pair hadroproduction.* JHEP, **08** (2006), p. 077. [hep-ph/0606275].

Eidesstattliche Versicherung

Hiermit erkläre ich an Eides statt, dass ich die vorliegende Dissertationsschrift selbst verfasst und keine anderen als die angegebenen Quellen und Hilfsmittel benutzt habe.

Die eingereichte schriftliche Fassung entspricht der auf dem elektronischen Speichermedium.

Die Dissertation wurde in der vorgelegten oder einer ähnlichen Form nicht schon einmal in einem früheren Promotionsverfahren angenommen oder als ungenügend bewertet.

Hamburg, den April 26, 2017 _____

Christian Weiss